WORLD METEOROLOGICAL ORGANIZATION

WMO SATELLITE REPORTS

APPLICATIONS WITH METEOROLOGICAL SATELLITES

by

W. Paul Menzel

NOAA/NESDIS
Office of Research and Applications
Cooperative Institute for Meteorological Satellite Studies
University of Wisconsin

2001

SAT-28

TECHNICAL DOCUMENT

WMO/TD No. 1078

National Oceanic and Atmospheric Administration
TIROS Satellites and Satellite Meteorology

ERRATA NOTICE

One or more conditions of the original document may affect the quality of the image, such as:

Discolored pages
Faded or light ink
Binding intrudes into the text

This has been a co-operative project between the NOAA Central Library and the Climate Database Modernization Program, National Climate Data Center (NCDC). To view the original document contact the NOAA Central Library in Silver Spring, MD at (301) 713-2607 x124 or Library.Reference@noaa.gov.

HOV Services
Imaging Contractor
12200 Kiln Court
Beltsville, MD 20704-1387
January 26, 2009

TABLE OF CONTENTS

CHAPTER 5 - THE RADIATIVE TRANSFER EQUATION (RTE)

CHAPTER 6 - CLOUDS

CHAPTER 7 - SURFACE TEMPERATURE

CHAPTER 8 - TECHNIQUES FOR DETERMINING ATMOSPHERIC PARAMETERS

CHAPTER 9 - TECHNIQUES FOR DETERMINING ATMOSPHERIC MOTIONS

CHAPTER 10 - APPLICATIONS OF GEOSTATIONARY SATELLITE SOUNDING DATA

CHAPTER 11 - SATELLITE ORBITS

CHAPTER 12 - RADIOMETER DESIGN CONSIDERATIONS

APPENDICES

CHAPTER 1

EVOLUTION OF SATELLITE METEOROLOGY

1.1 Before satellites

Since colonial times, the interest in today's weather and predicting tomorrow's has led to attempts at sensing the earth's atmosphere. Probing of the atmosphere before rockets and earth orbiting satellites consisted mostly of balloon and kite flights. Temperature and pressure sensing devices were attached and some method of recording the data was devised. Benjamin Franklin's kite flights are the most well known of the early meteorological observations. Early in the twentieth century, the Weather Bureau organized a regularly scheduled programme of kite observations that involved seven stations at most. In this programmed probing of the atmosphere, kites were launched for 4 or 5 hours to heights up to three or four miles. The reeling in of the kite was seldom trouble free, as witnessed in this account by a Bureau kite flyer.

> There seemed to be a thunderstorm approaching... My reeler and I commenced to pull in the kite. When the kite was still 3,000 feet up...a bolt from the clouds was seen, by others, to hit the kite. We stopped reeling; we had to. I have been nearly in front of a 6-inch naval rifle at its discharge, and the noise was very mild compared to the report which we heard at the reel... Fortunately, the kite reeler was wearing rubber overshoes, but I was not, and in consequence got a burn on the sole of my foot... Several really ludicrous events can occur when a kite is behaving badly. Sometimes the operators get knocked down and dragged about by the kite in attempting to land it, while the urchins, at a distance, shout humiliating taunts.

Even with these problems, the kite was more practical than the manned balloon, and its use continued until 1933, when airplanes replaced kites.

The rapid development of the airplane during World War I stimulated new ways to obtain upper air observations. In 1925 the Bureau began an experimental programme of daily observations from sensors that were attached on the wings of the aircraft. The comparative ease of this data gathering soon saw the kite phased out completely. With the aircraft flights, observations over a relatively large local area were now possible and early attempts at depicting synoptic flow began.

In 1929, Robert Goddard launched a payload on a rocket that included a barometer, a thermometer, and a camera. The origins of the meteorological satellite programme are often traced back to this effort. Advances in rocket technology during World War II led to the first composite photographs of the top of the atmosphere. Parallel advances in the development of television cameras made the first meteorological satellites possible.

1.2 Evolution of the Polar Orbiting Satellites

On 4 October 1957 the era of satellite meteorology began as the Soviet Union launched Sputnik I. Sputnik provided the first space views of our planet's surface and atmosphere. The United States accelerated its programme to launch the first meteorological satellite TIROS-1 (Television Infrared Observational Satellite) on 1 April 1960. The great advantage of a satellite platform for meteorological measurements over a large area was realized immediately. For the first time, complete pictures of the clouds associated with large weather systems were seen. The operational meteorological satellite programme evolved rapidly thereafter. A total of ten TIROS satellites were launched (the last on 2 July 1965) which carried vidicon camera systems for daytime visible imaging and passive infrared radiometers for sensing during both day and night. Important steps in the TIROS programme included:

(a) The Automatic Picture Transmission (APT) capability was demonstrated with TIROS-VIII; very simple ground receivers around the world could now receive real time satellite images - APT has been recognized as one of the United States' greatest "ambassadors" of goodwill (Popham, 1985);

(b) The change to a "wheel" mode of operation with TIROS-IX, which meant that television pictures were taken when the camera was pointed directly at satellite subpoint - this allowed for ease in navigation of the imagery; and,

(c) The introduction of sun synchronous orbits, which meant that a satellite crossed the equator at the same local solar time each orbit - this allowed for the development of worldwide mosaics of satellite images and opened the door for a number of important scientific projects, including the World Climate Research Programme.

The experimental TIROS series gave way to nine operational TOS satellites launched between 1966 and 1969, named ESSA-1 through ESSA-9 for the parent agency at that time, the Environmental Science Services Administration. In parallel with the operational ESSA series, NASA, developed and maintained a research series of seven NIMBUS satellites that had as one of its major goals to serve as a test bed for future operational polar orbiting instruments; in that area it was very fruitful (e.g., 3-axis stabilization, advanced vidicon camera systems, infrared imagers, microwave radiometers, and infrared sounders). Additional detail concerning the impact of NIMBUS instrumentation on the operational polar orbiting satellites may be found in Allison *et al,* (1977). NIMBUS provided a number of science firsts and laid the foundation for satellite data use in "Earth Applications Science." Hass and Shapiro (1982) provide an excellent overview of NIMBUS achievements in the areas of meteorology, oceanography, hydrology, geology, geomorphology, geography, cartography, and agriculture; they point out that the roots of the Landsat programme can be traced directly back to NIMBUS.

The NIMBUS satellites also served as pathfinders for global weather experiments organized by the Committee on Space and Atmospheric Research (COSPAR). COSPAR Working Group 6 deliberations and publications served as the foundation for the general nature and detailed composition of the satellite observing system in the First Global Atmospheric Research Programme Global Experiment and of the international operational system that followed.

Significant advances with the ESSA series included routine global coverage using on board recording systems on odd numbered spacecraft, and APT on even numbered satellites. As forecast by Oliver and Ferguson (1966), the global coverage provided by the on board storage capability allowed the National Environmental Satellite Service to provide operational satellite support to forecast centres for the first time. Based on the work of Oliver *et al,* (1964) jet streams, mid-tropospheric trough and ridge lines, and vorticity centres were readily located in the ESSA images. While the feasibility of using satellite imagery to locate and track tropical storms was recognized almost immediately in the satellite programme (Sadler, 1962), it was not until the ESSA series of satellites that routine surveillance was assured and techniques to estimate hurricane intensity from satellites became a regular part of weather forecasting (Dvorak, 1972). ESSA was followed by Improved TOS (ITS), which allowed the global remote coverage and APT services to be combined on one satellite. ITS-1, the first of an operational series of three axis stabilized satellites, was launched in January of 1970. Three axis stabilization allowed scanning radiometers to be flown on operational meteorological satellites and provided routine infrared window coverage both day and night. The launch of NOAA-2, on October 15, 1972, was significant to the operational cloud imaging programme: it marked the end of the vidicon era and the beginning of the era of multi-channel high resolution radiometers. The era of television cameras gave way to calibrated scanning radiometers, although initially only visible and infrared window data were available on the Very High Resolution Radiometer (VHRR). The next major step occurred in October of 1978 with the launch of TIROS-N. TIROS-N's imaging system was a four spectral channel Advanced VHRR (AVHRR). According to Rao *et al,* (1990) that step "provided data

for not only day and night imaging in the visible and infrared but also for sea surface temperature determination, estimation of heat budget components, and identification of snow and sea ice." AVHRR rapidly moved to a five spectral channel system, with all channels providing imagery at 1.1 km resolution at nadir. The following channels are the backbone of the imaging system: (a) 0.58-0.68 microns; (b) 0.72-1.1 microns; (c) 3.55-3.93 microns; (d) 10.3-11.3 microns; and, (e) 11.5-12.5 microns.

With the successful creation of a global picture of the earth's surface and atmosphere accomplished in 1964, the primary emphasis shifted toward measuring the atmosphere's vertical distribution of temperature and moisture to better initialize global numerical weather prediction models. King (1958) and Kaplan (1959) published works that indicated that it is possible to infer the temperature of the atmosphere or the concentration of the attenuating gas, as a function of atmospheric pressure level. King showed that measurements of the atmosphere at several tangential viewing angles could also provide information on temperature changes with altitude. Kaplan suggested this could be done through measurements in several narrow and carefully selected spectral intervals, by inverting the process of radiative transfer. Temperature profiles are derived using the emission from CO_2 in the atmosphere, and concentrations of moisture are then inferred with emissions from H_2O in the atmosphere. Surface temperatures are estimated from observations in the spectral regions where the atmosphere is most transparent. Wark and Fleming (1966) detailed indirect measurement of atmospheric profiles from satellites.

Meteorological observations from space are made through the electromagnetic radiation leaving the atmosphere. Outgoing radiation from earth to space varies with wavelength for two reasons: (a) Planck function dependence on wavelength, and (b) absorption by atmospheric gases of differing molecular structure (CO_2, H_2O, O_3...). Figure 1.1 shows an observed infrared spectrum of the radiance to space. Around absorbing bands of the constituent gases of the atmosphere, vertical profiles of atmospheric parameters can be derived. Sampling in the spectral region at the centre of the absorption band yields radiation from the upper levels of the atmosphere (e.g., radiation from below has already been absorbed by the atmospheric gas); sampling in spectral regions away from the centre of the absorption band yields radiation from successively lower levels of the atmosphere. Away from the absorption band are the windows to the bottom of the atmosphere. The IRIS (Infrared Interferometer Spectrometer) in 1969 observed surface temperatures of 320 K in the 11 micron window region of the spectrum and tropopause emissions of 210 K in the 15 micron absorption band. As the spectral region moves toward the centre of the CO_2 absorption band, the radiation temperature decreases due to the decrease of temperature with altitude in the lower atmosphere.

With careful selection of spectral bands in and around an absorbing band, it was suggested that multispectral observations can yield information about the vertical structure of atmospheric temperature and moisture. The concept of profile retrieval is based on the fact that atmospheric absorption and transmittance are highly dependent on the frequency of the radiation and the amount of the absorbing gas. At frequencies close to the centres of absorbing bands, a small amount of gas results in considerable attenuation in the transmission of the radiation; therefore most of the outgoing radiation arises from the upper levels of the atmosphere. At frequencies far from the centres of the band, a relatively large amount of the absorbing gas is required to attenuate transmission; therefore the outgoing radiation arises from the lower levels of the atmosphere. However, the derivation of temperature profiles is complicated by the fact that upwelling radiance sensed at a given wavelength arises from a rather large vertical depth (roughly 10 km) of the atmosphere. In addition, the radiance sensed in the neighbouring spectral regions arises from deep overlapping layers. This causes the radiance observations to be dependent and the inverse solution to the radiative transfer equation for temperature profiles to be non-unique. Differing analytical approaches and types of ancillary data are needed to constrain the solution in order to render temperature profiles.

The first temperature retrievals were accomplished with the Satellite Infrared Spectrometer (SIRS), a grating spectrometer aboard NIMBUS-3 in 1969 (Wark *et al*, 1970). Comparison with

radiosonde observed profiles showed that the satellite-derived temperature profiles were very representative overall, with detailed vertical features smoothed out. The major problems with the early SIRS observations were caused by clouds which usually existed within the instrument's 250 km diameter field of view. Also the SIRS observed only along the sub-orbital track and consequently there were large gaps in data between orbits. In spite of these problems, the SIRS data immediately showed promise of benefiting the current weather analysis/forecast operation and was put into operational use on 24 May 1969, barely one month after launch (Smith *et al*, 1970). An example of SIRS impact on model analyses is shown in Figure 1.2. Also on NIMBUS-3 was the Infrared Interferometer Spectrometer (IRIS), a Michelson interferometer that measured the earth emitted radiation at high spectral resolution (5 cm^{-1}). IRIS had 100 km resolution and was nadir viewing only. These interferometer measurements of the terrestrial spectrum revealed details of the carbon dioxide, water vapour, and ozone absorption bands never seen before (Hanel *et al*, 1971).

In 1972 a scheme was devised to reduce the influence of clouds by employing a higher spatial resolution (30 km) and by taking spatially continuous sounding observations, now possible with cross track scanning, using the seven channel Infrared Temperature Profile Radiometer (ITPR) on board NIMBUS-5 (Smith *et al*, 1974a). With an adjacent field of view method, clear radiances could now be inferred by assuming that the variation in radiance between two adjacent fields of view is due to cloud amount only. The ITPR concept was highly successful in alleviating the influence of clouds on the synoptic scale. In fact, soundings to the earth's surface were now possible over 95 percent of the globe with an average spacing of 250 nautical miles.

Also on board NIMBUS-5 was the first microwave sounding device, NIMBUS Experimental Microwave Spectrometer (NEMS), a nadir viewing 5-channel instrument (Staelin *et al*, 1973). The NEMS demonstrated the capability to probe through clouds, even dense overcast. Good comparisons of ITPR, NEMS, and radiosonde data were achieved. It was found, however, that best results were achieved from an amalgamation of infrared and microwave radiance data in the temperature profile inversion process thereby providing the maximum available thermal information, regardless of cloud conditions (Smith *et al*, 1974b).

The third satellite in the ITS series was launched in mid-October of 1972, called NOAA-2 for the parent agency renamed the National Oceanic and Atmospheric Administration. It carried the first Very High Resolution Radiometer (VHRR) and allowed operational thermodynamic soundings with its Vertical Temperature Profile Radiometer (VTPR). While input to numerical forecast models had relied on cloud image interpretation through a programme with the catchy acronym of SINAP, Satellite Input to Numerical Analysis and Prediction (Nagel and Hayden, 1971), soundings from satellites now allowed for quantitative input (Smith *et al*, 1986).

From the available results and studies in the early 1970s, it was recognized that the optimum temperature profile results would be achieved by taking advantage of the unique characteristics offered by the 4.3 micron, 15 micron, and 0.5 cm absorption bands. As a consequence, the Nimbus-6 High resolution Infrared Radiation Sounder (HIRS) experiment was designed to accommodate channels in both the 4.3 and 15 micron infrared regions and these were complimented by the 0.5 cm microwave wavelength channels of a Scanning Microwave Spectrometer (SCAMS). The HIRS also was designed with passively cooled detectors to allow for complete cross-track scanning and the SCAMS also scanned, but with lower spatial resolution. The HIRS experiment successfully demonstrated an improved sounding capability in the lower troposphere due to the inclusion of the 4.3 micron observations.

The operational implementation of these instruments was achieved on the TIROS-N spacecraft in 1978 which carried the HIRS and the Microwave Sounding Unit (MSU). The channels were carefully selected to cover the depth of the atmosphere. Infrared soundings of 30 km resolution horizontally were supplemented with microwave soundings of 150 km resolution horizontally (Smith *et al*, 1979). The complement of infrared and microwave instruments aboard each of the polar orbiting

spacecraft provided complete global coverage of vertical temperature and moisture profile data every 12 hours at 250 km spacing (Smith *et al*, 1981a). Figure 1.3 shows the global rms differences for the month of April 1980 between TIROS and radiosonde temperature profiles. The 2.5 C differences should not be interpreted literally as error; space and time discrepancies between the two types of observations contribute significantly as does atmospheric variability. Even with microwave assistance, it is evident that the sounding accuracy is degraded with increasing cloudiness.

The TIROS-N series of satellites evolved to the NOAA Advanced TIROS-N satellite series that carry:

(a) A five channel Advanced VHRR (AVHRR) for observing cloud cover and weather systems, deriving sea surface temperature (McClain, 1979), detecting urban heat islands (Matson *et al*, 1978) and fires (Matson and Dozier, 1981), and estimating vegetation indices (Tarpley *et al*, 1984);

(b) An improved High resolution Infrared Radiation Sounder (HIRS/2) for deriving global temperature and moisture soundings (Smith *et al*, 1986);

(c) A low spatial resolution Microwave Sounding Unit (MSU) primarily for deriving temperature soundings in cloud covered regions;

(d) A data collection system; and,

(e) Search And Rescue (SAR) instruments for aiding in search and rescue operations.

The current generation of NOAA polar satellites carry improved AVHRR (addition of a channel at 1.6 microns for cloud, ice and snow discrimination) and HIRS instruments that continue to provide their basic services; and, most exciting, two Advanced Microwave Sounding Units (AMSU) that provide temperature sounding information at about 50 km horizontal resolution and moisture sounding information at about 15 km horizontal resolution. With the advent in May 1998 of this enhanced microwave sounder (more channels, better spatial resolution) and continuation of the high spatial resolution infrared (good spatial resolution, evolving to higher spectral resolution), an all weather sounding capability was established.

The TIROS-N instruments are now used routinely to measure atmospheric temperature and moisture, surface temperature, and cloud parameters. A large range of applications have been developed that are pertinent to nowcasting as well as operational short-range forecasting; they include:

(a) Subsynoptic scale temperature and moisture analyses for severe weather monitoring and prediction;

(b) Subsynoptic scale analysis of surface temperature;

(c) Subsynoptic scale analysis of atmospheric stability;

(d) Subsynoptic scale updating of aviation grid point temperature and wind fields;

(e) Estimation of the cloud height and amount;

(f) Estimation of tropical cyclone intensity, maximum wind strength, and central position; and

(g) Estimation of total ozone amount.

These data have become part of the operational practices of weather services internationally (Chedin, 1989).

For details concerning scientific applications of polar orbiting satellite imagery and sounding data, the reader is referred to Rao *et al,* (1990). That book contains sections on applications of satellite data in meteorology, applications of satellite data to land and ocean sciences, satellites and climate applications, and the use of weather satellite data in agricultural applications. For details in the use of polar orbiting imagery, also see Scorer (1990).

1.3 The Geostationary Programme

For meteorological applications, two types of satellite orbits have been employed. Thus far, we have discussed instruments on the polar sun-synchronous orbit from which global observations can be collected every twelve hours. The other orbit (the geostationary orbit above the equator) has a period of 24 hours and thereby enables continuous surveillance of the weather. Polar orbits range from 600 to 1600 km in altitude, whereas the geostationary altitude is 38,000 km.

On 6 December 1966, a stellar day in satellite meteorology, the first Applications Technology Satellite (ATS-1) was launched. ATS-1's spin scan cloud camera (Suomi and Parent, 1968) was capable of providing full disk visible images of the earth and its cloud cover every 20 minutes. The inclusion of the spin scan cloud camera on ATS-1 occurred because of an extraordinary effort by Verner Suomi and Homer Newell, who made it possible to add this new capability to ATS-1 when the satellite was already well into its fabrication. Meteorologists were astounded by the first views of global animations of clouds and cloud systems in motion. According to Johnson (1982) "as Morris [Tepper of NASA] predicted, geostationary satellite images can be used to track clouds from which winds at cloud altitude can be inferred." Research into tracking clouds and producing winds using image sequences began almost immediately (Hubert and Whitney, 1971), and, as will be discussed in section 5, is still an area of intense investigation. By the early 1970s ATS imagery was being used in operational forecast centres, with the first movie loops being used at the National Severe Storm Forecast Centre (NSSFC) in the spring of 1972.

As with the polar programme, NASA research and development led to the operational geostationary satellite programme. ATS was mainly a communications system test bed; however, its success in the meteorological arena led to NASA's development of the Synchronous Meteorological Satellite (SMS), an operational prototype dedicated to meteorology. SMS-1 was launched May 1974 and SMS-2 was launched February 1975: those satellites were positioned above the equator at 75W and 135W, which today remain the nominal positions of the United States' eastern and western Geostationary Operational Environmental Satellites (GOES). The two NASA prototypes, SMS-1 and SMS-2, and the subsequent NOAA GOES provided three important functions which remain central to today's geostationary satellite programme:

(a) Multispectral imagery from the Visible and Infrared Spin Scan Radiometer (VISSR), which provided routine coverage of the earth and its cloud cover in the visible and infrared window channels. VISSR provided visible imagery at 1 km spatial resolution and infrared window channel imagery at 7 km spatial resolution;

(b) Weather Facsimile (WEFAX) which provided the transmission of low resolution satellite images and conventional weather maps to users with low cost receiving stations; and,

(c) Data Collection System (DCS) which allows for the relay of data from remote data collection platforms through the satellite to a central processing facility.

In 1977 the European Space Agency launched a geostationary Meteosat, which provided visible imagery at 2.5 km spatial resolution, infrared window band imagery at 5 km spatial resolution, and also water vapour band imagery at 5 km spatial resolution. These new images in the water vapour band provided a very different view of the planet earth. Upper tropospheric humidity and high cloud features dominate the image and indicate synoptic scale circulations. Three GOES and one Meteosat were used as part of a Global Atmospheric Research Programme (GARP) in 1979 to define atmospheric circulations. Organized by the Committee on Space and Atmospheric Research (COSPAR), this was the first international experiment to use satellites.

By 1980, the GOES system evolved to include an atmospheric temperature and moisture sounding capability with the addition of more spectral bands to the spin scan radiometer; it was called the VISSR Atmospheric Sounder (VAS). The first GOES-VAS, GOES-4, was launched in September of 1980. The addition of spectral channels represented a major improvement in satellite capabilities (Smith *et al*, 1981b); however, imaging and sounding could not be done at the same time. Furthermore, a spinning satellite, viewing the earth only 5 percent of the satellite's duty cycle, made it difficult to attain the instrument signal-to-noise needed for either high quality soundings or the high spatial resolution infrared views of the earth needed to satisfy the increased sophistication of the data's user community. Recognizing those limitations, NOAA developed its next generation of geostationary satellites, GOES I-M (Menzel and Purdom, 1994). The GOES I-M system was introduced with the launch of GOES-I on 13 April 1994, designated GOES-8 after attaining geostationary orbit. GOES-9 followed in May 1995.

As imagery from polar orbiting satellites helped advance understanding of synoptic scale phenomena, imagery from geostationary satellites helped advance understanding of the mesoscale. Prior to the geostationary satellite the mesoscale was a "data sparse" region; meteorologists were forced to make inferences about mesoscale phenomena from macroscale observations. Today, geostationary satellite imagery represent the equivalent of a "reporting station" every 1 km with visible data (every 4 km with infrared data) and hence shows features that are infrequently detected by fixed observing sites. The clouds and cloud patterns in a satellite image provide a visualization of mesoscale meteorological processes. When imagery is viewed in animation, the movement, orientation, and development of important mesoscale features can be observed, adding a new dimension to mesoscale reasoning. Furthermore, animation provides observations of convective behaviour at temporal and spatial resolutions compatible with the scale of the mechanisms responsible for triggering deep and intense convective storms (Purdom, 1993). A number of important discoveries using geostationary satellite imagery (see Figure 1.4) have had a dramatic impact on mesoscale meteorology and, in turn, short term forecasts and warnings. For example:

(a) Prior to squall line formation, organized cumulus development within a surface convergence zone is usually detectable in satellite imagery (Purdom, 1976). The ability to use satellite imagery to detect areas of incipient squall line development has aided in the location and orientation as well as the timing of severe weather watches;

(b) The importance of thunderstorm outflow boundaries, often termed arc cloud lines, in the development and evolution of all types of thunderstorms was first recognized using animated satellite imagery (Purdom, 1976). The recognition of one such large scale boundary resulted in a very accurate, long lead time watch box for a major tornado outbreak across North and South Carolina on 28 March 1984 (NOAA, 1984). Furthermore, Doppler radar has confirmed the importance of recognizing and tracking arc cloud lines for short term convective forecasting (COMET, 1992);

(c) The size, duration and high degree of organization of mesoscale convective complexes were not recognized prior to their discovery using infrared satellite imagery (Maddox, 1980). These complexes, which are responsible for much of the summer rainfall in the mid-west, have since been the focus of intense investigations;

(d) The location, tracking and monitoring of hurricanes and tropical storms has been one of the most successful aspects of the satellite programme (Rao *et al*, 1990), and a technique for using satellite data to estimate hurricane intensity (Dvorak, 1972, 1984) is used routinely at the National Hurricane Centre. According to Robert Sheets (1990) who was at the time the Director of the National Hurricane Centre: "in the estimation of the author, and many others, the development of the Dvorak technique (1972, 1984) has been the single greatest achievement in support of operational tropical cyclone forecasting by a researcher to date";

(e) Prior to the polar satellite programme the existence of polar lows (Twitchell *et al*, 1989) was not widely recognized, and recently, geostationary satellite imagery have been used to study polar low formation near the coast of Labrador (Rasmussen and Purdom, 1992);

(f) The influence of early morning cloud cover on the subsequent development of afternoon convection was not realized prior to the geostationary satellite era (Weiss and Purdom, 1974; Purdom and Gurka, 1974). The importance of this phenomenon has subsequently been simulated using a sophisticated mesoscale model (Segal *et al,* 1986);

(g) Satellite imagery has had a dramatic impact on our ability to detect and forecast fog behaviour. The role of inward mixing in forecasting the dissipation of fog was not well recognized prior to the work of Gurka (1978) with geostationary satellite imagery. Polar orbiting satellite imagery has been used for a number of years to detect fog, both day and night, using a multispectral technique (Eyre, 1984), and that technique has been extended with the GOES multispectral imagery (Ellrod, 1992) to include monitoring of fog formation at night;

(h) The GOES infrared channel at 6.7 microns is strongly affected by upper level water vapour, and is often called the water vapour channel. The ability of imagery from this channel to depict upper level flow has provided meteorologists with the ability to view atmospheric systems and their changes in time with a perspective never before possible. As has been shown by Velden (1987) and Weldon and Holmes (1991), this channel may be used for a variety of synoptic and mesoscale applications.

The advantage of continuous multispectral monitoring of atmospheric stability and moisture is well-demonstrated in an example from 8 July 1997. A sequence of the GOES LI DPI at two hour intervals over the western plains (Figure 1.5, top) shows strong de-stabilization in Kansas and northern Oklahoma during the afternoon (1746 to 2146 UTC) as LI values of -8 to -12 C give way to convective clouds. Radiosonde values (Figure 1.5, bottom) show generally very unstable air (LI of -5 to -6 C) across Nebraska, Missouri, Oklahoma, and northern Texas, while the GOES LI DPI emphasizes the Kansas and northern Oklahoma region within that area. Severe weather watch boxes from the Storm Prediction Center (SPC) covered Missouri and Arkansas as well as eastern Colorado (as the mesoscale vorticity center drifted southward across Missouri into Arkansas with a surface outflow ahead of it). However, storms also formed in west central Kansas by 2146 UTC and continued to develop across the state with numerous reports of hail. Although the Arkansas and eastern Colorado activity was well anticipated at the SPC, central Kansas convection did not appear within a watch area. The strong and focused de-stabilization as noted in the GOES LI DPI sequence over Kansas and northern Oklahoma presented good supporting evidence for development of strong storms in that region.

GOES data has become a critical part of National Weather Service operations, with direct reception of the full digital GOES data stream at national centres while local weather service forecast offices receive limited analogue imagery through a land line service known as GOES-TAP. All National Weather Service offices are expected to receive a full complement of digital imagery when a programme known as AWIPS (Advanced Weather Interactive Processing System) comes to fruition near the end of this century. Furthermore, quantitative products such as cloud drift winds,

thermodynamic soundings and stability parameters, and precipitation amount are routinely produced from GOES data.

Rapid interval imaging has been an important component of the GOES research programme since 1975. Research with SMS and GOES imagery included taking a series of images at 3 minute intervals to study severe storm development (Fujita, 1982; Shenk and Kreins, 1975; Purdom, 1982), In 1979 during a project known as SESAME (Severe Environmental Storm And Mesoscale Experiment) two GOES satellites were synchronized to produce 3 minute interval rapid scan imagery to study storm development. Fujita (1982) and Hasler (1981) used these data to produce very accurate cloud height assignments using stereographic techniques, similar to earlier work by Bristor and Pichel (1974). Other interesting studies with rapid interval GOES imagery include assessing thunderstorm severity (Adler and Fenn, 1979; Shenk and Mosher, 1987) and tracking cloud motions in the vicinity of hurricanes (Shenk, 1985; Shenk *et al*, 1987). Over the years, results from the research community filtered into satellite operations, and by the mid-1980s, five-minute interval imagery became a routine part of satellite operations during severe storm outbreaks. Today, with GOES-8, imagery at one minute intervals has been taken to study a variety of phenomena including severe storms, hurricanes and cloud motions (Purdom, 1995). Perhaps, based on research using that data and other special data sets, the United States will one day move to a three satellite configuration with an eastern, western and central satellite with the central satellite filling the role of a storm patrol, as envisioned decades ago.

1.4 Data Processing Capability

Interpretation and utilization of remote sensing data requires a ground processing capability that must perform the following functions:

(a) Downlink and reception of telemetry bit stream must yield sensor data, satellite orbit parameters, and spacecraft environment information;

(b) Preprocessing, calibration, and earth location (navigation) of the data must transform into physical units;

(c) Algorithms must be applied to derive geophysical parameters; and

(d) Validation and error analyses must be performed as part of the process investigation.

Considerable effort has been focused on developing interactive processing capabilities, where satellite data can be displayed and interpreted through efficient communication between an operator and the computer. Through manual editing and enhancement of the satellite data, it has been shown that derivation of geophysical parameters (such as temperature and moisture soundings) with high quality resolution was possible on a system such as the McIDAS (Man-computer Interactive Data Access System) developed at the University of Wisconsin. Utilizing a terminal consisting of digital, video, and graphics display devices with keyboard and cursor communication of instructions to the processor, an operator is able to rapidly interact with the data processing. For example, the operator can display images of sounding radiance data to aid him in selecting important meteorological phenomena and regions of extensive cloudiness where manual intervention is needed to insure high quality sounding output. The operator can instruct the computer to zoom in on the meteorologically active area and produce soundings that the operator can subjectively edit and enhance through the addition of soundings at specific locations selected by the operator through cursor control. The operator can check the meteorological consistency of the satellite sounding data. For example, he can instruct the computer to compute 300 mb geopotential heights and from their horizontal gradient thermal winds. Through cursor positioning, a sounding that is obviously erroneous and responsible for an unbalanced thermal (and implicitly wind) field, can be rapidly eliminated. The McIDAS application to satellite sounding data has also led to rapid improvements in the algorithms

used to process the data since visual inspection of the results revealed deficiencies in the processing procedures.

1.5 Summary

In the past thirty five years NOAA, with help from NASA, has established a remote sensing capability on polar and geostationary platforms that has proven useful in monitoring and predicting severe weather such as tornadic outbreaks, tropical cyclones, and flash floods in the short term, and climate trends indicated by sea surface temperatures, biomass burning, and cloud cover in the longer term. This has become possible first with the visible and infrared window imagery of the 1970s and has been augmented with the temperature and moisture sounding capability of the 1980s. The imagery from the NOAA satellites, especially the time continuous observations from geostationary instruments, dramatically enhanced our ability to understand atmospheric cloud motions and to predict severe thunderstorms. These data were almost immediately incorporated into operational procedures. Use of sounder data in the operational weather systems is more recently coming of age. The polar orbiting sounders are filling important data voids at synoptic scales. Applications include temperature and moisture analyses for weather prediction, analysis of atmospheric stability, estimation of tropical cyclone intensity and position, and global analyses of clouds. The TIROS Operational Vertical Sounder (TOVS) includes both infrared and microwave observations with the latter helping considerably to alleviate the influence of clouds for all weather soundings. The Geostationary Operational Environmental Satellite (GOES) VISSR Atmospheric Sounder (VAS) was used to develop procedures for retrieving atmospheric temperature, moisture, and wind at hourly intervals in the northern hemisphere. Temporal and spatial changes in atmospheric moisture and stability are improving severe storm warnings. Atmospheric flow fields (deep layer mean wind field composites from cloud drift, water vapour drift, and thermal gradient winds) are helping to improve hurricane trajectory forecasting. In 1994, the first of NOAA's next generation of geostationary satellites, GOES-8, dramatically improved the imaging and sounding capability. Applications of these NOAA data also extend to the climate programmes; archives from the last fifteen years offer important information about the effects of aerosols and greenhouse gases and possible trends in global temperature.

In the near future, forecasters will be able to use "modernization era" satellite and radar observing systems to investigate the evolution and structure of cloud systems and perform short term forecasts and warnings. Considering that convective activity ranges from air mass thunderstorms with life cycles well less than an hour to mesoscale convective systems with some aspects of their circulations that last for days, substantial benefits can be realized through correct interpretation of radar and satellite data. For example, there is obvious benefit in a forecaster distinguishing in real time between a supercell storm, associated with prolonged periods of severe weather, and a non-severe air mass thunderstorm. With the advent of improved mesoscale numerical models, the importance of interpretation of radar and satellite images and soundings is not diminished, but rather magnified as the forecaster now has the added task of using the observations critically to examine the predicted sequence of events.

The push for improved remote sensing from satellites must continue. There is a need for higher temporal, spatial, and spectral resolution in the future radiometers. Higher temporal resolution is becoming possible with detector array technology; higher spatial resolution may come with active cooling of infrared detectors so that smaller signals can be measured with adequate signal to noise. Higher spectral resolution is being considered through the use of interferometers and grating spectrometers. Advanced microwave radiometers measuring moisture as well as temperature profiles will soon be flying in polar orbit; a geostationary complement is being investigated. Ocean colour observations with multispectral narrow band visible measurements are being planned. The challenge of the future is to further the progress realized in the past decades so that environmental remote sensing of the oceans, atmosphere, and earth increases our understanding the processes affecting our lives and future generations.

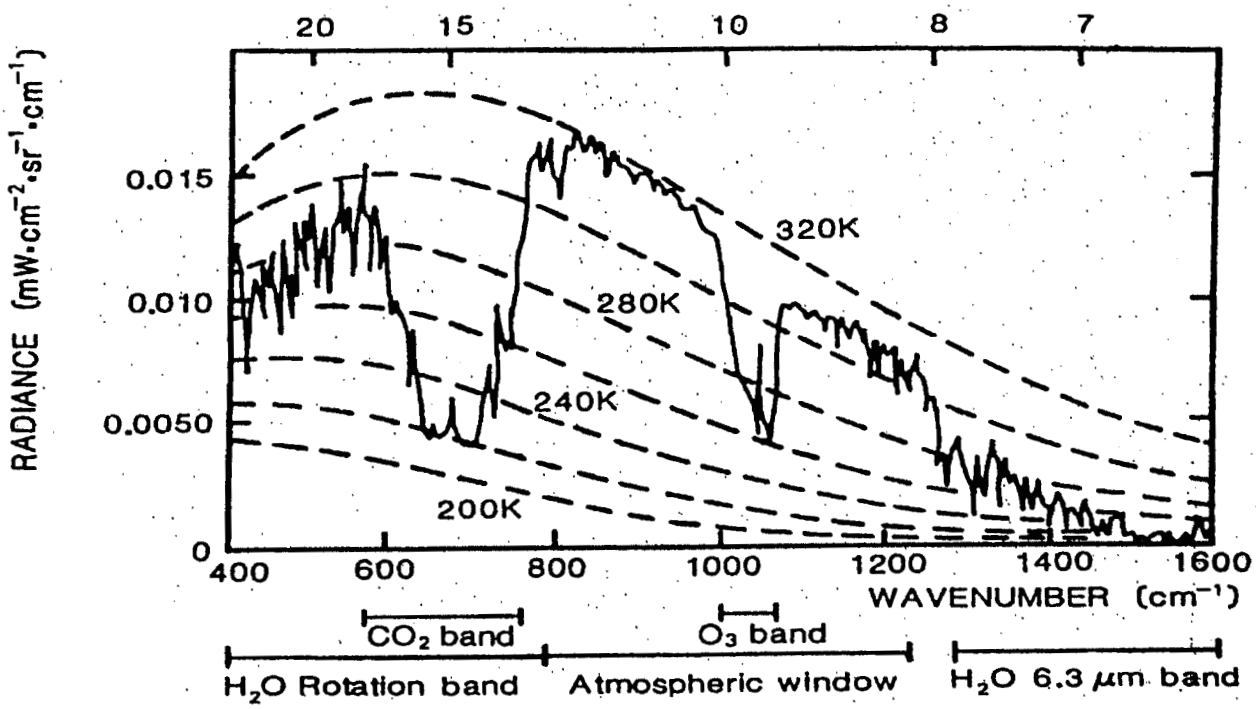

Figure 1.1. Infrared portion of the earth-atmosphere emitted radiation to space observed from Nimbus 4. Planck emission and line spectra are indicated.

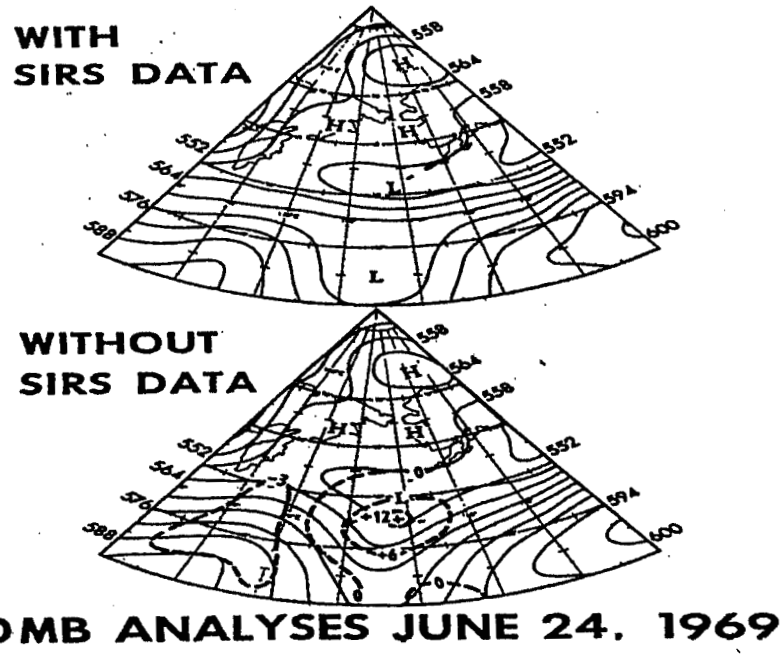

Figure 1.2 Comparison of objective analyses of 500 mb height obtained with and without SIRS soundings. The differences in decameters are shown by the dashed isolines. Note the difference over the Pacific where the SIRS data indicate a cut-off low with an intense jet to the north instead of a diffusely defined trough. Extended range (72 hr) forecasts for North America displayed maximum errors based on the analyses with SIRS of only half the magnitude of those resulting without the use of the data.

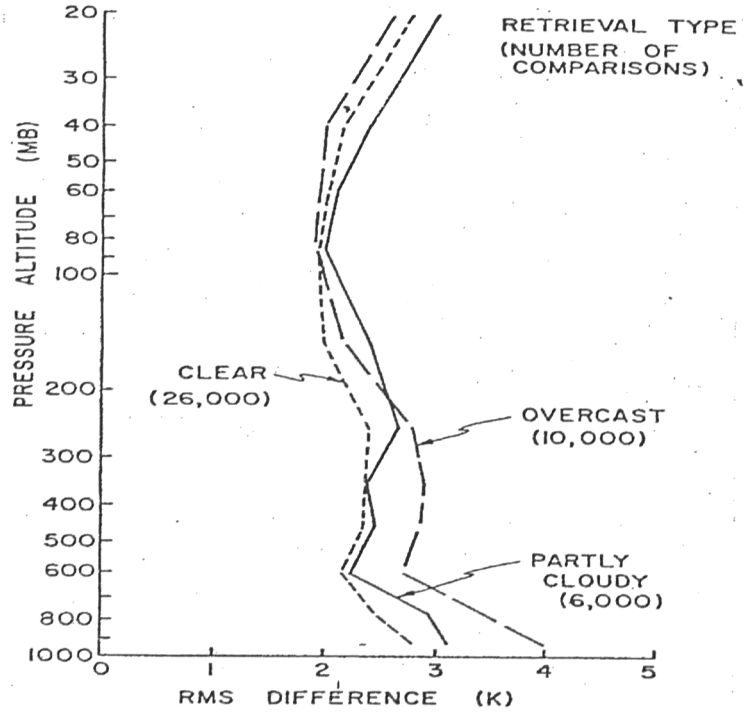

Figure 1.3. RMS differences between radiosonde and satellite temperature soundings for April 1980.

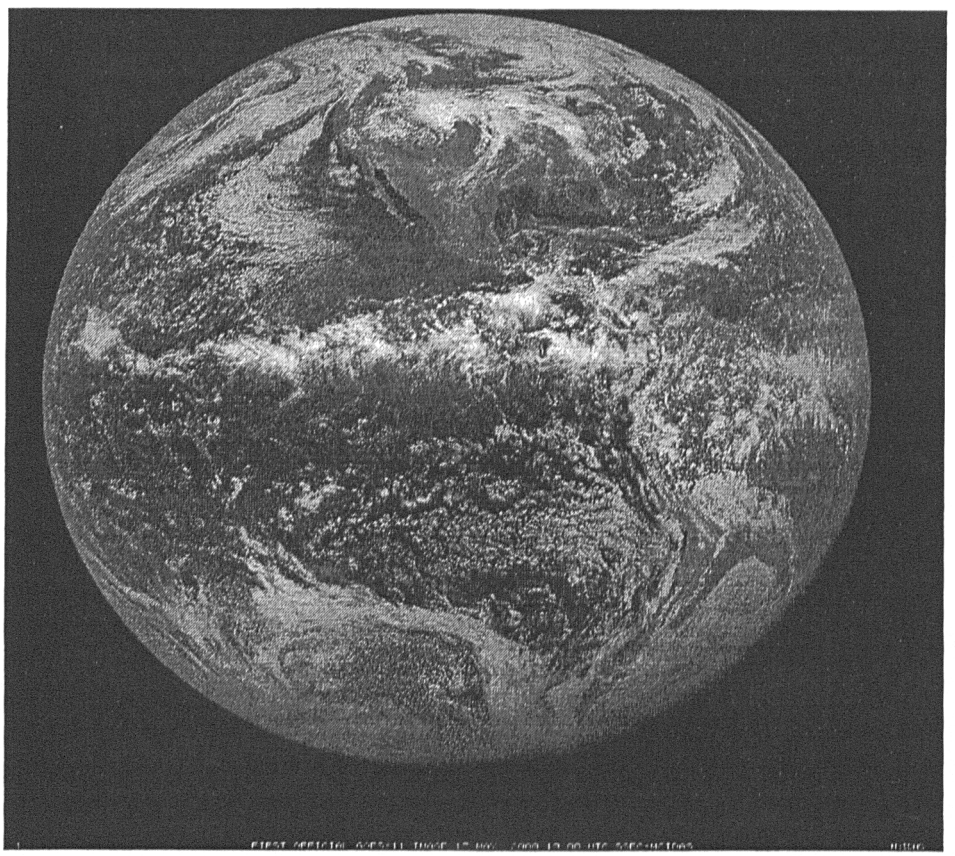

Figure 1.4. Image of visible reflectance sensed by the GOES-11, in which the light areas correspond to clouds or snow/ice regions.

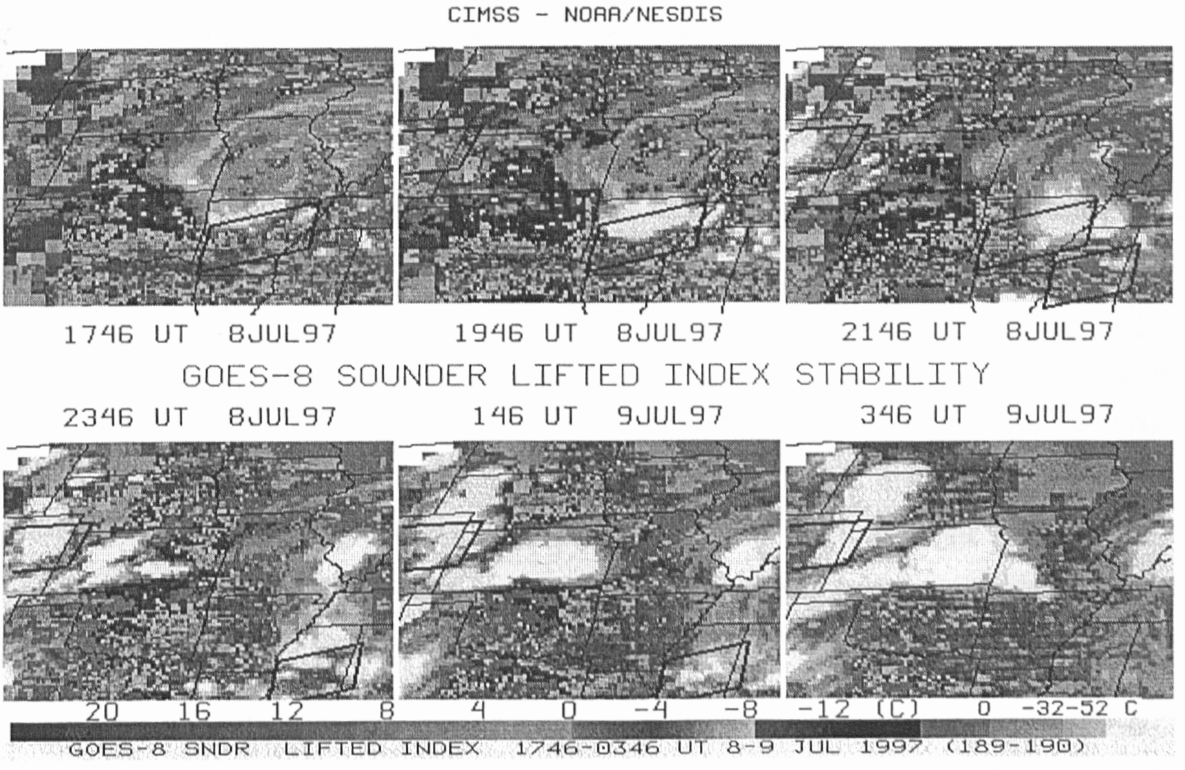

Figure 1.5. (top) Two hourly GOES LI DPI on 8 - 9 July 1997 showing focused strongly unstable conditions over Kansas and northern Oklahoma where severe storms subsequently developed. The severe weather watch boxes are overlaid. (bottom) The GOES-8 sounder LI DPI at 2346 UTC on 8 July 1997 along with the radiosonde values from the 0000 UTC launches.

Table 1.1
Comparison of geostationary (geo) and low earth orbiting (leo) or polar orbiting satellite capabilities

GEO	LEO
Observes process itself (motion and targets of opportunity)	Observes effects of process
Repeat coverage in minutes(Δt = 30 minutes)	Repeat coverage twice daily (Δt = 12 hours)
Full earth disk only	Global coverage
Best viewing of tropics	Best viewing of poles
Same viewing angle	Varying viewing angle
Differing solar illumination	Same solar illumination
Visible, IR imager (1, 4 km resolution)	Visible, IR imager (1, 1 km resolution)
One visible band	Multispectral in visible(veggie index)
IR only sounder(8 km resolution)	IR and microwave sounder (17, 50 km resolution)
Noise of .5 mW/ster/m2/cm^{-1} (several tenths of a degree)	Noise of .5 mW/ster/m2/cm^{-1} (several tenths of a degree)
Constant viewing helps with clouds	Microwave helps with clouds
Filter radiometer	Filter radiometer, interferometer, and grating spectrometer

CHAPTER 2

NATURE OF RADIATION

2.1 Remote Sensing of Radiation

Energy transfer from one place to another is accomplished by any one of three processes. Conduction is the transfer of kinetic energy of atoms or molecules (heat) by contact among molecules travelling at varying speeds. Convection is the physical displacement of matter in gases or liquids. Radiation is the process whereby energy is transferred across space without the necessity of transfer medium (in contrast with conduction and convection).

The observation of a target by a device separated by some distance is the act of remote sensing (for example ears sensing acoustic waves are remote sensors). Remote sensing with satellites for meteorological research has been largely confined to passive detection of radiation emanating from the earth/atmosphere system.

All satellite remote sensing systems involve the measurement of electromagnetic radiation. Electromagnetic radiation has the properties of both waves and discrete particles, although the two are never manifest simultaneously.

2.2 Basic Units

All forms of electromagnetic radiation travel in a vacuum at the same velocity, which is approximately 3 x 10**10 cm/sec and is denoted by the letter c. Electromagnetic radiation is usually quantified according to its wave-like properties, which include intensity and wavelength. For many applications it is sufficient to consider electromagnetic waves as being a continuous train of sinusoidal shapes.

If radiation has only one colour, it is said to be monochromatic. The colour of any particular kind of radiation is designated by its frequency, which is the number of waves passing a given point in one second and is represented by the letter f (with units of cycles/sec or Hertz). The length of a single wave (i.e., the distance between two successive maxima) is called the wavelength and is denoted by λ (with units of microns to meters).

For monochromatic radiation, the number of waves passing a fixed point in one second multiplied by the length of each wave is the distance the wave train travelled on one second. But that distance is equal in magnitude to the velocity of light c. Hence,

$$c = f \lambda = 3 \times 10^{10} \text{ cm/sec} .$$

Since the frequency of a wave, f, is equal to the number of wavelengths in a distance of 3 x 10**10 cm, it is usually a large number. Therefore, it is often much more convenient (especially in the infrared region of the spectrum) to consider the number of waves in one centimetre, called the wavenumber. This new unit the wavenumber is designated by ν (cm^{-1}) and

$$\nu = 1 / \lambda \ (cm^{-1}).$$

However, wavenumber becomes a relatively small unit in the microwave region; so, we use frequency in giga-Hertz units in that region. Similarly, because centimetres are usually too large for wavelength units, we use micrometers (um) for most of the spectrum and for the very short wavelength region we use Angstrom units (Å). Conversion of wavelength units is demonstrated below:

$$1\ \text{Å} = 10^{-10}\ \text{m} = 10^{-8}\ \text{cm} = 10^{-4}\ \mu\text{m, and}$$

$$1\ \mu\text{m} = 10^{-6}\ \text{m} = 10^{-4}\ \text{cm} = 10^{4}\ \text{Å.}$$

Conversion of frequency units follows:

$$1\ \text{cm}^{-1} = 3 \times 10^{10}\ \text{Hz} = 30\ \text{GHz, and}$$

$$1\ \text{GHz} = 10^{9}\ \text{Hz} = 1/30\ \text{cm}^{-1}.$$

Table 2.1 summarizes the regions and units of the electromagnetic spectrum commonly encountered in satellite meteorology.

2.3 Definitions of Radiation

The rate of energy transfer by electromagnetic radiation is called the radiant flux, which has units of energy per unit time. It is denoted by

$$F = dQ / dt$$

and is measured in joules per second or watts. For example, the radiant flux from the sun is about 3.90 x 10**26 W.

The radiant flux per unit area is called the irradiance (or radiant flux density in some texts). It is denoted by

$$E = dQ / dt / dA$$

and is measured in watts per square metre. The irradiance of electromagnetic radiation passing through the outermost limits of the visible disk of the sun (which has an approximate radius of 7 x 10**8 m) is given by

$$E\ (\text{sun sfc}) = \frac{3.90 \times 10^{26}}{4\pi\ (7 \times 10^{8})^{2}} = 6.34 \times 10^{7}\ \text{W m}^{-2}.$$

The solar irradiance arriving at the earth can be calculated by realizing that the flux is a constant, therefore

$$E\ (\text{earth sfc}) * 4\pi R_{es}^{2} = E\ (\text{sun sfc}) * 4\pi R_{s}^{2},$$

where R_{es} is the mean earth to sun distance (roughly 1.5 x 10^{11} m) and R_s is the solar radius. This yields

$$E\ (\text{earth sfc}) = 6.34 \times 10^{7}\ (7 \times 10^{8} / 1.5 \times 10^{11})^{2} = 1380\ \text{W m}^{-2}.$$

The irradiance per unit wavelength interval at wavelength λ is called the monochromatic irradiance,

$$E_{\lambda} = dQ / dt / dA / d\lambda\ ,$$

and has the units of watts per square metre per micrometer. With this definition, the irradiance is

readily seen to be

$$E = \int_0^\infty E_\lambda \, d\lambda \, .$$

In general, the irradiance upon an element of surface area may consist of contributions which come from an infinity of different directions. It is sometimes necessary to identify the part of the irradiance that is coming from directions within some specified infinitesimal arc of solid angle $d\Omega$. The irradiance per unit solid angle is called the radiance,

$$I = dQ / dt / dA / d\lambda / d\Omega,$$

and is expressed in watts per square metre per micrometer per steradian. This quantity is often also referred to as intensity and denoted by the letter B (when referring to the Planck function). Table 2.2 summarizes these definitions.

In order to express the relationship between irradiance and radiance quantitatively, it is necessary to define the zenith angle, θ, as the angle between the direction of the radiation and the normal to the surface in question. The component of the radiance normal to the surface is then given by $I \cos \theta$. The irradiance represents the combined effects of the normal component of the radiation coming from the whole hemisphere; that is,

$$E = \int_\Omega I \cos \theta \, d\Omega$$

where in spherical coordinates

$$d\Omega = \sin \theta \, d\theta \, d\varphi \, .$$

Figure 2.1 illustrates the radiance geometry.

Radiation whose radiance is independent of direction is called isotropic radiation. In this case, the integration over $d\Omega$ can be readily shown to be equal to π so that

$$E = \pi I \, .$$

Radiance is often expressed per unit frequency, $I(f)$, rather than per unit wavelength, $I(\lambda)$. Since the transformation from wavelength to frequency is given by $f = c / \lambda$, it follows that

$$I(\lambda) = I(f) \, c / \lambda^2 .$$

$I(\lambda)$ must not be confused with $I(f)$: they are different quantities. More will be said about this later in this chapter.

2.4 Historical Development of Planck's Radiation Law

It had long been observed that the surface of all bodies at a temperature greater than absolute zero (0 K) emits energy, in the form of thermal radiation. These electromagnetic waves were thought to be due to the motion of electric charges near the surface of the radiating body.

The study of radiation focused on the properties of a hypothetical black body, which is characterized by (a) complete absorption of all incident radiation (hence the term black), and (b) maximum possible emission in all wavelengths in all directions. In other words, it is the perfect absorber and emitter of all radiation.

Many attempts, both empirical and theoretical in approach, were made in the years up to and about 1900 to understand the black body spectrum. In 1879, Stefan had empirically found that the irradiance of a black body was related to temperature by the law

$$E = \sigma T^4,$$

where

$$\sigma = 5.67 \times 10^{-8} \text{ W m}^{-2} \text{ deg}^{-4}.$$

In 1884, Boltzmann produced a theoretical derivation of this equation.

Earliest accurate measurements of monochromatic irradiance are credited to Lummer and Pringsheim in 1899. They observed the now well-known emission spectra for black bodies at several different temperatures (shown in Figure 2.2).

Thermodynamical reasoning, while not giving a complete answer, did predict two characteristic features of the radiation. Wien, in 1893, was able to shown that the monochromatic radiance was related to temperature and wavelength by

$$I(\lambda) = f(\lambda T) / \lambda^5,$$

where the form of the single function $f(\lambda T)$ was not evaluated. Also, the peak emission wavelength of a black body was shown to be inversely proportional to temperature, so that

$$\lambda_{max} = \text{const} / T .$$

In this derivation, he considered a cylindrical cavity with reflecting walls, one of which is a movable piston, filled with radiation at a temperature T. Radiation was known to exert a pressure proportional to its energy density. Taking this system through a Carnot cycle, a relation between the work done by the radiation (expressed in terms of monochromatic radiance) and temperature was obtained.

To evaluate the function $f(\lambda T)$ some of the detailed properties of a black body must be taken into account. In 1900, Rayleigh and Jeans attempted to evaluate $f(\lambda T)$ by considering a cubical cavity containing electromagnetic standing waves with nodes at the metallic surfaces and the energy of these waves obeying the Boltzmann probability distribution. Assuming a continuum of energy states, the average total energy of this system can be expressed as

$$\varepsilon_{av} = \left[\int_0^\infty \varepsilon \, e^{-\varepsilon / kT} \, d\varepsilon \right] / \left[\int_0^\infty e^{-\varepsilon / kT} \, d\varepsilon \right]$$

where the Boltzmann constant is given by

$$k = 1.381 \times 10^{-23} \text{ J/deg.}$$

This leads to

$$f(\lambda T) = 2ck\lambda T ,$$

which is in agreement with experiment only for long wavelengths. At short wavelengths the monochromatic radiance becomes infinite (often referred to as the ultraviolet catastrophe). The form of f(λT) obtained by Rayleigh and Jeans was a necessary consequence of the theories of classical physics, yet it failed!

The discrepancy between experiment and theory was resolved by Planck in 1901, but at the expense of some of the concepts known to classical physics. Assuming that electromagnetic harmonic oscillations can only exist in quanta of hf (h is a constant, f is a frequency) and that oscillators emit energy only when changing from one to another of their quantized energy states, then the average total energy of this system is expressed as

$$\varepsilon_{av} = \left[\sum_{n=o}^{\infty} nhf\, e^{-nhf/kT} \right] / \left[\sum_{n=o}^{\infty} e^{-nhf/kT} \right]$$

or

$$\varepsilon_{av} = hf / (e^{hf/kT} - 1) .$$

This yields the proper form of f(λT),

$$f(\lambda T) = 2hc^2 /(e^{hc/\lambda kT} - 1) ,$$

and predicts the observed results if the Planck constant

$$h = 6.63 \times 10^{-34}\ J*s .$$

And the Planck law for radiation intensity (or monochromatic radiance) can be expressed as

$$B(\lambda,T) = c_1 / [\lambda^5 (e^{c_2/\lambda T} - 1)]$$

where

$$c_1 = 2hc^2 = 1.191044 \times 10^{-8}\ W/(m^2*ster*cm^{-4})$$

and

$$c_2 = hc/k = 1.438769\ K*cm$$

and B(λ,T) has units of W/(m²*ster*cm).

Written in terms of wavenumber rather than wavelength,

$$B(\nu,T) = c_1\nu^3 / (e^{c_2\nu/T} - 1)$$

where B(ν,T) has units of W/(m²*ster*cm⁻¹). The difference in the Planck radiance curves when measured with respect to unit wavelength versus unit wavenumber is seen in Figure 2.3.

Thus, in the course of his successful attempt at resolving certain discrepancies between the observed energy spectrum of thermal radiation and the predictions of the classical theory, Planck was led to the idea that a system executing simple harmonic oscillations only can have energies which are integral multiples of a certain finite amount of energy (1901). A closely related idea was later applied by Einstein in explaining the photo-electric effect (1905), and by Bohr in a theory which predicted with great accuracy many of the complex features of atomic spectra (1913). The work of these three physicists, plus subsequent developments by de Broglie, Schroedinger, and Heisenberg (ca. 1925), constitutes what is known as the quantum theory. Quantum theory and the theory of relativity together comprise the two most significant features of modern physics.

2.5 Related Derivations

2.5.1 Wien's Displacement Law

The peak of Planck function curve shifts to shorter wavelengths with an increase in temperature. The wavelength λ_{max} for which the Planck function peaks at a given temperature T can be found from Planck's law by differentiating it with respect to λ and equating the result to zero. This yields the nonlinear equation

$$x = 5\,(1 - e^{-x})$$

where $x = c_2 / (\lambda_{max}\, T)$ whose solution is $x = 4.965114$. Therefore,

$$\lambda_{max} = .2897 / T \ \ (cm)$$

which is Wien's displacement law. This law indicates that the wavelength of maximum Planck radiance varies inversely with temperature. Note that when the Planck function is expressed in terms of wavenumber, differentiating with respect to ν and equating the result to zero yields $y = 3\,(1 - e^{-y})$ where $y = c_2\, \nu_{max}/T$ with the solution $\nu_{max} = 1.95{*}T\ (cm^{-1})$. It is important to realize that $\nu_{max} \neq 1/\lambda_{max}$.

The Planck radiance at the Wien wavelength varies as temperature to the fifth power. To see this more clearly consider

$$B(\lambda_{max}, T) = c_1 / [\lambda_{max}^5 (e^{c_2 / \lambda maxT} - 1)]$$

$$= c_1\, T^5 / [\,(.2897)^5 (e^{c_2 / .2897} - 1)]$$

$$= c_3\, T^5$$

where c_3 is a constant. In a similar way, it can be shown that $B(\nu_{max}, T) = c_4 T^3$.

The radiative temperature of the surface of the sun is roughly 5780 K. Applying Wien's Law at the sun's surface temperature, one finds the maximum Planck radiance to be at 0.50 um, which is near the centre of the visible region of the spectrum. Since the sun radiates nearly as a black body, we can say that the solar energy reaching the earth is a maximum in the visible region.

On the other hand, the earth's atmospheric temperature averaged vertically is around 255 K; therefore, the maximum emitted energy of the earth's atmosphere occurs roughly at 11 um, that is, well into the infrared region. In fact, if the black body curves (Planck functions) for temperatures of 255 K and 5780 K are plotted next to each other, the curves are almost entirely separate. Thus, the spectral distribution of the incoming solar radiation is quite different from that of the outgoing terrestrial radiation (see Figure 2.4).

Wien's displacement law derives its name from the fact that as the temperature increases, the point of maximum intensity of the black body curve is displaced toward the shorter wavelengths.

Since the wavelength of the maximum value determines the colour perceived while observing the complete spectrum, we have an explanation for the transition in colour of a heated iron bar from red to a white glow with increased heat. As the temperature is raised the longer wavelength red light becomes visible first. Then higher temperatures make additional wavelengths visible. Finally, when the temperature is sufficiently high, the radiation consists of a mixture of all the visible wavelengths and, hence, appears white hot. For similar reasons, the filament of an incandescent lamp must be heated to thousands of degrees K in order to be an efficient emitter of visible light, while infrared lamps operate at lower temperatures.

2.5.2 Rayleigh-Jeans Radiation Law

In the microwave region of the electromagnetic spectrum, when $\lambda > 0.5$ cm and T is at terrestrial temperatures, the exponent in the Planck function is small, and hence one can make the approximation

$$e^{c2/\lambda T} = 1 + c_2/\lambda T$$

that yields the following asymptotic expansion:

$$B(\lambda,T) = c_1 T/(c_2 \lambda^4)$$

Similarly,

$$B(\nu,T) = c_1 \nu^2 T/c_2$$

for sufficiently small v. These formulas represent the Rayleigh-Jeans law of radiation and the spectral region $\lambda > 0.5$ cm is called the Rayleigh-Jeans region in atmospheric physics. Note that in the Rayleigh-Jeans region the Planck function is linear to T. For $\lambda T > 10$ cm K, the Rayleigh-Jeans approximation is within 2% or better.

2.5.3 Wien's Radiation Law

In the near infrared region and beyond into the visible and ultraviolet regions, i.e., $\lambda < 10^{-3}$ cm, and when T is at terrestrial temperatures, the exponent in the Planck function is large and, hence

$$e^{c2/\lambda T} >> 1.0$$

Consequently, the constant 1.0 can be ignored in the denominator to yield another asymptotic expansion for the Planck function, namely,

$$B(\lambda,T) = c_1 \lambda^{-5} e^{-c2/\lambda T},$$

or

$$B(\nu,T) = c_1 \nu^3 e^{-c2\,\nu/T}$$

for sufficiently large ν. These are two forms of Wien's law of radiation. The spectral region $\lambda < 10^{-3}$ cm is called the Wien region when dealing with atmospheric temperatures. In the Wien region, the Planck function is highly nonlinear in temperature. . For $\lambda T < 0.5$ cm K, the Wein approximation is within 2% or better.

2.5.4 *Stefan-Boltzmann Law*

The black body irradiance is obtained by integrating the Planck function over all wavelengths and angles,

$$E = \int_0^\infty E_\lambda \, d\lambda = \pi \int_0^\infty \frac{c_1 \, d\lambda}{\lambda^5 [e^{c_2/\lambda T} - 1]}$$

Let $x = c_2/\lambda T$ then

$$E = \frac{\pi c_1 T^4}{c_2^4} \int_0^\infty \frac{x^3 \, dx}{(e^x - 1)} = \frac{\pi^5 c_1 T^4}{15 c_2^4} = \sigma T^4$$

Note that

$$\int_0^\infty B(\lambda,T) \, d\lambda = \int_0^\infty B(\nu,T) \, d\nu ,$$

which implies for a given temperature

$$B(\lambda,T) = \nu^2 B(\nu,T) \ .$$

It is often useful to know the fraction of the total blackbody radiance coming from below a specific wavelength, expressed by

$$\int_0^\lambda E_\lambda \, d\lambda / \sigma T^4 = \pi \int_0^\lambda B_\lambda \, d\lambda / \sigma T^4$$

Figure 2.5 shows the fraction of total blackbody radiance emitted below a specific wavelength as a function of λT. Note that for $\lambda = \lambda_{max}$ the fraction is .23, or less than 25% of the radiance comes from wavelengths shorter than the peak wavelength. Figure 2.5 illustrates that less than 1% of the solar energy comes from wavelengths longer than 4 microns, while less than 1% of terrestrial energy from a blackbody at 250 K comes from wavelengths shorter than 4 microns.

2.5.5 *Brightness Temperature*

Ultimately, one is interested in the temperature that corresponds to a particular Planck function value B_λ. This temperature is determined by inverting the Planck function,

$$T = c_2 \ / \ [\lambda \ln(\frac{c_1}{\lambda^5 B_\lambda} + 1)] = c_2 \nu \ / \ [\ln(\frac{c_1 \nu^3}{B_\nu} + 1)]$$

The temperature derived is called brightness temperature because of its historical connection with radio astronomy; however, the terms radiance temperature or equivalent black body temperature are also frequently used.

In the Rayleigh-Jeans regions, one can write

$$T = (c_2/c_1)\,\lambda^4\,B_\lambda = (c_2/c_1)\,B_\nu\ /\ \nu^2,$$

where $c_2/c_1 = 1.208021 \times 10^5$. On the other hand in the Wien region

$$T = c_2\ /\ \left[\lambda \ln\left(\frac{c_1}{\lambda^5 B_\lambda}\right)\right] = c_2\nu\ /\ \left[\ln\left(\frac{c_1\nu^3}{B_\nu}\right)\right]$$

where $B(\nu,T)$ has units of $W/(m^2*ster*cm^{-1})$.

As we have seen from Planck's Law, as temperature increases the radiance also increases; the percentage increase varies as a function of wavelength and temperature. The percentage change in radiance to a corresponding percentage change in temperature, called temperature sensitivity, α, of a given spectral band is defined as $dB/B = \alpha\, dT/T$. For infrared wavelengths, we find that $\alpha \approx c_2\nu/T = c_2/\lambda T$. Thus the larger wavenumbers (shorter wavelengths) have a greater temperature sensitivity than the smaller wavenumbers (longer wavelengths). Consider the two infrared windows for example; at 300 K, the temperature sensitivity for 900 cm-1 (long-wave window at 11 um) is 4.3 and for 2500 cm-1 (short-wave window at 4 um) it is 12. The temperature sensitivity indicates the power to which the Planck radiance depends on temperature, since B proportional to T^α satisfies the equation. Thus the radiance in the short-wave window is varying roughly as temperature to the twelfth power and in the long-wave window roughly as temperature to the fourth power. Table 2.3 indicates the temperature sensitivity of some of the other spectral regions.

Table 2.1
Regions and Units of the Electromagnetic Spectrum

WAVELENGTH			FREQUENCY		WAVENUMBER
cm	μm	Å	Hz	GHz	cm^{-1}
10^{-5} Near Ultraviolet (UV)	0.1	1,000	$3x10^{15}$		
$4x10^{-5}$ Visible	0.4	4,000	$7.5x10^{14}$		
$7.5x10^{-5}$ Near Infrared (IR)	0.75	7,500	$4x10^{14}$		13,333
$2x10^{-3}$ Far Infrared (IR)	20	$2x10^{5}$	$1.5x10^{13}$		500
0.1 Microwave (MW)	10^{3}		$3x10^{11}$	300	10

Table 2.2
Definitions of Radiation

QUANTITY	SYMBOL	UNITS
Energy	DQ	Joules
Flux	dQ/dT	Joules/sec = Watts
Irradiance	dQ/dT/dA	$Watts/m^2$
Monochromatic Irradiances	$dQ/dT/dA/d\lambda$ or $dQ/dT/dA/d\nu$	$W/m^2/micron$ W/m^2cm^{-1}
Radiance	$dQ/dT/dA/d\lambda/d\Omega$ or $dQ/dT/dA/d\nu/d\Omega$	$W/m^2/micron/ster$ $W/m^2/cm^{-1}/ster$

Table 2.3
Temperature sensitivity of various spectral regions.

Wavenumber	Typical Scene Temperature	Temperature Sensitivity
700	220	4.58
900	300	4.32
1200	300	5.76
1600	240	9.59
2300	220	15.04
2500	300	11.99

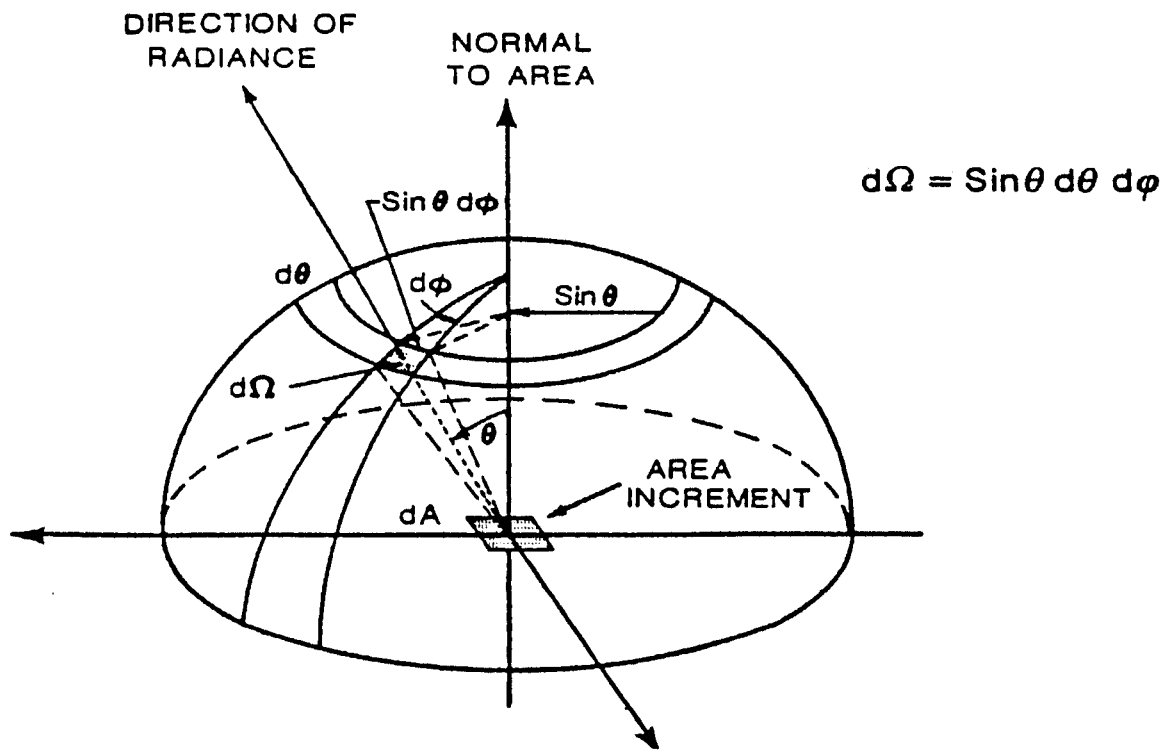

Figure 2.1: The Radiance Geometry

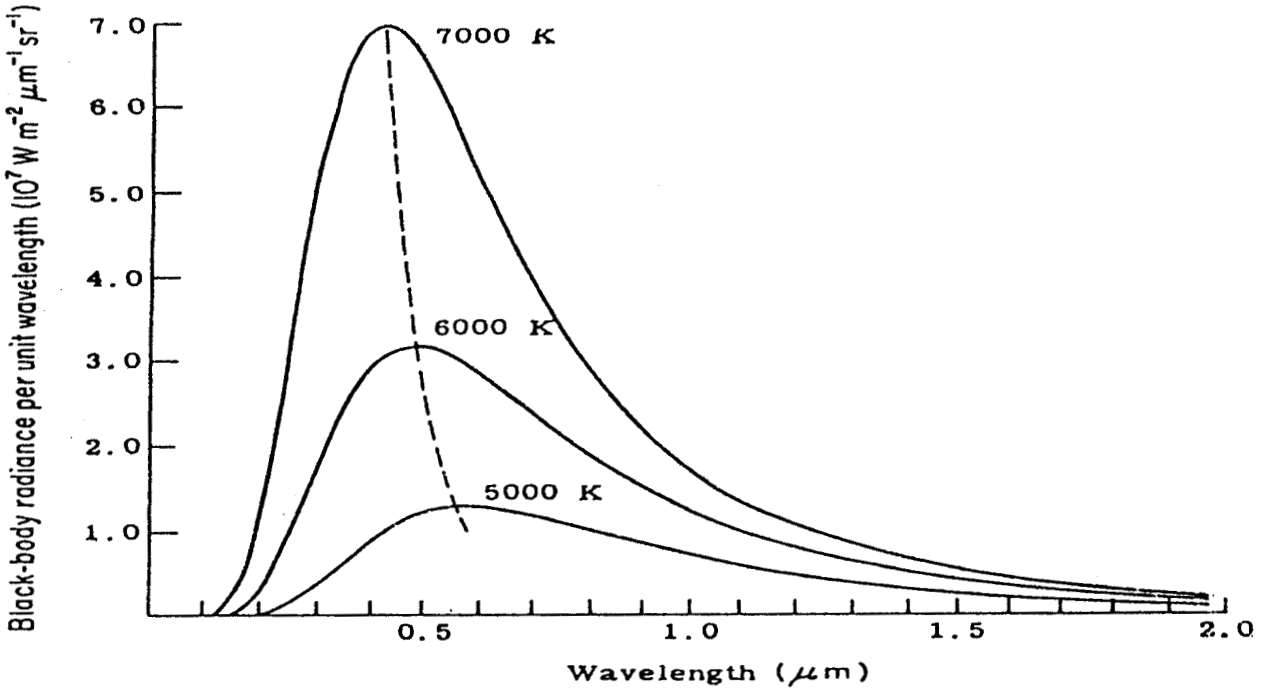

Figure 2.2: Emission Spectra for Black Bodies with the Indicated Temperatures

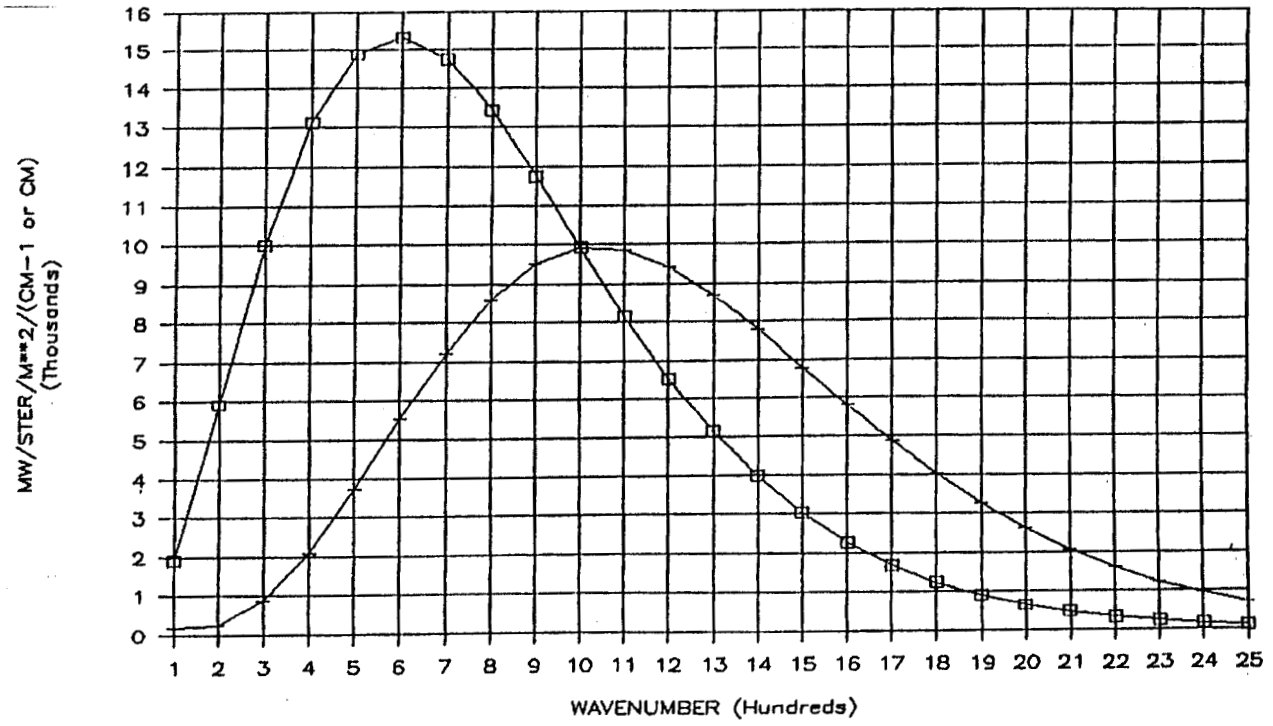

Figure 2.3: Planck radiance curves at 300 K. □ indicates B(λ,T) in units of mW/ster/m^2/cm (per unit wavelength) and + indicates B(ν,T) in units of mW/ster/m^2/cm^{-1} (per unit wavenumber). B(λ,T) is shown multiplied by a factor of 10^{-7} (e.g., B(10 μm, 300 K) is 9.9x10^7) while B(ν,T) is shown multiplied by a factor of 10^{-1} (e.g., B(1000 cm^{-1}, 300 K) is 99.0). Note that Wiens law for B(ν,T) becomes ν(max) = 1.95*T (cm^{-1}) while the more familiar form for B(λ,T) is λ(max) = .2897/T (cm).

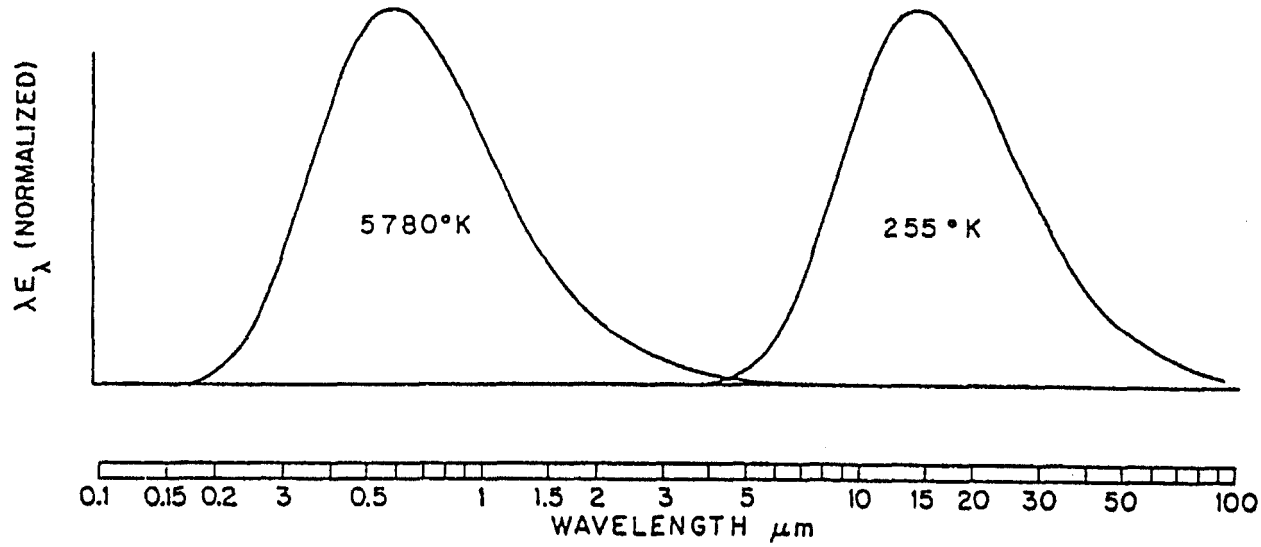

Figure 2.4: Normalized black body spectra representative of the sun (left) and earth (right), plotted on a logarithmic wavelength scale. The ordinate is multiplied by wavelength so that the area under the curves is proportional to irradiance.

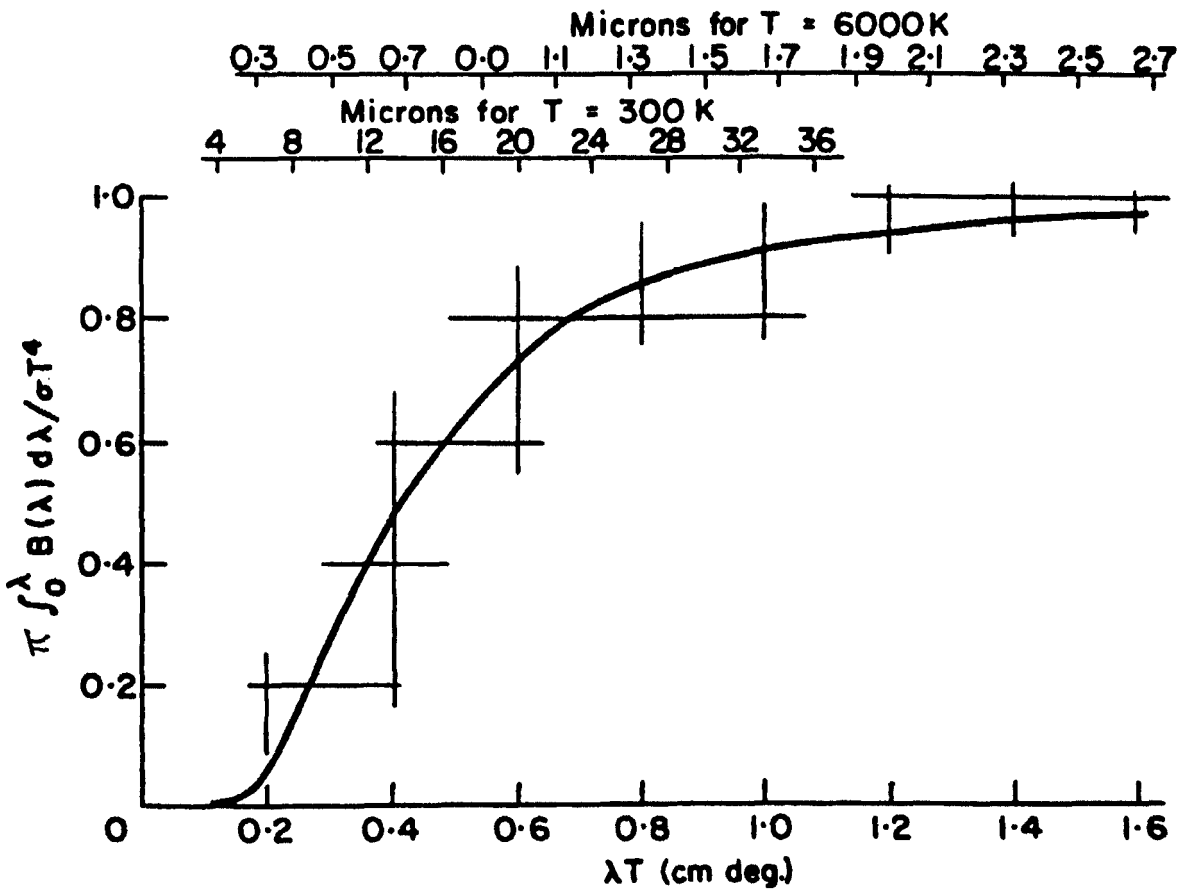

Figure 2.5: Fraction of total blackbody radiance coming from below a given wavelength for a given temperature.

CHAPTER 3

ABSORPTION, EMISSION, REFLECTION, AND SCATTERING

3.1 Absorption and Emission

As we noted earlier, blackbody radiation represents the upper limit to the amount of radiation that a real substance may emit at a given temperature. At any given wavelength λ, emissivity is defined as the ratio of the actual emitted radiance, R_λ, to that from an ideal blackbody, B_λ,

$$\varepsilon_\lambda = R_\lambda / B_\lambda \ .$$

It is a measure of how strongly a body radiates at a given wavelength, and it ranges between zero and one for all real substances. A gray body is defined as a substance whose emissivity is independent of wavelength. In the atmosphere, clouds and gases have emissivities that vary rapidly with wavelength. The ocean surface has near unit emissivity in the visible regions.

For a body in local thermodynamic equilibrium the amount of thermal energy emitted must be equal to the energy absorbed; otherwise the body would heat up or cool down in time, contrary to the assumption of equilibrium. In an absorbing and emitting medium in which I_λ is the incident spectral radiance, the emitted spectral radiance R_λ is given by

$$R_\lambda = \varepsilon_\lambda B_\lambda = a_\lambda I_\lambda \ ,$$

where a_λ represents the absorptance at a given wavelength. If the source of radiation is in thermal equilibrium with the absorbing medium, then

$$I_\lambda = B_\lambda \ ,$$

so that

$$\varepsilon_\lambda = a_\lambda \ .$$

This is often referred to as Kirchhoff's Law. In qualitative terms, it states that materials which are strong absorbers at a given wavelength are also strong emitters at that wavelength; similarly weak absorbers are weak emitters.

3.2 Conservation of Energy

Consider a slab of absorbing medium and only part of the total incident radiation I_λ is absorbed, then the remainder is either transmitted through the slab or reflected from it (see Figure 3.1). In other words, if a_λ, r_λ, and τ_λ represent the fractional absorptance, reflectance, and transmittance, respectively, then the absorbed part of the radiation must be equal to the total radiation minus the losses due to reflections away from the slab and transmissions through it. Hence

$$a_\lambda I_\lambda = I_\lambda - r_\lambda I_\lambda - \tau_\lambda I_\lambda \ ,$$

or

$$a_\lambda + r_\lambda + \tau_\lambda = 1 \ ,$$

which says that the processes of absorption, reflection, and transmission account for all the incident radiation in any particular situation. This is simply conservation of energy. For blackbody $a_\lambda = 1$, so it follows that $r_\lambda = 0$ and $\tau_\lambda = 0$ for blackbody radiation. In any window region $\tau_\lambda = 1$, and $a_\lambda = 0$ and $r_\lambda = 0$.

Radiation incident upon any opaque surface, $\tau_\lambda = 0$, is either absorbed or reflected, so that

$$a_\lambda + r_\lambda = 1 \ .$$

At any wavelength, strong reflectors are weak absorbers (i.e., snow at visible wavelengths), and weak reflectors are strong absorbers (i.e., asphalt at visible wavelengths). The reflectances for selected surfaces for the wavelengths of solar radiation are listed in Table 3.1.

From Kirchhoff's Law we can also write

$$\varepsilon_\lambda + r_\lambda + \tau_\lambda = 1 \ ,$$

which says emission, reflection, and transmission account for all the incident radiation for media in thermodynamical equilibrium.

3.3 Planetary Albedo

Planetary albedo is defined as the fraction of the total incident solar irradiance, S, that is reflected back into space. Radiation balance then requires that the absorbed solar irradiance is given by

$$E = (1 - A)\, S/4.$$

The factor of one-fourth arises because the cross sectional area of the earth disc to solar radiation, πr^2, is one-fourth the earth radiating surface, $4\pi r^2$. Thus recalling that S = 1380 Wm^{-2}, if the earth albedo is 30 percent, then E = 241 Wm^{-2}.

3.4 Selective Absorption and Emission

The atmosphere of the earth exhibits absorptance which varies drastically with wavelength. The absorptance is small in the visible part of the spectrum, while in the infrared it is large. This has a profound effect on the equilibrium temperature at the surface of the earth. The following problem illustrates this point. Assume that the earth behaves like a blackbody and that the atmosphere has an absorptivity a_S for incoming solar radiation and a_L for outgoing long-wave radiation. Let Y_a be the irradiance emitted by the atmosphere (both upward and downward); Y_s the irradiance emitted from the earth's surface; and E the solar irradiance absorbed by the earth-atmosphere system. Then, at the surface, radiative equilibrium requires

$$(1-a_S)\, E - Y_s + Y_a = 0 \ ,$$

and at the top of the atmosphere

$$E - (1-a_L)\, Y_s - Y_a = 0 \ .$$

Solving yields

$$Y_s = \frac{(2-a_S)}{(2-a_L)}\, E \ ,$$

and

$$Y_a = \frac{(2-a_L) - (1-a_L)(2-a_S)}{(2-a_L)}\, E \ .$$

Since $a_L > a_S$, the irradiance and hence the radiative equilibrium temperature at the earth surface is increased by the presence of the atmosphere. With $a_L = .8$ and $a_S = .1$ and $E = 241\ Wm^{-2}$, Stefans Law yields a blackbody temperature at the surface of 286 K, in contrast to the 255 K it would be if the atmospheric absorptance was independent of wavelength ($a_S = a_L$). The atmospheric gray body temperature in this example turns out to be 245 K.

A gas in a planetary atmosphere that is a weak absorber in the visible and a strong absorber in the infrared contributes toward raising the surface temperature of the planet. The warming results from the fact that incoming irradiance can penetrate to the ground with relatively little absorption, while much of the outgoing long-wave irradiance is "trapped" by the atmosphere and emitted back to the ground. In order to satisfy radiation balance, the surface must compensate by emitting more radiation than it would in the absence of such an atmosphere. To emit more, it must radiate at a higher temperature.

The trapping of the long-wave radiation also can explain the gradual decrease of effective blackbody temperature of atmospheric layers as altitude increases. Expanding on the previous example, let the atmosphere be represented by two layers and let us compute the vertical profile of radiative equilibrium temperature. For simplicity in our two layer atmosphere, let $a_S = 0$ and $a_L = a = .5$, u indicate upper layer, l indicate lower layer, and s denote the earth surface. Schematically we have:

$\downarrow E \quad \uparrow (1-a)^2 Y_s \quad \uparrow (1-a) Y_l \quad \uparrow Y_u$ — top of the atmosphere

$\downarrow E \quad \uparrow (1-a) Y_s \quad \uparrow Y_l \quad \downarrow Y_u$ — middle of the atmosphere

$\downarrow E \quad \uparrow Y_s \quad \downarrow Y_l \quad \downarrow (1-a) Y_u$ — earth surface.

Radiative equilibrium at each surface requires

$$E = .25\, Y_s + .5\, Y_l + Y_u ,$$

$$E = .5\, Y_s + Y_l - Y_u ,$$

$$E = Y_s - Y_l - .5\, Y_u .$$

Solving yields $Y_s = 1.6\ E$, $Y_l = .5\ E$ and $Y_u = .33\ E$. The radiative equilibrium temperatures (blackbody at the surface and gray body in the atmosphere) are readily computed.

$$T_s = [1.6E / \sigma]^{1/4} = 287\ K ,$$

$$T_l = [0.5E / 0.5\sigma]^{1/4} = 255\ K ,$$

$$T_u = [0.33E / 0.5\sigma]^{1/4} = 231\ K .$$

Thus, a crude temperature profile emerges for this simple two-layer model of the atmosphere.

3.5 Absorption (Emission) Line Formation

The Planck explanation of the continuous spectra of the blackbody was founded in the idea of quantization of available energy levels. Planck successfully explained the nature of radiation from heated solid objects of which the cavity blackbody radiator formed the prototype. Such radiation generates continuous spectra and is contrary to line spectra. However, when properly extended, the theory of quantization also led to the understanding of the line spectra of the atom. Let us investigate the development of the Bohr atomic model briefly.

In 1913, Bohr postulated that: (a) the angular momentum of the electrons in their circular orbits about the nucleus are quantized,

$$mvr = nh/2\pi \ ,$$

where m is the electron mass, v the velocity, r the radius, n the quantum number, and h Planck's constant; and (b) the atoms radiate (absorb) only when the electron makes a transition from one energy state to another state of lower (higher) energy,

$$E_{n1} - E_{n2} = hf \ .$$

The mechanical stability of the electron in a circular orbit about a proton is given by the Coulomb force offset by the centrifugal force

$$\frac{e^2}{r^2} = \frac{mv^2}{r} \ ,$$

where e is the electron charge. The total energy of the electron n^{th} state is given by

$$E_n = \frac{1}{2} mv^2 - \frac{e^2}{r}$$

$$= \frac{-2\pi^2 me^4}{h^2} \frac{1}{n^2} \ .$$

Therefore, the frequency of the emission (absorption) lines in the hydrogen spectrum is given by

$$f = \frac{2\pi^2 me^4}{h^3} \left(\frac{1}{n_2^2} - \frac{1}{n_1^2} \right)$$

or

$$f = K \left(\frac{1}{n_2^2} - \frac{1}{n_1^2} \right) \ ,$$

where $K = 3.28 \times 10^{15}$ Hz.

Monochromatic emission is practically never observed. Energy levels during energy transitions are normally changed slightly due to external influences on atoms and molecules, and due to the loss of energy in emission. As a consequence, radiation emitted during repeated energy transitions is non-monochromatic and spectral lines are caused by: (1) the damping of vibrations of oscillators resulting from the loss of energy in emission (the broadening of lines in this case is

considered to be normal); (2) the perturbations due to collisions between the absorbing molecules and between the absorbing and non-absorbing molecules; and (3) the Doppler effect resulting from the difference in thermal velocities of atoms and molecules. The broadening of lines due to the loss of energy in emission (natural broadening) is practically negligible as compared with that caused by collisions and the Doppler effect. In the upper atmosphere, we find a combination of collision broadening and Doppler broadening, whereas in the lower atmosphere, below about 40 km, the collision broadening prevails because of increased pressure.

In general, spectral lines are assumed to be symmetric about the central wavelength λ_o which corresponds to a maximum absorbing power. In the case of a symmetric line, well separated from neighbouring lines of the absorption spectrum, the line shape may be fitted by the Lorentz form

$$k_\lambda = \frac{k_o \alpha^2}{(\lambda - \lambda_o)^2 + \alpha^2} ,$$

where k is a measure of the absorbing power and a is the half width of the line. The half width is the displacement from the line centre to the wavelength where $k_\lambda = k_o/2$. In such an individual spectral line, the absorbing power approaches zero asymptotically at increasing distance in the line wings from the centre. More generally, however, the absorbing power does not become zero between lines because of the overlapping effects of many lines.

3.6 Vibrational and Rotational Spectra

The Bohr theory of the hydrogen atom explained the quantized energy states available to an electron in orbit about a hydrogen nucleus. Additional consideration of elliptical orbits, relativistic effects, and magnetic spin orbit interaction was needed to explain the observed emission spectra in more detail (including the fine structure). Explanation of molecular emission lines requires still more work. Gaseous emission spectra are found to have atomic spectral lines with many additional molecular emission lines superimposed. As indicated earlier, three major types of molecular excitation are observed.

(a) The electronic excitation when the orbital states of the electrons change in the individual atoms;

(b) The vibrational excitation when the individual atoms vibrate with respect to the combined molecular centre of mass;

(c) The rotational excitation when the molecule rotates about the centre of mass.

To understand the vibrational spectra more clearly, consider a typical potential energy curve for a diatomic molecule (shown in Figure 3.2). Stable equilibrium occurs with the nuclei separated by a distance R_o. If the nuclei are separated by a slightly greater or smaller distance R, the energy is raised and a spring-like restoring force is effected. This restoring force can be represented by

$$F = - \left(\frac{d^2E}{dR^2}\right)_{R=R_o} (R - R_o) ,$$

which has a classical frequency of vibration

$$f_o = \frac{1}{2\pi\mu^{1/2}} \left(\frac{d^2E}{dR^2}\right)^{1/2}_{R=R_o}$$

with the reduced mass of the vibrating system

$$\mu = \frac{M_1 M_2}{M_1 + M_2} .$$

The energy levels can be shown to have the form of the Planck postulate

$$E_m = (m + 2)\, hf_o, \quad m = 0, 1, 2, \ldots$$

where the additional 2 is a consequence of solving the Schroedinger wave equation for a harmonic oscillator. The vibrational energy levels of a diatomic molecule are shown in Figure 3.2, the upper energy levels are not equally spaced since the actual energy well is wider than the parabolic approximation and hence these energy levels are closer together than the lower levels.

The rotational spectra appears as fine structure of the combined electronic and vibrational lines. The kinetic energy of rotation of the nuclei about their common centre of mass is readily solved with the Schroedinger equation and the following energy levels emerge:

$$E_J = \frac{h^2}{8\pi^2\mu R_o^2} J(J + 1), \quad J = 1, 2, 3, \ldots$$

These rotational energies are very small, and therefore, lines of the pure rotation spectrum are in the far infrared or microwave regions of the spectrum.

The total energy of a molecule is given by

$$E = E_{electronic} + E_{vibration} + E_{rotation} .$$

The typical separation between the lowest state and the first excited state is about 2 to 10 eV for electronic energies, about .2 to 2 eV for vibration energies and about 10^{-5} to 10^{-3} eV for rotation energies. Note that 1 eV = 1.6 x 10^{-19}J which corresponds to emission at a wavelength of 1.24 μm. Figure 3.3 illustrates this schematically.

Each transition involving a change in electron energy produces a whole series of emission or absorption lines, since many combinations of changes in vibration and rotation energy are possible. If such a system of lines is observed under low resolution conditions, it appears to be a band with practically a continuous distribution of frequencies. With higher resolution the individual lines can be resolved and the energy differences measured. In this way, the energies of the vibrational states and of the rotational states can be measured. It is apparent that in the higher vibrational states the average internuclear distance R is larger because of the asymmetry of the binding energy curve. This fact produces a higher moment of inertia μR^2 when the vibrational quantum number is large and a correspondingly smaller separation in the rotational energy levels. Thus, precision measurement of

the rotational levels as a function of vibrational quantum number permits the study of the asymmetry of the binding energy curve; it is this asymmetry that is responsible for the thermal expansion of molecules.

3.7 Summary of the Interactions between Radiation and Matter

One basic type of interaction between radiation and matter can be summarized by a photon transferring all of its energy to an atom or a molecule and thus being removed from the radiation field. The energy of the photon raises an electron to a higher energy level or a molecule to higher rotational or vibrational states. This increase in energy of the receiving atom or molecule can be released in several different ways.

One mechanism is for the activated molecule to collide with another molecule, and to drop back into a lower energy state; the energy thus freed becomes kinetic energy of the molecules and corresponds to warming the gas. This is absorption. The photon is permanently lost or attenuated from the radiation field.

A second mechanism for release of the energy increase is the spontaneous transition of the molecule (in about one nanosecond) into its original state by emitting a photon which is identical to the absorbed one except for its direction of propagation. This is scattering, where the photon remains part of the radiation field but the direct beam is attenuated.

A third mechanism is the activated molecule releases its energy spontaneously but in two stages. Two photons with different lower energies result; the sum of the energies of the two photons equals the energy of the absorbed photon. The direct beam is attenuated; the original photon has been replaced by two photons at longer wavelengths and is no longer part of the radiation field. This is Raman-scattering.

Other mechanisms for energy release are fluorescence and phosphorescence. These occur when the energy is not released spontaneously, but after relaxation times of nanoseconds to hours.

Another basic type of interaction involves the conversion of molecular kinetic energy (thermal energy) into electromagnetic energy (photons). This occurs when molecules are activated by collisions with each other and the activation energy is emitted as photons. This is emission.

3.8 Beer's Law and Schwarzchild's Equation

In the absence of scattering, the absorption of parallel beam radiation as it passes downward through a horizontal layer of gas of infinitesimal thickness dz is proportional to the number of molecules per unit area that are absorbing radiation along the path. This relationship can be expressed in the form

$$da_\lambda = - dI_\lambda / I_\lambda = - k_\lambda \rho \sec \varphi \, dz \ ,$$

where ρ is the density of the gas and φ is the zenith angle. Here absorbed monochromatic radiance is expressed as an incremental amount of depletion of the incident beam. dI_λ and dz are both negative quantities, so da_λ is positive. The product $\rho \sec \varphi \, dz$ is the mass within the volume swept out by a unit cross-sectional area of the incident beam as it passes through the layer, as pictured in Figure 3.4. The absorption coefficient k_λ is a measure of the fraction of the gas molecules per unit wavelength interval that are absorbing radiation at the wavelength in question. k_λ is a function of composition, temperature, and pressure of the gas within the layer. It has units of square metres per kilogram, which makes the product $k_\lambda \rho \, dz$ dimensionless. Integrating from z up to the top of the atmosphere yields

$$\ln I_{\lambda\infty} - \ln I_\lambda = \sec\varphi \int_z^\infty k_\lambda \rho \, dz \, .$$

Taking the anti-log of both sides and assuming k_λ is independent of height,

$$I_\lambda = I_{\lambda\infty} \exp(-k_\lambda u) \, ,$$

where

$$u = \sec\varphi \int_z^\infty \rho \, dz \, .$$

This relation, often referred to as Beer's Law, states that radiance decreases monotonically with increasing path length through the layer. The quantity u is called the density weighted path length. $k_\lambda u$ is a measure of the cumulative depletion that the beam of radiation has experienced as a result of its passage through the layer and is often called the optical depth σ_λ. The transmittance of the layer of gas lying above the level z is given by

$$\tau_\lambda = I_\lambda / I_{\lambda\infty} = e^{-k_\lambda u}$$

and it follows that, in the absence of scattering, the absorptance

$$a_\lambda = 1 - \tau_\lambda = 1 - e^{-k_\lambda u}$$

approaches unity exponentially with increasing optical depth. At wavelengths close to the centre of absorption lines, k_λ is large so that a very short (density weighted) path length is sufficient to absorb virtually all the incident radiation. At wavelengths away from absorption lines, a path length many orders of magnitude longer may be required to produce any noticeable absorption.

Indirect calculation of the spectrum of solar radiation incident on the top of the atmosphere, on the basis of ground-based measurements, provides an interesting example of the application of Beer's law. Such calculations were made quite successfully many years before direct measurements of undepleted solar radiation were available from satellites. Writing Beer's Law in another form, we have

$$\ln I_\lambda = \ln I_{\lambda\infty} - \sec\varphi \int_z^\infty k_\lambda \rho \, dz \, .$$

Over the course of a single day, I_λ is measured at frequent intervals at a ground station. During this period, the numerical value of the integrand changes very little in comparison to the large changes in solar zenith angle. Thus, to a good approximation, the above expression assumes the form

$$\ln I_\lambda = A - B\,x \, ,$$

where $x = \sec\varphi$ and A and B are constants; that is to say, when the individual data points for I_λ are plotted on a logarithmic scale as function of sec φ, they tend to fall along a straight line. Since the

path length is directly proportional to x, it is possible to deduce the radiance upon the top of the atmosphere simply by extending the straight line that makes the best fit to the data points back to x = 0 (that is, zero path length through the atmosphere).

At the wavelengths of solar radiation, atmospheric emission is negligible, and only absorption needs to be considered. However, at the wavelengths of terrestrial radiation, absorption and emission are equally important and must be considered simultaneously. The absorption of terrestrial radiation along an upward path through the atmosphere is described with the sign reversed by the relation

$$-dL_\lambda^{abs} = L_\lambda k_\lambda \rho \sec \varphi \, dz \, .$$

The emission of radiation from a gas can be treated in much the same manner as the absorption. Making use of Kirchhoff's law it is possible to write an analogous expression for the emission,

$$dL_\lambda^{em} = B_\lambda \, d\varepsilon_\lambda = B_\lambda \, da_\lambda = B_\lambda k_\lambda \rho \sec \varphi \, dz$$

where B_λ is the blackbody monochromatic radiance specified by Planck's law. Now we subtract the absorption from the emission to obtain the net contribution of the layer to the monochromatic radiance of the radiation passing upward through it:

$$dL_\lambda = - (L_\lambda - B_\lambda) k_\lambda \rho \sec \varphi \, dz \, .$$

This expression, known as Schwarzchild's equation, is the basis for computations of the transfer of infrared radiation. For an isothermal gas, with constant k_λ, this may be integrated to obtain

$$(L_\lambda - B_\lambda) = (L_{\lambda o} - B_\lambda) \exp (- k_\lambda u)$$

where $L_{\lambda o}$ is the radiance incident on the layer from below. This expression shows that L_λ should exponentially approach B_λ as the optical thickness of the layer increases. For a layer of infinite optical thickness the emission from the top is B_λ regardless of the value of $L_{\lambda o}$; that is to say, such a layer behaves as a blackbody.

It is often useful to transform the height variable z to pressure p through the hydrostatic equation and the definition of mixing ratio $q = \rho/\rho_a$ where ρ and ρ_a are the density of gas and air respectively,

$$g \rho \, dz = - q \, dp$$

Thus, the optical depth becomes

$$u(p) = \sec \varphi \int_o^p q \, g^{-1} \, dp$$

and the monochromatic transmittance (the probability that a photon of wavelength l leaving pressure level p will reach the top of the atmosphere) is given by

$$\tau_\lambda(p) = \exp \left[- \sec \varphi \int_o^p k_\lambda \, g^{-1} \, q \, dp \right]$$

3.9 Atmospheric Scattering

Scattering is a physical process by which a particle in the path of an electromagnetic wave continuously abstracts energy from the incident wave and re-radiates that energy in all directions. Therefore, the particle may be thought of as a point source of the scattered energy. In the atmosphere, the particles responsible for scattering cover the sizes from gas molecules (~10^{-8} cm) to large raindrops and hail particles (~1 cm). The relative intensity of the scattering pattern depends strongly on the ratio of particle size to wavelength of the incident wave. If scattering is isotropic, the scattering pattern is symmetric about the direction of the incident wave. A small anisotropic particle tends to scatter light equally into the forward and backward directions. When the particle becomes larger, the scattered energy is increasingly concentrated in the forward directions. Distribution of the scattered energy involving spherical and certain symmetrical particles may be quantitatively determined by means of the electromagnetic wave theory. When particles are much smaller than the incident wavelength, the scattering is called Rayleigh scattering. For particles whose sizes are comparable to or larger than the wavelength, the scattering is customarily referred to as Mie scattering.

Rayleigh scattering indicates that the intensity scattered by air molecules in a specific direction is inversely proportional to the fourth power of the wavelength. A large portion of solar energy, lying between the blue to red portion of the visible spectrum, is Rayleigh scattered by the atmosphere. Blue light ($\lambda \approx 0.425$ μm) has a shorter wavelength than red light ($\lambda \approx 0.650$ μm). Consequently, blue light scatters about 5.5 more than red light. It is apparent that the λ^{-4} law causes more of the blue light to be scattered than the red, the green, and the yellow, and so the sky, when viewed away from the sun's disk, appears blue. Moreover, since the molecular density decreases drastically with height, it is anticipated that the sky should gradually darken to become completely black in outer space in directions away from the sun. And the sun itself should appear whiter and brighter with increasing height. As the sun approaches the horizon (at sunset or sunrise), sunlight travels through more air molecules, and therefore more and more blue light and light with shorter wavelengths are scattered out of the beam of light, and the luminous sun shows a deeper red colour than at the zenith.

Larger particles in the atmosphere such as aerosols, cloud droplets, and ice crystals also scatter sunlight and produce many fascinating optical phenomena. However, their single scattering properties are less wavelength selective and depend largely upon the particle size. As a result of this, clouds in the atmosphere generally appear white instead of blue. In a cloudy atmosphere, the sky appears blue diluted with white scattered light, resulting in a less pure blue sky than would have been expected just from Rayleigh scattering. Scattering by a spherical particle of arbitrary size has been treated exactly by Mie in 1908 by means of solving the electromagnetic wave equation derived from the fundamental Maxwell equations.

It is possible to formulate an expression analogous to absorption for ds_λ, the fraction of parallel beam radiation that is scattered when passing downward through a layer of infinitesimal thickness, namely

$$ds_\lambda = dI_\lambda / I_\lambda = K A \sec \varphi \, dz \ ,$$

where K is a dimensionless coefficient and A is the cross-sectional area that the particles in a unit volume present to the beam of incident radiation. If all the particles which the beam encounters in its passage through the differential layer were projected onto a plane perpendicular to the incident beam, the product A sec φ dz would represent the fractional area occupied by the particles. Thus, K plays the role of a scattering area coefficient which measures the ratio of the effective scattering cross section of the particles to their geometric cross section. In the idealized case of scattering by spherical particles of uniform radius r, the scattering area coefficient K can be prescribed on the basis of theory. It is convenient to express K as a function of a dimensionless size parameter $\alpha = 2\pi r/\lambda$,

which is a measure of the size of the particles in comparison to the wavelength of the incident radiation. Figure 3.5a shows a plot of α as a function of r and λ. The scattering area coefficient K depends not only upon the size parameter, but also upon the index of refraction of the particles responsible for the scattering. Figure 3.5b shows K as a function of a for two widely differing refractive indices. When $\alpha << 1$ we have Rayleigh scattering ($K \sim \alpha^4$), and between .1 and 50 we are in the Mie regime. For $\alpha > 50$ the angular distribution of scattered radiation can be described by the principles of geometric optics. The scattering of visible radiation by cloud droplets, raindrops, and ice particles falls within this regime and produces a number of distinctive optical phenomena such as rainbows, halos, and so forth.

It should be noted that the scattering of terrestrial radiation in the atmosphere is of secondary importance compared to absorption and emission of terrestrial radiation.

3.10 The Solar Spectrum

The solar spectrum refers to the distribution of electromagnetic radiation emitted by the sun as a function of the wavelength incident on the top of the atmosphere. The solar constant S is a quantity denoting the amount of total solar irradiance reaching the top of the atmosphere. We recall that it is defined as the flux of solar energy (energy per time) across a surface of unit area normal to the solar beam at the mean distance between the sun and earth. The solar spectrum and solar constant have been extensively investigated for some time. Abbot undertook a long series of ground-based measurements, resulting in a value of about 1350 Wm^{-2} for the solar constant. Subsequent to Abbot's work and prior to more recent measurements carried out from high-altitude platforms, solar constant values of 1396 and 1380 Wm^{-2}, proposed by Johnson and Nicolet respectively, were widely accepted. Since July 1985, the Earth Radiation Budget Experiment (ERBE) has been monitoring the sun's radiation . The solar constant measurements from Nimbus 7 indicate a value of 1372 Wm^{-2} with generally less than a 0.1% variation. There are some significant short term fluctuations due to decreases associated with the development of sunspots.

The standard solar spectrum in terms of the spectral irradiance is shown in the top solid curve of Figure 3.6. Also shown in this diagram is the spectral solar irradiance reaching sea level in a clear atmosphere. The shaded areas represent the amount of absorption by various gases in the atmosphere, primarily H_2O, CO_2, O_3, and O_2. Absorption and scattering of solar radiation in clear atmospheres will be discussed later. If one matches the solar spectral irradiance curve with theoretical blackbody values, we find that a temperature around 6000 K fits the observed curve closely in the visible and infrared wavelengths. Most of the electromagnetic energy reaching the earth originates from the sun's surface, called the photosphere. Of the electromagnetic energy emitted from the sun, approximately 50% lies in wavelengths longer than the visible region, about 40% in the visible region (0.4-0.7 μm), and about 10% in wavelengths shorter than the visible region.

3.11 Composition of the Earth's Atmosphere

To describe the interaction of the earth's atmosphere with solar radiation, the atmosphere's composition must be understood. The atmosphere is composed of a group of nearly permanent gases and a group of gases with variable concentration. In addition, the atmosphere also contains various solid and liquid particles such as aerosols, water drops, and ice crystals, which are highly variable in space and time.

Table 3.2 lists the chemical formula and volume ratio for the concentrations of the permanent and variable gases in the earth's atmosphere. It is apparent from this table that nitrogen, oxygen, and argon account for more than 99.99% of the permanent gases. These gases have virtually constant volume ratios up to an altitude of about 60 km in the atmosphere. It should be noted that although carbon dioxide is listed here as a permanent constituent, it's concentration varies as a result of the combustion of fossil fuels, absorption and release by the ocean, and photosynthesis. Water vapour

concentration varies greatly both in space and time depending upon the atmospheric condition. Its variation is extremely important in the radiative absorption and emission processes. Ozone concentration also changes with respect to time and space, and it occurs principally at altitudes from about 15 to about 30 km, where it is both produced and destroyed by photochemical reactions. Most of the ultraviolet radiation is absorbed by ozone, preventing this harmful radiation from reaching the earth's surface.

3.12 Atmospheric Absorption and Emission of Solar Radiation

The absorption and emission of solar radiation in the atmosphere is accomplished by molecular storing of the electromagnetic radiation energy. Molecules can store energy in various ways. Any moving particle has kinetic energy as a result of its motion in space. This is known as translational energy. The averaged translational kinetic energy of a single molecule in the x, y and z directions is found to be equal to kT/2, where k is the Boltzmann constant and T is the absolute temperature. A molecule which is composed of atoms can rotate, or revolve, about an axis through its centre of gravity and, therefore, has rotational energy. The atoms of the molecule are bounded by certain forces in which the individual atoms can vibrate about their equilibrium positions relative to one another. The molecule, therefore, will have vibrational energy. These three molecular energy types (translational, rotational, and vibrational) are based on a rather mechanical model of the molecule that ignores the detailed structure of the molecule in terms of nuclei and electrons. It is possible, however, for the energy of a molecule to change due to a change in the energy state of the electrons of which it is composed. Thus, the molecule also has electronic energy. The energy levels are quantized and take discrete values only. As we have pointed out, absorption and emission of radiation takes place when the atoms or molecules undergo transitions from one energy state to another. In general, these transitions are governed by selection rules. Atoms exhibit line spectra associated with electronic energy levels. Molecules, however, also have rotational and vibrational energy levels that lead to complex band systems.

Solar radiation is mainly absorbed in the atmosphere by O_2, O_3, N_2, CO_2, H_2O, O, and N, although NO, N_2O, CO, and CH_4, which occur in very small quantities, also exhibit absorption spectra. Absorption spectra due to electronic transitions of molecular and atomic oxygen and nitrogen, and ozone occur chiefly in the ultraviolet (UV) region, while those due to the vibrational and rotational transitions of triatomic molecules such as H_2O, O_3, and CO_2 lie in the infrared region. There is very little absorption in the visible region of the solar spectrum.

3.13 Atmospheric Absorption and Emission of Thermal Radiation

Just as the sun emits electromagnetic radiation covering all frequencies, so does the earth. However, the global mean temperature of the earth-atmosphere system is only about 250 K. This temperature is obviously much lower than that of the sun's photosphere. As a consequence of Planck's law and Wien's displacement law discussed earlier, we find that the radiance (intensity) peak of the Planck function is smaller for the earth's radiation field and the wavelength for the radiance (intensity) peak of the earth's radiation field is longer. We call the energy emitted from the earth-atmosphere system thermal infrared (or terrestrial) radiation. In Figure 1.1, the earth radiance to space measured by the Infrared Interferometer Spectrometer Instrument (IRIS) on board Nimbus IV was also shown. We plotted the spectral distribution of radiance emitted by a blackbody source at various temperatures in the terrestrial range in terms of wavenumber. We saw that in some spectral regions the envelope of the emission spectrum is very close to the spectrum emitted from a blackbody with a temperature of about 300 K, which is about the temperature of the surface. This occurs in spectral regions where the atmosphere is transparent to that radiation. In other spectral regions the emission spectrum is close to the spectrum emitted from a blackbody with a temperature of about 220 K, which is about the temperature at the tropopause. This occurs in spectral regions where the atmosphere is opaque or absorbing to that radiation. In these spectral regions the atmosphere is said to be trapping the radiation. In Figure 3.7, the radiance from .1 μm to 10 cm emitted by the earth-

atmosphere system transmitted to space is shown. Clearly, certain portions of the infrared radiation are trapped by various gases in the atmosphere.

Among these gases, carbon dioxide, water vapour, and ozone are the most important absorbers. Some minor constituents, such as carbon monoxide, nitrous oxide, methane, and nitric oxide, which are not shown, are relatively insignificant absorbers insofar as the heat budget of the earth-atmosphere is concerned. Carbon dioxide absorbs infrared radiation significantly in the 15 μm band from about 600 to 800 cm^{-1}. This spectral region also corresponds to the maximum intensity of the Planck function in the wavenumber domain. Water vapour absorbs thermal infrared in the 6.3 μm band from about 1200 to 2000 cm^{-1} and in the rotational band (< 500 cm^{-1}). Except for ozone, which has an absorption band in the 9.6 μm region, the atmosphere is relatively transparent from 800 to 1200 cm^{-1}. This region is referred to as the atmospheric window. In addition to the 15 μm band, carbon dioxide also has an absorption band in the shorter wavelength of the 4.3 μm region. The distribution of carbon dioxide is fairly uniform over the global space, although there has been observational evidence indicating a continuous global increase over the past century owing to the increase of the combustion of the fossil fuels. This leads to the question of the earth's climate and possible climatic changes due to the increasing carbon dioxide concentration. Unlike carbon dioxide, however, water vapour and ozone are highly variable both with respect to time and the geographical location. These variations are vital to the radiation budget of the earth-atmosphere system and to long-term climatic changes.

In a clear atmosphere without clouds and aerosols, a large portion (about 50%) of solar energy transmits through the atmosphere and is absorbed by the earth's surface. Energy emitted from the earth, on the contrary, is absorbed largely by carbon dioxide, water vapour, and ozone in the atmosphere as evident in Figure 1.1. Trapping of thermal infrared radiation by atmospheric gases is typical of the atmosphere and is, therefore, called the atmospheric effect.

Solar radiation is referred to as short-wave radiation because solar energy is concentrated in shorter wavelengths with its peak at about 0.5 μm. Thermal infrared radiation from the earth's atmosphere is referred to as long-wave radiation because its maximum energy is in the longer wavelength at about 10 μm. The solar and infrared spectra are separated into two spectral ranges above and below about 4 μm, and the overlap between them is relatively insignificant. This distinction makes it possible to treat the two types of radiative transfer and source functions separately and thereby simplify the complexity of the transfer problem.

3.14 Atmospheric Absorption Bands in the Infrared Spectrum

Inspection of high resolution spectroscopic data reveals that there are thousands of absorption lines within each absorption band. The fine structure of molecular absorption bands for the 320-380 cm^{-1} is due to water vapour, and for the 680-740 cm^{-1} region it is due to carbon dioxide. The optically active gases of the atmosphere, carbon dioxide, water vapour, and ozone are all triatomic molecules. Figure 3.8 shows the absorption spectra for H_2O and CO_2. Spectroscopic evidence indicates that the three atoms of CO_2 form a symmetrical straight line array having the carbon atom in the middle flanked by oxygen atoms in either side. Because of linear symmetry it cannot have a static electric dipole moment. Figure 3.9a shows the three normal modes of vibration of such a configuration. The symmetrical motion v_1 should not give rise to an electric dipole moment and, therefore, should not be optically active. The v_1 vibration mode has been identified in the Raman spectrum near 7.5 μm. In the v_2 vibration mode, the dipole moment is perpendicular to the axis of the molecule. The 15 μm band represents this particular vibration. The band is referred to as a fundamental because it is caused by a transition from the ground state to the first excited vibrational state. Another fundamental corresponding to the v_3 vibration mode is the 4.3 μm band, which appears at the short-wave edge of the blackbody curve of atmospheric temperatures.

The water molecule forms an isosceles triangle which is obtuse. Figure 3.9b shows the three normal modes of vibration for such a structure. The 6.3 μm band has been identified as the v_2 fundamental. The two fundamentals, v_1 and v_3, are found close together in a band near 2.7 μm, i.e., on the short-wave side of the infrared spectral region.

The band covering the region from 800 to 400 cm^{-1} shown in Figure 1.1 represents the purely rotational spectrum of water vapour. The water molecule forms an asymmetrical top with respect to rotation, and the line structure of the spectrum does not have the simplicity of a symmetrical rotator such as found in the CO_2 molecule. Close inspection shows that the absorption lines have no clear-cut regularity. The fine structure of the 6.3 μm band is essentially similar to that of the pure rotational band.

In the region between the two water vapour bands, i.e. between about eight and 12 μm, the so-called atmospheric window, absorption is continuous and is primarily due to water vapour. Absorption by carbon dioxide is typically a small part of the total in this region. The overlap of water vapour with ozone in this region is insignificant in the computations of cooling rates since water vapour is important mainly in the lower atmosphere, while cooling due to ozone takes place primarily in the stratosphere and higher.

The ozone molecule is of the triatomic non-linear type (Figure 3.9b) with a relatively strong rotation spectrum. The three fundamental vibrational bands v_1, v_2, and v_3 occur at wavelengths of 9.066, 14.27, and 9.597 μm, respectively. The very strong v_3 and moderately strong v_1 fundamentals combine to make the well-known 9.6 μm band of ozone. The v_2 fundamental is well-masked by the 15 μm band of CO_2. The strong band of about 4.7 μm produced by the overtone and combination frequencies of 0_3 vibrations is in a weak portion of the Planck energy distribution for the atmosphere. Note that the absorption bands of 0_3 in the UV part of the solar spectrum are due to electronic transitions in the ozone molecule.

3.15 Atmospheric Absorption Bands in the Microwave Spectrum

While most of the focus of this chapter has been the visible and infrared spectral regions, a brief summary of the absorption lines in the microwave spectral region follows. Molecular oxygen and water vapour are the major absorbing constituents here. Figure 3.10 shows the transmittance for frequencies below 300 GHz. Below 40 GHz only the weakly absorbing pressure broadened 22.235 GHz water vapour line is evident; this line is caused by transitions between the rotational states. At about 60 and 118.75 GHz, there are strong oxygen absorption lines due to magnetic dipole transitions. For frequencies greater than 120 GHz, water vapour absorption again becomes dominant due to the strongly absorbing line at 183 GHz.

A special problem in the use of microwave from a satellite platform is the emissivity of the earth surface. In the microwave region of the spectrum, emissivity values of the earth surface range from .4 to 1.0. This complicates interpretation of terrestrial and atmospheric radiation with earth surface reflections. More will be said about this later.

3.16 Remote Sensing Regions

Several spectral regions are considered useful for remote sensing from satellites. Figure 3.11 summarizes this. Windows to the atmosphere (regions of minimal atmospheric absorption) exist near 4 μm, 10 μm, 0.3 cm, and 1 cm. Infrared windows are used for sensing the temperature of the earth surface and clouds, while microwave windows help to investigate the surface emissivity and the liquid water content of clouds. The CO_2 and O_2 absorption bands at 4.3 μm, 15 μm, 0.25 cm, and 0.5 cm are used for temperature profile retrieval; because these gases are uniformly mixed in the atmosphere in known portions they lend themselves to this application. The water vapour absorption bands near

6.3 μm, beyond 18 μm, near 0.2 cm, and near 1.3 cm are sensitive to the water vapour concentration in the atmosphere.

Table 3.1
Reflectance (in percent) of various surfaces in the spectral range of solar radiation (using the US Standard Atmosphere of 1976)

Bare soil	10 - 25
Sand, desert	25 - 40
Grass	15 - 25
Forest	10 - 20
Snow (clean, dry)	75 - 95
Snow (wet, dirty)	25 - 75
Sea surface (sun angle) > 25	< 10
Sea surface (low sun angle)	10 - 70

Table 3.2
Composition of the Atmosphere (from the US Standard Atmosphere of 1976)

Permanent Constituents		**Variable Constituents**	
Constituent	**% by volume**	**Constituent**	**% by volume**
Nitrogen (N_2)	78.084	Water vapour (H_2O)	0-0.04
Oxygen (O_2)	20.948	Ozone (O_3)	0-12x10^{-4}
Argon (Ar)	0.934	Sulphur dioxide (SO_2)1	0.001x10^{-4}
Carbon dioxide (CO_2)	0.033	Nitrogen dioxide (NO_2)1	0.001x10^{-4}
Neon (Ne)	18.18x10^{-4}	Ammonia (NH_3)1	0.004x10^{-4}
Helium (He)	5.24x10^{-4}	Nitric oxide (NO)1	0.0005x10^{-4}
Krypton (Kr)	1.14x10^{-4}	Hydrogen sulphide (H_2S)	10.00005x10^{-4}
Xenon (Xe)	0.089x10^{-4}	Nitric acid vapour (HNO_3)	Trace
Hydrogen (H_2)	0.5x10^{-4}		
Methane (CH_4)	1.5x10^{-4}		
Nitrous oxide (N_2O)1	0.27x10^{-4}		
Carbon monoxide (CO)1	0.19x10^{-4}		

[1]Concentration near the earth's surface.

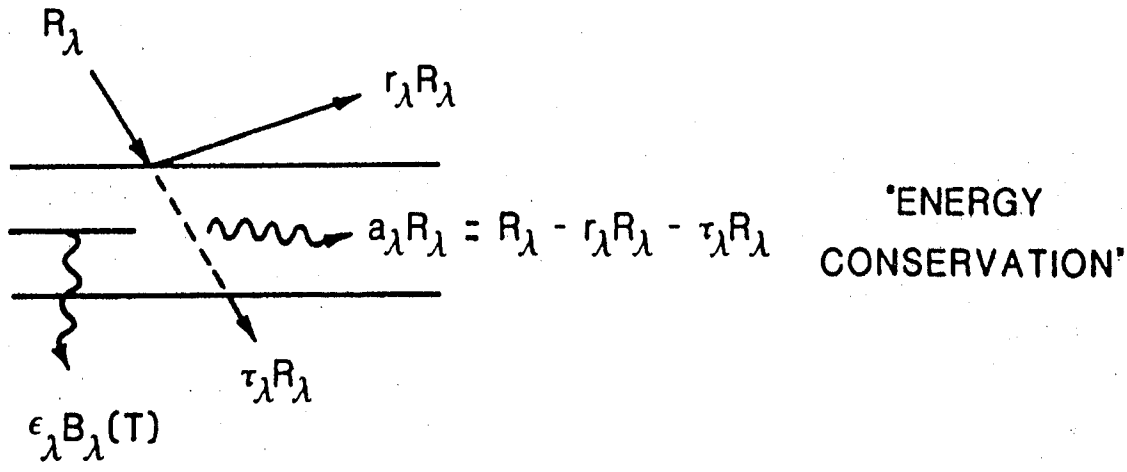

Figure 3.1: A schematic for reflectance, absorptance, and transmittance in a layer of gases.

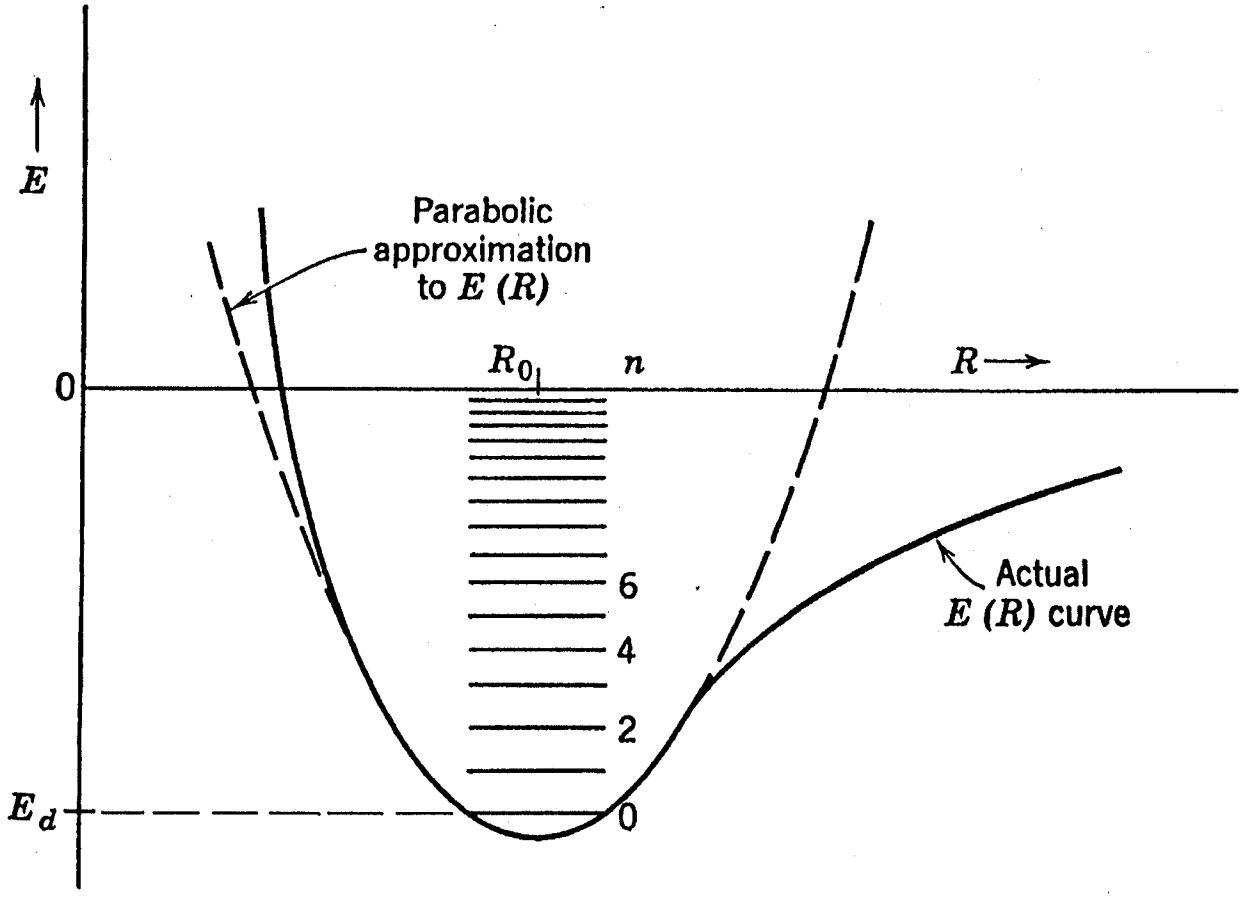

Figure 3.2: Vibrational energy levels of a diatomic molecule.

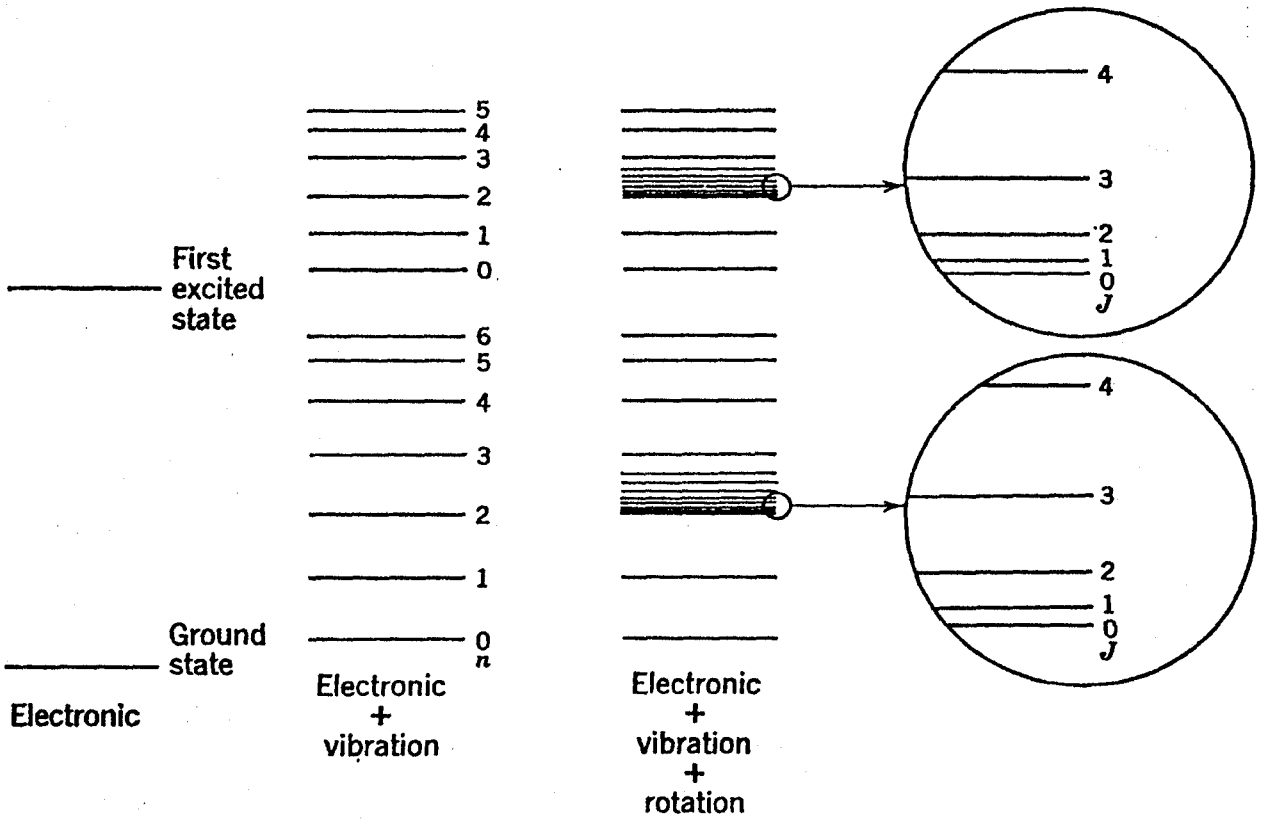

Figure 3.3: The energy levels of a diatomic molecule are shown. Every level of electronic + vibrational energy has rotational fine structure, but this structure is illustrated only for the n = 2 states.

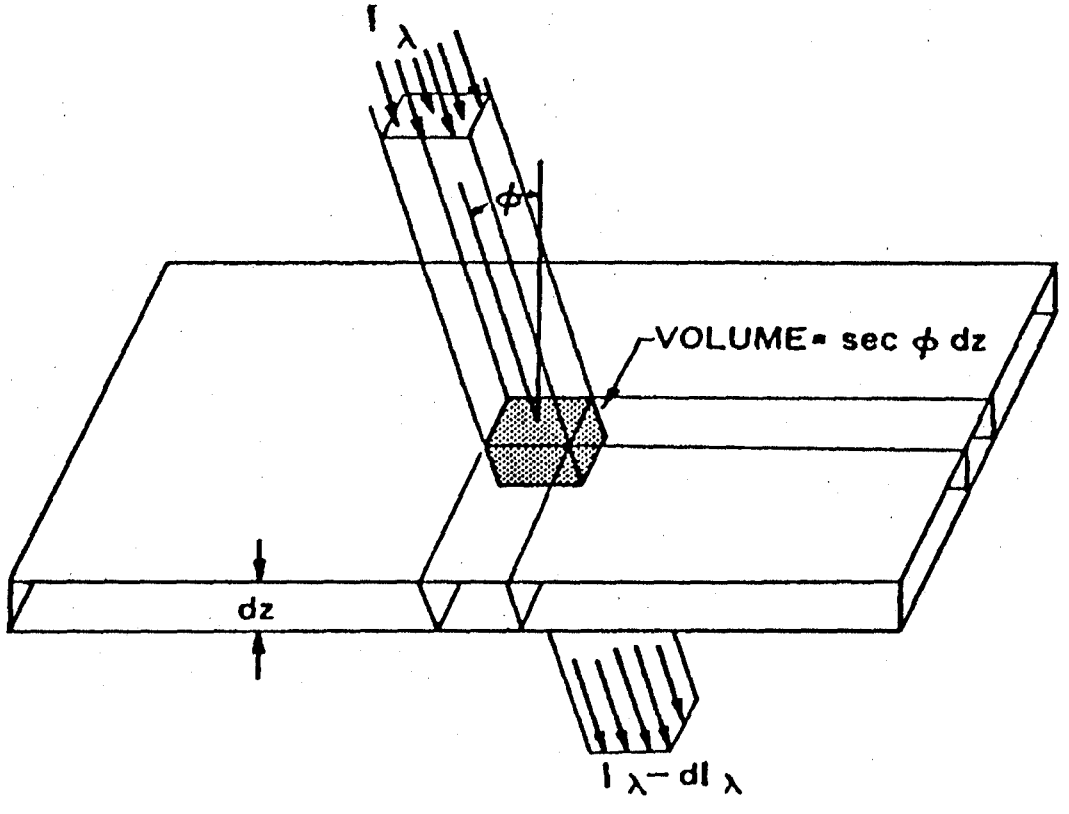

Figure 3.4: Depletion of an incident beam of unit cross-section while passing through an absorbing layer of infinitesimal thickness.

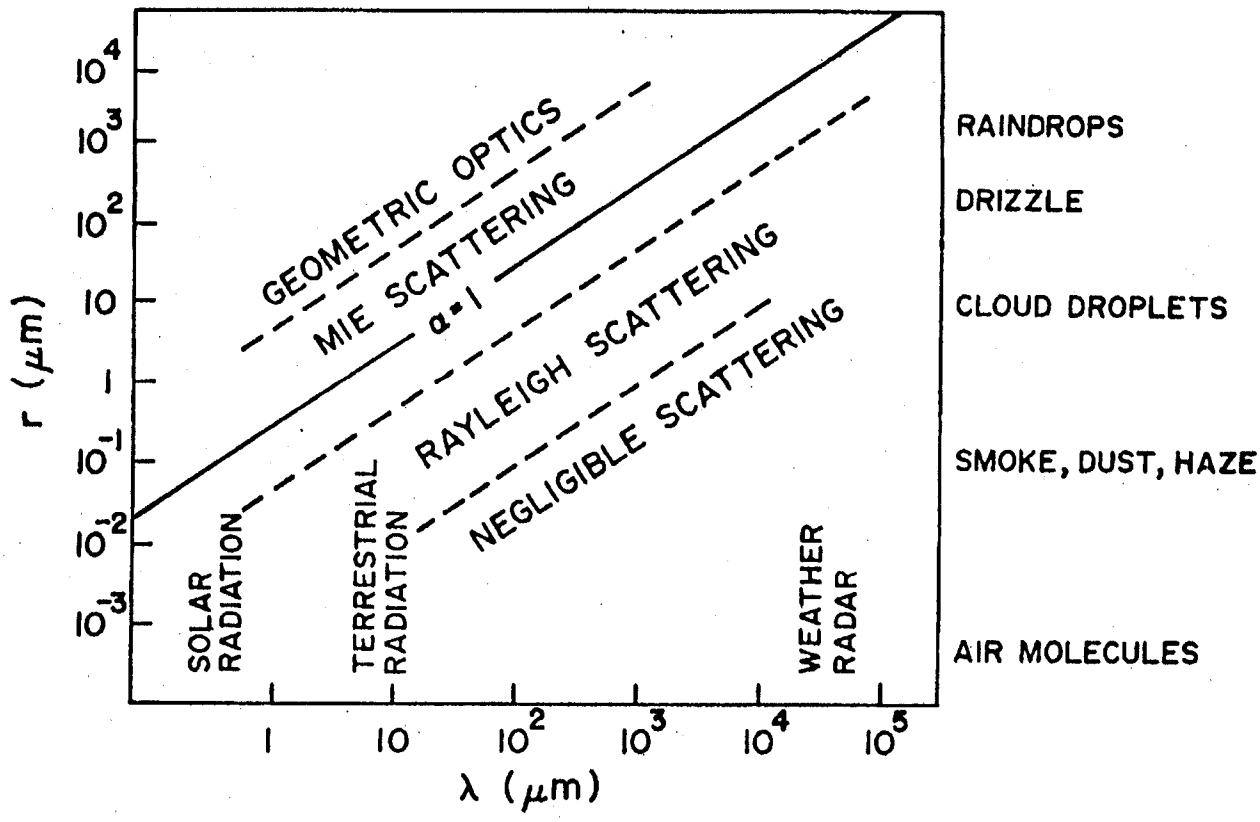

Figure 3.5a: Size parameter a as a function of incident radiation and particle radius.

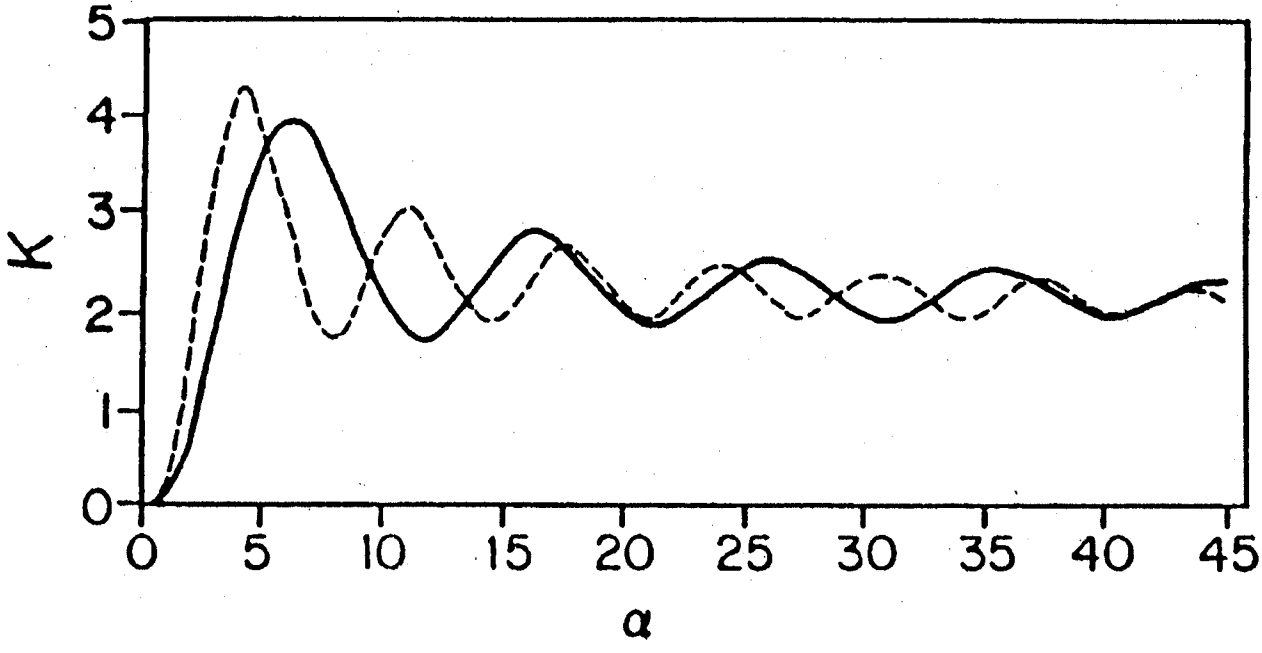

Figure 3.5b: Scattering area coefficient K as a function of size parameter for refractive indices of 1.330 (solid curve) and 14.86 (dashed curve).

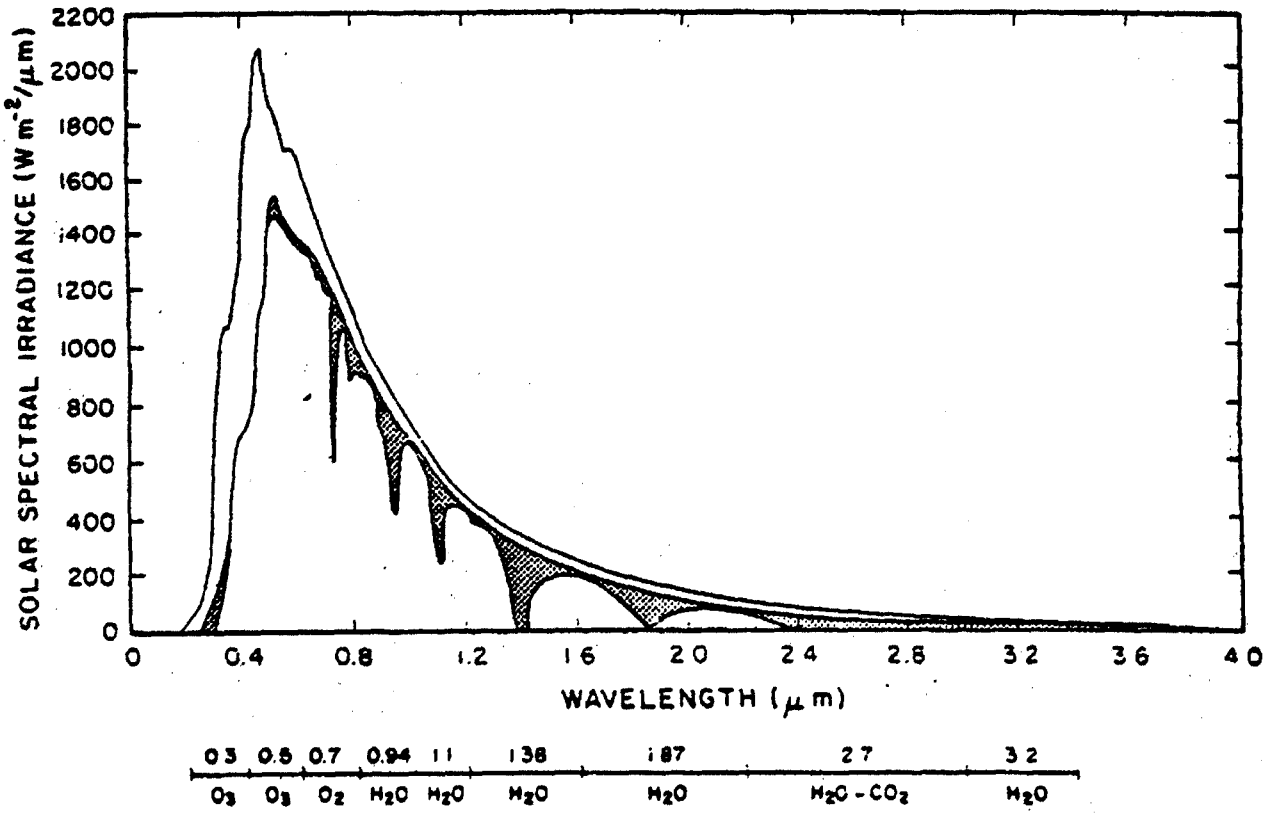

Figure 3.6: Spectral irradiance distribution curves related to the sun: (1) the observed solar irradiance at the top of the atmosphere (after Thekaekara, 1976); and (2) solar irradiance observed at sea level. The shaded areas represent absorption due to various gases in a clear atmosphere.

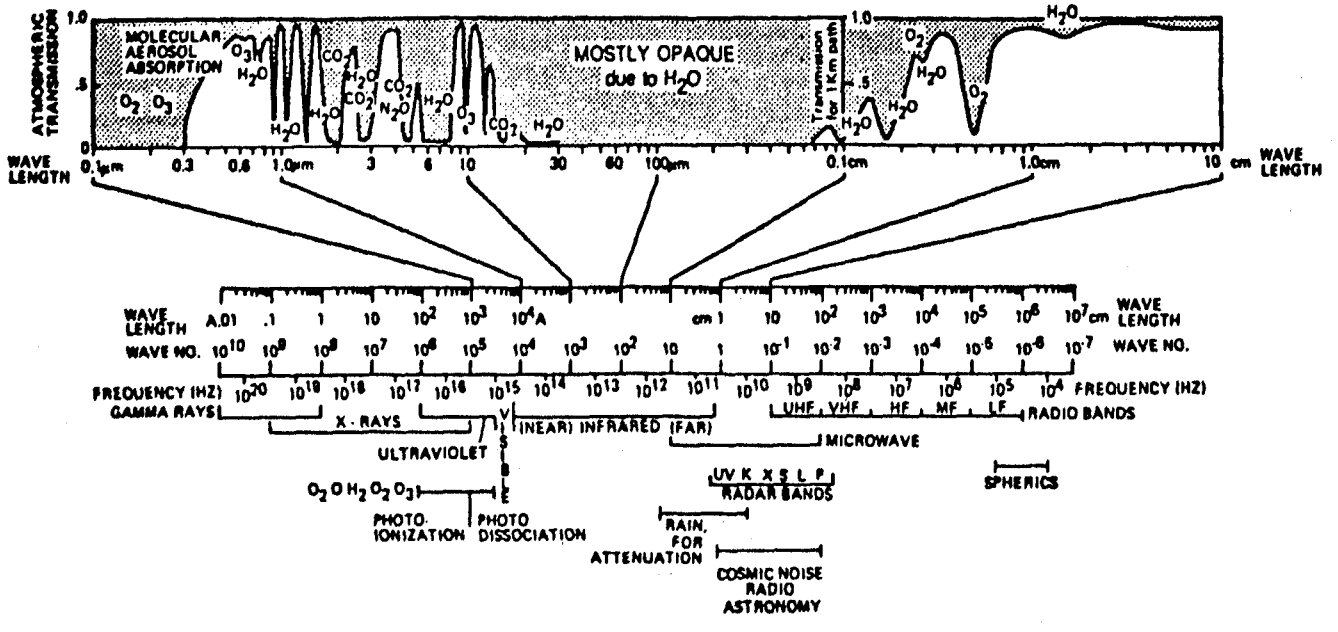

Figure 3.7: Atmospheric transmission characteristics showing the major absorption bands.

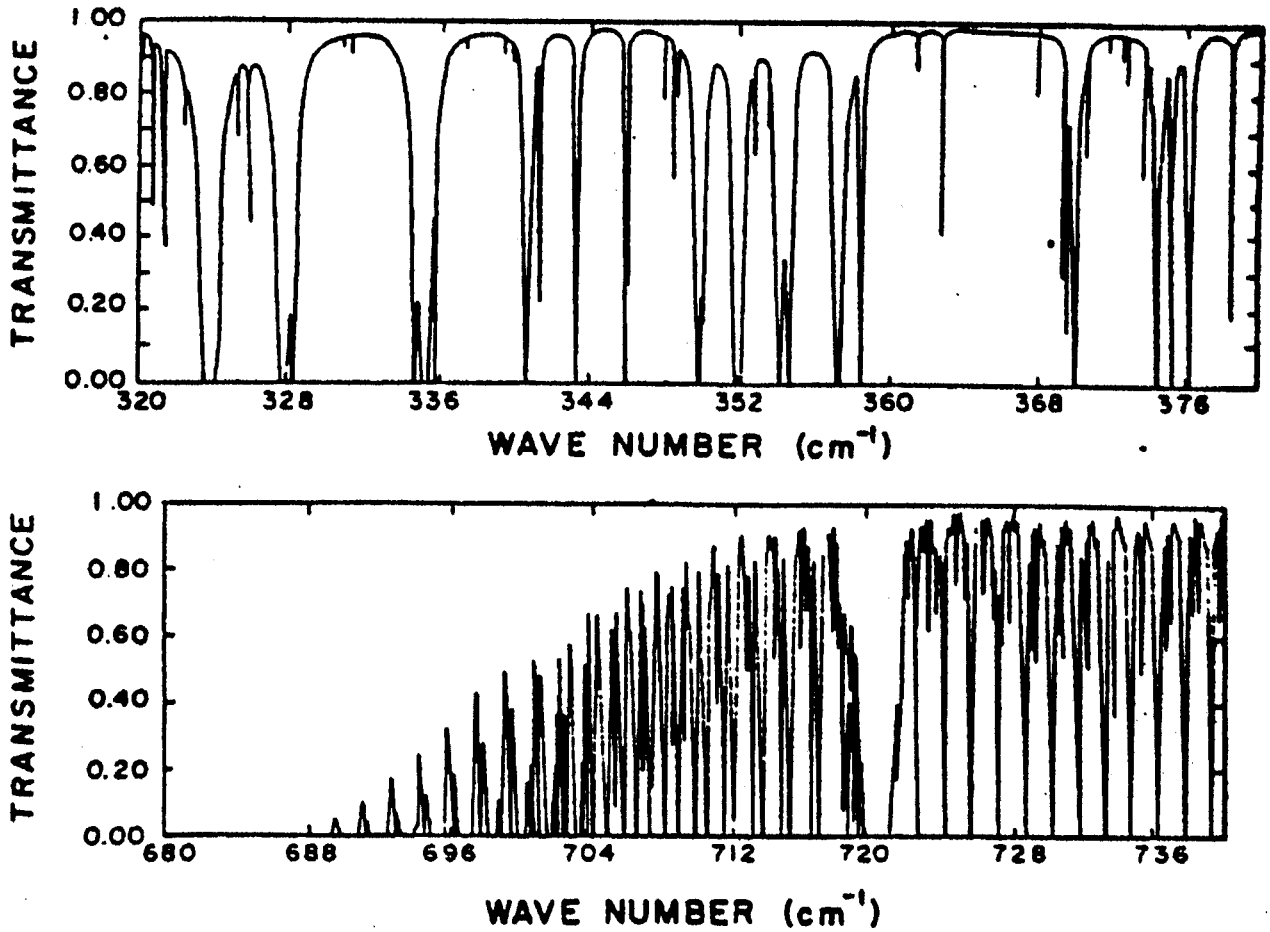

Figure 3.8: Absorption spectrum of the water vapour rotational band and the 15 μm carbon dioxide band at high resolution.

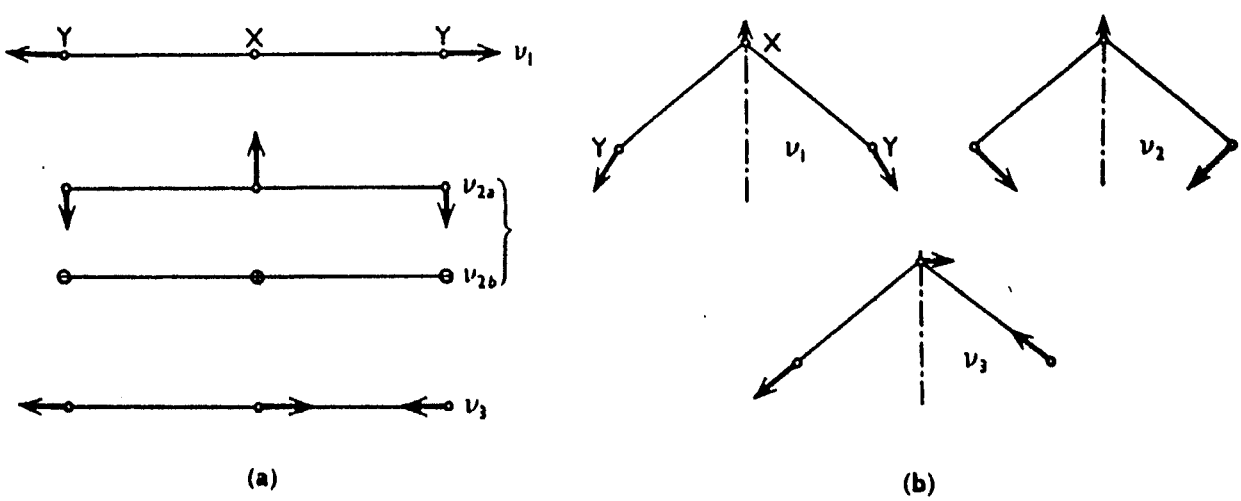

Figure 3.9: Normal modes of a linear (a) and triangular (b) molecules.

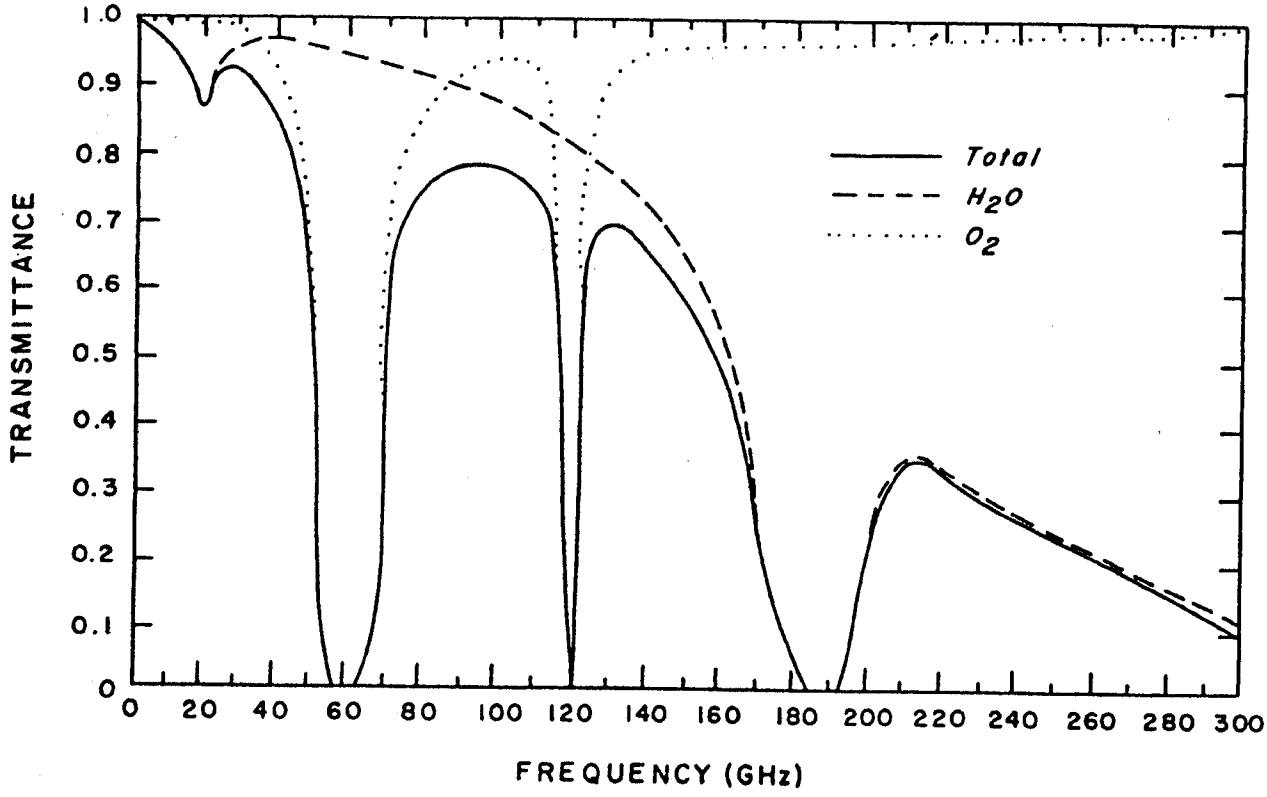

Figure 3.10: Atmospheric transmittance in the microwave region of the spectrum as a function of frequency.

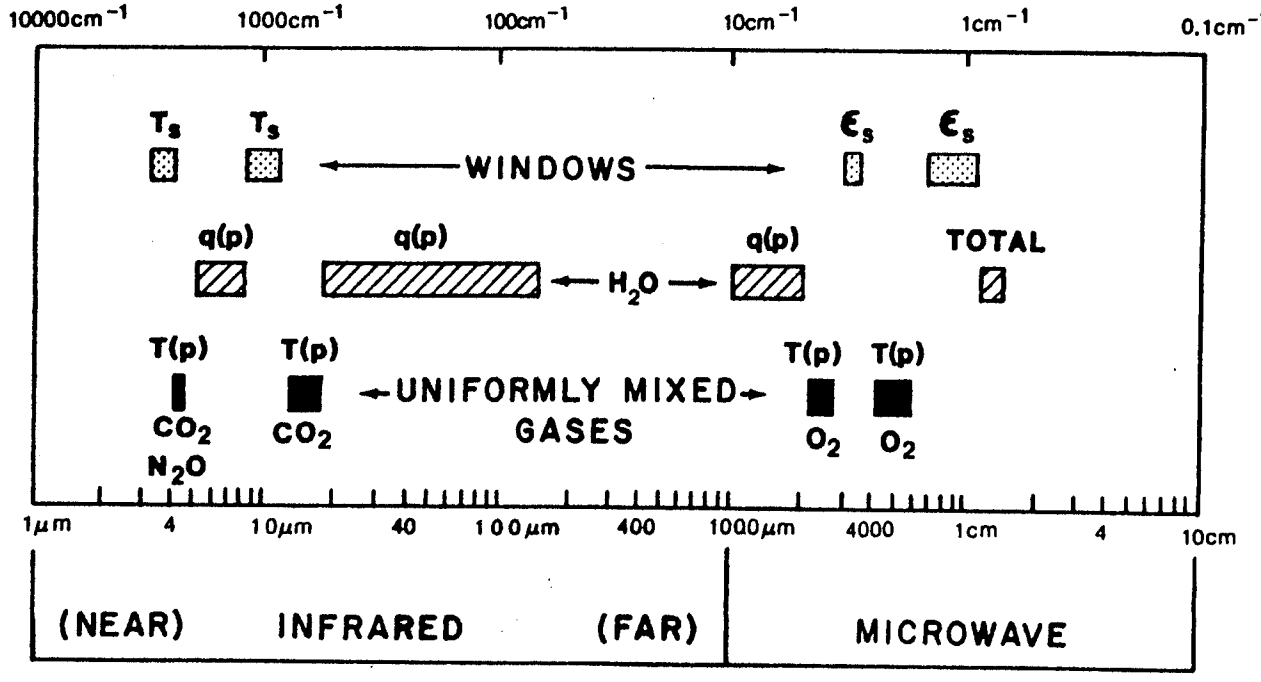

Figure 3.11: Spectral regions used for remote sensing of the earth atmosphere and surface from satellites. ε indicates emissivity, q denotes water vapour, and T represents temperature.

CHAPTER 4

THE RADIATION BUDGET

4.1 The Mean Global Energy Balance

Figure 4.1 summarizes the annual mean global energy balance for the earth-atmosphere system and indicates some of the atmospheric processes that come into play. Of the 100 units of incident solar radiation, 19 are absorbed during passage through the atmosphere: 16 in cloud-free air and three in clouds. A total of 30 units are reflected back to space: 20 from clouds, six from cloud-free air, and four from the earth's surface. The remaining 51 units are absorbed at the earth's surface. The earth disposes of this energy by a combination of infrared radiation and sensible and latent heat flux. The net infrared emission, which represents the upward emission from the earth's surface, minus the downward emission from the atmosphere, amounts to 21 units, 15 of which are absorbed in passing through the atmosphere and six of which reach space. The remaining 30 units are transferred from the earth's surface to the atmosphere by a combination of latent and sensible heat flux.

From the viewpoint of the atmosphere alone, there is a net loss of 49 units of infrared radiation (70 units emitted to space from the top of the atmosphere minus 21 units of net upward flux from the earth's surface) which exceeds by 30 units, the energy gained as a result of the absorption of solar radiation. This deficit is balanced by an influx of 30 units of latent and sensible heat from the earth's surface. Thus, in the global average, the atmosphere experiences a net radiative cooling which is balanced by the latent heat of condensation that is released in regions of precipitation, and by the conduction of sensible heat from the underlying surface. Were it not for the fluxes of latent and sensible heat, the earth's surface would have to be considerably hotter (on the order of 340 K as compared with the observed value of 288 K) in order to emit enough infrared radiation to satisfy the balance requirements for thermal equilibrium.

4.2 The First Satellite Experiment to Measure the Net Radiation

The radiation budget of net radiation, N, of the entire earth-atmosphere system is the difference between the absorbed solar radiation and the outgoing long-wave radiation; therefore,

$$N = (1 - A)\, S/4 - R_{LW}$$

where A is the fraction of incoming solar energy reflected back to space (the planetary albedo), S is the incoming solar irradiance and R_{LW} is the outgoing long-wave irradiance. The radiation budget equation can be written for a specific location of the earth at a given instant of time by replacing the planetary mean incoming solar radiation term (S/4) with the term S cos φ, where φ is the solar zenith angle at the location and time of interest. In this case, A is no longer the planetary albedo, but instead the bi-directional reflectance of the earth-atmosphere for that specific location and time.

The first meteorological satellite experiment flew prior to TIROS-I on the Explorer VII satellite in 1959. The experiment was devised by Suomi and Parent to provide this most basic meteorological measurement, the balance between the radiation input to the atmosphere from the sun and the radiation exiting from the atmosphere as a result of reflection and emission processes. The spatial distribution of the radiation imbalances between incoming and outgoing radiation (the net radiation) is the primary driving force of atmospheric circulation. The solar input had already been measured from ground-based and balloon borne platforms. Suomi's experiment was the first to measure the energy loss to space.

Suomi's radiometer consisted of two heat sensing detectors, one painted black to absorb radiation at all wavelengths, and the other painted white to reflect the short-wave sun's energy and thereby absorbed only earth emitted radiation. Thus, Suomi was able to differentiate between the

energy leaving the earth's atmosphere due to reflected sunlight (provided by the difference between the radiation sensed by the black and white sensors) and that emitted by the earth and atmosphere (the radiation measured by the white sensor).

In a short time after exposure to various radiative components involving the direct solar flux, solar flux reflected by the earth and atmosphere (short-wave), and thermal infrared flux emitted by the earth and atmosphere (long-wave), each sensor achieves radiative equilibrium. It is assumed that the absorptivity of the black sensor a_b is the same for short-wave and long-wave radiation. However, the absorptivity of the white sensor for short-wave and long-wave radiation are given by a_w^S and a_w^L, respectively. Let the temperatures measured by the black sensors and white sensors be T_b and T_w, respectively. On the basis of the Stefan-Boltzmann and Kirchhoff laws, radiative equilibrium equations for both sensors may be expressed by

$$4\pi r^2 a_b \sigma T_b^4 = \pi r^2 a_b (E_o + E_S + E_{IR})$$

and

$$4\pi r^2 a_w^L \sigma T_w^4 = \pi r^2 [a_w^S (E_o + E_s) + a_w^L E_{IR}] .$$

These two equations show that the emitted energy per unit time is equal to the absorbed energy per unit time, where $4\pi r^2$ and πr^2 represent the emission and absorption areas, respectively, for the two spherical sensors each with a radius r. The irradiances of the reflected short-wave, long-wave radiation, and direct solar are denoted by E_S, E_{IR}, and E_O, respectively.

Upon solving the sum of the short-wave and the long-wave irradiances, we obtain

$$E_o + E_S = [4 \sigma a_w^L / (a_w^L - a_w^S)] (T_b^4 - T_w^4)$$

and

$$E_{IR} = [4 \sigma /(a_w^L - a_w^S)] (a_w^L T_w^4 - a_w^S T_b^4)$$

The direct solar irradiance E_O can be evaluated from the solar constant, which is specified prior to the experiment.

In order to convert the measured irradiances into radiances emitted and reflected by the earth, one must consider the solid angle Ω which the earth subtends to the satellite sensor. For a satellite at height h above the earth surface, it can be shown from simple geometric considerations that

$$\Omega = 2\pi [1 - (2Rh + h^2)^{1/2} / (R + h)],$$

where R represents the radius of the earth. Then the radiance I is given by

$$I = E/\Omega ,$$

since the spherical sensor is equally sensitive to radiation from all directions, eliminating the cosine dependence with respect to angle of incidence.

4.3 The Radiation Budget

The circulation of the earth's atmosphere and oceans can be thought of as being powered by a heat engine. The short-wave radiation from the sun provides the fuel supply while the infrared radiation heat loss to space from the earth's surface and atmosphere is the exhaust. The engine is

throttled, to a large extent, by storms and ocean disturbances associated with the transformation of radiative heat to latent and sensible heat.

The distribution of sunlight with latitude is responsible for our major climatic zones (Tropical, Temperate and Polar). The composition of the atmosphere and the characteristics of the earth's surface also play an important role in the climate of local regions such as deserts. Small changes in the sun's radiation or the terrestrial radiation due to natural or man induced changes in atmosphere and surface composition might lead to major variations in our climate.

The net radiation for the earth may vary through the year in accordance with earth-sun distance since S varies 6% between January and July. However, when integrated over an entire year, the net radiation must be near zero, otherwise long-term climatic changes would occur. On the planetary and regional scales, clouds play the major role in upsetting the normal state of radiation balance. The importance of clouds in the radiation balance is demonstrated in Figure 4.2. It shows the relation between the long-wave radiation to space as a function of cloud amount and height for a standard atmospheric temperature and moisture condition. Also shown is the absorbed solar radiation as a function of cloud amount. The long-wave radiation to space decreases with increasing cloud cover and cloud height because cloud temperatures are considerably lower than the earth's surface and they decrease with cloud elevation. However, clouds are also good reflectors of solar radiation and consequently the global albedo increases the absorbed solar energy decreases with increasing cloud cover since clouds generally have higher albedos than the earth's surface.

Figure 4.3a displays the globally averaged monthly mean values of various radiation budget parameters from July 1975 through December 1976. The annual cycles seem to repeat, as the values observed during July 1976 through December 1976 are nearly the same as those observed one year earlier. The albedo and long-wave radiation cycles are nearly 180 degrees (six months) out of phase, possibly the result of two phenomena. The variation of the long-wave radiation with time is the first consideration. In the Northern Hemisphere, the heating and cooling rates correspond to that expected for land surfaces, so outgoing long-wave radiation reaches a maximum in July and a minimum in December. In the Southern Hemisphere, it is dominated by sea surfaces, so only a weak cycle is observed because the seasonal variation of sea-surface temperature is negligible. Therefore, the variation of the globally averaged long-wave radiation with time is dominated by the Northern Hemisphere. During the months when the long-wave radiation is at a minimum, the snow and ice cover and thus albedo in the Northern Hemisphere are close to a maximum. When the long-wave radiation is at a maximum, the snow and ice cover are greatly reduced. A second consideration of equal importance is the annual cycle of cloudiness. There tends to be more cloudiness in the Northern Hemisphere winter than in the Southern Hemisphere winter. This tends to increase the albedo and decrease the long-wave radiation. The opposite effect occurs around June when the cloudiness is least. It is uncertain at this time which of the two effects discussed above is the dominant cause of the variations of the long-wave radiation and albedo.

As shown in Figure 4.3b, the variation with time in the absorbed solar radiation (incoming minus reflected solar radiation) appears to be principally dependent upon the variation of the incoming solar radiation. The annual variation of the incoming solar radiation about its mean value is ± 11.4 W m^{-2}, while the variation of the net energy about its mean value is only about ± 7.6 W m^{-2}, both nearly in phase with each other. If the earth were in a perfectly circular orbit around the sun so that there were no variations in the incoming radiation due to variations in the earth-sun distance, then the variation in absorbed solar radiation would be dominated by variation in the reflected energy. This would cause the phase of the absorbed solar radiation to be shifted about 180 degrees from that observed. Minima and maxima of the absorbed solar radiation correspond to maxima and minima, respectively, of the reflected radiation. Since the net radiation is the difference of the absorbed solar radiation and the outgoing long-wave radiation, which are nearly 180 degrees out of phase with each other, the variation in the net radiation has an amplitude exceeding that of the absorbed and outgoing components and nearly the same phase as the absorbed solar radiation.

4.4 Distribution of Solar Energy Intercepted by the Earth

The solar irradiance at the top of the atmosphere depends strongly on the zenith angle of the sun and much less strongly on the variable distance of the earth from the sun. If the zenith angle, θ, is assumed to be constant over the solid angle subtended by the sun, the irradiance on a horizontal surface varies as cos θ. The zenith angle depends on latitude, time of day, and the tilt of the earth's axis to the rays of the sun (celestial longitude). The mean value of the earth-sun distance, R_{es}^m, is about 1.495×10^{11} metres. The minimum distance occurs on about 3 January during perihelion and is 1.47×10^{11} metres; the maximum distance occurs on about 5 July during aphelion and is 1.52×10^{11} metres.

The total energy received per unit area per day, called insolation and denoted by Q_O, may be calculated by integrating over the daylight hours as follows:

$$Q_o = S \, (R_{es}^m / R_{es})^2 \int_{\text{sunrise}}^{\text{sunset}} \cos \theta \, dt$$

where S represents the mean solar irradiance.

Figure 4.4 shows the results of evaluating Q_O for a variety of latitudes and dates. The maximum insolation is shown to occur at summer solstice at either pole. This is the result of the 24 hour solar day. The maximum in the Southern Hemisphere is higher than in the Northern Hemisphere because the earth is closer to the sun during the northern winter than during the northern summer.

4.5 Solar Heating Rates

Absorption of solar radiation by various gases results in heating in the atmosphere. Heating rate variation with atmospheric pressure is derived in a straightforward manner from net flux considerations. Starting with a plane parallel absorbing and scattering atmosphere, let the differential thickness within the atmosphere be Δz and the monochromatic downward and upward irradiances at wavelength λ be $E_\lambda^{\downarrow}$ and $E_\lambda^{\uparrow}$ respectively. The net monochromatic irradiance (downward) at a given altitude is then given by

$$E_\lambda (z) = E_\lambda^{\downarrow} (z) - E_\lambda^{\uparrow} (z) .$$

Because of absorption, the net monochromatic irradiance decreases from the upper levels to the lower levels. The loss of net monochromatic irradiance or the divergence for the differential layer is given by

$$\Delta E_\lambda (z) = E_\lambda (z) - E_\lambda (z + \Delta z)$$

From the definition of absorption, we also have

$$\Delta E_\lambda (z) = -E_\lambda^{\downarrow} (z + \Delta z) \, a_\lambda (\Delta z)$$

Energy conservation requires that the absorbed energy has to be used to heat the layer, so that

$$\Delta E_\lambda (z) = -\rho \, C_p \, \Delta z \, dT / dt$$

where ρ is the air density in the layer, C_p is the specific heat capacity at constant pressure, and t is the time. Combining these expressions yields the heating rate

$$dT/dt = E_\lambda^{\downarrow} (z + \Delta z) \, a_\lambda (\Delta z) / (\rho \, C_p \, \Delta z)$$

The heating rate is explicitly a function of the spectral interval; to derive a total heating rate it is necessary to sum the spectral intervals where the absorption coefficient is non zero.

Figure 4.5 shows the solar heating rate profile up to 30 km using two different atmospheric profiles (mid latitude winter and tropical) for a clear atmosphere with the sun directly overhead. Effects of absorption by O_3, H_2O, O_2, and CO_2, multiple scattering by molecules, and the ground reflection are accounted for. The maximum heating rate is seen to occur at 3 km and have a value as high as 4 degrees Centigrade per day. The heating rate decreases drastically with increasing altitude due to the decrease of water vapour concentration and reaches a minimum at roughly 15 km. Above 20 km, the increased solar heating is caused by the absorption of ozone, which has a maximum concentration at about 25 km.

4.6 Infrared Cooling Rates

Emission (absorption) of infrared radiation by various gases produces a cooling (heating) effect in the atmosphere. In the same way that solar heating is a function of the net transfer of radiation in the downward direction (as solar radiation enters from the top of the atmosphere), infrared cooling is a function of the net transfer of radiation in the upward direction (as thermal radiation can be thought of as originating from the earth surface). An analogous derivation yields

$$dT/dt = - (\Delta E_\lambda / \Delta z) / (\rho C_p)$$

where ΔE_λ represents the net loss of irradiance in the layer Δz.

A calculation of infrared cooling rates as a function of height in the clear tropical atmosphere is illustrated in Figure 4.6. In the lower 2 km the most important band influencing the cooling is the water vapour continuum. This is due to the rapid increase in the temperature and the partial pressure of water vapour as one gets closer to the surface. Above 5 km the water vapour continuum contributes very little to the infrared cooling rate. In the middle and upper troposphere, absorption is mostly in the water vapour rotational band. A large increase in ozone concentration between 18 and 27 km results in a strong heating. Above 30 km the cooling rate increases rapidly due to the CO_2 15 μm and O_3 9.6 μm bands.

4.7 Radiative Equilibrium in a Gray Atmosphere

The concept of a balanced atmosphere that transfers energy only through radiative transfer (no conduction or convection) is useful to derive some of the characteristics of the earth atmosphere. Given a heated surface and a gray atmosphere in balance, one can write that the net irradiance at any level is constant, since

$$d/dz [E^{\uparrow} - E^{\downarrow}] = \rho C_p dT/dt = 0 \qquad (1)$$

The irradiance going up through a layer can be written

$$d/d\chi^* [E^{\uparrow}] = E^{\uparrow} - \pi B \qquad (2)$$

and similarly for the irradiance going down through a layer

$$-d/d\chi^* [E^{\downarrow}] = E^{\downarrow} - \pi B \qquad (3)$$

where πB is given by Stefan's Law and χ^* is an effective optical depth integrated from the top of the atmosphere down over all angles in the hemisphere. Adding equations (2) and (3) yields

$$d/d\chi^* [E^{\uparrow} - E^{\downarrow}] = E^{\uparrow} + E^{\downarrow} - 2\pi B = 0 , \qquad (4)$$

and subtracting (2) - (3) gives

$$d/d\chi^* [E^{\uparrow} + E^{\downarrow}] = [E^{\uparrow} - E^{\downarrow}] = \Delta = \text{const.} \qquad (5)$$

or using (4)

$$\pi B = \Delta \chi^*/2 + \pi B_o \, . \qquad (6)$$

The boundary conditions are such that there is no downward irradiance at the top of the atmosphere

$$E^{\downarrow} (\text{top}) = 0 \, , \text{ and}$$

$$\chi^* (\text{top}) = 0 \, ,$$

and at the bottom of the atmosphere the upward irradiance must be dictated by Stefan's Law applied to the surface temperature

$$E^{\uparrow} (\text{bot}) = \sigma \, T (\text{sfc})^4 \, , \text{ and}$$

$$\chi^* (\text{top}) = \chi^* (\text{tot})$$

where $\chi^*(\text{tot})$ is the effective optical depth of the total atmosphere. Then we find that

$$\pi B = \Delta (\chi^*+1) / 2 \text{ and} \qquad (7)$$

$$\pi [B (\text{sfc}) - B (\text{bot})] = \Delta/2 \qquad (8)$$

The function πB is plotted against χ^* in Figure 4.7. At the surface there is a discontinuity in temperature, as dictated by Eq. (8). Combining Eq. (7) and (8)

$$\pi B (\text{sfc}) = \Delta (\chi^* (\text{tot}) +2) /2 \, . \qquad (9)$$

Or written more simply in terms of temperature

$$T (\text{sfc})^4 - T (\text{top})^4 = T (\text{bot})^4 \qquad (10)$$

and

$$\chi^* (\text{tot}) = [T (\text{sfc})^4 / T (\text{top})^4] - 2 \, . \qquad (11)$$

When the atmosphere effective optical depth is large, the surface temperature is enhanced, as expected by the greenhouse effect. The optical depth of an atmosphere depends on the concentration of H_2O, CO_2, and O_3. In the case of H_2O the concentration may increase with increasing temperature (through evaporation) and thus creating positive feedback for the greenhouse effect. This effect is very noticeable on Venus, which exhibits "runaway greenhouse effect."

Figure 4.8 is the equivalent diagram in terms of temperature and height to Figure 4.7. The lower part of the atmosphere shows a very steep lapse rate of temperature that is unstable with respect to vertical motion; in a more realistic atmosphere, convection would tend to establish a mean adiabatic lapse rate. Air from near the surface would tend to rise along the mean adiabatic lapse rate of -6 K / km and intersect with the radiative equilibrium curve at a height of about 10 km or near the tropopause. In mid-latitudes the tropopause divides the troposphere where convection is dominant from the stratosphere where radiative transfer is dominant.

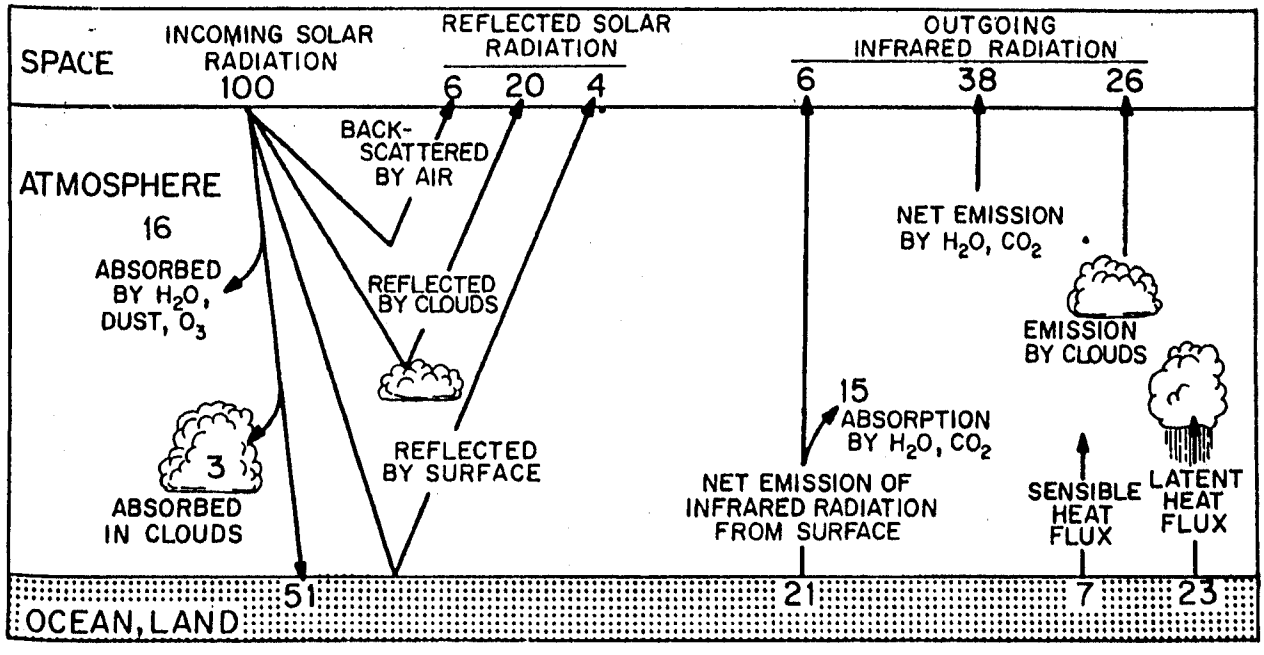

Figure 4.1: The annual mean global energy balance for the earth-atmosphere system. (Numbers are given as percentages of the globally averaged solar irradiance incidence upon the top of the atmosphere.)

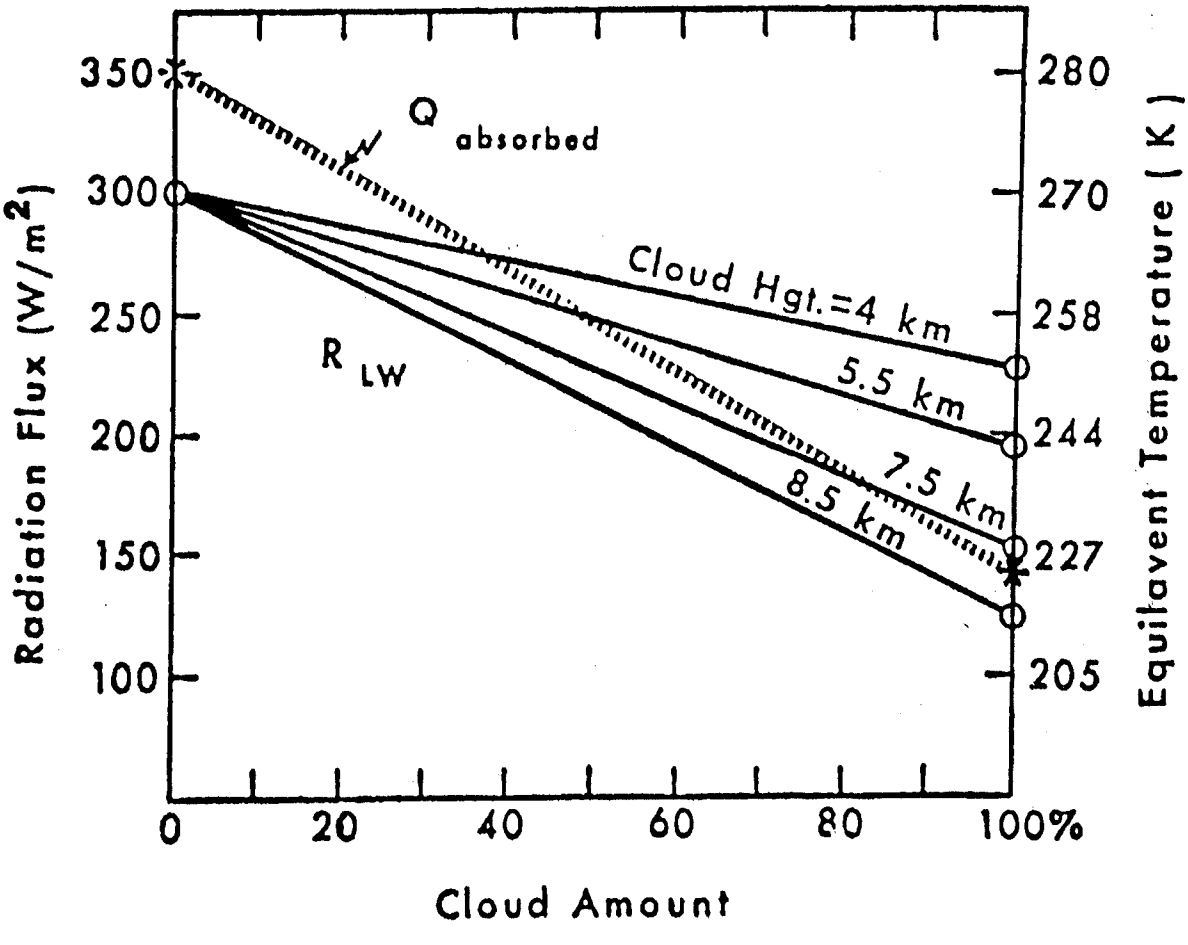

Figure 4.2: Long-wave radiation to space, R, and absorbed solar radiation, Q, as a function of cloud amount.

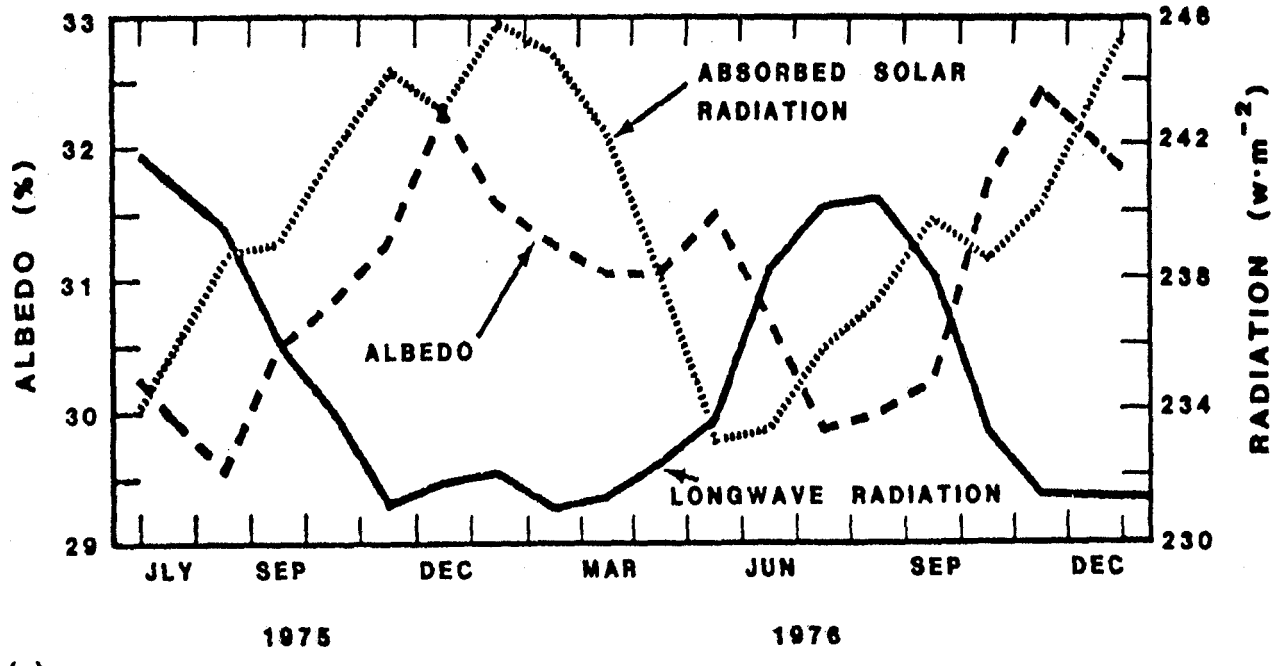

(a)

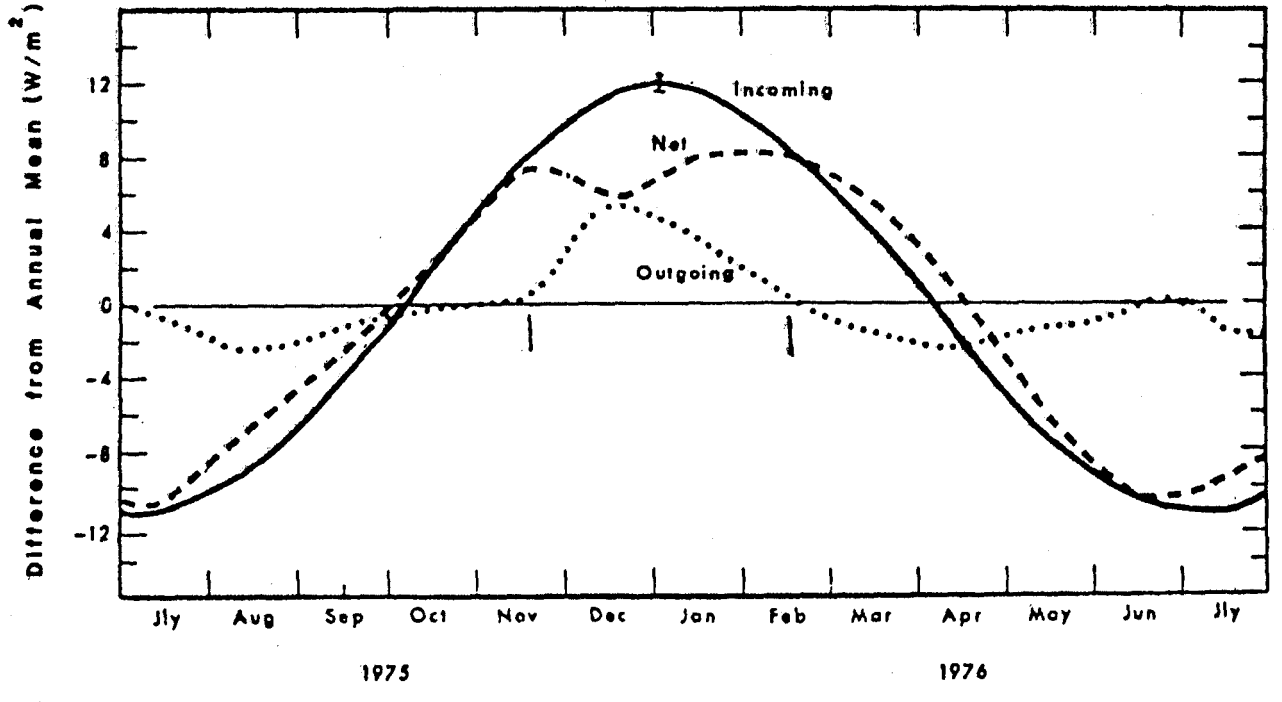

(b)

Figure 4.3: (a) Globally averaged monthly mean values of radiation budget parameters. (b) Variation in time with respect to an annual mean of net, incoming, and outgoing radiation.

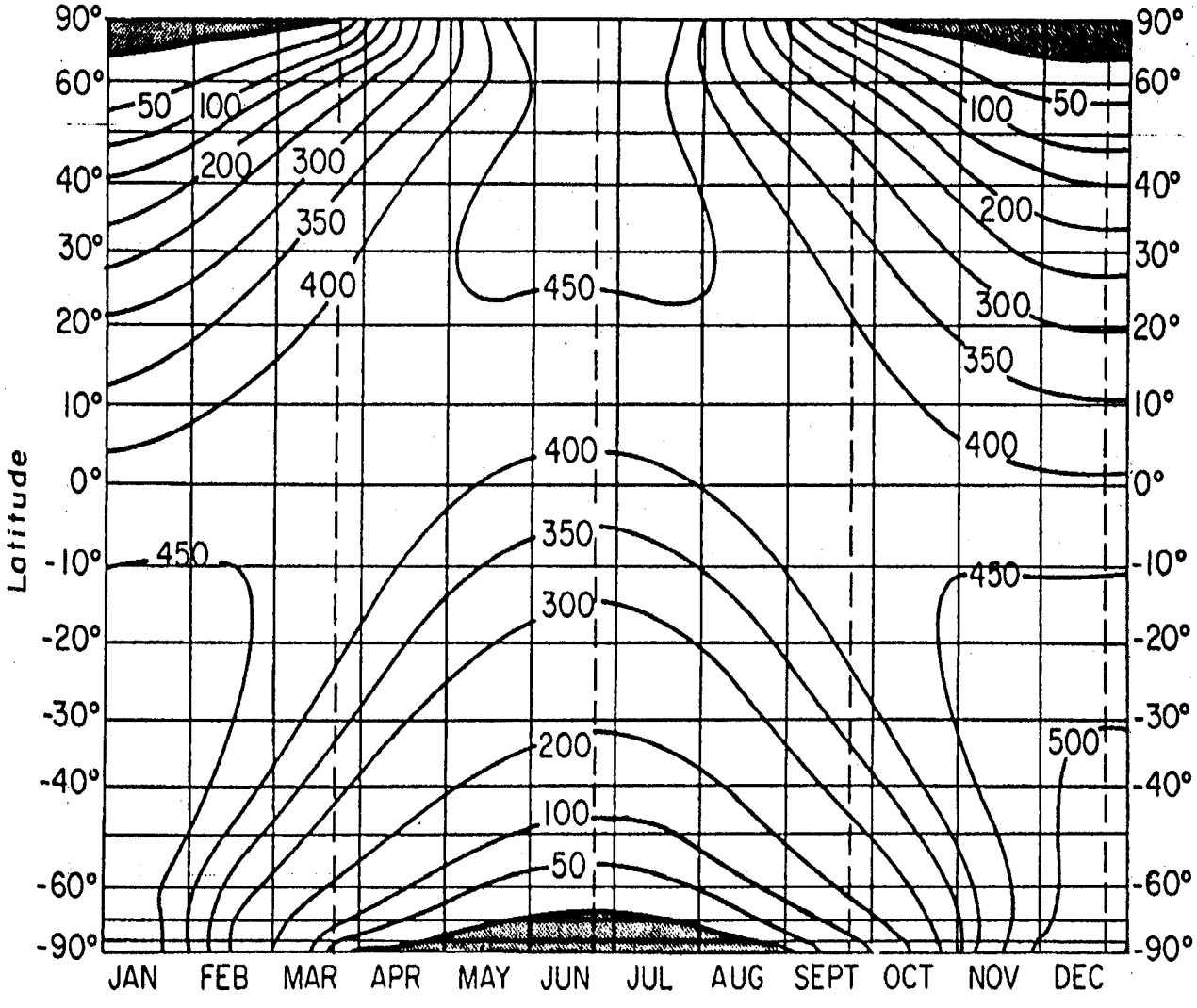

Figure 4.4: Daily solar insolation in W/m^2 incident on a horizontal surface at the top of the atmosphere as a function of latitude and date (adapted from Milankovitch, 1930).

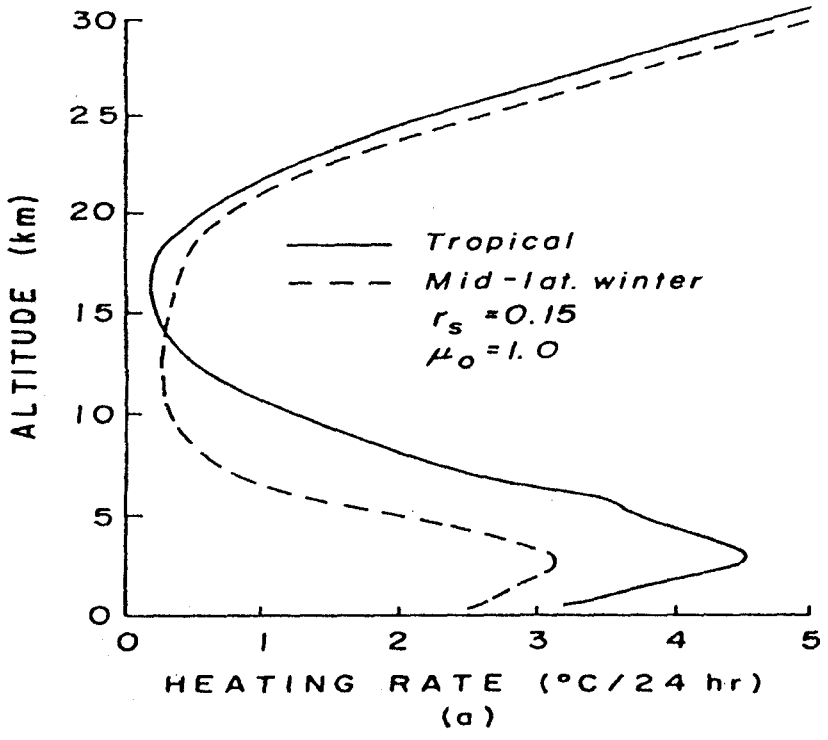

Figure 4.5: Solar heating rate calculated from atmospheric profiles appropriate for tropical and mid latitude winter conditions (Liou, 1980).

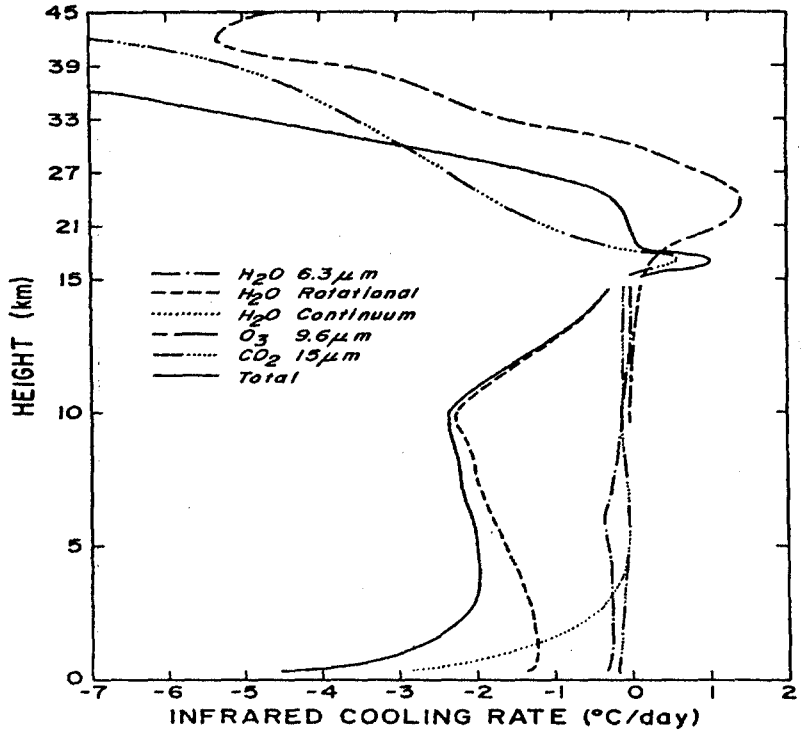

Figure 4.6: Calculation of total and partial cooling rates with an atmospheric profile appropriate for clear tropical conditions (after Roewe and Liou, 1978).

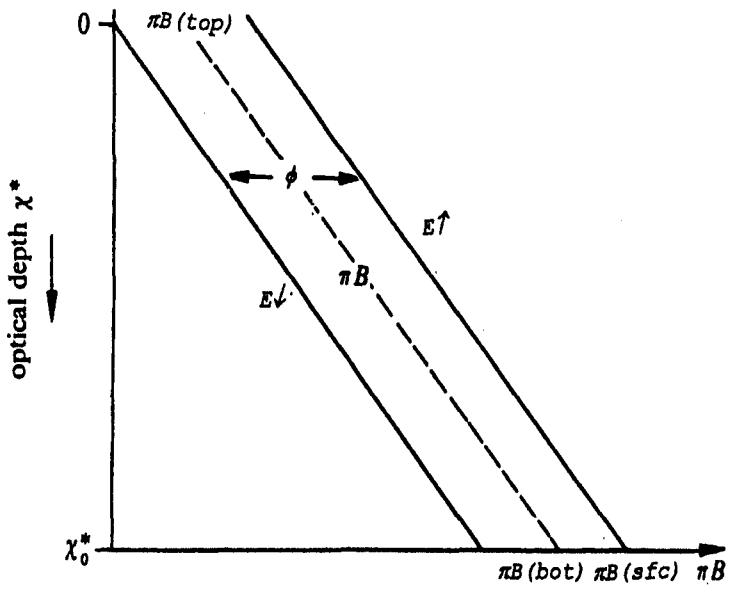

Figure 4.7: Upward E↑ and downward E↓ irradiance and emitted radiance from a given layer πB (given by Stefan's Law) plotted as a function of effective optical depth χ* in an atmosphere in radiative equilibrium.

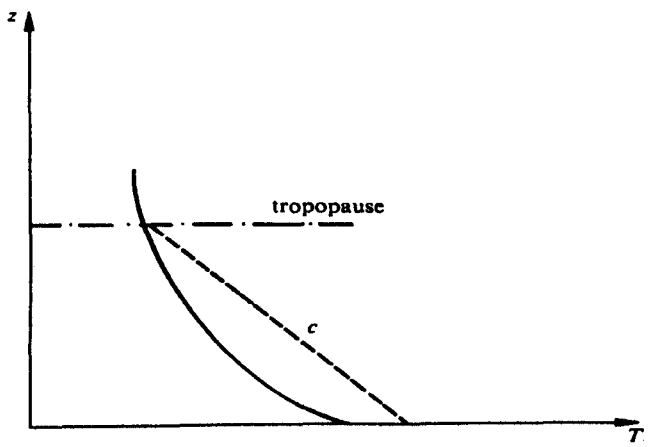

Figure 4.8: Radiative equilibrium temperature plotted versus altitude z. The line c indicates an adiabatic lapse rate of -6 K / km originating from the surface temperature.

CHAPTER 5

THE RADIATIVE TRANSFER EQUATION (RTE)

5.1 Derivation of RTE

Radiative transfer serves as a mechanism for exchanging energy between the atmosphere and the underlying surface and between different layers of the atmosphere. Infrared radiation emitted by the atmosphere and intercepted by satellite sensors is the basis for remote sensing of the atmospheric temperature structure.

The radiance leaving the earth-atmosphere system which can be sensed by a satellite borne radiometer is the sum of radiation emissions from the earth surface and each atmospheric level that are transmitted to the top of the atmosphere. Considering the earth's surface to be a blackbody emitter (with an emissivity equal to unity), the upwelling radiance intensity, I_λ, for a cloudless atmosphere is given by the expression

$$I_\lambda = B_\lambda(T(p_s))\,\tau_\lambda(p_s) + \sum_{p} \varepsilon_\lambda(\Delta p)\, B_\lambda(T(p))\,\tau_\lambda(p)$$

where the first term is the surface contribution and the second term is the atmospheric contribution to the radiance to space. Using Kirchhoff's law, the emissivity of an infinitesimal layer of the atmosphere at pressure p is equal to the absorptance (one minus the transmittance of the layer). Consequently,

$$\varepsilon_\lambda(\Delta p)\,\tau_\lambda(p) = [1 - \tau_\lambda(\Delta p)]\,\tau_\lambda(p)$$

Since the transmittance is an exponential function of depth of the absorbing constituent,

$$\tau_\lambda(\Delta p)\,\tau_\lambda(p) = \exp\left[-\sec\varphi \int_{p}^{p+\Delta p} k_\lambda\, q\, g^{-1}\, dp\right]$$

$$* \exp\left[-\sec\varphi \int_{o}^{p} k_\lambda\, q\, g^{-1}\, dp\right]$$

$$= \tau_\lambda(p+\Delta p)$$

Therefore

$$\varepsilon_\lambda(\Delta p)\,\tau_\lambda(p) = \tau_\lambda(p) - \tau_\lambda(p+\Delta p) = -\Delta\tau_\lambda(p)\,.$$

So we can write

$$I_\lambda = B_\lambda(T(p_s))\,\tau_\lambda(p_s) - \sum_{p} B_\lambda(T(p))\,\Delta\tau_\lambda(p)\,.$$

which when written in integral form reads

$$I_\lambda = B_\lambda(T(p_s))\,\tau_\lambda(p_s) + \int_{p_s}^{o} B_\lambda(T(p))\,\frac{d\tau_\lambda(p)}{dp}\,dp\,.$$

The first term is the spectral radiance emitted by the surface and attenuated by the atmosphere, often called the boundary term and the second term is the spectral radiance emitted to space by the atmosphere.

Another approach to the derivation of the RTE is to start from Schwarzchild's equation written in pressure coordinates

$$dI_\lambda = (I_\lambda - B_\lambda)\, k_\lambda\, g^{-1}\, q \sec\varphi\, dp .$$

This is a first order linear differential equation, and to solve it we multiply by the integrating factor

$$\tau_\lambda = \exp\left[-\sec\varphi \int_o^p g^{-1}\, q\, k_\lambda\, dp\right]$$

which has the differential

$$d\tau_\lambda = -\tau_\lambda \sec\varphi\, g^{-1}\, q\, k_\lambda\, dp .$$

Thus,

$$\tau_\lambda\, dI_\lambda = -(I_\lambda - B_\lambda)\, d\tau_\lambda$$

or

$$d(\tau_\lambda I_\lambda) = B_\lambda\, d\tau_\lambda .$$

Integrating from p_s to 0, we have

$$I_\lambda(0)\,\tau_\lambda(0) - I_\lambda(p_s)\,\tau_\lambda(p_s) = \int_{p_s}^{o} B_\lambda(T(p))\, \frac{d\tau_\lambda(p)}{dp}\, dp .$$

The radiance detected by the satellite is given by $I_\lambda(0)$, $\tau_\lambda(0)$ is 1 by definition, and the surface of the earth is treated as a blackbody so $I_\lambda(p_s)$ is given by $B_\lambda(T(p_s))$. Therefore,

$$I_\lambda = B_\lambda(T(p_s))\,\tau_\lambda(p_s) + \int_{p_s}^{o} B_\lambda(T(p))\, \frac{d\tau_\lambda(p)}{dp}\, dp$$

as before. Writing this in terms of height

$$I_\lambda = B_\lambda(T(0))\,\tau_\lambda(0) + \int_{o}^{\infty} B_\lambda(T(z))\, \frac{d\tau_\lambda}{dz}\, dz .$$

$d\tau_\lambda/dz$ is often called the weighting function which, when multiplied by the Planck function, yields the upwelling radiance contribution from a given altitude z. An alternate form of the weighting function is $d\tau_\lambda/d\ln p$.

To investigate the RTE further consider the atmospheric contribution to the radiance to space of an infinitesimal layer of the atmosphere at height z,

$$dI_\lambda(z) = B_\lambda(T(z))\, d\tau_\lambda(z) .$$

Assume a well-mixed isothermal atmosphere where the density drops off exponentially with height

$$\rho = \rho_o \exp(-\gamma z) ,$$

and assume k_λ is independent of height, so that the optical depth can be written for normal incidence

$$\sigma_\lambda = \int_z^\infty k_\lambda \rho \, dz = \gamma^{-1} k_\lambda \rho_o \exp(-\gamma z)$$

and the derivative with respect to height

$$\frac{d\sigma_\lambda}{dz} = -k_\lambda \rho_o \exp(-\gamma z) = -\gamma \sigma_\lambda .$$

Therefore, we may obtain an expression for the detected radiance per unit thickness of the layer as a function of optical depth,

$$\frac{dI_\lambda(z)}{dz} = B_\lambda(T_{const}) \frac{d\tau_\lambda(z)}{dz} = B_\lambda(T_{const}) \gamma \sigma_\lambda \exp(-\sigma_\lambda) .$$

The level which is emitting the most detected radiance is given by

$$\frac{d}{dz}\left\{\frac{dI_\lambda(z)}{dz}\right\} = 0 ,$$

or where $\sigma_\lambda = 1$. Most of the monochromatic radiance impinging upon the satellite is emitted by layers near the level of unit optical depth. Much of the radiation emanating from deeper layers is absorbed on its way up through the atmosphere, while far above the level of unit optical depth there is not enough mass to emit very much radiation. The assumption of an isothermal atmosphere with a constant absorption coefficient was helpful in simplifying the mathematics in the above derivation. However, it turns out that for realistic vertical profiles of T and k_λ the above result is still at least qualitatively valid; most of the satellite detected radiation emanates from that portion of the atmosphere for which the optical depth is of order unity.

The fundamental principle of atmospheric sounding with meteorological satellites detecting the earth-atmosphere thermal infrared emission is based on the solution of the radiative transfer equation. In this equation, the upwelling radiance arises from the product of the Planck function, the spectral transmittance, and the weighting function. The Planck function consists of temperature information, while the transmittance is associated with the absorption coefficient and density profile of the relevant absorbing gases. Obviously, the observed radiance contains the temperature and gaseous profiles of the atmosphere, and therefore, the information content of the observed radiance from satellites must be physically related to the temperature field and absorbing gaseous concentration.

The mixing ratio of CO_2 is fairly uniform as a function of time and space in the atmosphere. Moreover, the detailed absorption characteristics of CO_2 in the infrared region are well-understood and its absorption parameters (i.e., half width, line strength, and line position) are known rather accurately. Consequently, the spectral transmittance and weighting functions for a given level may be calculated once the spectral interval and the instrumental response function have been given. To see the atmospheric temperature profile information we rewrite the RTE so that

$$I_\lambda - B_\lambda(T(p_s)) \tau_\lambda(p_s) = \int_{p_s}^{o} B_\lambda(T(p)) \frac{d\tau_\lambda(p)}{dp} dp .$$

It is apparent that measurements of the upwelling radiance in the CO_2 absorption band contain information regarding the temperature values in the interval from p_s to O, once the surface temperature has been determined. However, the information content of the temperature is under the integral operator which leads to an ill-conditioned mathematical problem. We will discuss this problem

further and explore a number of methods for the recovery of the temperature profile from a set of radiance observations in the CO_2 band.

Finally, to better understand the information regarding the gaseous concentration profile contained in the solution of the radiative transfer equation, we perform integration by parts on the integral term to yield

$$I_\lambda - B_\lambda(T(0)) = \int_{p_s}^{o} \tau_\lambda(p) \frac{dB_\lambda(T(p))}{dp} dp .$$

Now, if measurements are made in the H_2O or O_3 spectral regions, and if temperature values are known, the transmittance profile may be inferred just as the temperature profile may be recovered when the spectral transmittance is given. Relating the gaseous concentration profile to the spectral transmittance, we see that the density values are hidden in the exponent of an integral which is further complicated by the spectral integration over the response function. Because of these complications, retrieval of the gaseous density profile is very difficult. No clear-cut mathematical analyses may be followed in the solution of the density values. Therefore, we focus our attention on the temperature inversion problem.

5.2 Temperature Profile Inversion

Inference of atmospheric temperature profile from satellite observations of thermal infrared emission was first suggested by King (1956). In his pioneering paper, King pointed out that the angular radiance (intensity) distribution is the Laplace transform of the Planck intensity distribution as a function of the optical depth, and illustrated the feasibility of deriving the temperature profile from the satellite intensity scan measurements.

Kaplan (1959) advanced the sounding concepts by demonstrating that vertical resolution of the temperature field could be inferred from the spectral distribution of atmospheric emission. Kaplan pointed out that observations in the wings of a spectral band sense deeper into the atmosphere, whereas observations in the band centre see only the very top layer of the atmosphere since the radiation mean free path is small. Thus, by properly selecting a set of different sounding spectral channels, the observed radiances could be used to make an interpretation of the vertical temperature distribution in the atmosphere.

Wark (1961) proposed a satellite vertical sounding programme to measure atmospheric temperature profiles. Polar orbiting sounders were first flown in 1969 and a geostationary sounder was first launched in 1980.

In order for atmospheric temperatures to be determined by measurements of thermal emission, the source of emission must be a relatively abundant gas of known and uniform distribution. Otherwise, the uncertainty in the abundance of the gas will make ambiguous the determination of temperature from the measurements. There are two gases in the earth-atmosphere which have uniform abundance for altitudes below about 100 km, and which also show emission bands in the spectral regions that are convenient for measurement. Carbon dioxide, a minor constituent with a relative volume abundance of 0.003, has infrared vibrational-rotational bands. In addition, oxygen, a major constituent with a relative volume abundance of 0.21, also satisfies the requirement of a uniform mixing ratio and has a microwave spin-rotational band.

The outgoing radiance observed by IRIS (Infrared Interferometer and Spectrometer) on the Nimbus 4 satellite is shown in Figure 5.1 in terms of the blackbody temperature in the vicinity of the 15 μm band. The equivalent blackbody temperature generally decreases as the centre of the band is approached. This decrease is associated with the decrease of tropospheric temperature with altitude. Near about 690 cm^{-1}, the temperature shows a minimum which is related to the colder tropopause. Decreasing the wave number beyond 690 cm^{-1}, however, increases the temperature. This is due to the increase of the temperature in the stratosphere, since the observations near the band centre see only the very top layers of the atmosphere. On the basis of the sounding principle already discussed, we can select a set of sounding wave numbers such that a temperature profile in

the troposphere and lower stratosphere are be largely covered. The arrows in Figure 5.1 indicate an example of such a selection.

There is no unique solution for the detailed vertical profile of temperature or an absorbing constituent because (a) the outgoing radiances arise from relatively deep layers of the atmosphere, (b) the radiances observed within various spectral channels come from overlapping layers of the atmosphere and are not vertically independent of each other, and (c) measurements of outgoing radiance possess errors. As a consequence, there are a large number of analytical approaches to the profile retrieval problem. The approaches differ both in the procedure for solving the set of spectrally independent radiative transfer equations (e.g., matrix inversion, numerical iteration) and in the type of ancillary data used to constrain the solution to insure a meteorologically meaningful result (e.g., the use of atmospheric covariance statistics as opposed to the use of an a priori estimate of the profile structure). There are some excellent papers in the literature which review the retrieval theory which has been developed over the past few decades (Fleming and Smith, 1971; Fritz *et al*, 1972; Rodgers, 1976; and Twomey, 1977). The next sections present the mathematical basis for some of the procedures which have been utilized in the operational retrieval of atmospheric profiles from satellite measurements and include some example problems that are solved by using these procedures.

5.3 Transmittance Determinations

Before proceeding to the retrieval problem, a few comments regarding the determination of transmittance are necessary.

So far, we have expressed the upwelling radiance at a monochromatic wavelength. However, for a practical instrument whose spectral channels have a finite spectral bandwidth, all quantities given in the RTE must be integrated over the bandwidth and are weighted by the spectral response of the instrument. The measured radiance over an interval λ_1 to λ_2 is given by

$$I_{\lambda eff} = \int_{\lambda_1}^{\lambda_2} \varphi(\lambda)\, I_\lambda \, d\lambda \; / \int_{\lambda_1}^{\lambda_2} \varphi(\lambda)\, d\lambda$$

where φ denotes the instrument spectral response (or slit) function and λ denotes the mean wavelength of the bandwidth. However, since B varies slowly with λ while τ varies rapidly and without correlation to B within the narrow spectral channels of the sounding spectrometer, it is sufficient to perform the spectral integrations of B and τ independently and treat the results as if they are monochromatic values for the effective wavelength λeff.

For simplicity, we shall let the spectral response function $\varphi(\lambda) = 1$ so that the spectral transmittance may be expressed by

$$\tau_\lambda(p) = \frac{1}{\Delta\lambda} \int_{\Delta\lambda} d\lambda \quad \exp\left[-\frac{q}{g} \int_o^p k_\lambda(p')\, dp' \right]$$

Here we note that the mixing ratio q is a constant, and $\Delta\lambda = \lambda_1 - \lambda_2$. In the lower atmosphere, collision broadening dominates the absorption process and the shape of the absorption lines is governed by the Lorentz profile

$$k_\lambda = \frac{S}{\pi} \frac{\alpha}{(\lambda - \lambda_o)^2 + \alpha^2}$$

The half width α is primarily proportional to the pressure (and to a lesser degree to the temperature), while the line strength S also depends on the temperature. Hence, the spectral transmittance may be explicitly written as

$$\tau_\lambda(p) = \int_{\Delta\lambda} \frac{d\lambda}{\Delta\lambda} \exp\left[-\frac{q}{g}\int_o^p \frac{S(p')}{\pi} \frac{\alpha(p')dp'}{(\lambda-\lambda_o)^2 + \alpha^2(p')}\right] .$$

The temperature dependence of the absorption coefficient introduces some difficulties in the sounding of the temperature profile. Nevertheless, the dependence of the transmittance on the temperature may be taken into account in the temperature inversion process by building a set of transmittances for a number of standard atmospheric profiles from which a search could be made to give the best transmittances for a given temperature profile.

The computation of transmittance through an inhomogeneous atmosphere is rather involved, especially when the demands for accuracy are high in infrared sounding applications. Thus, accurate transmittance profiles are normally derived by means of line-by-line calculations, which involve the direct integration of monochromatic transmittance over the wavenumber spectral interval, weighted by an appropriate spectral response function. Since the monochromatic transmittance is a rapidly varying function of wavenumber, numerical quadrature used for the integration must be carefully devised, and the required computational effort is generally enormous.

All of the earlier satellite experiments for the sounding of atmospheric temperatures of meteorological purposes have utilized the 15 μm CO_2 band. As discussed earlier, the 15 μm CO_2 band consists of a number of individual bands which contribute significantly to the absorption. The most important of these is the v_2 fundamental vibrational rotational band. In addition, there are several weak bands caused by the vibrational transitions between excited states, and by molecules containing less abundant isotopes.

For temperature profile retrievals, the transmittance is assumed to be determined.

5.4 Fredholm Form of RTE and the Direct Linear Inversion Method

Upon knowing the radiances from a set of sounding channels and the associated transmittances, the fundamental problem is to solve for the function $B_\lambda(T(p))$. Because there are several wavelengths at which the observations are made, the Planck function differs from one equation to another depending on the wavelength. Thus, it becomes vitally important for the direct inversion problem to eliminate the wavelength dependence in this function. In the vicinity of the 15 μm CO_2 band, it is sufficient to approximate the Planck function in a linear form as

$$B_\lambda(T(p)) = c_\lambda B_{\lambda o}(T(p)) + d_\lambda$$

where λ_o denotes a fixed reference wavelength and c_λ and d_λ are empirically derived constants. Assuming without loss of generality that $\tau_\lambda(p_s) = 0$, we have the following form of the RTE

$$r_\lambda = \int_{p_s}^{o} b(p)\, W_\lambda(p)\, dp,$$

where

$$r_\lambda = \frac{I_\lambda - d_\lambda}{c_\lambda},$$

$$b(p) = B_{\lambda o}(T(p)) ,$$

and

$$W_\lambda(p) = \frac{d\tau_\lambda(p)}{dp}$$

This is the well-known Fredholm equation of the first kind. W_λ (p), the weighting function, is the kernel, and b(p), the Planck radiance profile, is the function to be recovered from a set of observed radiances r_λ, $\lambda = 1,2,...,M$, where M is the total number of spectral channels observed.

The solution of this equation is an ill-posed problem, since the unknown profile is a continuous function of pressure and there are only a finite number of observations. It is convenient to express b(p) as a linear function of L variables in the form

$$b(p) = \sum_{j=1}^{L} b_j f_j(p) ,$$

where b_j are unknown coefficients, and $f_j(p)$ are the known representation functions which could be orthogonal functions, such as polynomials or Fourier series. It follows that

$$r_\lambda = \sum_{j=l}^{L} b_j \int_{p_s}^{o} f_j(p) W_\lambda(p) dp, \quad \lambda = 1,2,...,M.$$

Upon defining the known values in the form

$$H_{\lambda j} = \int_{p_s}^{o} f_j(p) W_\lambda(p) dp ,$$

we obtain

$$r_\lambda = \sum_{j=1}^{L} H_{\lambda j} b_j, \quad \lambda = 1,2,...,M.$$

In order to find $b_j (j = 1,...,L)$, one needs to have the $r_\lambda (\lambda = 1,...,M)$ where $M \geq L$. In matrix form (see Appendix A on matrices), radiances are then related to temperature

$$r = H b .$$

We can write a solution

$$b = H^{-1} r .$$

To find the solution b, the inverse matrix must be calculated.

It has been pointed out in many studies that the solution is unstable because the equation is under-constrained. Furthermore, the instability of this solution may also be traced to the following sources of error: (a) the errors arising from the numerical quadrature used for the calculation of $H_{\lambda j}$, (b) the approximation to the Planck function, and (c) the numerical round-off errors. In addition, sounding radiometers possess inherent instrumental noise, and thus the observed radiances generate errors probably in a random fashion. All of these errors make the direct inversion from the solution of transfer equation difficult.

5.5 Linearization of the RTE

Many of the techniques for solving the RTE require linearization in which the dependence of Planck radiance on temperature is linearized, often with a first order Taylor expansion about a mean condition. Defining the mean temperature profile condition as $T_m(p)$, then

$$B_\lambda(T) = B_\lambda(T_m) + \frac{\partial B_\lambda(T)}{\partial T}\Big|_{T=T_m} (T - T_m)$$

and the RTE can be written

$$I_\lambda + \frac{\partial B_\lambda(T)}{\partial T}\Big|_{T=T_{mb\lambda}} (T_{b\lambda} - T_{mb\lambda}) =$$

$$B_\lambda(T_s)\,\tau_\lambda(p_s) + \int_{p_s}^{o} \{B_\lambda(T_m) + \frac{\partial B\lambda(T)}{\partial T}\Big|_{T=T_m} (T - T_m)\} \frac{\partial \tau_\lambda(p)}{\partial \ln p}\, d\ln p$$

where $T_{b\lambda}$ represents the brightness temperature for spectral band λ. Reducing to simplest form

$$(\Delta T_{b\lambda}) = \int_{p_s}^{o} (\Delta T) \left(\frac{\partial B_\lambda(T)}{\partial T}\Big|_{T=T_m} \Big/ \frac{\partial B_\lambda(T)}{\partial T}\Big|_{T=T_{mb\lambda}} \right) \frac{\partial \tau_\lambda(p)}{\partial \ln p}\, d\ln p$$

where Δ denotes temperature difference from the mean condition. This linear form of the RTE can then be written in numerical quadrature form

$$(\Delta T_b)_\lambda = \sum_{j=1}^{N} W_{\lambda j} (\Delta T)_j \quad \lambda = 1,\ldots,M$$

where $W_{\lambda j}$ is the obvious weighting factor, M is the number of spectral bands, and N is the number of levels at which a temperature determination is desired.

5.6 Statistical Solutions for the Inversion of the RTE

We now discuss a number of methods which can be utilized to stabilize the solution and give reasonable results.

5.6.1 Statistical Least Squares Regression

Consider a statistical ensemble of simultaneously observed radiances and temperature profiles. One can define a least squares regression solution as the one that minimizes the error

$$\frac{\partial}{\partial b_k} \sum_{\lambda=1}^{M} \{ \sum_{j=1}^{L} H_{\lambda j} b_j - r_\lambda \}^2 = 0 ,$$

which leads to

$$b = (H^t H)^{-1} H^t r .$$

The least squares regression solution was used for the operational production of soundings from the very first sounding spectrometer data by Smith (1970). The form of the direct inverse solution, where r_λ are observations which include the measurement error, is found to be

$$b = A\,r$$

where A is a matrix of solution coefficients. One can define A as that matrix which gives the best least squares solution for b in a statistical ensemble of simultaneously observed radiances and temperature profiles.

The advantages of the least squares regression method over other methods are: (a) if one uses real radiance and radiosonde data comparisons to form the statistical sample, one does not require knowledge of the weighting functions or the observation errors, (b) the instrument need not be calibrated in an absolute sense, and (c) the regression is numerically stable.

Some shortcomings of the regression method are: (a) it disregards the physical properties of the RTE in that the solution is linear whereas the exact solution is non-linear because the weighting function W and consequently the solution coefficients A are functions of temperature, (b) the solution uses the same operator matrix for a range of radiances depending upon how the sample is stratified, and thus the solution coefficients are not situation dependent, and (c) radiosonde data is required, so that the satellite sounding is dependent on more than just surface data.

5.6.2 Constrained Linear Inversion of RTE

The instrument error must be taken into account. The measured radiances always contain errors due to instrument noise and biases. Therefore we write,

$$r_\lambda^{meas} = r_\lambda^{true} + e_\lambda$$

where e_λ represents the measurement errors. Thus to within the measurement error, the solution b(p) is not unique. To determine the best solution, constrain the following function to be a minimum

$$\sum_{\lambda=1}^{M} e_\lambda^2 + \gamma \sum_{j=1}^{L} (b_j - b^{mean})^2$$

where γ is a smoothing coefficient which determines how strongly the solution is constrained to be near the mean. A least squares solution with quadratic constraints implies

$$\frac{\partial}{\partial b_k}\left[\sum_{\lambda=1}^{M} e_\lambda^2 + \gamma \sum_{j=1}^{L} (b_j - b^{mean})^2 \right] = 0 .$$

But

$$e_\lambda = \sum_{j=1}^{L} H_{\lambda j} b_j - r_\lambda^{true}$$

which leads to

$$\sum_{\lambda=1}^{M} \left[\sum_{j=1}^{L} H_{\lambda j} b_j - r_\lambda^{true} \right] H_{\lambda k} + \gamma \left[b_k - b^{mean} \right] = 0 .$$

By definition

$$b^{mean} = \frac{1}{L} \sum_{j=1}^{L} b_j ,$$

and

$$b_k - b^{mean} = -L^{-1} b_1 - L^{-1} b_2 - \ldots + (1-L^{-1}) b_k - \ldots - L^{-1} b_L .$$

So the constrained least squares solution can be written in matrix form

$$H^t H\, b - H^t r + \gamma\, Mb = 0 ,$$

4
where

$$M = \begin{bmatrix} 1-L^{-1} & -L^{-1} & . & . & . \\ -L^{-1} & 1-L^{-1} & & & \\ -L^{-1} & -L^{-1} & 1-L^{-1} & & \\ -L^{-1} & -L^{-1} & -L^{-1} & 1-L^{-1} & \\ . & . & . & . & \\ . & . & . & . & 1-L^{-1} \end{bmatrix}$$

which becomes the identity matrix as L approaches ∞. Thus the solution has the form

$$b = (H^t H + \gamma\, M)^{-1} H^t r .$$

This is the equation for the constrained linear inversion derived by Phillips (1962) and Twomey (1963). We will discuss this further in the section on the Minimum Information Solution.

5.6.3 Statistical Regularization

To make explicit use of the physics of the RTE in the statistical method, using the linearized form of the RTE, one can express the brightness temperatures for the statistical ensemble of profiles as

$$T_b = TW + E ,$$

where E is a matrix of the unknown observational errors. We have dropped the temperature difference notation for simplicity. Solving with the least squares approach, as explained earlier, yields

$$A = (W^t T^t T W + E^t E)^{-1} W^t T^t T ,$$

where covariances between observation error and temperature ($E^t T$) are assumed to be zero since they are uncorrelated. Defining the covariance matrices

$$S_T = \frac{1}{S-1} (T^t T) \text{ and } S_E = \frac{1}{S-1} (E^t E)$$

where S indicates the size of the statistical sample; then

$$A = (W^t S_T W + S_E)^{-1} W^t S_T.$$

The solution for the temperature profile is

$$T = T_b(W^t S_T W + S_E)^{-1} W^t S_T .$$

This solution was developed independently by Strand and Westwater (1968), Rodgers (1968), and Turchin and Nozik (1969).

The objections raised about the regression method do not apply to this statistical regularization solution, namely: (a) W is included and its temperature dependence can be taken into account through interation; (b) the solution coefficients are re-established for each new temperature profile retrieval; and (c) there is no need for coincident radiosonde and satellite observations so that one can use an historical sample to define S_T.

The advantages of the regression method are, however, the disadvantages of the statistical regularization method, namely: (a) the weighting functions must be known with higher precision; and (b) the instrument must be calibrated accurately in an absolute sense.

As with regression, the statistical regularization solution is stable because S_T and S_E are strongly diagonal matrices which makes the matrix

$$(S^t S_T W + S_E)$$

well-conditioned for inversion.

5.6.4 Minimum Information Solution

Twomey (1963) developed a temperature profile solution to the radiances that represents a minimal perturbation of a guess condition such as a forecast profile. In this case T represents deviations of the actual profile from the guess and T_b represents the deviation of the observed brightness temperatures from those which would have arisen from the guess profile condition. S_T is then a covariance matrix of the errors in the guess profile, which is unknown. Assume that the errors in the guess are uncorrelated from level to level such that

$$S_T = \sigma_T^2 I$$

where I is the identity matrix and σ_T^2 is the expected variance of the errors in the guess. If one also assumes that the measurement errors are random, then

$$S_E = \sigma_E^2 I .$$

Simplifying the earlier expression for a solution using statistical regularization, we get

$$T = T_b (W^t W + \gamma I)^{-1} W^t$$

where

$$\gamma = \sigma_\epsilon^2/\sigma_T^2 \ (\approx 10^{-3}) .$$

The solution given is the Tikhonov (1963) method of regularization.

The solution is generally called the Minimum Information Solution since it requires only an estimate of the expected error of the guess profile. One complication of this solution is that γ is unknown. However, one can guess at γ (e.g., 10^{-3}) and iterate it until the solution converges

$$\frac{1}{M}\sum_{j=1}^{M}(T_{bi} - T_{bi})^2 \leq \sigma_\varepsilon^2.$$

The minimum information solution was used for processing sounding data by the SIRS-B and VTPR instruments.

5.6.5 Empirical Orthogonal Functions

It is often advantageous to expand the temperature profile for the N pressure levels so that

$$T(p_j) = \sum_{k=1}^{L} a_k f_k(p_j) \quad j = 1,....,N$$

where L is the number of basis functions (less than M the number of spectral bands) and $f_k(p_j)$ are some type of basis functions (polynomials, weighting functions, or empirical orthogonal functions).

An empirically optimal approximation is achieved by defining $f_k(p_j)$ as empirical orthogonal functions (EOF) which are the eigenvectors of a statistical covariance matrix of temperature T^tT. When the eigenvectors and associated eigenvalues of (T^tT) are determined and the N eigenvalues are ordered from largest to smallest, the associated eigenvectors will be ordered according to the amount of variance they explain in the empirical sample of soundings used to determine T^tT. The EOF's are optimal basis functions in that the first EOF $f_1(p_j)$ is the best single predictor of T(p) that can be found in a mean squared error sense to describe the values used to form T^tT. The second EOF is the best prediction of the variance unexplained by $f_1(p_j)$, and so on. Wark and Fleming (1966) first used the EOF approximation in the linear RTE.

The eigenvectors of the temperature covariance matrix (empirical orthogonal functions) provide the most economical representation of a large sample of observations, where each observation consists of a set of numbers which are not statistically independent of each other. Each observation can be represented as a linear combination of functions (vectors) so that the coefficients in the representation are statistically independent. These functions, which are the eigenvectors of the statistical covariance matrix, are the optimum descriptors in the sense that the progressive explanation of variance is maximized. In other words, among all possible sets of orthogonal functions of a physical variable, the first n empirical functions explain more variance than the first n functions of any other set.

To see this more clearly, consider the representation of the temperature T_{is} at level I from sample observation s. The covariance matrix of the atmospheric profile is given by

$$\hat{T}_{ij} = \frac{1}{S}\sum_{s=1}^{S}(T_{is} - T_i^{mean})(T_{js} - T_j^{mean}),$$

where without loss of generality we declare the mean temperatures for each level to be zero, so that

$$\hat{T}_{ij} = \frac{1}{S}\sum_{s=1}^{S} T_{is} T_{js}$$

or

$$\hat{T} = T^t T .$$

This represents an NxN matrix. If we consider that T is an NxS matrix (S measurements at N levels),

$$\begin{bmatrix} T_{11}, & T_{12}, & \cdots, & T_{1S} \\ T_{21}, & T_{22}, & \cdots, & T_{1S} \\ T_{N1} & T_{N2}, & \cdots, & T_{NS} \end{bmatrix}$$

then $\hat{T}$ is the product of an SxN (T^t) and an NxS (T) matrices. It should be noted that $\hat{T}_{ij}$ is the covariance of temperature at levels I and j and is zero only if temperatures at these two levels are uncorrelated. The diagonal element T_{kk} is the variance of the atmospheric temperature at the level

We diagonalize $\hat{T}$ by performing an eigenvalue analysis. We write

$$\hat{T}E = E\Lambda$$

where E is matrix of eigenvector columns and Λ is diagonal matrix of eigenvalues. In expanded notation, the eigenvalue problem can be stated

$$\begin{bmatrix} \hat{T} \\ \cdot \\ \cdot \\ \cdot \end{bmatrix} \begin{bmatrix} E_{1i} \\ E_{2i} \\ \cdot \\ \cdot \\ E_{Ni} \end{bmatrix} = \lambda_i \begin{bmatrix} E_{1i} \\ E_{2i} \\ \cdot \\ \cdot \\ E_{Ni} \end{bmatrix}$$

in matrix notation

$$\begin{bmatrix} \hat{T} \\ \cdot \\ \cdot \\ \cdot \end{bmatrix} \begin{bmatrix} E_{11} & E_{12} \cdots E_{1N} \\ E_{21} & E_{22} & E_{2N} \\ \cdot & \cdot & \cdot \\ \cdot & \cdot & \cdot \\ E_{N1} & E_{N2} & E_{NN} \end{bmatrix} = \begin{bmatrix} E_{11} & E_{12} \cdots E_{1N} \\ E_{21} & E_{22} & E_{2N} \\ \cdot & \cdot & \cdot \\ \cdot & \cdot & \cdot \\ E_{N1} & E_{N2} & E_{NN} \end{bmatrix} \begin{bmatrix} \lambda_1 & & & \\ & \lambda_2 & & \\ & & \cdot & \\ & & & \lambda_N \end{bmatrix}$$

where

$$E = \begin{bmatrix} E_1 & E_2 & \cdots & E_N \\ \downarrow & \downarrow & & \downarrow \end{bmatrix}$$

Since $\hat{T}$ is real and symmetric, it is Hermitian and therefore has eigenvectors that are orthonormal and eigenvalues that are real and greater than zero. Thus, E is an orthogonal matrix

$$E^t E = I \quad \text{or} \quad E^t = E^{-1} .$$

The eigenvectors form a basis for the temperature variances. Any temperature variance can be expressed as an expansion of these EOFs.

The transformation that diagonalizes $\hat{T}$ emerges

$$E^t \hat{T} E = \Lambda \quad \text{or} \quad \hat{T} = E \Lambda E^t .$$

When the square root of the eigenvalue of the temperature covariance matrix is less than the accuracy of the temperature measurements, its contribution to the solution of the temperature profile is unreliable (it is merely fitting noise). The eigenvectors are ordered in such a way that the first eigenvector explains largest amount of variance, describing largest scale of variability, and subsequent eigenvectors account for the residual variance in successively decreasing order. The first few eigenvectors account for all significant variance, the remaining eigenvectors are merely fitting noise. This suggests a desired representation of each profile

$$\underset{(NxS)}{T_{is}} = \sum_{k=1}^{L} \underset{(LxS)}{A_{ks}} \; \underset{(NxL)}{E_{ik}} \quad \text{or} \quad \underset{(NxS)}{T} = \underset{(NxL)}{E} \; \underset{(LxS)}{A}$$

where L is the number of EOFs associated with eigenvalues whose square root is greater than the noise. The sample of coefficients a_{ks} are statistically independent, hence

$$\frac{1}{S} \sum_{s=1}^{S} A_{is} A_{js} = \lambda_i \delta_{ij} \quad \text{or} \quad \frac{1}{S} A^t A = \Lambda .$$

Therefore, the temperature profile retrieval from empirical orthogonal functions has N equal to 25 levels, M equal to 18 channels, L equal to 10 EOF, and S equal to the sample of 1200. Using the convention that capital letters denote matrices and lower case letters denote vectors in the following paragraphs, we can write the expansion of atmospheric temperature in terms of EOF as

$$\underset{(Nx1)}{t} = \underset{(NxL)}{E} \; \underset{(Lx1)}{a}$$

where the solution rests in finding the expansion coefficients a, which are dependent on the atmospheric situation. Also the observed brightness temperatures can be expanded in terms of the EOF for the brightness temperature covariance matrix, so that

$$\underset{(Mx1)}{t_b} = \underset{(MxL)}{E_b} \; \underset{(Lx1)}{a_b} ,$$

where all components of this equation are known. Note that in expanded form

$$\begin{bmatrix} T_{1s} \\ T_{2s} \\ . \\ . \\ . \\ T_{25S} \end{bmatrix} = \begin{bmatrix} E_{11} & E_{21} \cdots E_{10,1} \\ E_{12} & E_{22} \\ . & . \\ . & . \\ . & . \\ E_{1,25} & E_{10,25} \end{bmatrix} \begin{bmatrix} A_{1s} \\ A_{2s} \\ . \\ . \\ . \\ A_{10s} \end{bmatrix}$$

which is different from $a^t E^t$

$$\begin{bmatrix} A_{1s}, A_{2s}, \ldots, A_{10s} \end{bmatrix} \qquad \begin{bmatrix} E_{11} & E_{21} \cdots E_{25,1} \\ E_{12} & E_{22} \\ . & \\ . & \\ . & \\ E_{1,10} & E_{25,10} \end{bmatrix}$$

We are trying to solve for t from t_b; a more stable solution occurs when an intermediate step is inserted to get a from a_b. In this formulation a transformation matrix D is used. Then

$$\underset{(Lx1)}{a} = \underset{(LxL)}{D} \underset{(Lx1)}{a_b} = D\,(E_b^t E_b)^{-1} E_b^t t_b = D\,E_b^t t_b$$

where the least squares solution has been inferred and the orthogonality property has been used. D is best determined from a statistical sample of 1200 radiosonde and rocketsonde profiles covering all seasons of the year throughout both hemispheres. So we write

$$\underset{(LxS)}{A} = \underset{(LxL)}{D} \underset{(LxS)}{A_b}$$

then least squares solution for D yields

$$D = A\,A_b^t\,(A_b\,A_b^t)^{-1}.$$

Using the 1200 samples we have

$$\underset{(NxS)}{T} = \underset{(NxL)}{E} \underset{(LxS)}{A}$$

which implies that the least squares solution for A yields

$$A = (E^tE)^{-1}\,E^tT = E^tT\,.$$

since by orthogonality $E^tE = 1$. Similarly for the brightness temperature terms

$$\underset{(MxS)}{T_b} = \underset{(MxL)}{E_b} \underset{(LxS)}{A_b}$$

where a least squares solution for A_b gives

$$A_b = (E^tE_b)^{-1}\,E_b^tT_b = E_b^tT_b\,.$$

Through the solutions for A and A_b, D is known,

$$D = E^t T [E_b^t T_b]^t [(E_b^t T_b)(E_b^t T_b)^t]^{-1}$$

$$= E_t T T_b^t E_b [E_b^t T_b T_b^t E_b]^{-1}$$

$$= E^t T T_b^t E_b E_b^{-1} T_b^{t-1} T_b^{-1} E_b ,$$

or

$$\underset{(LxL)}{D} = \underset{(LxN)}{E^t} \quad \underset{(NxS)}{T} \quad \underset{(SxM)}{T_b^{-1}} \quad \underset{(MxL)}{E_b} .$$

Solving for t

$$t = E a = E D a_b = E D E_b^t t_b = H t_b$$

$$= E E^t T T_b^{-1} E_b E_b^t t_b$$

which becomes

$$\underset{(Nx1)}{t} = \underset{(NxS)}{T} \quad \underset{(SxM)}{T_b^{-1}} \quad \underset{(Mx1)}{t_b}$$

The ordinary least squares solution yields

$$t = (T T_b^t) (T_b T_b^t)^{-1} t_b .$$

The advantage of eigenvector approach is that it is less sensitive to instrument noise (low eigenvalue eigenvectors have been discarded). But if all eigenvectors are used (L=M) then the EOF solution is same as the least squares solution. It is better conditioned because L<M and noise has not been fit, but true variance has been. The advantages of regression are: (1) you don't need to know the weighting functions or the measurement errors, (2) instrument calibration is not critical, and (3) the regression is numerically stable. The disadvantages are: (1) there is no physics of the RTE included, (2) there is a linear assumption, (3) sample stratification is crucial, and (4) it is dependent on radiosonde data.

In practice, the empirical function series is truncated either on the basis of the smallness of the eigenvalues (thus, the smallness of explained variance) of higher order eigenvectors or on the basis of numerical instabilities which result when L approaches M. If $L \leq M$ and L is small (e.g., ≤ 5), a stable solution can usually be obtained by the direct inverse. The matrix H, in this case, is better conditioned with respect to matrix inversion. This is because the basis vector f_k is smooth and acts as a constraint on the solution thereby stabilizing it. However, in practice, best results are obtained by choosing an optimum L<M or by conditioning the H matrix prior to its inversion.

5.7 Numerical Solutions for the Inversion of the RTE

We have discussed several statistical matrix solutions of the direct linear inversion of the RTE; we now turn our attention to numerical iterative techniques producing solutions.

5.7.1 Numerical Iteration Solution by Chahine Relaxation Method

The difficulty in reconstructing the temperature profile from radiances at several selected wavelengths is due to the fact that the Fredholm equation with fixed limits may not always have a solution for an arbitrary function. Since the radiances are obtained from measurements which are only approximate, the reduction of this problem to a linear system is mathematically improper, and a

nonlinear approach to the solution of the full radiative transfer equations appears to become necessary. The basic radiance equation is:

$$I_\lambda = B_\lambda(T_s)\,\tau_\lambda(p_s) + \int_{p_s}^{o} B_\lambda(T(p))\,\frac{d\tau_\lambda(p)}{d\ln p}\,d\ln p, \quad \lambda = 1,2,\ldots,M,$$

where λ denotes the different spectral channels and the weighting function is expressed in logarithmic scale. Since the weighting function reaches a strong maximum at different pressure levels for different spectral channels, the actual upwelling radiance observed by the satellite, R_λ, can be approximated through the use of the mean value theorem, by

$$R_\lambda = B_\lambda(T_s)\,\tau_\lambda(p_s) + B_\lambda(T(p_\lambda))\,\left[\frac{d\tau_\lambda(p)}{d\ln p}\right]_{p_\lambda}\Delta_\lambda \ln p\,,$$

where p_λ denotes the pressure level at which the maximum weighting function is located, and $\Delta_\lambda \ln p$ is the differential of the pressure at the λth level and is defined as the effective width of the weighting function for wavelength λ. Let the guessed temperature at p_λ level be $T'(p_\lambda)$. Thus, the guessed upwelling radiance I_λ is given by:

$$I_\lambda = B_\lambda(T_s)\,\tau_\lambda(p_s) + B_\lambda(T'(p_\lambda))\,\left[\frac{d\tau_\lambda(p)}{d\ln p}\right]_{p_\lambda}\Delta_\lambda \ln p\,,$$

where the transmittance and the surface temperature are assumed to be known.

Upon dividing and noting that the dependence of the Planck function on temperature variations is much stronger than that of the weighting function, we obtain

$$\frac{R_\lambda - B_\lambda(T_s)\,\tau_\lambda(p_s)}{I_\lambda - B_\lambda(T_s)\,\tau_\lambda(p_s)} \approx \frac{B_\lambda(T(p_\lambda))}{B_\lambda(T'(p\lambda))}$$

When the surface contribution to the upwelling radiance is negligible or dominant, the equation may be approximated by

$$\frac{R_\lambda}{I_\lambda} \approx \frac{B_\lambda(T(p_\lambda))}{B_\lambda(T'(p_\lambda))}$$

or in iteration form

$$\frac{R_\lambda}{I_\lambda^{old}} = \frac{B_\lambda(T^{new}(p_\lambda))}{B_\lambda(T^{old}(p_\lambda))}.$$

This is the relaxation equation developed by Chahine (1970).

Since most of the upwelling radiance at the strong absorption bands arises from the upper parts of the atmosphere, whereas the radiance from the less attenuating bands comes from progressively lower levels, it is possible to select a set of wave numbers to recover the atmospheric temperature at different pressure levels. The size of a set of sounding wave numbers is defined by

the degree of the vertical resolution required and is obviously limited by the capacity of the sounding instrument.

Assuming now that the upwelling radiance is measured at a discrete set of M spectral channels, and that the composition of carbon dioxide and the level of the weighting function peaks p_λ are all known, the following integration procedures are utilized to recover the temperature profile $T^{(n)}(p_\lambda)$ at level p_λ, where n is the order of the iterations:

(a) Make an initial guess for $T^{(n)}(p_\lambda)$, n = 0;

(b) Substitute $T^{(n)}(p_\lambda)$ into the RTE and use an accurate quadrature formula to evaluate the expected upwelling radiance $I_\lambda^{(n)}$ for each sounding channel;

(c) Compare the computed radiance values $I_\lambda^{(n)}$ with the measured data R_λ. If the residuals

$$[R_\lambda - I_\lambda^{(n)}] / R_\lambda$$

are less than a preset small value (say, 10^{-4}) for each sounding channel, then $T^{(n)}(p_\lambda)$ is a solution;

(d) If the residuals are greater than the preset criterion, we apply the relaxation equation to each wavelength (M times) to generate a new guess for the temperature values

$T^{(n+1)}(p_\lambda)$

at the selected pressure levels p_λ. Note that

$$T^{(n+1)}(p_\lambda) = B^{-1}\left[B(T^{(n)}(p_\lambda)) \frac{R_\lambda}{I_\lambda^{(n)}} \right] .$$

In this calculation, each sounding channel acts at only one specific pressure level p_λ to relax

$$T^{(n)}(p_\lambda) \quad \text{to} \quad T^{(n+1)}(p_\lambda) \quad ;$$

(e) Carry out the interpolation between the temperature value at each given level p_λ to obtain the desirable profile (it is sufficient to use linear interpolation);

(f) Finally, with this new temperature profile, go back to step (b) and repeat until the residuals are less than the preset criterion.

5.7.2 Example Problem Using the Chahine Relaxation Method

Consider a three channel radiometer with spectral bands centred at 676.7, 708.7, and 746.7 wavenumbers. Their weighting functions peak at 50, 400, and 900 mb, respectively. The transmittance is summarized in the following table:

Pressure (mb)	Transmittance		
	676.7	708.7	746.7 (cm^{-1})
10	.86	.96	.98
150	.05	.65	.87
600	.00	.09	.61
1000	.00	.00	.21

The surface temperature is assumed to be 280 K. The radiometer senses the radiances R_i for each spectral band I to be 45.2, 56.5, and 77.8 $mW/m^2/ster/cm^{-1}$, respectively.

(a) Guess $T^{(o)}(50) = T^{(o)}(400) = T^{(o)}(900) = 260$ K;

(b) Compute the radiance values for this guess profile by writing:

$$I_i^{(o)} = B_i(1000)\,\tau_i(1000) + B_i(900)\,(\tau_i(600) - \tau_i(1000)) + B_i(400)\,(\tau_i(150) - \tau_i(600)) + B_i(50)\,(\tau_i(10) - \tau_i(150))$$

yielding 76.9, 82.3, and 85.2 $mW/m^2/ster/cm^{-1}$, respectively;

(c) Convergence has not been reached;

(d) Iterate to a new profile using the relaxation equation

$$T^{(1)}(p_i) = B_i^{-1}\left[\, B(T^{(o)}(p_i)) \frac{R_i}{I_i^{(o)}} \,\right]$$

yielding 228, 238, and 254 K, respectively.

(e) Disregard interpolation of temperature to other pressure levels in this example and go back to (b).

(b') 45.7, 55.3, 71.6 $mW/m^2/ster/cm^{-1}$
(c') no convergence
(d') 228, 239, 259 K

(b'') 45.3, 56.4, 74.4 $mW/m^2/ster/cm^{-1}$
(c'') no convergence
(d'') 228, 239, 262 K

(b''') 45.2, 56.7, 75.9 $mW/m^2/ster/cm^{-1}$
(c''') no convergence
(d''') 228, 239, 264 K

(b'''') 45.2, 56.8, 76.7 mW/m^2/ster/cm^{-1}
(c'''') convergence within 1 mW/m^2/ster/cm^{-1}

Thus, the temperature retrieval yields T(50) = 228 K, T(400) = 239 K, and T(900) = 264 K.

5.7.3 Smith's Numerical Iteration Solution

Smith (1970) developed an iterative solution for the temperature profile retrieval, which differs somewhat from that of the relaxation method introduced by Chahine. As before, let R_λ denote the observed radiance and $I_\lambda^{(n)}$ the computed radiance in the nth iteration. Then the upwelling radiance expression may be written as:

$$I_\lambda^{(n)} = B_\lambda^{(n)}(T_s)\,\tau_\lambda(p_s) + \int_{p_s}^{o} B_\lambda^{(n)}(T(p)) \frac{d\tau_\lambda(p)}{d \ln p}\, d \ln p.$$

Further, for the (n+1) step we set:

$$R_\lambda = I_\lambda^{(n+1)}$$
$$= B_\lambda^{(n+1)}(T_s)\,\tau_\lambda(p_s) + \int_{p_s}^{o} B_\lambda^{(n+1)}(T(p)) \frac{d\tau_\lambda(p)}{d \ln p}\, d \ln p.$$

Upon subtracting, we obtain

$$R_\lambda - I_\lambda^{(n)} = [\, B_\lambda^{(n+1)}(T_s) - B_\lambda^{(n)}(T_s)\,]\,\tau_\lambda(p_s)$$
$$+ \int_{p_s}^{o} [B_\lambda^{(n+1)}(T(p)) - B_\lambda^{(n)}(T(p))\,] \frac{d\tau_\lambda(p)}{d \ln p}\, d \ln p$$

An assumption is made at this point that for each sounding wavelength, the Planck function difference for the sensed atmospheric layer is independent of the pressure coordinate. Thus,

$$R_\lambda - I_\lambda^{(n)} = B_\lambda^{(n+1)}(T(p)) - B_\lambda^{(n)}(T(p)).$$

That is,

$$B_\lambda^{(n+1)}(T(p)) = B_\lambda^{(n)}(T(p)) + (R_\lambda - I_\lambda^{(n)})\,.$$

This is the iteration equation developed by Smith. Moreover, for each wavelength we have

$$T_\lambda^{(n+1)}(p) = B_\lambda^{-1}[\, B_\lambda(T^{(n+1)}(p))\,]\,.$$

Since the temperature inversion problem now depends on the sounding wavelength λ, the best approximation of the true temperature at any level p would be given by a weighted mean of independent estimates so that

$$T^{(n+1)}(p) = \sum_{\lambda=1}^{M} T_\lambda^{(n+1)}(p)\, W_\lambda(p) \Big/ \sum_{\lambda=1}^{M} W_\lambda(p)\,,$$

where the proper weights should be approximately

$$W_\lambda(p) = \begin{cases} d\tau_\lambda(p), & p < p_s \\ \tau_\lambda(p), & p = p_s \end{cases} .$$

It should be noted that the numerical technique presented above makes no assumption about the analytical form of the profile imposed by the number of radiance observations available. The following iteration schemes for the temperature retrieval may now be employed:

(a) Make an initial guess for $T^{(n)}(p)$, n = 0;

(b) Compute $B_\lambda^{(n)}(T(p))$ and $I_\lambda^{(n)}$;

(c) Compute $B_\lambda^{(n+1)}(T(p))$ and $T_\lambda^{(n+1)}(p)$ for the desired levels;

(d) Make a new estimate of $T^{(n+1)}(p)$ using the proper weights;

(e) Compare the computed radiance values $I_\lambda^{(n)}$ with the measured data R_λ. If the residuals

$$\Delta^{(n)} = \left| R_\lambda - I_\lambda^{(n)} \right| / R_\lambda .$$

are less than a preset small value, then $T^{(n+1)}(p)$ would be the solution. If not, repeat steps (b)-(d) until convergence is achieved.

5.7.4 *Example Problem Using Smith's Iteration*

Using the data from the three channel radiometer discussed in the previous example involving the relaxation method, we proceed as before.

(a) Guess $T^{(o)}(50) = T^{(o)}(400) = T^{(o)}(900) = 260$ K;

(b) Compute the estimated radiance values as before yielding 76.9, 82.3, 85.2 mW/m^2/ster/cm^{-1} for $I_i^{(o)}$;

(c) For each spectral band I, calculate a new profile from

$$T_i^{(1)}(p_j) = B_i^{-1} \{ B(T^{(o)}(p_j)) + (R_i - I_i^{(o)}) \}$$

where j runs over all desired pressure levels. This yields

233, 233, 233 K for $T_1^{(1)}$, and

239, 239, 239 K for $T_2^{(1)}$, and

254, 254, 254 K for $T_3^{(1)}$.

(d) The next iteration profile will be given by the weighted mean

$$T^{(1)}(p_j) = \sum_{i=1}^{3} T_i^{(1)}(p_j)\, \Delta\tau(p_j) \Big/ \sum_{i=1}^{3} \Delta\tau_i(p_j)$$

which yields 237, 243, 251 K.

(e) No convergence yet, using the arbitrary criterion that:

$| R_i - I_i | < 1$ mW/m^2/ster/cm^{-1}.

(b') 52.9, 60.8, 72.5 mW/m^2/ster/cm^{-1} are $I_i^{(1)}$.

(c') $T_1^{(2)}$ is 229, 236, 245 K

$T_2^{(2)}$ is 232, 239, 248 K

$T_3^{(2)}$ is 242, 248, 256 K

(d') $T^{(2)}$ is 231, 241, 254 K

(e') No convergence yet.

(b'') 48.2, 58.4, 72.8 mW/m^2/ster/cm^{-1} are $I_i^{(2)}$

(c'') $T_1^{(3)}$ is 228, 239, 252 K

$T_2^{(3)}$ is 229, 240, 253 K

$T_3^{(3)}$ is 236, 246, 258 K

(d'') $T^{(3)}$ is 229, 241, 257 K

(e'') No convergence yet.

(b''') 46.5, 58.2, 74.1 mW/m^2/ster/cm^{-1} are $I_i^{(4)}$

(c''') $T_1^{(4)}$ is 228, 240, 256 K

$T_2^{(4)}$ is 227, 240, 256 K

$T_3^{(4)}$ is 233, 245, 260 K

(d''') $T^{(4)}$ is 228, 241, 259 K

(e''') Convergence in next iteration.

(b'''') 45.7, 58.1, 75.1 mW/m^2/ster/cm^{-1} are $I_i^{(4)}$ which are within 1 mW/m^2/ster/cm^{-1} are $I_i^{(3)}$.

(c'''') $T_1^{(5)}$ is 228, 241, 259 K

$T_2^{(5)}$ is 226, 240, 258 K

$T_o^{(5)}$ is 231, 244, 261 K

(d'''') $T^{(5)}$ is 228, 241, 261 K

Thus the temperature retrieval yields T(50) = 228 K, T(400) = 241 K, and T(900) = 261 K. This result compares reasonably well with the earlier result obtained by the relaxation method.

5.7.5 Comparison of the Chahine and Smith Numerical Iteration Solution

Figure 5.2 illustrates a retrieval exercise using both Chahine's and Smith's methods. The same transmittances were used and the true temperature profile is shown. A climatological profile was used as an initial guess, and the surface temperature was fixed at 279.5 K. The observed radiances utilized were obtained by direct computations for six VTPR channels at 669.0, 676.7, 694.7, 708.7, 723.6, and 746.7 cm^{-1} using a forward difference scheme. Numerical procedures already outlined were followed, and a linear interpolation with respect to ln p was used in the relaxation method to get the new profile. With the residual set at 1%, the relaxation method converged after six iterations, and results are given by the solid line with black dots. Since the top level at which the temperature was calculated was about 20 mb, extrapolation to the level of 1 mb was used. Recovered results using Smith's method are displayed by the dashed line. No interpolation is necessary since this method gives temperature values at desirable levels. It took five iterations to converge the solution to within 1%. Both methods do not adequately recover the temperature at upper levels due to the fact that the highest weighting function peak is at about 30 mb. It should be noted that the retrieval exercise presented here does not account for random errors and therefore, it is a hypothetical one.

The major problems with the Chahine method are: (a) the profile is not usually well-represented by a series of line segments between pressure levels where the weighting functions peak, particularly for a small number of channels (levels), and (b) the iteration and hence the solution can become unstable since one is attempting to extract M distinct pieces of information from M non-independent observations.

While the Smith method does avoid the problems of the Chahine method (no interpolation is required for a temperature at any pressure level and the solution is stable in the averaging scheme because the random error propagating from R_λ to T(p) is suppressed to the average value of the errors in all channels, which will be near zero), it does have the main disadvantage that the averaging process can prevent obtaining a solution that satisfies the observations to within their measurement error levels. There is no guarantee that the solution converges to one which satisfies the radiances by this criterion.

5.8 Direct Physical Solution

5.8.1 Example Problem Solving Linear RTE Directly

The linear form of the RTE can be solved directly (often with rather poor results). For the example problem presented earlier, we have that T_b equals 223, 232, and 258 K for the spectral bands, respectively. As before, take T(1000) = 280 K and assume a mean temperature profile condition T (900) = T (400) = T (50) = 260 K. Therefore, T_b equals 250, 258, and 263 K, respectively. We set up the matrix solution by writing

$$\Delta T_{bi} = \Delta T_{900} \left[\frac{\partial B_i}{\partial T} \Big|_{T_{900}} \Big/ \frac{\partial B_i}{\partial T} \Big|_{T_{bi}} \right] (\tau_i(600) - \tau_i(1000))$$

$$+ \Delta T_{400} \left[\left. \frac{\partial B_i}{\partial T} \right|_{T_{400}} \Big/ \left. \frac{\partial B_i}{\partial T} \right|_{T_{bi}} \right] (\tau_i(150) - \tau_i(600))$$

$$+ \Delta T_{50} \left[\left. \frac{\partial B_i}{\partial T} \right|_{T_{50}} \Big/ \left. \frac{\partial B_i}{\partial T} \right|_{T_{bi}} \right] (\tau_i(10) - \tau_i(150))$$

which gives

$$-27 = \Delta T_{900}(.89/.77)(.00) + \Delta T_{400}(.89/.77)(.05) + \Delta T_{50}(.89/.77)(.81)$$

$$-26 = \Delta T_{900}(.86/.83)(.09) + \Delta T_{400}(.86/.83)(.56) + \Delta T_{50}(.86/.83)(.31)$$

$$-5 = \Delta T_{900}(.81/.85)(.40) + \Delta T_{400}(.81/.85)(.26) + \Delta T_{50}(.81/.85)(.11)$$

Solving we find that

$\Delta T_{900} = 15$ K,

$\Delta T_{400} = -33$ K,

$\Delta T_{50} = -25$ K,

so that the temperature profile solution is

T(900) = 275 K,

T(400) = 227 K,

T(50) = 235 K.

Obviously, this example was ill-conditioned since Taylor expansion of differences larger than 10 K is foolhardy. However, this does demonstrate how to set up a direct solution, which should be representative of the mean temperature condition used in the expansion is close to the actual temperature profile.

Typically, the direct solution is unstable because there are the unknown observation errors and W is nearly singular due to strong overlapping of the weighting functions. Since W is ill-conditioned with respect to matrix inversion, the elements of the inverse matrix are greatly inflated which, in turn, greatly amplifies the experimental error of the observations. This renders the solution virtually useless. The ill-conditioned solution results since one does not have N independent pieces of information about T from M radiation observations. The solution is further complicated because M is usually much smaller than the number of temperature points, N, needed to represent the temperature profile.

5.8.2 *Simultaneous Direct Physical Solution of the RTE for Temperature and Moisture*

Solution of the RTE often involves several iterations between solving for the temperature and moisture profiles. As pointed out earlier, they are interrelated but most solutions only solve for each one separately, assuming the other is known. Recently Smith (1985) has developed a simultaneous direct physical solution of both.

In order to solve for the temperature and moisture profiles simultaneously, a simplified form of the integral of the radiative transfer equation is considered,

$$R = B_o + \int_o^{p_s} \tau \, dB$$

which comes integrating the atmospheric term by parts in the more familiar form of the RTE. R represents the radiance, τ the transmittance, and B the Planck radiance. Dependency on angle, pressure, and frequency are neglected for simplicity. The subscript s refers to the surface level and o refers to the top of the atmosphere. Then in perturbation form, where δ represents a perturbation with respect to an a priori condition

$$\delta R = \int_o^{p_s} (\delta\tau) \, dB + \int_o^{p_s} \tau \, d(\delta B)$$

Integrating the second term on right side of the equation by parts,

$$\int_o^{p_s} \tau \, d(\delta B) = \tau \, \delta B \Big|_o^{p_s} - \int_o^{p_s} \delta B \, d\tau = \tau_s \, \delta B_s - \int_o^{p_s} \delta B \, d\tau \, ,$$

yields

$$\delta R = \int_o^{p_s} (\delta\tau) \, dB + \tau_s \, \delta B_s - \int_o^{p_s} \delta B \, d\tau$$

Now write the differentials with respect to temperature

$$\delta R = \delta T_b \frac{\partial B}{\partial T_b}, \qquad \delta B = \delta T \frac{\partial B}{\partial T}$$

and with respect to pressure

$$dB = \frac{\partial B}{\partial T} \frac{\partial T}{\partial p} \, dp \, , \quad d\tau = \frac{\partial \tau}{\partial p} \, dp \, .$$

Substituting this in

$$\delta T_b = \int_o^{p_s} \delta\tau \frac{\partial T}{\partial p} \left[\frac{\partial B}{\partial T} \Big/ \frac{\partial B}{\partial T_b} \right] dp - \int_o^{p_s} \delta T \frac{\partial \tau}{\partial p} \left[\frac{\partial B}{\partial T} \Big/ \frac{\partial B}{\partial T_b} \right] dp$$

$$+ \delta T_s \left[\frac{\partial B_s}{\partial T_s} \Big/ \frac{\partial B}{\partial T_b} \right] \tau_s$$

where T_b is the brightness temperature. Finally, assume that the transmittance perturbation is dependent only on the uncertainty in the column of precipitable water density weighted path length u according to the relation

$$\delta\tau = \frac{\partial\tau}{\partial u}\ \delta u\ .$$

Thus

$$\delta T_b = \int_o^{p_s} \delta u \frac{\partial T}{\partial p}\frac{\partial \tau}{\partial u}\left[\frac{\partial B}{\partial T} / \frac{\partial B}{\partial T_b}\right] dp - \int_o^{p} \delta T \frac{\partial \tau}{\partial p}\left[\frac{\partial B}{\partial T} / \frac{\partial B}{\partial T_b}\right] dp$$

$$+ \delta T_s \left[\frac{\partial B_s}{\partial T_s} / \frac{\partial B}{\partial T_b}\right] \tau_s$$

$$= f[\delta u, \delta T, \delta T_s]$$

where f represents a functional relationship.

The perturbations are with respect to some a priori condition which may be estimated from climatology, regression, or more commonly from an analysis or forecast provided by a numerical model. In order to solve for δu, δT, and δT_s from a set spectrally independent radiance observations δT_b, the perturbation profiles are represented in terms of arbitrary basis functions φ (p); so

$$\delta T_s = \alpha_o \varphi_o$$

$$\delta u(p) = \sum_{i=1}^{Q} \alpha_i \int_o^{p} q(p)\, \varphi_i(p)\, dp\ ,$$

where the water vapour mixing ratio is given by $q(p) = g\, \partial u/\partial p$ and $\delta q = g \Sigma \alpha q \varphi$,

$$\delta T(p) = -\sum_{i=Q+1}^{L} \alpha_i\ \varphi_i(p)\ .$$

Then for M spectral channel observations

$$\delta T_{bj} = \sum_{i=0}^{L} \alpha_i \psi_{ij} \quad \text{where} \quad j = 1,...,M$$

and

$$\psi_{oj} = \left[\frac{\partial Bj}{\partial T_s} / \frac{\partial B_j}{\partial T_{bj}}\right] \tau_{sj}$$

$$\psi_{ij} = \int_o^{p_s} \left[\int_o^{p} q\, \varphi_i\, dp\right] \left[\frac{\partial T}{\partial p}\ \frac{\partial \tau_j}{\partial u}\right] \left[\frac{\partial B_j}{\partial T} / \frac{\partial B_j}{\partial T_{bj}}\right] dp \qquad i=1,...,Q$$

$$\psi_{ij} = \int_o^{p_s} \varphi_i \frac{\partial \tau_j}{\partial p} \left[\frac{\partial B_j}{\partial T} / \frac{\partial B_j}{\partial T_{bj}}\right] dp \qquad i=Q+1,...,L$$

or in matrix form

$$\underset{(Mx1)}{t_b} = \underset{(M \times L+1)}{\psi} \; \underset{(L+1 \times 1)}{\alpha}$$

A least squares solution suggests that

$$\alpha = (\psi^t \psi)^{-1} \psi^t t_b \approx (\psi^t \psi + \gamma I)^{-1} \psi^t t_b$$

where $\gamma = .1$ has been incorporated to stabilize the matrix inverse.

There are many reasonable choices for the pressure basis functions $\varphi(p)$. For example empirical orthogonal functions (eigenvectors of the water vapour and temperature profile covariance matrices) can be used in order to include statistical information in the solution. Also the profile weighting functions of the radiative transfer equation can be used. Or gaussian functions that peak in different layers of the atmosphere can be used.

Ancillary information, such as surface observations, are readily incorporated into the profile solutions as additional equations (M+2 equations to solve L unknowns).

$$q_o - q(p_s) = g \sum_{i=1}^{Q} \alpha_i \, q(p_s) \, \varphi_i(p_s)$$

$$T_o - T(p_s) = - \sum_{i=Q+1}^{L} \alpha_i \, \varphi_i(p_s)$$

In summary we have the following characteristics (a) the RTE is in perturbation form, (b) δT and δu are expressed as linear expansions of basis functions (EOF or W(p)), (c) ancillary observations are used as extra equations, (d) a least squares solution is sought, and (e) a simultaneous temperature and moisture profile solution produces improved moisture determinations. The simultaneous solution addresses the interdependence of water vapour radiance upon temperature and carbon dioxide channel radiance upon water vapour concentration. The dependence of the radiance observations on the surface emissions is accounted for by the inclusion of surface temperature as an unknown. A single matrix solution is computationally efficient compared to an iterative calculation.

5.9 Water Vapour Profile Solutions

The direct physical solution of the RTE provides a simultaneous solution of both the temperature and moisture profiles. It is currently the preferred solution. On the other hand, iterative numerical techniques involve several determinations of each profile separately before self consistent convergence is achieved. The iterative numerical solution for the moisture profile is presented here. It should be viewed as a companion to the iterative numerical solution of the temperature profile presented in section 5.7.

The linear form of the RTE can be written in terms of the precipitable water vapour profile as

$$(\Delta T_b)_\lambda = \int_0^{u_s} (\Delta T) \, V_\lambda \, du$$

where

$$V_\lambda = \left[\frac{\partial B_\lambda(T)}{\partial T} \Big|_{T=T_{av}} \Big/ \frac{\partial B_\lambda(T)}{\partial T} \Big|_{T=T_{b\lambda}} \right] \frac{\partial \tau_\lambda}{\partial u}$$

and $T_{av}(p)$ represents a mean or initial profile condition.

One manner of solving for the water vapour profile from a set of spectrally independent water vapour radiance observations is to employ one of the linear direct temperature profile solutions discussed earlier. In this case, however, one solves for the function T(u) rather than T(p). Given T(p) from a prior solution of carbon dioxide and/or oxygen channel radiance observations, u(p) can be found by relating T(p) to T(u). The mixing ratio profile, q(p), can then be obtained by taking the vertical derivative of u(p), $q(p) = g\,\partial u/\partial p$ where g is gravity.

Rosenkranz *et al,* (1982) have applied this technique to microwave measurements of water vapour emission. They used the regression solution for both the temperature versus pressure and temperature versus water vapour concentration profiles. The regression solutions have the form

$$T(p_j) = t_o(p_j) + \sum_{i=1}^{N} t_i(p_i)\, T_{bi}$$

and

$$T(u_k) = t_o(u_k) + \sum_{m=1}^{M} t_m(u_k)\, T_{bm}$$

where T_{bi} are the N brightness temperature observations of oxygen emission and T_{bm} are the M brightness temperature observations of water vapour emission and $t_i(p_j)$ and $t_m(u_k)$ are the regression coefficients corresponding to each pressure and water vapour concentration level. u(p) is found from the intersections of the T(p) and T(u) profiles obtained by interpolation of the discrete values given by the regression solutions. An advantage of the linear regression retrievals is that they minimize the computer requirements for real time data processing since the regression coefficient matrices are predetermined.

Various non-linear iterative retrieval methods for inferring water vapour profiles have been developed and applied to satellite water vapour spectral radiance observations. The formulation shown below follows that given by Smith (1970). Integrating the linear RTE by parts one has

$$T_{b\lambda} - T_{b\lambda}^{(n)} = \int_{o}^{p_s} [\tau_\lambda(p) - \tau_\lambda^{(n)}(p)]\; X_\lambda(p)\, \frac{dp}{p}$$

where

$$X_\lambda(p) = \left[\frac{\partial B_\lambda(T)}{\partial T}\Big|_{T=T_{av}} \Big/ \frac{\partial B_\lambda(T)}{\partial T}\Big|_{T=T_{b\lambda}}\right] \frac{\partial T(p)}{\partial \ln p}$$

and the (n) superscript denotes the n^{th} estimate of the true profile. Expanding $\tau_\lambda(p)$ as a logarithmic function of the precipitable water vapour concentration u(p) yields

$$\tau_\lambda(p) - \tau_\lambda^{(n)}(p) = \frac{\partial \tau_\lambda(p)}{\partial \ln u^{(n)}(p)} \ln \frac{u(p)}{u^{(n)}(p)}\,.$$

Using the approximation

$$\frac{\partial \tau_\lambda(p)}{\partial \ln u^{(n)}(p)} = \tau_\lambda^{(n)}(p) \ln \tau_\lambda^{(n)}(p)$$

which is valid for the exponential transmission function, then

$$T_{b\lambda} - T_{b\lambda}^{(n)} = \int_o^{p_s} \ln \frac{u(p)}{u^{(n)}(p)} \; Y_\lambda^{(n)}(p) \; \frac{dp}{p}$$

with

$$Y_\lambda^{(n)}(p) = \tau_\lambda^{(n)}(p) \ln \tau_\lambda^{(n)}(p) \; X_\lambda(p)$$

Following the same strategy employed in Smith's generalized iterative temperature profile solution, we realize that from each water vapour channel brightness temperature an estimate of the ratio of the true precipitable water vapour profile with respect to the nth estimate can be calculated by

$$\left[\frac{u(p)}{u^{(n)}(p)}\right]_\lambda = \exp\left[\frac{T_{b\lambda} - T_{b\lambda}^{(n)}}{\int_o^{p_s} Y_\lambda^{(n)}(p) \frac{dp}{p}}\right]$$

As in the temperature profile solution, the best average estimate of the precipitable water vapour profile is based upon the weighted mean of all water vapour channel estimates using the weighting function $Y_\lambda^{(n)}(p)$.

It follows that the mixing ratio profile $q^{(n+1)}(p)$ can be estimated from $u^{(n+1)}(p_j) / u^{(n)}(p_j)$ and from $q^{(n)}(p_j)$ by using

$$q^{(n+1)}(p) = q^{(n)}(p) \frac{[u^{(n+1)}(p)]}{[u^{(n)}(p)]} + g\, u^{(n)}(p) \frac{\partial}{\partial p} \frac{[u^{(n+1)}(p)]}{[u^{(n)}(p)]}$$

The advantage of using this expression to compute q(p) is that the second term on the right hand side is small compared to the first term so that numerical errors produced by the vertical differentiation are small.

It should be noted that relative humidity is an immediate by-product of the above derivation. Assuming that the relative humidity is constant within the radiating layer, one can write $\ln (RH/RH^{(n)}) = \ln (u/u^{(n)})$ and thus determine true RH from the n^{th} estimate $RH^{(n)}$.

5.10 Microwave Form of RTE

In the microwave region, the emissivity of the earth atmosphere system is normally less than unity. Thus, there is a reflection contribution from the surface. The radiance emitted from the surface would therefore be given by

$$I_\lambda^{sfc} = \varepsilon_\lambda B_\lambda(T_s) \tau_\lambda(p_s) + (1-\varepsilon_\lambda) \tau_\lambda(p_s) \int_o^{p_s} B_\lambda(T(p)) \frac{\partial \tau'_\lambda(p)}{\partial \ln p} \, d \ln p$$

The first term in the right-hand side denotes the surface emission contribution, whereas the second term represents the emission contribution from the entire atmosphere to the surface, which is reflected back to the atmosphere at the same frequency. The transmittance $\tau'_\lambda(p)$ is now expressed

with respect to the surface instead of the top of the atmosphere (as $\tau_\lambda(p)$ is). Thus, the upwelling radiance is now expressed as

$$I_\lambda = \varepsilon_\lambda B_\lambda(T_s)\,\tau_\lambda(p_s) + (1-\varepsilon_\lambda)\,\tau_\lambda(p_s)\int_o^{p_s} B_\lambda(T(p))\,\frac{\partial \tau'_\lambda(p)}{\partial \ln p}\,d\ln p$$

$$+ \int_{p_s}^{o} B_\lambda(T(p))\,\frac{\partial \tau_\lambda(p)}{\partial \ln p}\,d\ln p$$

In the wavelength domain, the Planck function is given by

$$B_\lambda(T) = c_1 / [\,\lambda^5 (e^{c_2/\lambda T} - 1)\,] .$$

In the microwave region $c_2/\lambda T << 1$, so the Planck function may be approximated by

$$B_\lambda(T) \approx \frac{c_1}{c_2}\,\frac{T}{\lambda^4} ;$$

the Planck radiance is linearly proportional to the temperature. Analogous to the above approximation, we may define an equivalent brightness temperature T_b such that

$$I_\lambda = \frac{c_1}{c_2}\,\frac{T_b}{\lambda^4} .$$

Thus, the microwave radiative transfer equation may now be written in terms of temperature

$$T_{b\lambda} = \varepsilon_\lambda T_s\,\tau_\lambda(p_s) + (1-\varepsilon_\lambda)\,\tau_\lambda(p_s)\int_o^{p_s} T(p)\,\frac{\partial \tau'_\lambda(p)}{\partial \ln p}\,d\ln p$$

$$+ \int_{p_s}^{o} T(p)\,\frac{\partial \tau_\lambda(p)}{\partial \ln p}\,d\ln p .$$

The transmittance to the surface can be expressed in terms of transmittance to the top of the atmosphere by remembering

$$\tau'_\lambda(p) = \exp\left[-\frac{1}{g}\int_p^{p_s} k_\lambda(p)\,g(p)\,dp\right]$$

$$= \exp\left[-\int_o^{p_s} + \int_o^{p}\right]$$

$$= \tau_\lambda(p_s) / \tau_\lambda(p) .$$

So

$$\frac{\partial \tau'_\lambda(p)}{\partial \ln p} = -\frac{\tau_\lambda(p_s)}{(\tau_\lambda(p))^2}\,\frac{\partial \tau_\lambda(p)}{\partial \ln p} .$$

And thus to achieve a form similar to that of the infrared RTE, we write

$$T_{b\lambda} = \varepsilon_\lambda T_s(p_s)\, \tau_\lambda(p_s) + \int_{p_s}^{o} T(p)\, F_\lambda(p)\, \frac{\partial \tau_\lambda(p)}{\partial \ln p}\, d \ln p$$

where

$$F_\lambda(p) = \{ 1 + (1 - \varepsilon_\lambda) \left[\frac{\tau_\lambda(p_s)}{\tau_\lambda(p)}\right]^2 \}.$$

A special problem area in the use of microwave for atmospheric sounding from a satellite platform is surface emissivity. In the microwave spectrum, emissivity values of the earth's surface vary over a considerable range, from about 0.4 to 1.0. The emissivity of the sea surface typically ranges between 0.4 and 0.5, depending upon such variables as salinity, sea ice, surface roughness, and sea foam. In addition, there is a frequency, dependence with higher frequencies displaying higher emissivity values. Over land, the emissivity depends on the moisture content of the soil. Wetting of a soil surface results in a rapid decrease in emissivity. The emissivity of dry soil is on the order of 0.95 to 0.97, while for wet bare soil it is about 0.80 to 0.90, depending on the frequency. The surface emissivity appearing in the first term has a significant effect on the brightness temperature value.

The basic concept of inferring atmospheric temperatures from satellite observations of thermal microwave emission in the oxygen spectrum was developed by Meeks and Lilley (1963) in whose work the microwave weighting functions were first calculated. The prime advantage of microwave over infrared temperature sounders is that the longer wavelength microwaves are much less influenced by clouds and precipitation. Consequently, microwave sounders can be effectively utilized to infer atmospheric temperatures in all weather conditions. We will not pursue microwave retrievals in this course, except to say that the techniques are similar to those for infrared retrieval.

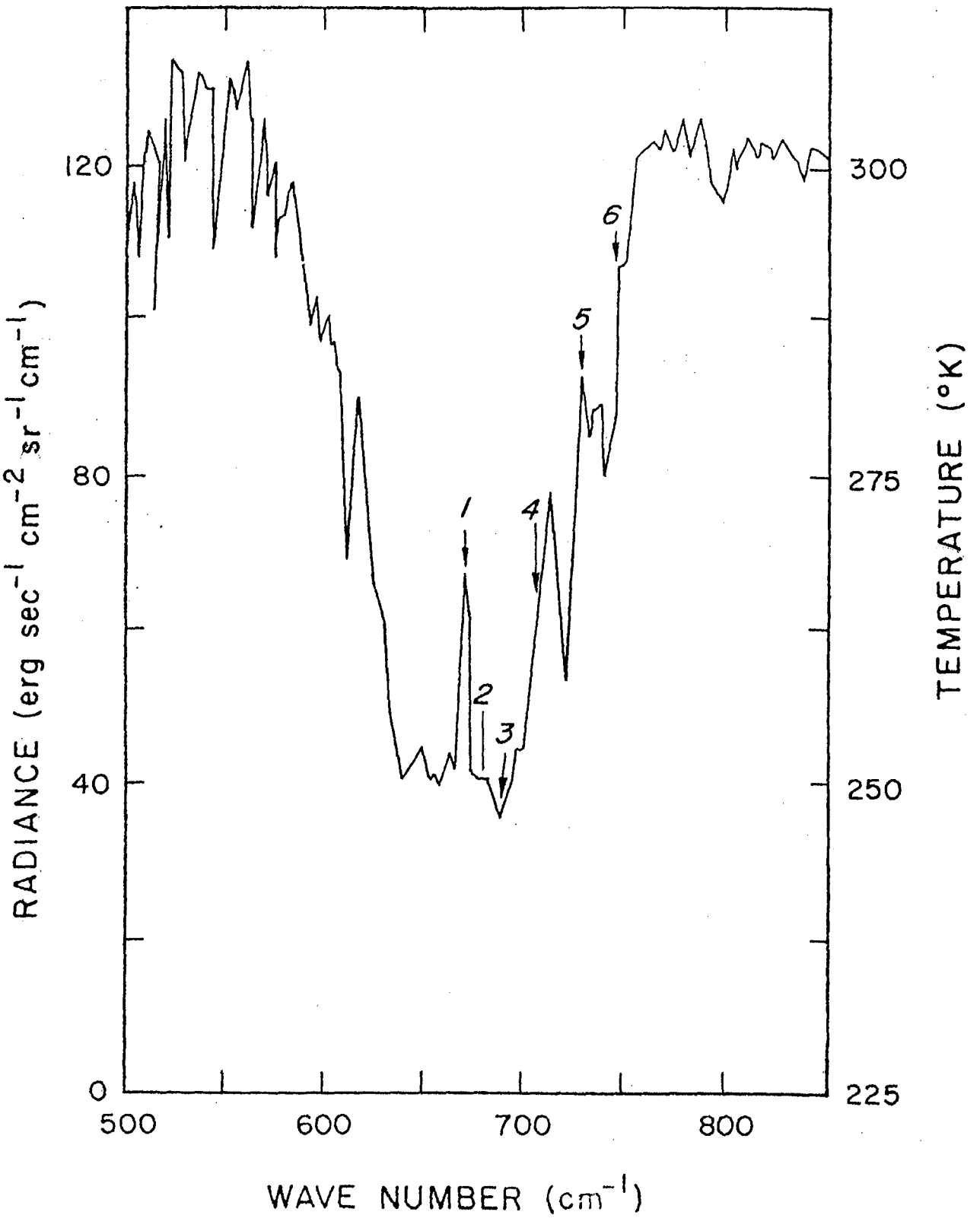

Figure 5.1: Outgoing radiance in terms of black body temperature in the vicinity of 15μm CO_2 band observed by the IRIS on Nimbus IV. The arrows denote the spectral regions sampled by the VTPR instrument.

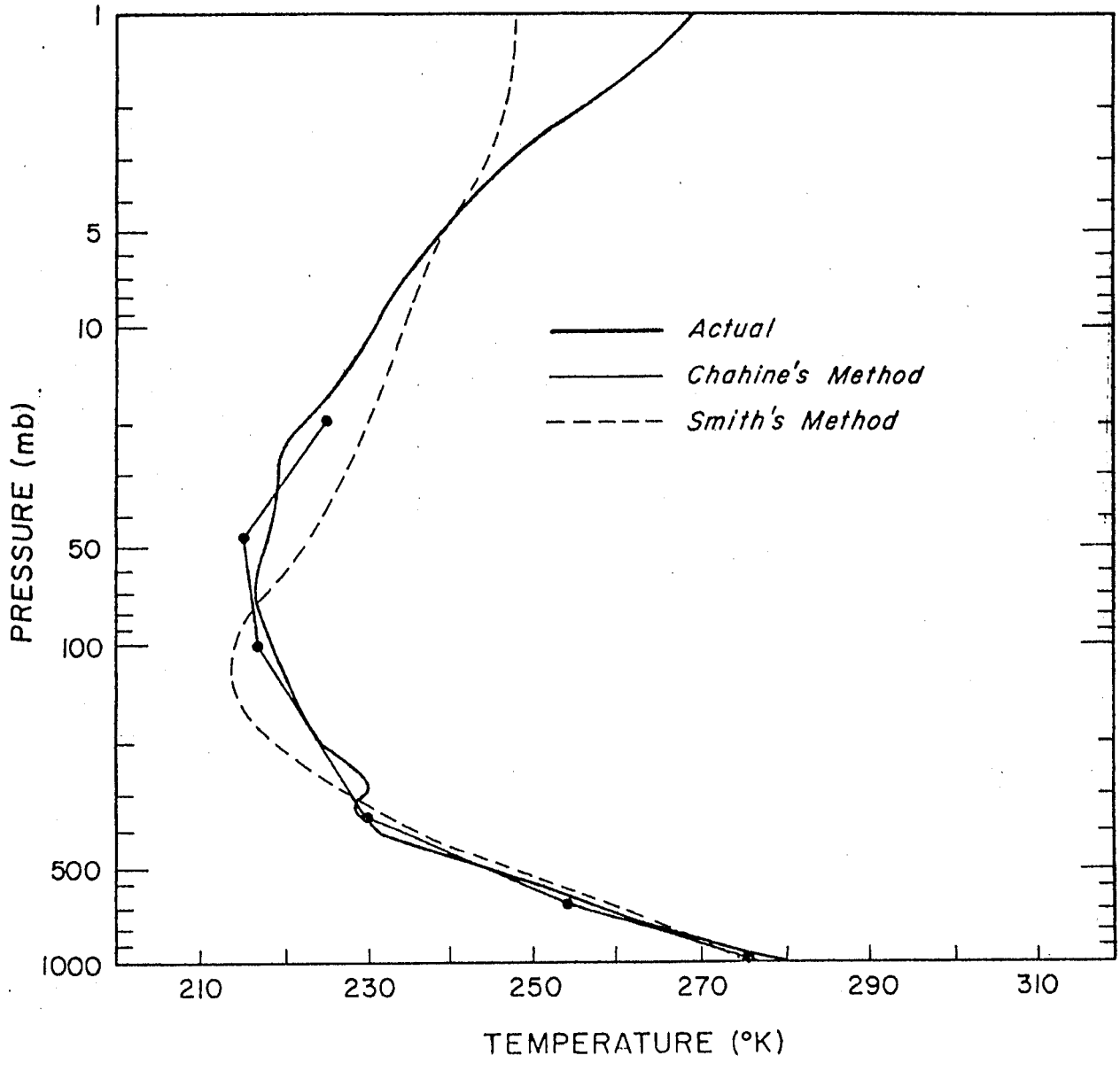

Figure 5.2: Temperature retrieval using Chahine's relaxation and Smith's iterative methods for the VTPR channels.

CHAPTER 6

CLOUDS

6.1 RTE in Cloudy Conditions

Thus far, we have considered the RTE only in a clear sky condition. When we introduce clouds into the radiation field of the atmosphere the problem becomes more complex. The following notes indicate some of the fundamental problems concerning clouds.

If we assume that the fractional cloud cover within the field of view of the satellite radiometer is represented by η and the cloud top pressure by p_o, then the spectral radiance measured by the satellite radiometer at the top of the atmosphere is given by

$$I_\lambda = \eta I_\lambda^{cd} + (1 - \eta) I_\lambda^{c}$$

where cd denotes cloud and c denotes clear. As before, we can write for the clear radiance

$$I_\lambda^{c} = B_\lambda(T_s)\, \tau_\lambda(p_s) + \int_{p_s}^{o} B_\lambda(T(p))\, d\tau_\lambda \, .$$

The cloud radiance is represented by

$$I_\lambda^{cd} = (1-\varepsilon_\lambda)\, B_\lambda(T_s)\, \tau_\lambda(p_s) + (1-\varepsilon_\lambda) \int_{p_s}^{p_c} B_\lambda(T(p))\, d\tau_\lambda$$

$$+ \varepsilon_\lambda\, B_\lambda(T(p_c))\, \tau_\lambda(p_c) + \int_{p_c}^{o} B_\lambda(T(p))\, d\tau_\lambda$$

where ε_λ represents the emittance of the cloud. The first two terms are contributions from below the cloud, the third term is the cloud contribution, and the fourth term is the contribution from above the cloud. After some rearranging these expressions can be combined to yield

$$I_\lambda - I_\lambda^{c} = \eta\, (I_\lambda^{cd} - I_\lambda^{c})$$

$$= \eta\, \varepsilon_\lambda \left[B_\lambda(T(p_c))\, \tau_\lambda(p_c) - B_\lambda(T_s)\, \tau_\lambda(p_s) - \int_{p_s}^{p_c} B_\lambda(T(p))\, d\tau_\lambda \right]$$

A simpler form is available by using integration by parts, so

$$I_\lambda - I_\lambda^{c} = \eta \varepsilon_\lambda \int_{p_s}^{p_c} \tau(p)\, \frac{dB_\lambda}{dp}\, dp$$

The techniques for dealing with clouds generally fall into three different categories: (a) searching for cloudless fields of view, (b) specifying cloud top pressure and sounding down to cloud level as in the cloudless case, and (c) employing adjacent fields of view to determine the clear sky signal from partly cloudy observations.

6.2 Inferring Clear Sky Radiances in Cloudy Conditions

Employing adjacent fields of view proceeds as follows. For a given wavelength λ, the radiances from two spatially independent, but geographically close, fields of view are written

$$I_{\lambda,1} = \eta_1 I_{\lambda,1}^{cd} + (1 - \eta_1) I_{\lambda,1}^{c} \quad ,$$

$$I_{\lambda,2} = \eta_2 I_{\lambda,2}^{cd} + (1 - \eta_2) I_{\lambda,2}^{c} \quad ,$$

If the clouds are at a uniform altitude, and the clear air radiance is the same from the two yields of view

$$I_\lambda^{cd} = I_{\lambda,1}^{cd} = I_{\lambda,2}^{cd}$$

and

$$I_\lambda^{c} = I_{\lambda,1}^{c} = I_{\lambda,2}^{c}$$

then

$$\frac{\eta_1 (I_\lambda^{cd} - I_\lambda^{c})}{\eta_2 (I_\lambda^{cd} - I_\lambda^{c})} = \frac{\eta_1}{\eta_2} = \eta^* = \frac{I_{\lambda,1} - I_\lambda^{c}}{I_{\lambda,2} - I_\lambda^{c}} \quad ,$$

where η^* is the ratio of the cloud amounts for the two geographically independent fields of view of the sounding radiometer. Therefore, the clear air radiance from an area possessing broken clouds at a uniform altitude is given by

$$I_\lambda^{c} = \frac{I_{\lambda,1} - \eta^* I_{\lambda,2}}{1 - \eta^*}$$

where η^* still needs to be determined. Given an independent measurement of the surface temperature, T_s, and measurements $I_{w,1}$ and $I_{w,2}$ in a spectral window channel, then η^* can be determined by

$$\eta^* = \frac{I_{w,1} - B_w(T_s)}{I_{w,2} - B_w(T_s)}$$

and I_λ^c for the different spectral channels can be solved. Another approach to determining η^* is to use simultaneous microwave observations and regression relations between a lower tropospheric microwave sounding brightness temperature and the associated infrared brightness temperatures observed for cloud-free conditions. So if

$$I_{mw} = \sum_\lambda a_\lambda I_\lambda^{c} \quad ,$$

then

$$I_{mw} = \sum_\lambda a_\lambda \frac{I_{\lambda,1} - \eta^* I_{\lambda,2}}{1 - \eta^*} \quad ,$$

and

$$\eta^* = \frac{I_{mw} - \sum_\lambda a_\lambda I_{\lambda,1}}{I_{mw} - \sum_\lambda a_\lambda I_{\lambda,2}}$$

The partly cloud η^* solution has been the basis of the design of the operational infrared sounders (VTPR, ITPR, HIRS, VAS, and GOES Sounder). The technique is largely credited to Smith. With this correction for cloud contamination, a solution for the temperature profile can be pursued using the techniques presented in this chapter 5.

When there is a differing amount of the same cloud present in two adjacent or nearby fields of view, the cloud corrected radiance is available from the 3.7 and 11.0 micron infrared windows (when reflected sunlight does not interfere with the observations in the short-wave region). Given a partly cloudy atmospheric column then the ratio of the cloud fraction in the two FOVs, η^*, can be estimated from each window channel separately viewing two adjacent fields of view as before

$$\eta^* = \frac{I_{w1,1} - B_{w1}(T_s)}{I_{w1,2} - B_{w1}(T_s)} = \frac{I_{w2,1} - B_{w2}(T_s)}{I_{w2,2} - B_{w2}(T_s)}$$

T_s is the value that satisfies this equality. Also one can show that

$$B_{w1}(T_s) = A_o + A_1 B_{w2}(T_s)$$

where

$$A_o = \frac{I_{w2,1} I_{w1,2} - I_{w1,1} I_{w2,2}}{I_{w2,1} - I_{w2,2}}$$

and

$$A_1 = \frac{I_{w1,1} - I_{w1,2}}{I_{w2,1} - I_{w2,2}}$$

For constant cloud height and surface temperature conditions, the observed radiances for the two window channels will both vary linearly with cloud amount. As a consequence, cloud amount variations produces a linear variation of the radiance observed in one window channel relative to that radiance observed in another window channel. This linear relation can be used to determine the value of the window radiances for zero cloud amount (N = 0). As shown in Figure 6.1, zero cloud amount must be at the intersection of the observed linear relationship and the known Planck radiance relationship. The brightness temperature associated with this point is the surface temperature. Another common point for the observed and Planck functions is for the case of complete overcast cloud (N = 1). The brightness temperature associated with this point is the cloud temperature. It follows that the constants of the observed linear relationship are the A_o and A_1 constants of the previous equation.

6.3 Finding Clouds

Clouds are generally characterized by higher reflectance and lower temperature than the underlying earth surface. As such, simple visible and infrared window threshold approaches offer considerable skill in cloud detection. However there are many surface conditions when this characterization of clouds is inappropriate, most notably over snow and ice. Additionally, some cloud types such as cirrus, low stratus, and roll cumulus are difficult to detect because of insufficient contrast with the surface radiance. Cloud edges cause further difficulty since the field of view is not always completely cloudy or clear. Multispectral approaches offer several opportunities for improved cloud

detection so that many of these concerns can be mitigated. Finally, spatial and temporal consistency tests offer confirmation of cloudy or clear sky conditions.

The purpose of a cloud mask is to indicate whether a given view of the earth surface is unobstructed by clouds. The question of obstruction by aerosols is somewhat more difficult and will be addressed only in passing in this chapter. This chapter describes algorithms for cloud detection and details multispectral applications. Several references are listed as suggested reading regarding cloud detection: Ackerman *et al*, 1998; Gao *et al*, 1993; King *et al*, 1992; Rossow and Garder, 1993; Stowe *et al*, 1991; Strabala *et al*, 1994; and Wylie and Menzel, 1999.

In the following sections, the satellite measured visible (VIS) reflectance is denoted as r, and refer to the infrared (IR) radiance as brightness temperature (equivalent blackbody temperature using the Planck function) denoted as Tb. Subscripts refer to the wavelength at which the measurement is made.

6.3.1 Threshold and Difference Tests to Find Clouds

As many as eight single field of view (FOV) cloud mask tests are indicated for daylight conditions (given that the sensor has the appropriate spectral channels). Many of the single FOV tests rely on radiance (temperature) thresholds in the infrared and reflectance thresholds in the visible. These thresholds vary with surface emissivity, atmospheric moisture, aerosol content, and viewing scan angle.

(a) IR Window Temperature Threshold and Difference Tests

Several infrared window threshold and temperature difference techniques are practical. Thresholds will vary with moisture content of the atmosphere as the long-wave infrared windows exhibit some water vapour absorption (see Figure 6.2). Threshold cloud detection techniques are most effective at night over water. Over land, the threshold approach is further complicated by the fact that the emissivity in the infrared window varies appreciably with soil and vegetation type (see Figure 6.3). Over open ocean when the brightness temperature in the 11 micron channel (T_{b11}) is less than 270 K, we can safely assume a cloud is present. As a result of the relative spectral uniformity of surface emittance in the IR, spectral tests within various atmospheric windows (such as those at 8.6, 11, and 12 microns respectively) can be used to detect the presence of a cloud. Differences between T_{b11} and T_{b12} have been widely used for cloud screening with AVHRR measurements and this technique is often referred to as the split window technique.

The anticipation is that the threshold techniques will be very sensitive to thin clouds, given the appropriate characterization of surface emissivity and temperature. For example, with a surface at 300 K and a cloud at 220 K, a cloud with emissivity at .01 affects the sensed brightness temperature by .5 K. Since the a noise equivalent temperature of many current infrared window channels is .1 K, the cloud detecting capability is obviously very good.

The basis of the split window technique for cloud detection lies in the differential water vapour absorption that exists between the window channels (8.6 and 11 micron and 11 and 12 micron). These spectral regions are considered to be part of the atmospheric window, where absorption is relatively weak (see Figure 6.2). Most of the absorption lines are a result of water vapour molecules, with a minimum occurring around 11 microns. Since the absorption is weak, T_{b11} can be corrected for moisture absorption by adding the scaled brightness temperature difference of two spectrally close channels with different water vapour absorption coefficients; the scaling coefficient is a function of the differential water vapour absorption between the two channels. This is the basis for sea surface temperature retrievals (see Chapter 6). Thus,

$$T_s = T_{b\lambda 1} + a_{PW}(T_{b\lambda 1} - T_{b\lambda 2})$$

where a_{PW} is a function of wavelengths of the two window channels and the total precipitable water vapour in the atmosphere.

Thus, given an estimate of the surface temperature, T_s, and the total precipitable water vapour, PW, one can develop appropriate thresholds for cloudy sky detection

$$T_{b11} < 270\ K\ ,$$

$$T_{b11} + a_{PW}(T_{b11} - T_{b12}) < T_s\ ,$$

$$T_{b11} + b_{PW}(T_{b11} - T_{b8.6}) < T_s\ ,$$

where a_{PW} and b_{PW} are determined from a look up table as a function of total precipitable water vapour. This approach has been used operationally for 6 years using 8.6 and 11 micron bandwidths from the NOAA-10 and NOAA-12 and the 11 and 12 micron bandwidths from the NOAA-11, with a coefficient independent of PW (Menzel *et al* 1993, Wylie *et al* 1994).

The dependence on PW of the brightness temperature difference between the various window channels is seen in Figure 6.4. A global data set of collocated AVHRR GAC 11 and 12 micron and HIRS 8.6 and 11 micron scenes were collected and the total column PW estimated from integrated model mixing ratios to determine a direct regression between PW and the split window thresholds. Linear regression fits indicate the appropriate values for a_{PW} and b_{PW}.

A disadvantage of the split window brightness temperature difference approach is that water vapour absorption across the window is not linearly dependent on PW, thus second order relationships are sometimes used. With the measurements at three wavelengths in the window, 8.6, 11 and 12 micron this becomes less problematic. The three spectral regions mentioned are very useful in determination of a cloud free atmosphere. This is because the index of refraction varies quite markedly over this spectral region for water, ice, and minerals common to many naturally occurring aerosols. As a result, the effect on the brightness temperature of each of the spectral regions is different, depending on the absorbing constituent. Figure 6.5 summarizes the behaviour of the thresholds for different atmospheric conditions.

A tri-spectral combination of observations at 8.6, 11 and 12 micron bands was suggested for detecting cloud and cloud properties by Ackerman *et al*, (1990). Strabala *et al*, (1994) further explored this technique by utilizing very high spatial-resolution data from a 50 channel multispectral radiometer called the MODIS Airborne Simulator (MAS). The premise of the technique is that ice and water vapour absorption is larger in the window region beyond 10.5 microns (see Figure 6.6); so that positive 8.6 minus 11 micron brightness temperature differences indicate cloud while negative differences, over oceans, indicate clear regions. The relationship between the two brightness temperature differences and clear sky have also been examined using collocated HIRS and AVHRR GAC global ocean data sets as depicted in Figure 6.7. As the atmospheric moisture increases, $T_{b8.6} - T_{b11}$ decreases while $T_{b11} - T_{b12}$ increases.

The short-wave infrared window channel at 3.9 micron also measures radiances in another window region near 3.5 - 4 microns so that the difference between T_{b11} and $T_{b3.9}$ can also be used to detect the presence of clouds. At night the difference between the brightness temperatures measured in the short-wave (3.9 micron) and in the long-wave (11 micron) window regions $T_{b3.9}$-T_{b11} can be used to detect partial cloud or thin cloud within the sensor field of view. Small or negative differences are observed only for the case where an opaque scene (such as thick cloud or the surface) fills the field of view of the sensor. Negative differences occur at night over extended clouds due to the lower cloud emissivity at 3.9 microns.

Moderate to large differences result when a non-uniform scene (e.g., broken cloud) is observed. The different spectral response to a scene of non-uniform temperature is a result of Planck's law; the brightness temperature dependence on the warmer portion of the scene increasing with decreasing wavelength (the short-wave window Planck radiance is proportional to temperature to the thirteenth power, while the long-wave dependence is to the fourth power). Table 6.1 gives an example of radiances (brightness temperatures) observed for different cloud fractions in a scene where cold cloud partially obscures warm surface. Differences in the brightness temperatures of the long-wave and short-wave channels are small when viewing mostly clear or mostly cloudy scenes; however for intermediate situations the differences become large. It is worth noting in Table 6.1 that the brightness temperature of the short-wave window channel is relatively insensitive to small amounts of cloud (compared to the long-wave window channel), thus making it the preferred channel for surface temperature determinations.

Cloud masking over land surface from thermal infrared bands is more difficult than ocean due to potentially larger variations in surface emittance (see Figure 6.3 and Table 6.2). Nonetheless, simple thresholds can be established over certain land features. For example, over desert regions we can expect that $T_{b11} < 273$ K indicates cloud. Such simple thresholds will vary with ecosystem, season and time of day and are still under investigation.

Brightness temperature difference testing can also be applied over land with careful consideration of variation in spectral emittance. For example, $T_{b11} - T_{b8.6}$ has large negative values over daytime desert and is driven to positive differences in the presence of cirrus. Some land regions have an advantage over the ocean regions because of the larger number of surface observations, which include air temperature, and vertical profiles of moisture and temperature.

Infrared window tests at high latitudes are difficult. Distinguishing clear and cloud regions from satellite IR radiances is a challenging problem due to the cold surface temperatures. Yamanouchi *et al,* (1987) describe a night-time polar (Antarctic) cloud/surface discrimination algorithm based upon brightness temperature differences between the AVHRR 3.7 and 11 micron channels and between the 11 and 12 micron channels. Their cloud/surface discrimination algorithm was more effective over water surfaces than over inland snow-covered surfaces. A number of problems arose over inland snow-covered surfaces. First, the temperature contrast between the cloud and snow surface became especially small, leading to a small brightness temperature difference between the two infrared channels. Second, the AVHRR channels are not well-calibrated at extremely cold temperatures (< 200 K). Under clear sky conditions, surface radiative temperature inversions often exists. Thus, IR channels whose weighting function peaks down low in the atmosphere, will often have a larger brightness temperature than a window channel. For example $T_{b8.6} > T_{b11}$ in the presence of an inversion. The surface inversion can also be confused with thick cirrus cloud, but this can be mitigated by other tests (e.g., the magnitude of T_{b11} or T_{b11}-T_{b12}). Recent analysis of T_{b11}-$T_{b6.7}$ (the 6.7 micron water vapour channel peaks around 400 mb) has shown large negative difference in winter time over the Antarctic Plateau and Greenland, which may be indicative of a strong surface inversion and thus clear skies.

(b) CO_2 Channel Test for High Clouds

A spectral channel sensitive to CO_2 absorption at 13.9 micron provides good sensitivity to the relatively cold regions of the atmosphere. Its weighting function peaks near 300 Hpa, so that only clouds above 500 HPa will have strong contributions to the radiance to space observed at 13.9 microns; negligible contributions come from the earth surface. Thus, a 13.9 micron brightness temperature threshold test for cloud versus ambient atmosphere can reveal clouds above 500 HPa or high clouds. This test should be used in conjunction with the near infrared thin cirrus test, described next.

(c) Near Infrared Thin Cirrus Test

This relatively new approach to cirrus detection is suggested by the work of Gao *et al* (1993). A near infrared channel sensitive to H2O absorption at 1.38 micron can be used in reflectance threshold tests to detect the presence of thin cirrus cloud in the upper troposphere under daytime viewing conditions. The strength of this cloud detection channel lies in the strong water vapour absorption in the 1.38 micron region. With sufficient atmospheric water vapour present (estimated to be about 0.4 cm precipitable water) in the beam path, no upwelling reflected radiance from the earth's surface reaches the satellite. The transmittance is given by

$$\tau(p_{sfc}) = \exp(-\delta_{H2O} \cdot \sec\theta_o - \delta_{H2O} \cdot \sec\theta)$$

$$\delta_{H2O} = k_{H2O}\, du$$

As $\tau(p_{sfc}) \rightarrow 0$, $r_{sfc} \rightarrow 0$. τ is the two-way atmospheric transmittance from the top of the atmosphere down to the surface and back to the top of the atmosphere, δ_{H2O} is the water vapour optical depth, θ_o and θ are the solar and viewing zenith angles respectively, k_{H2O} is the water vapour absorption coefficient, u is the water vapour path length and r_{sfc} is the surface radiance reaching the sensor. Since 0.4 cm is a small atmospheric water content, most of the earth's surface will indeed be obscured in this channel. With relatively little of the atmosphere's moisture located high in the troposphere, high clouds appear bright and unobscured in the channel; reflectance from low and mid level clouds is partially attenuated by water vapour absorption.

Simple low and high reflectance (normalized by incoming solar at the top of the atmosphere) thresholds can be used to separate thin cirrus from clear and thick (near infrared cloud optical depth $> \sim 0.2$) cloud scenes. These thresholds are set initially using a multiple-scattering model. New injections of volcanic aerosols into the stratosphere impact the thresholds, which thus require periodic adjustment. Any ambiguity of high thin versus low or mid level thick cloud is resolved by a test on the cloud height using a CO_2 sensitive channel at 13.9 microns (see previous section).

(d) Short-wave Infrared Window Reflectance Threshold Test

The reflectance threshold test uses the 3.9 micron channel where values > 6% are considered to be cloudy. However, "cloudy" pixels with 3.9 micron reflectance values < 3% are considered to be snow/ice (Stowe *et al*, 1994). Note that this reflectance test cannot be applied over deserts, as bright desert regions with highly variable emissivities tend to be classified incorrectly as cloudy. Thermal contrast needs to be examined in conjunction with 3.9 micron reflectivity. In addition, thresholds must be adjusted to ecosystem type because of the different surface emissivities (see Table 6.2).

(e) Reflectance Threshold Test

Visible thresholds tests are best used in combination with infrared window observations; during daytime they can be combined as follows. Low reflectance measurements will result from thin cirrus cloud or cloud free conditions, the two being easily separable in the infrared window measurements by the large difference in the emitting temperature of the high cold cirrus and the warm underlying surface. High reflectance measurements result from thick clouds at all levels, and the infrared window brightness temperature provides a good indication of the cloud level. Intermediate reflectance data are subject to ambiguous interpretations since they result from a mixture of cloud and surface contributions.

Visible data used in the determination of the cloud mask must be uncontaminated by sun glint. Algorithms which include solar reflectance data are constrained to solar zenith angles less than 85°. Sun glint occurs when the reflected sun angle, θ_r, lies between 0° and approximately 36°, where

$$\cos\theta_r = \sin\theta \sin\theta_o \cos\phi + \cos\theta \cos\theta_o$$

where θ_o is the solar zenith angle, θ is the viewing zenith angle, and ϕ is the azimuthal angle. Sun glint is also a function of surface wind and sea state.

(f) Reflectance Ratio Test

The reflectance ratio takes advantage of the difference in reflection from cloud versus earth surface in wavelengths above and below 0.75 microns. Many earth surfaces are less reflecting below 0.75 microns than above, but clouds do not exhibit any great difference in reflectance. Figure 6.8 shows the albedo variations for ice, snow, and vegetation from 0.5 to 3.5 microns. Vegetation shows a sharp increase above 0.72 microns. Snow/ice shows a sharp decrease above 1.4 microns. These step function changes are useful in detecting vegetation or snow/ice versus clouds with spectral band pairs above and below the change. One version of the reflectance ratio test can use the 0.87 micron reflectance divided by 0.66 micron reflectance ($r_{.87}/r_{.66}$). With AVHRR data, this ratio has been found to be between 0.9 and 1.1 in cloudy regions. If the ratio falls within this range, cloud is indicated. New analyses (McClain, 1993) suggest that the minimum value may need to be lowered to about 0.8, at least for some cases. For cloud-free ocean, the ratio is expected to be less than 0.75 (Saunders and Kriebel, 1988).

(g) Low Cloud Test

Clouds that are low in the atmosphere are often difficult to detect. The thermal contrast between clear sky and low cloud is small and sometimes undetectable by infrared techniques. Reflectance techniques, including the Reflectance Ratio Test (see previous section) can be applied during daylight hours. Use of a channel at .936 microns also offers help under daytime viewing conditions. As documented by the work of Gao and Goetz (1991), this channel is strongly affected by low level moisture. When low clouds are present they obstruct the low level moisture, hence increasing the reflectance. A reflectance ratio of .936 over .865 microns, an atmospheric window with similar surface reflectance characteristics also shows promise.

(h) Microwave Tests

The brightness temperature of a lower tropospheric sounding microwave channel can be regressed against the brightness temperatures of several lower tropospheric infrared sounding channels for clear situations. Therefore, the microwave brightness temperature for a given fov can be calculated from the observed infrared brightness temperatures. This will be valid in clear sky conditions only. If the observed microwave brightness temperature is greater than the calculated, it is indicative of cloud contamination in the infrared observations and the fov should be classified accordingly.

(i) Resultant Cloud Mask

All of the single pixel tests mentioned so far rely on thresholds. Thresholds are never global. There are always exceptions and the thresholds must be interpreted carefully. For example, the reflectance ratio test identifies cloud for values in the range 0.9 to 1.1. However, it seems unrealistic to label a pixel with the ratio = 1.1 as cloudy, and a neighbouring pixel with the ratio of 1.11 as non-cloudy. Rather, as one approaches the threshold limits, the certainty or confidence in the labelling becomes more and more uncertain. An individual confidence flag must be assigned and used with the single pixel test results to work towards a final determination.

Each threshold determination is pass, conditional pass, or fail along with a confidence assessment. Conditional pass involves those radiances that fall within an uncertainty region of the threshold. The uncertainty is a measure of instrument noise in that channel and the magnitude of the correction due to non blackbody surface emissivity as well as atmospheric moisture and/or aerosol reflection contributions. The individual confidence flag indicates a one, two, or three sigma confidence level for each single pixel test result. The initial FOV obstruction determination is a sum of the squares of all the confidence flags and single pixel test results.

6.3.2 Spatial Uniformity Tests To Find Cloud

When the single field of view tests do not definitively determine an unobstructed FOV, spatial and temporal consistency tests are often useful. Temporal consistency compares composited previous 30 day clear sky radiances and yesterday's cloud mask to today's clear sky single pixel results. Spatial consistency checks neighbouring clear sky pixel radiances (same ecosystem). If any consistency test fails, the confidence in the final cloud/no cloud determination is reduced by 1 sigma level.

(a) Infrared Window One-Dimensional Histogram Tests

One-dimensional histogram tests have a long history of determining clear sky scenes. As with the IR threshold tests, it is most effective over water and must be used with caution in other situations. The method is physically based on the assumption that for a uniform scene, such as a small geographic region of the ocean, the observed radiances will be normally distributed, the width of the normal curve defined by the instrument noise. This test is not a single FOV test, but requires a number of observations over a given region with similar surface radiative properties. To improve the clear sky estimate, the histogram can be constructed only from the FOVs that pass one or more of the single FOV thresholds previously discussed. A one-dimensional IR channel histogram is constructed over a given geographical region (with 1km FOVs an area of 10 km x 10 km is appropriate). A gaussian function is fit to the warmest peak of the histogram; the temperature (T_{peak}) and the noise limits (σ) are determined. The clear sky brightness temperature threshold is the temperature that corresponds to one-sigma (σ) towards the cold side of the gaussian function peak.

$$T_{thres} = T_{peak} - \sigma \ .$$

An example of this approach is demonstrated in Figure 6.9 using AVHRR global observations.

(b) Infrared Window Radiance Spatial Uniformity

The infrared window spatial uniformity test (often applied on 10 by 10 pixel segments) is also most effective over water and must be used with caution in other situations. Most ocean regions are well suited for spatial uniformity tests; such tests may be applied with less confidence in coastal regions or regions with large temperature gradients (e.g., the Gulf Stream). The spatial coherence test is based on the assumption of a uniform background and singled-layered, optically thick cloud systems. The emitted radiance is

$$I = (1 - A_c)\, I_{clr} + A_c\, I_{cld}$$

The method is based upon the computation of the mean and standard deviation for a group of pixels using 11 micron radiances. When the standard deviation is plotted versus the mean an arch shaped structure is often observed (see Figure 6.10). The feet with low standard deviations are associated with clear sky for high mean values and cloudy conditions for low mean values. The clear sky FOVs can be selected as those within a standard deviation threshold (which is fixed at a small value) of the warm foot of the arch. Note that the derived clear sky foot of the arch should have a temperature consistent with the thresholds derived using the individual FOV tests. Uniform stratus can also give

the appearance of a uniform ocean, thus the spatial tests must often complement the threshold tests (e.g., the tri-spectral test).

Surface temperature variability, both spatial and temporal, is larger over land than ocean, making land scene spatial uniformity tests difficult. If the spatial uniformity tests over land are constrained to similar ecosystems, then better results are obtained.

The spatial coherence method developed by Coakley and Bretherton (1982) is recognized for being especially useful in determining clear and cloudy sky radiances over uniform backgrounds. It has been applied to single-layered and sometimes multi-layered cloud systems that extend over moderately large regions, greater than (250 km)^2, and which have completely cloudy and completely clear pixels. The spatial coherence test is not run over regions of varying topography; however, it is applied for relatively homogeneous topographical regions of similar ecosystem.

(c) Visible Reflectance Uniformity Test

A reflectance uniformity test can be applied by computing the maximum and minimum values of the .66 micron channel and the 0.87 micron channel reflectances within a 10 x 10 pixel array. Pixel arrays with 0.66 micron reflectance differences greater than threshold 1 (around 9%) over land or 0.87 micron reflectance differences greater than threshold 2 (possibly 0.3%) over ocean are labelled as mixed (Stowe *et al*, 1993). The value over ocean is low because a cloud-free ocean is almost uniformly reflective, while non-uniformity is assumed to be caused by cloudiness. This test again works better by requiring that the ecosystem be the same for the pixel array. Further, the reflectance threshold is a function of satellite zenith and view angle.

(d) Two-Dimensional Infrared and Visible Histogram Analysis

As with the 1-D histogram approach, 2-D histograms can be used which make use of the measurements of IR emitted radiances as well as the reflected solar visible radiances. A 2-D Gaussian surface can be fitted to the peak with the warmest temperature and/or lowest reflectance. The Gaussian surface equation is

$$G(IR,VIS) = G_{peak} \exp[- P(IR,VIS)]$$

with

$$P(IR,VIS) = (Tb-Tb_{peak})^2 /\sigma_{IR}^2 - 2(Tb-Tb_{peak})(r-r_{peak})/\sigma_{IR}\sigma_{VIS} + (r-r_{peak})^2/\sigma_{VIS}^2$$

where σ_{IR} and σ_{VIS} are the IR and VIS standard deviation respectively; VIS and IR are measurements in the solar and IR. VIS channels may be replaced with NIR channels when necessary. The solar and infrared radiances can be a combination of various channels. The best solar channels to use are those for which the difference in reflectance between cloud and water is a maximum.

6.4 The Cloud Mask Algorithm

The tests detailed in the previous sections are applied as follows. Single pixel threshold tests are engaged first. If the confidence level reads uncertain (less than 2 sigma confidence), then spatial uniformity tests on 10 by 10 pixel segments are used. Temporal and spatial continuity tests follow; these utilize data from 50 by 50 pixel segments, the cloud mask from yesterday, and the clear sky radiance composite from the last month.

6.4.1 *Thick High Clouds (Group 1 Tests)*

Thick high clouds are detected with threshold tests that rely on brightness temperatures in three infrared spectral bands; they are BT_{11}, $BT_{13.9}$, and $BT_{6.7}$. Infrared window thresholds, BT_{11}, are practical in certain conditions, however they will vary with moisture content of the atmosphere. Over land, BT_{11} is further complicated by the fact that the surface emissivity varies appreciably with soil and vegetation type. Thus, BT_{11} is used primarily to detect high, thick clouds and thresholds are set accordingly. For example, clouds are likely present when BT_{11} is less than 270 K over tropical oceans. $BT_{13.9}$ provides good sensitivity to the relatively cold regions of the atmosphere because of CO_2 absorption. The same is true for $BT_{6.7}$ because of H_2O absorption. These spectral bands receive most of their radiation near 300 hPa and only clouds above 500 hPa make strong radiance contributions; negligible contributions come from the earth surface. Thus, a threshold for $BT_{13.9}$ and $BT_{6.7}$ can isolate clouds above 500 hPa.

6.4.2 *Thin Clouds (Group 2 Tests)*

Thin clouds tests rely on brightness temperature difference tests BT_{11}- BT_{12}, $BT_{8.6}$ - BT_{11}, BT_{11}- $BT_{3.9}$, and, BT_{11}- $BT_{6.7}$. These tests will catch many of the clouds missed by the thick high cloud tests. Differences between BT_{11} and BT_{12} have been widely used for cloud screening with AVHRR measurements; this technique is often referred to as the split window technique.

Split window techniques have been used operationally for more than 6 years using 8.6 and 11 μm bandwidths from the NOAA-10 and NOAA-12 and the 11 and 12 μm bandwidths from the NOAA-11, with a coefficient independent of precipitable water [Menzel *et al*, 1993, Wylie *et al,* 1994]. The tri-spectral combination of observations at 8.6, 11 and 12 μm bands [Ackerman *et al*, 1990, Strabala *et al*, 1994] is being tested. $BT_{8.6}$ - BT_{11} greater than zero indicates cloud, while negative differences, over oceans, indicate clear regions. As atmospheric moisture increases, $BT_{8.6}$ - BT_{11} decreases while BT_{11} - BT_{12} increases.

Brightness temperature difference techniques for many of the infrared window spectral bands on the newer sensors with better than .05 K noise are being used successfully in thin clouds.

At night positive values of $BT_{3.9}$- BT_{11} are used to detect partial cloud or thin cloud within the sensor field of view. Negative differences occur over extended clouds due to the lower cloud emissivity at 3.9 μm. In daylight hours, solar reflection at 3.9 μm is used for detecting water clouds.

In polar regions during winter, large negative values in $BT_{8.6}$ - BT_{11} during winter time over the Antarctic Plateau and Greenland indicate a strong surface inversion and thus clear skies. This test is proving useful in the MODIS cloud mask algorithm.

6.4.3 *Low Clouds (Group 3 Tests)*

Low clouds are best detected using solar reflectance tests that include reflectance thresholds ($r_{0.87}$, $r_{0.65}$, and $r_{.936}$), reflectance ratio tests, and brightness temperature differences $BT_{3.9}$- $BT_{3.7}$. These tests work well when there is a high contrast in the reflectance between the surface and the cloud, for example, clouds over dark vegetation and water. Group 3 tests complement Group 1 tests; Group 3 is sensitive to thick, low level clouds while Group 1 has difficulty with low clouds that have small thermal contrast between cloud and background. Spectral reflectance thresholds are routinely used in many cloud detection algorithms. A wide variety of thresholds exist in the literature, depending on surface type and solar and view angle geometry. It is likely that pre-launch threshold estimates will require adjustment post-launch.

The reflectance ratio ($r_{0.87}/r_{0.66}$) is between 0.9 and 1.1 in cloudy regions and outside in clear regions. The lower value is adjusted to below 0.75 for cloud-free ocean.

The short-wave infrared window bands at 3.7 and 3.9 μm are also used to detect the presence of clouds. Over land, long-wave infrared window spectral variation in surface emissivity presents difficulties for brightness temperature difference tests. Short-wave infrared window spectral variation in surface emissivity is much smaller for some ecosystems, while spectral variation in cloud emissivity remains substantial. Thus brightness temperature differences between $BT_{3.7}$ and $BT_{3.9}$ are usually small in clear sky but larger in clouds. During the daylight hours the difference increases because of the increased solar energy at 3.7 μm.

6.4.4 High Thin Clouds (Group 4 Tests)

Initial detection of high thin clouds is attempted with a threshold test at 1.38 μm. No upwelling reflected radiance from the earth's surface reaches the sensor when sufficient atmospheric water vapour is present (estimated to be about 0.4 cm precipitable water) in the FOV. Simple low and high reflectance thresholds are used to separate thin cirrus from clear and thick (near-infrared cloud optical depth > ~ 0.2) cloud scenes.

Further detection of high thin cirrus is attempted with inspection of brightness temperature difference tests BT_{11}- BT_{12}, BT_{12}- BT_4, and $BT_{13.7}$- $BT_{13.9}$. The Group 4 tests are similar to those in Group 2, but they are specially tuned to detect the presence of thin cirrus. BT_{11}- BT_{12} is greater than zero in ice clouds due to the larger absorption at the longer wavelength in the infrared window. BT_{12}- BT_4 is less than zero in semitransparent cirrus as subpixel warm features dominate the short-wave window radiances within a FOV. $BT_{13.7}$- $BT_{13.9}$ is nominally positive in clear skies, but goes to zero when viewing cirrus. The large differences between ground and cloud temperatures make these tests useful for thin cirrus detection.

6.4.5 Ancillary Data Requirements

A number of pre-processing steps are necessary before a cloud masking algorithm is applied. First, each pixel in the scene must be tagged as being land or water, and if land, a land/water percentage. Second, each land pixel must be designated as relatively flat, valley, isolated mountainous region, low mountains or hills, generally mountainous, or extremely rugged mountains. Each pixel must also be designated as probably/probably not snow covered. Each land pixel must be classified as to its ecosystem, along with a more general ecosystem classification of urban, forest, woodland, grassland, shrub land, tundra, arid vegetation and highland vegetation. Ocean regions must be classified as water, coastline (including islands), possibility of isolated icebergs, marginal ice zone, and nearly solid sea ice (leads may be present). This requires ancillary data described below.

Earth surface character type must be available in various databases which categorize features such as:

- salt or lake bed;
- flat or relatively flat desert (or for high latitudes, glaciers or permanent ice);
- marsh;
- lake country or atoll;
- major valleys or river beds;
- isolated mountains, ridge or peak;
- low mountains;
- mountainous;
- extremely rugged mountains;
- ocean.

The different surface emissivities should be estimated according to different ecosystems. Table 6.5 shows some representative values for the infrared windows. Also Figure 6.3 provides further information.

Sea ice coverage is available from the US NAVY/NOAA Sea Ice Product, which provides weekly reports of fractional ice coverage at spatial resolution of about 18 km.

Snow cover is available in the NOAA Snow Data Product, which provides weekly reports of snow cover at a spatial resolution of 150-200 km; snow is reported if the grid cell is more than 50% covered.

Information on surface temperature and sea state is available from surface observations, Reynolds blended analysis, and NMC model 3-hour surface analyses of temperature and wind speed.

6.4.6 *Implementation of the Cloud Mask Algorithms*

The cloud mask has the following stages:

(a) Note pixels that have sun glint (possible effect on visible tests);

(b) Note pixels that have high solar zenith angle (possible effect on visible tests);

(c) Apply single FOV masking tests and set initial unobstructed FOV determination:
- IR temperature threshold and difference tests;
- CO_2 test for high clouds;
- Near infrared thin cirrus test;
- SWIR Reflectance threshold test;
- Reflectance ratio test;
- Low cloud test;
- microwave test.

(d) Check for consistency:
- clear FOVs in same ecosystem have similar radiances;
- compare with clear sky composites from yesterday and from the past month (if clear today is radiance within sigma interval of past clear).

(e) If pixel is uncertain, use spatial uniformity tests in 10 x 10 pixel regions:
- Spatial IR uniformity test applied using σ = 3.5 K;
- Spatial reflectance uniformity test;
- IR and VIS 2-D histogram test.

(f) Reset quality flag if successful in increasing confidence levels.

6.4.7 *Short-term and Long-term Clear Sky Radiance Composite Maps*

Composite maps have been found to be very useful. A cloud mask must rely on composite maps, but good spatial resolution and the many spectral bands mitigate the dependence. Clear-sky reflectance and temperature composites have been successfully used to detect clouds by comparing the pixel radiances to the clear-sky composite values with some added thresholds (Rossow and Garder 1993). These composites are based on the observation that variations in VIS clear reflectances usually are smaller in time than in space, especially over land. Variations of surface VIS reflectances generally are smaller than variations of cloud reflectances. Therefore, it is assumed that

the characteristic shape of the darker part of the VIS radiance distribution is at most weakly dependent upon surface type (Seze and Rossow, 1991 a, b). The minimum reflectance values are used to estimate clear values. Corrections to the minimum values are inferred from the shapes of the visible reflectance distribution associated with different surface types.

Rossow and Garder (1993) classify the surface into nine types depending on the time scale and magnitude of the reflectance variations (see below). The clear sky reflectance values for land and ocean regions whose surface characteristics vary the most rapidly are estimated. Sparsely vegetated surfaces generally exhibit more spatial variability than heavily vegetated surfaces (cf. Matthews and Rossow, 1987), but are also generally less cloudy. Sparsely vegetated arid regions generally exhibit more spatial variability (Matthews and Rossow, 1987) and are less cloudy. Vegetated areas show less small scale spatial variability. They also tend to be more uniform from one geographic location to another. Individual pixel reflectance values within each latitude zone are compared to the distributions of values for the same ecosystem type; they are required to be within some limit of the distribution mode value. Similar assumptions are used for the determination of clear sky temperature fields.

6.5 Ongoing Climatologies

Several cloud studies have been ongoing for some time. The following paragraphs summarize a few.

The International Satellite Cloud Climatology Project (ISCCP) has developed cloud detection schemes using visible and infrared window radiances. The NOAA Cloud Advanced Very High Resolution Radiometer (CLAVR) algorithm uses the five visible and infrared channels of the AVHRR for cloud detection using spectral and spatial variability tests. CO_2 Slicing characterizes global high cloud cover, including thin cirrus, using infrared radiances in the carbon dioxide sensitive portion of the spectrum. Additionally, spatial coherence of infrared radiances in cloudy and clear skies has been used successfully in regional cloud studies. The following paragraphs briefly summarize these prior approaches.

6.5.1 ISCCP

The ISCCP algorithm is described by Rossow (1989, 1993), Rossow *et al*, (1989), Seze and Rossow (1991) and Rossow and Garder (1993). Only two channels are used, the narrow band visible (0.6 micron) and the infrared window (11 micron). Each observed radiance value is compared against its corresponding Clear-Sky Composite value. Clouds are assumed to be detected only when they alter the radiances by more than the uncertainty in the clear values. In this way the "threshold" for cloud detection is the magnitude of the uncertainty in the clear radiance estimates.

The ISCCP algorithm is based on the premise that the observed VIS and IR radiances are caused by only two types of conditions, 'cloudy' and 'clear', and that the ranges of radiances and their variability that are associated with these two conditions do not overlap (Rossow and Garder 1993). As a result, the algorithm is based upon thresholds, where a pixel is classified as "cloudy" only if at least one radiance value is distinct from the inferred "clear" value by an amount larger than the uncertainty in that "clear" value. The uncertainty can be caused both by measurement errors and by natural variability. This algorithm is constructed to be "cloud-conservative," minimizing false cloud detections but missing clouds that resemble clear conditions.

The ISCCP cloud-detection algorithm consists of five steps (Rossow and Garder 1993): (1) space contrast test on a single IR image; (2) time contrast test on three consecutive IR images at constant diurnal phase; (3) cumulation of space/time statistics for IR and VIS images; (4) construction of clear-sky composites for IR and VIS every 5 days at each diurnal phase and location; and (5) radiance threshold for IR and VIS for each pixel. ISCCP detects high clouds from (a) only infrared

11 μm window channel data where it misses some thin cirrus clouds because there is no correction for the transmission of terrestrial radiation through the clouds; and (b) infrared window data corrected for cloud semi-transparency using the solar reflection measurements at 0.6 μm with a radiative transfer model. ISCCP D2 data can be obtained from the Web page at http://isccp.giss.nasa.gov/dataview.html.

6.5.2 *CLAVR*

The NOAA Cloud and AVHRR algorithm uses all five channels of AVHRR (0.63, 0.86, 3.7, 11.0, 12.0 micron) to derive a global cloud mask (Stowe *et al*, 1991). It examines multispectral information, channel differences, and spatial differences and then employs a series of sequential decision tree tests. Cloud free, mixed (variable cloudy) and cloudy regions are identified for 2x2 global area coverage (GAC) pixel (4 km resolution) arrays. If all four pixels in the array fail all the cloud tests, then the array is labelled as cloud-free (0% cloudy); if all four pixels satisfy just one of the cloud tests, then the array is labelled as 100% cloudy. If 1 to 3 pixels satisfy a cloud test, then the array is labelled as mixed and assigned an arbitrary value of 50% cloudy. If all four pixels of a mixed or cloudy array satisfy a clear-restoral test (required for snow/ice, ocean specula reflection, and bright desert surfaces) then the pixel array is re-classified as "restored-clear" (0% cloudy). The set of cloud tests is subdivided into daytime ocean scenes, daytime land scenes, night-time ocean scenes and night-time land scenes.

Subsequent improvements to the CLAVR, now under development, will use dynamic clear/cloud thresholds predicted from the angular pattern observed from the clear sky radiance statistics of the previous 9-day repeat cycle of the NOAA satellite for a mapped one degree equal area grid cell (Stowe *et al*, 1994). As a further modification, CLAVR will include pixel by pixel classification based upon different threshold tests to separate clear from cloud contaminated pixels, and to separate cloud contaminated pixels into partial and total (overcast) cover. Cloud contaminated pixels will be radiatively "typed" as belonging to low stratus, thin cirrus, and deep convective cloud systems. A fourth type indicates all other clouds, including mixed level clouds.

6.5.3 *CO_2 slicing*

CO_2 slicing (Wylie *et al*, 1994) has been used to distinguish transmissive clouds from opaque clouds and clear sky using High resolution Infrared Radiation Sounder (HIRS) multispectral observations. With radiances around the broad CO_2 absorption band at 15 microns, clouds at various levels of the atmosphere can be detected. Radiances from near the centre of the absorption band are sensitive to only upper levels while radiances from the wings of the band (away from the band centre) see successively lower levels of the atmosphere. The CO_2 slicing algorithm determines both cloud level and cloud amount from radiative transfer principles. It has been shown to be especially effective for detecting thin cirrus clouds that are often missed by simple infrared window and visible approaches. Difficulties arise when the spectral cloud forcing (clear minus cloudy radiance for a spectral band) is less than the instrument noise. The technique is described in more detail in Chapter 8.

A statistical summary of over 60 million cloud observations from HIRS between June 1989 through May 1993 is shown in Table 6.3. High clouds above 400 hPa comprise 24% of the observations. 27% of the observations are of clouds between 400 hPa and 700 hPa. Low clouds below 700 hPa are found 26% of the time. Cloud free conditions are found 23% of the time. Cirrus and transmissive clouds (with effective emissivities less than 0.95) are found in 42% of our observations; they range from 100 to 800 hPa. The 12% transmissive observations below 500 hPa are most likely broken clouds. Clouds opaque to infrared radiation (with effective emissivities greater than 0.95) are found 35% of the time. The global average cloud effective emissivity (global average of $N\varepsilon$) is found to be 0.54; Warren *et al,* (1988) report a global cloud fraction of 0.61 from ground observations.

Figure 6.11 shows the geographical distribution of all clouds in the summer and winter seasons (lighter regions indicate more frequent cloud detection). The months of December, January, and February represent the boreal winter (austral summer) and the months of June, July, and August represent the boreal summer (austral winter). The seasonal summaries are compiled using a uniformly spaced grid of 2° latitude by 3° longitude. Each grid box for each season has at least 1000 observations. The Inter-Tropical Convergence Zone (ITCZ) is readily discernible as the region of more frequent clouds (white band in the tropics); the mid-latitude storm belts are also evident. The ITCZ is seen to move north with the sun from boreal winter to summer. The subtropical high pressure systems are seen in the regions of less frequent cloud cover. Over the Indonesian region the ITCZ expands in latitudinal coverage from boreal winter to summer. In the central Pacific Ocean, the ITCZ shows both a southern and northern extension during the boreal winter months. In the southern hemisphere, the eastern Pacific Ocean off South America and the eastern Atlantic Ocean off Africa remain relatively free of clouds throughout the year. The southern hemispheric storm belt is evident throughout the year. In the northern hemisphere's mid-latitude storm belts, the frequency of clouds increases during the winter with the strengthening of the Aleutian Low in the north Pacific Ocean and the Icelandic Low in the north Atlantic Ocean. The North American cloud cover shows little seasonal change. Large convective development occurs during the austral summer (boreal winter) in South America and Africa, which is readily apparent in the increased detection of clouds. Some regions exhibit cloudy conditions for a complete season. In two grid boxes in the African ITCZ (8N, 10.5W and 2N, 19.5E), all HIRS observations found cloud during all boreal summers of this study. Eight grid boxes were cloudy for all boreal winters of this study; four were located in the central Amazon (centered at 8S, 58W), two in the African Congo (6S, 26E), and two in the Indonesian area (2S, 113E and 4S, 146E). With each grid box covering approximately 75,000 square kilometers, in the boreal winter there are about 300,000 square kilometers in the Amazon that are always cloud covered. There were no grid boxes where all HIRS observations found cloud in all seasons.

Observations of clouds above 6 km (Figure 6.12) exhibit the same general geographical patterns found for total clouds in Figure 6.11. They are most predominant in the tropical ITCZ and move with the seasons. During the boreal winter in a few areas such as Southern Brazil, Tropical South Africa and Indonesia, high clouds are found in more than 90% of the observations. Less frequent occurrence is found in the mid-latitude storm belts. Differences in observations of high clouds and observations of all clouds are evident in the subtropical highs over the extra-tropical oceans where marine stratus clouds are prevalent and higher clouds are far less frequent. This is evident along the west coasts of North and South America and Africa.

Comparison with ISCCP data reveals that the UW HIRS multispectral analysis is finding roughly twice as many transmissive clouds than the ISCCP visible and infrared window analysis. The corrected data are reported in three categories: Daytime Cirrus, Cirrostratus, and Deep Convective Cloud Amounts. For this comparison, the cloud frequencies from the three ISCCP daytime categories were added together to form ISCCP's best estimate of high cloud frequency. The average frequencies of total cloud (also called All Clouds) and high clouds reported by UW HIRS and ISCCP are shown in Figure 6.13; there is general agreement at most latitudes. The exceptions occur in the tropics and the polar regions. UW HIRS finds more thin cirrus in the tropics. In the polar regions, ISCCP finds more total cloud in the winter hemisphere while UW HIRS reports more in the summer hemisphere. Overall, UW HIRS averaged 6% more Total Cloud detection than the ISCCP. The High Cloud frequencies also are shown in Figure 6.12. UW HIRS is consistently higher than the ISCCP at mid- and tropical latitudes. The greatest differences occur in the Intertropical Convergence Zone (ITCZ) from 10° S to 10° N reaching 27%. UW HIRS and ISCCP High Cloud detections differed by an average of 16% over all latitudes.

Figure 6.14 shows a ten-year record of the frequency of cirrus detection in the ISCCP and HIRS cloud studies. A gradual increase of about 1% per year in the detection of cirrus is evident in both studies. The explanation for this increase is not obvious.

Table 6.1

Long-wave and Short-wave Window Planck Radiances (mW/m**2/ster/cm-1) and Brightness Temperatures (degrees K) as a function of Fractional Cloud Amount (for cloud of 220 K and surface of 300 K) using $B(T) = (1-N)*B(T_{sfc}) + N*B(T_{cld})$.

Cloud Fraction N	Long-wave Window Rad	Temp	Short-wave Window Rad	Temp	$T_s - T_1$
1.0	23.5	220	.005	220	0
.8	42.0	244	.114	267	23
.6	60.5	261	.223	280	19
.4	79.0	276	.332	289	13
.2	97.5	289	.441	295	6
.0	116.0	300	.550	300	0

Table 6.2
Estimates of emissivities for different surface types

	(3.5-3.9)	(10.3-11.3)	(11.5-12.5)
Rocks:			
Igneous			
Granite.h2	.91	.91	.95
Andesite.h1	.96	.90	.95
Basalt.h1	.96	.90	.95
Sedimentary			
Limestone.h1	.89	.94	.97
Sandstone.h1	.83	.96	.98
Shale.h1	.86	.97	.98
Metamorphic			
Marble.h2	.94	.95	.98
Quartzite.h1	.78	.97	.98
Schist.h3a	.90	.94	.96
Slate.h1a	.89	.95	.97
Soils:			
Entisols			
(quartz-rich)	.85	.97	.98
Vertisols			
(high clay content)	.87	.97	.98
Aridisols			
(desert,fine quartz, clay, carbonate soil)	.75	.97	.97
Mollisols			
(black organic-rich)	.83	.97	.98
Vegetation			
Lichens	.95	.97	.98
Green Foliage			
Beech	.95	.95	.96
Hickory	.95	.98	.98
Red Oak	.97	.95	.95
Conifer	.98	.98	.98
Indian Grass	.97	.96	.98
Senescent Foliage			
Sen Beech	.75	.82	.85
Sen Red Oak	.84	.91	.92
Sen Pine	.96	.98	.98
Sen Rye Grass	.85	.91	.91
Decomposing Soil Litter			
Deciduous	.92	.96	.96
Coniferous	.94	.98	.98
Seawater and Distilled	.97	.99	.99
Ice			
Sea Ice smooth	.96	.98	.97
Sea Ice 100 grit	.93	.99	.97
Water Coatings			
Foam	.97	.99	.99
Oil 42667	.96	.96	.96
Soil Float	.97	.98	.98

(Estimates made from average reflectance values reported in Salisbury and D'Aria (1992, 1994)).

Table 6.3

UW HIRS cloud statistics from 11 years of global near nadir HIRS measurements for the boreal summers and winters from June 1989 through February 2000 between 65 N and 65 S

	Boreal Summer (June-August)				Boreal Winter (December-February)			
	All Clouds	Thin Clouds	Thick Clouds	Opaque Clouds	All Clouds	Thin Clouds	Thick Clouds	Opaque Clouds
High >6km	36%	16%	15%	5%	36%	16%	16%	4%
Mid 3-6 km	25%	9%	11%	5%	30%	9%	11%	9%
Low <3 km	45%	2%	0	44%	44%	0	2%	42%
All Clouds	73%	23%	21%	29%	75%	22%	24%	29%

Frequency of cloud observations in a given level of the atmosphere are percentages of observations only to that level. Effective emissivity refers to the product of the fractional cloud cover, N, and the cloud emissivity, ε, for each HIRS observational area (roughly 20 km resolution). Thin clouds have $N\varepsilon < 0.5$ and IR optical depths <0.7. Thick clouds have $0.5 < N\varepsilon < 0.95$ and IR optical depths from 0.7 to 3.0. Opaque clouds are opaque to the IR window with $N\varepsilon > 0.95$ and IR optical depths > 3.0. Comparisons with 1 km AVHRR data have indicated that the FOV is totally obscured by cloud when $N\varepsilon \geq 0.5$ and 72% obscured by cloud when $N\varepsilon < 0.5$. 6 km averaged 441 hPa in pressure height; 3 km averaged 665 hPa in pressure height.

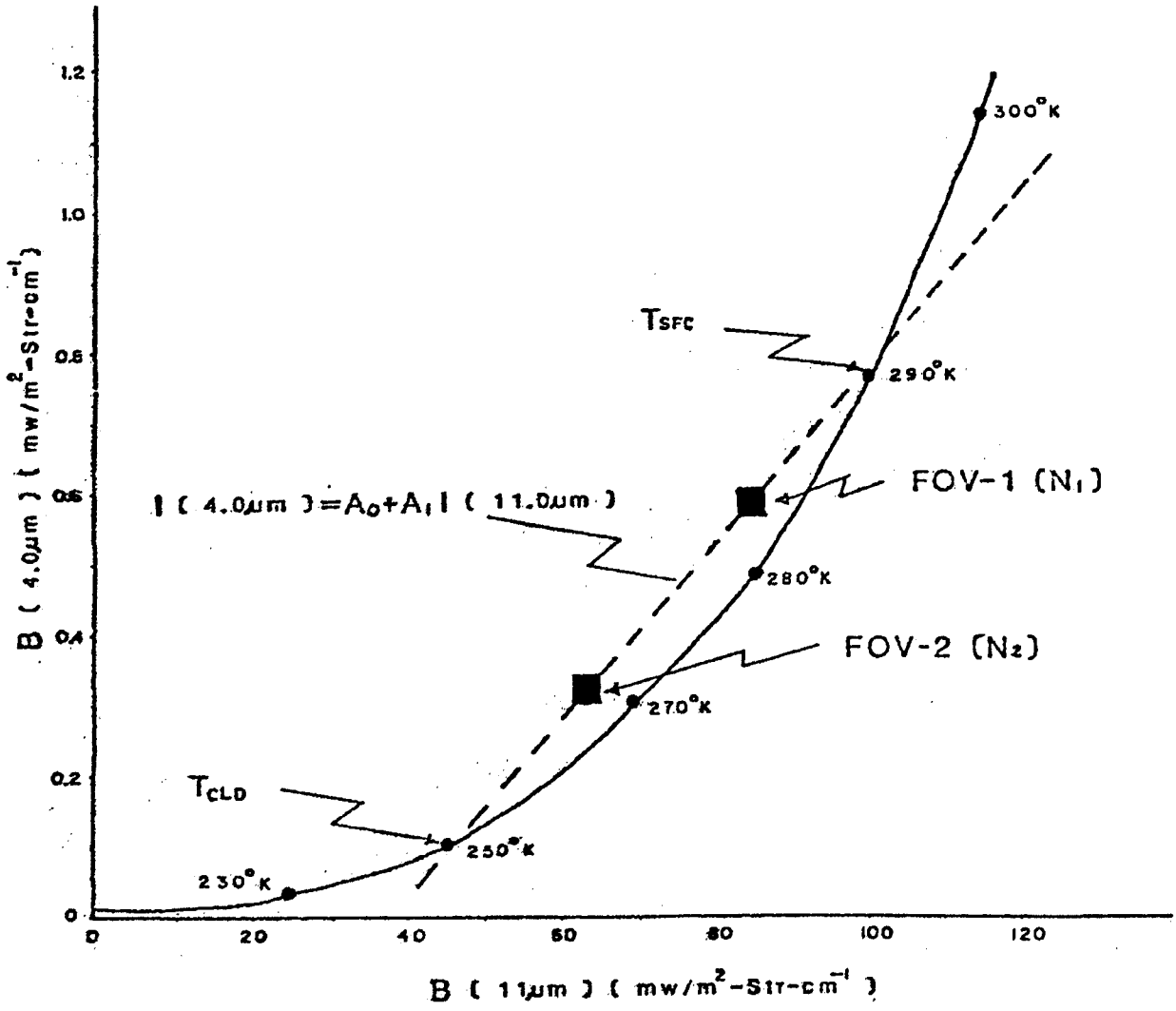

Figure 6.1: Ratio of the radiances for the two window channels; solid curve is the theoretical cloud free curve and dashed curve is the linear variation with cloud amount.

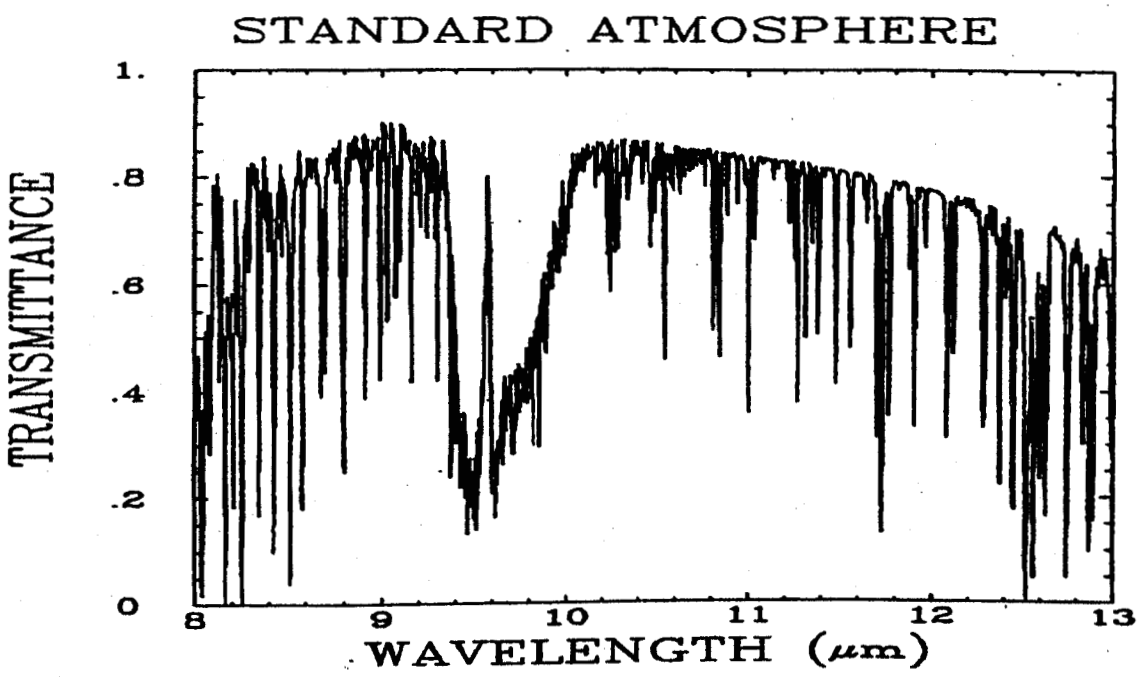

Figure 6.2. High resolution total transmittance spectra for a standard atmosphere across the 8 to 13 micron spectral region.

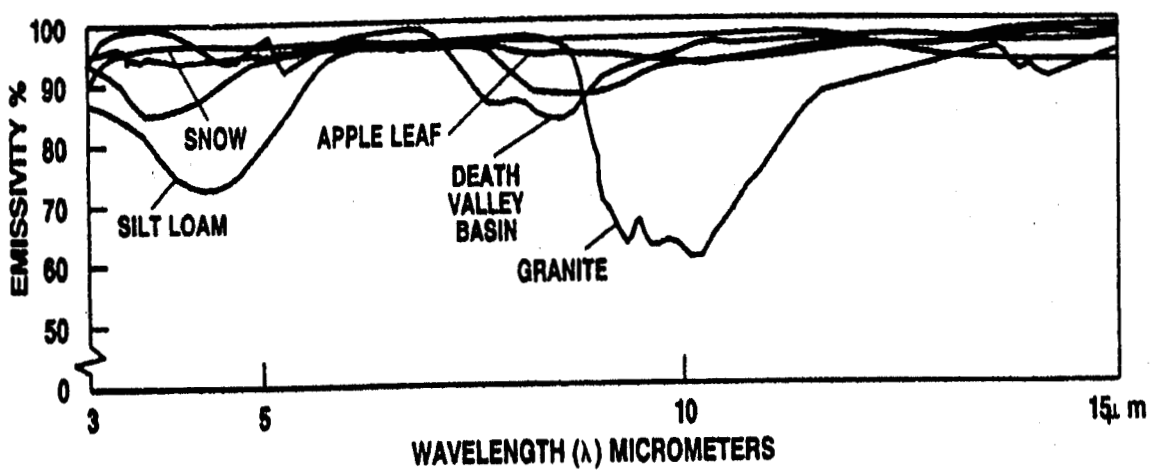

Figure 6.3. Emissivity of various soil and vegetation types as a function of wavelength.

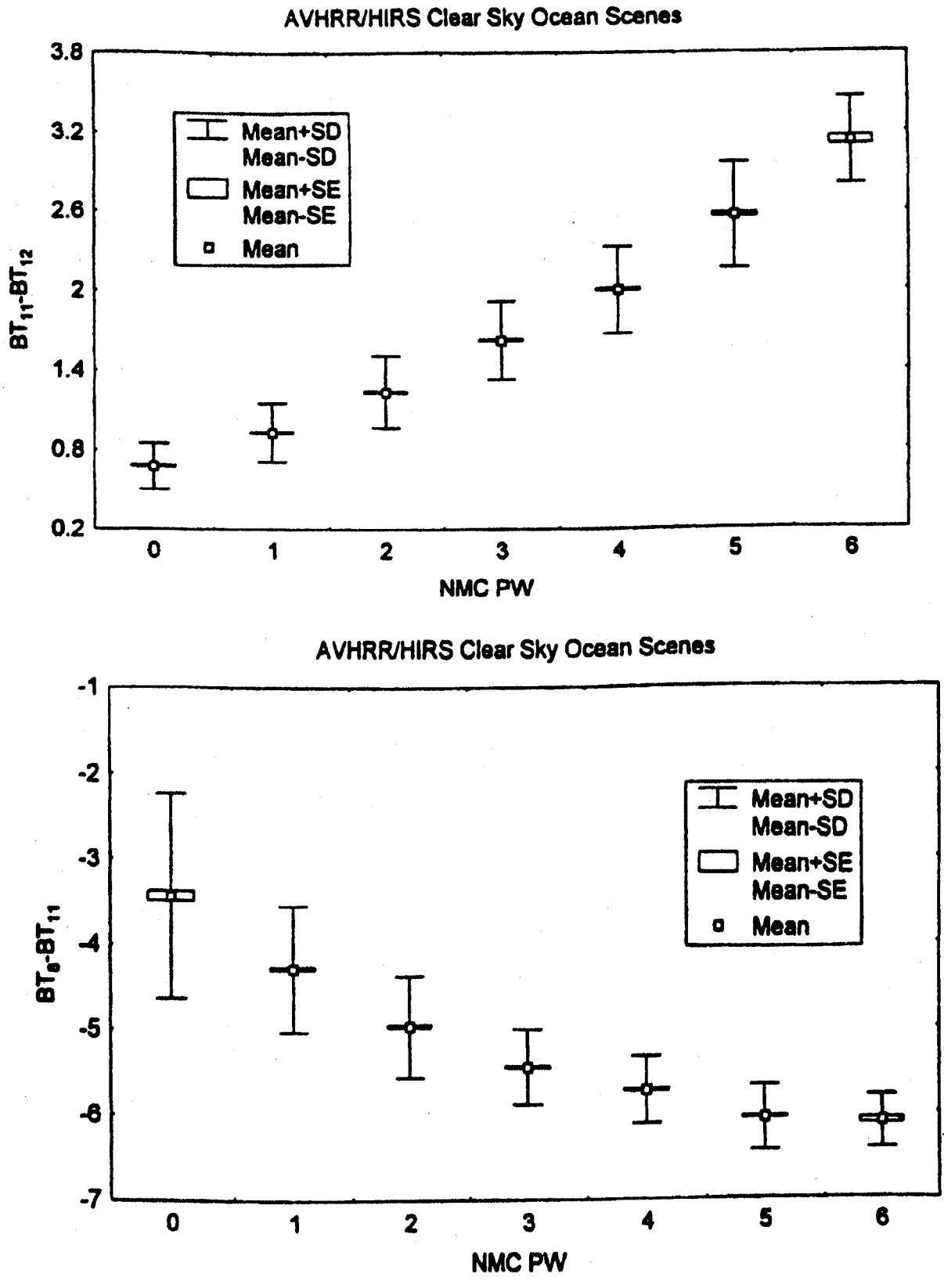

Figure 6.4. The dependence on PW of the brightness temperature difference between the various window channels. Observed AVHRR 11-12 micron (top panel) and collocated HIRS 8-11 micron (bottom panel) brightness temperature differences plotted versus NMC total column PW for January 1994 over clear ocean scenes.

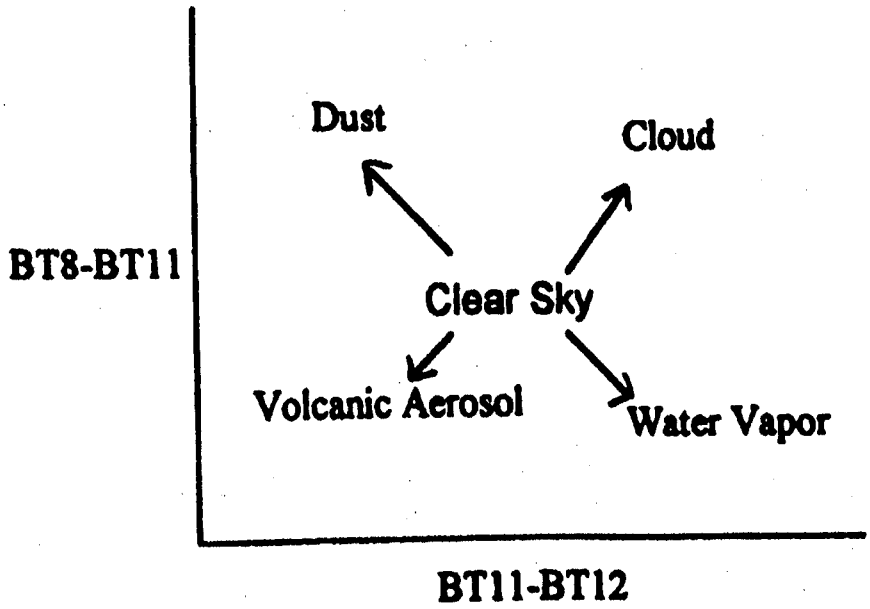

Figure 6.5. Schematic diagram of the effects of different atmospheric constituents on the brightness temperature differences 11 minus 12 microns and 8.6 minus 11 microns.

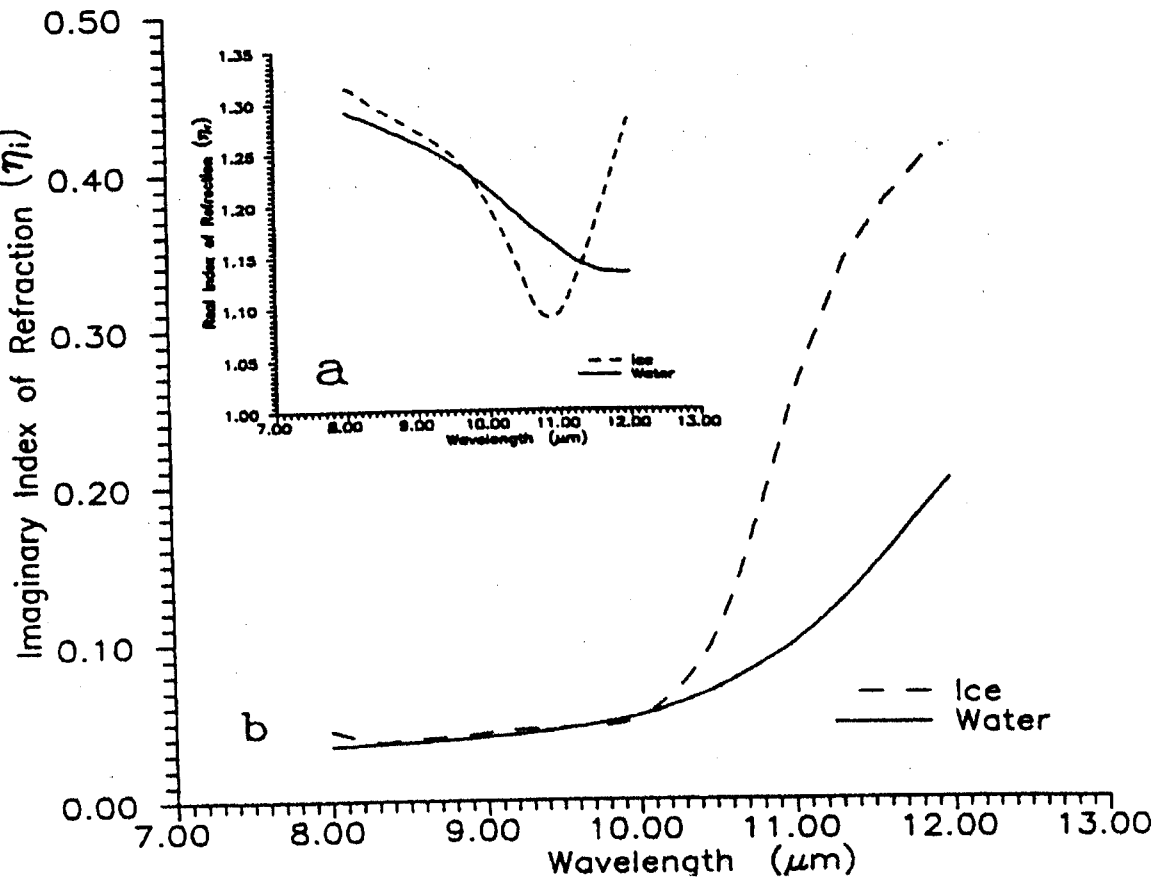

Figure 6.6. Indices of refraction of ice and water across the window region (a) real part and (b) imaginary part (associated with absorption). Note the greater absorption of ice over water for wavelengths greater than 10.5 microns.

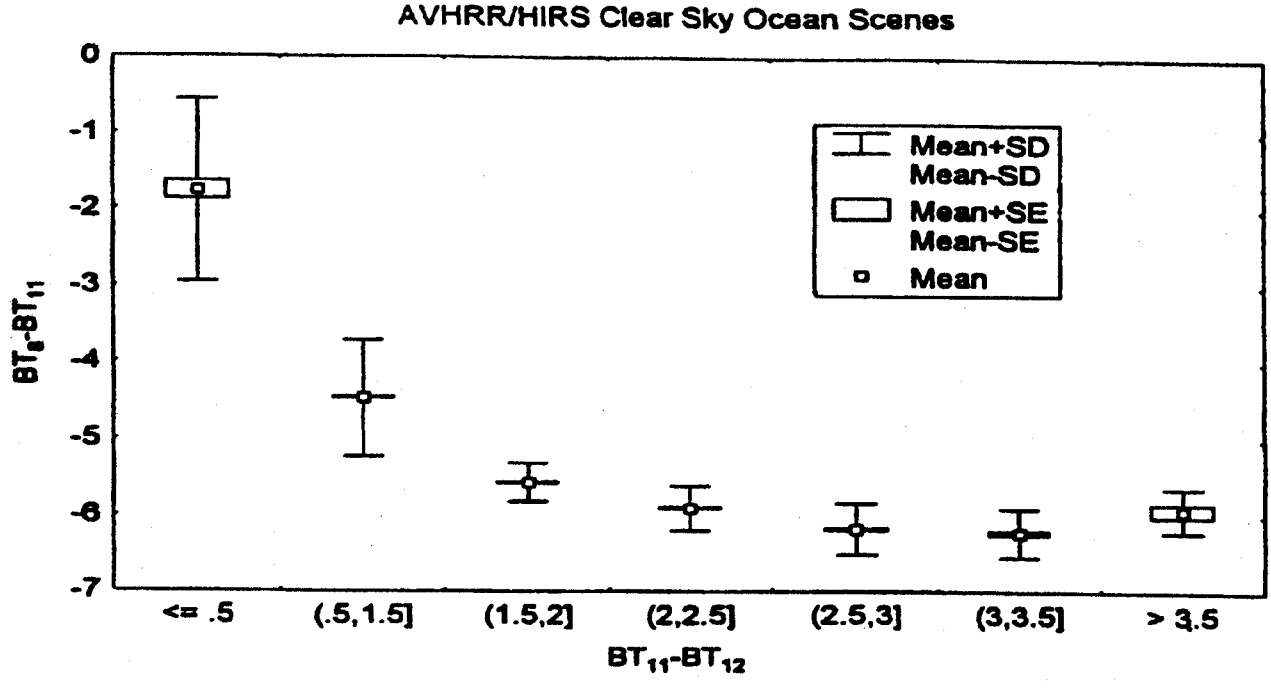

Figure 6.7. Scatter diagram of collocated HIRS 8-11 versus AVHRR 11-12 micron brightness temperature differences for January 1994 over clear ocean scenes. As moisture increases, the 11-12 micron brightness temperature difference increases while the 8888-11 micron brightness temperature difference decreases.

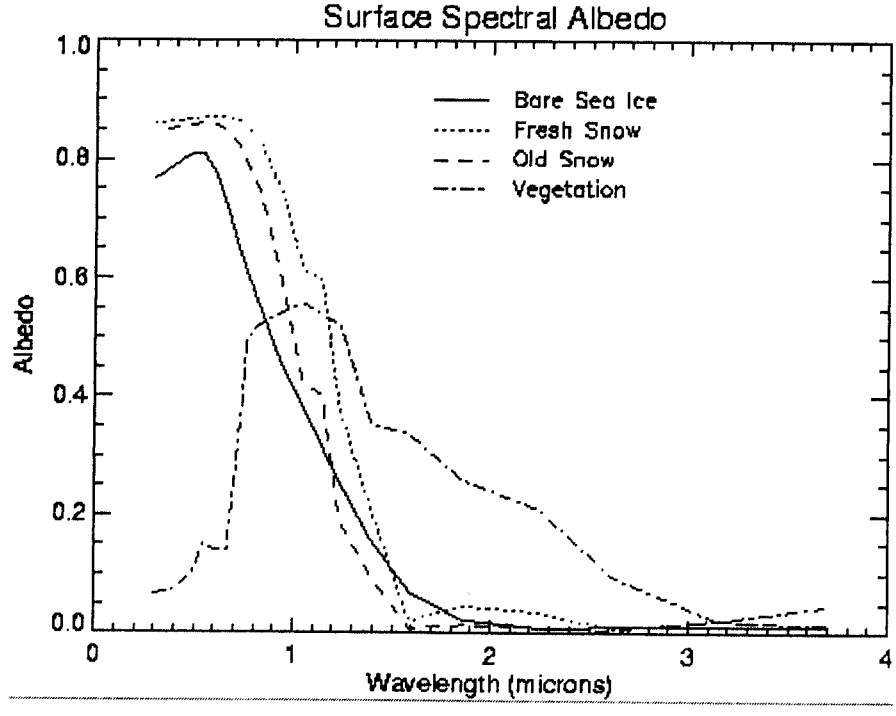

Figure 6.8. Albedo variations for ice, snow, and vegetation from 0.5 to 3.5 microns. Vegetation shows a sharp increase above 0.72 microns. Snow/ice shows a sharp decrease above 1.4 microns.

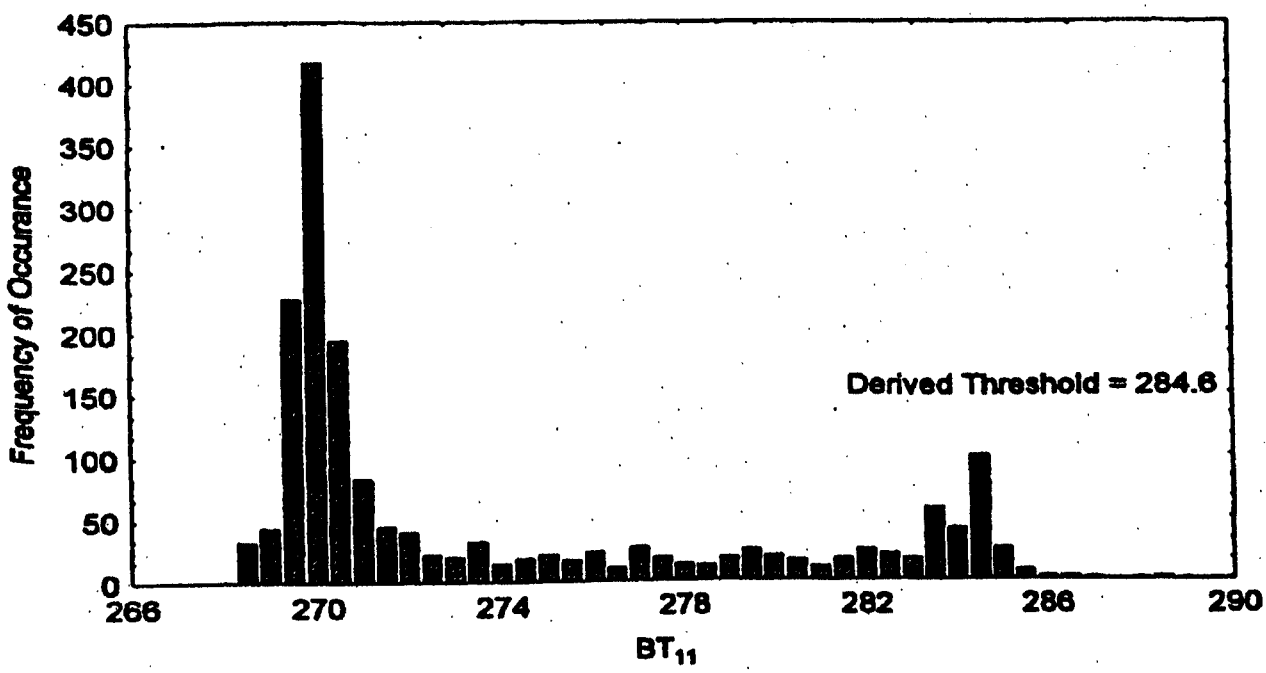

Figure 6.9. Example of infrared histogram analysis technique using AVHRR GAC data for 2.5 by 2.5 degree ocean region. The derived clear sky brightness temperature threshold is 284.6 K.

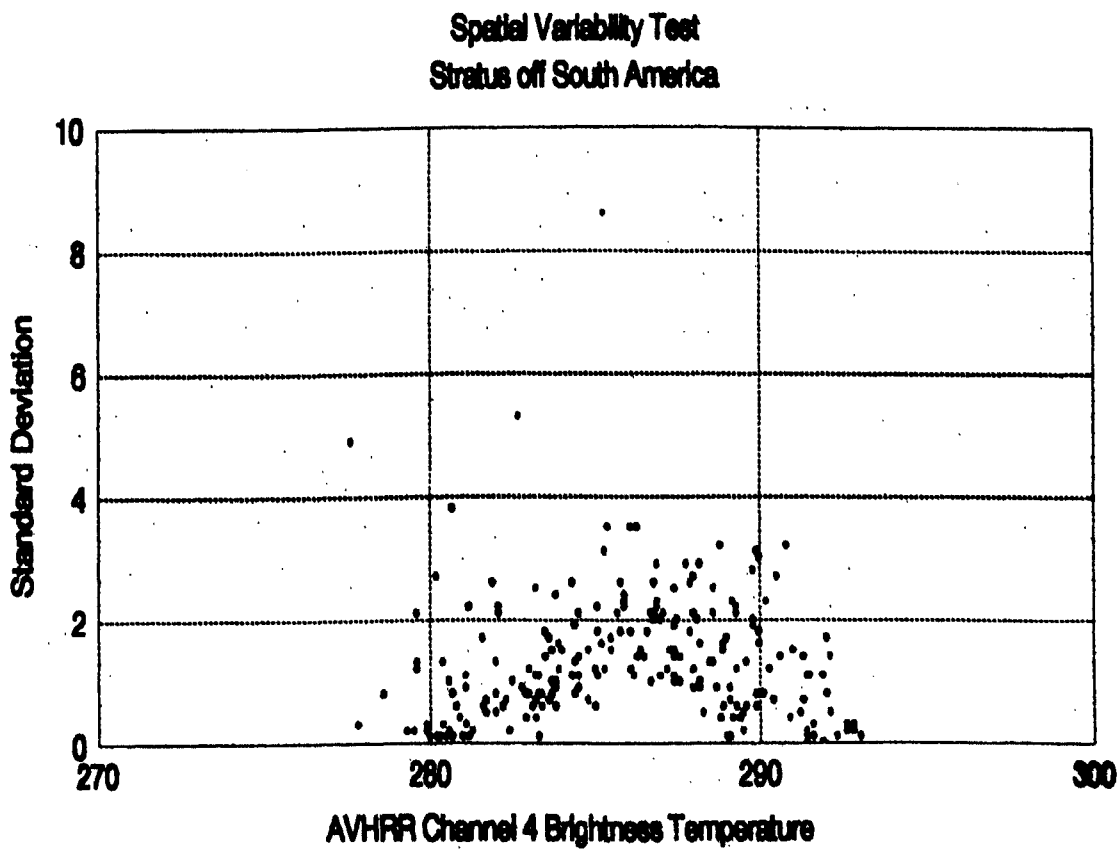

Figure 6.10. Example of the arches obtained when plotting local deviation from mean with respec to temperature.

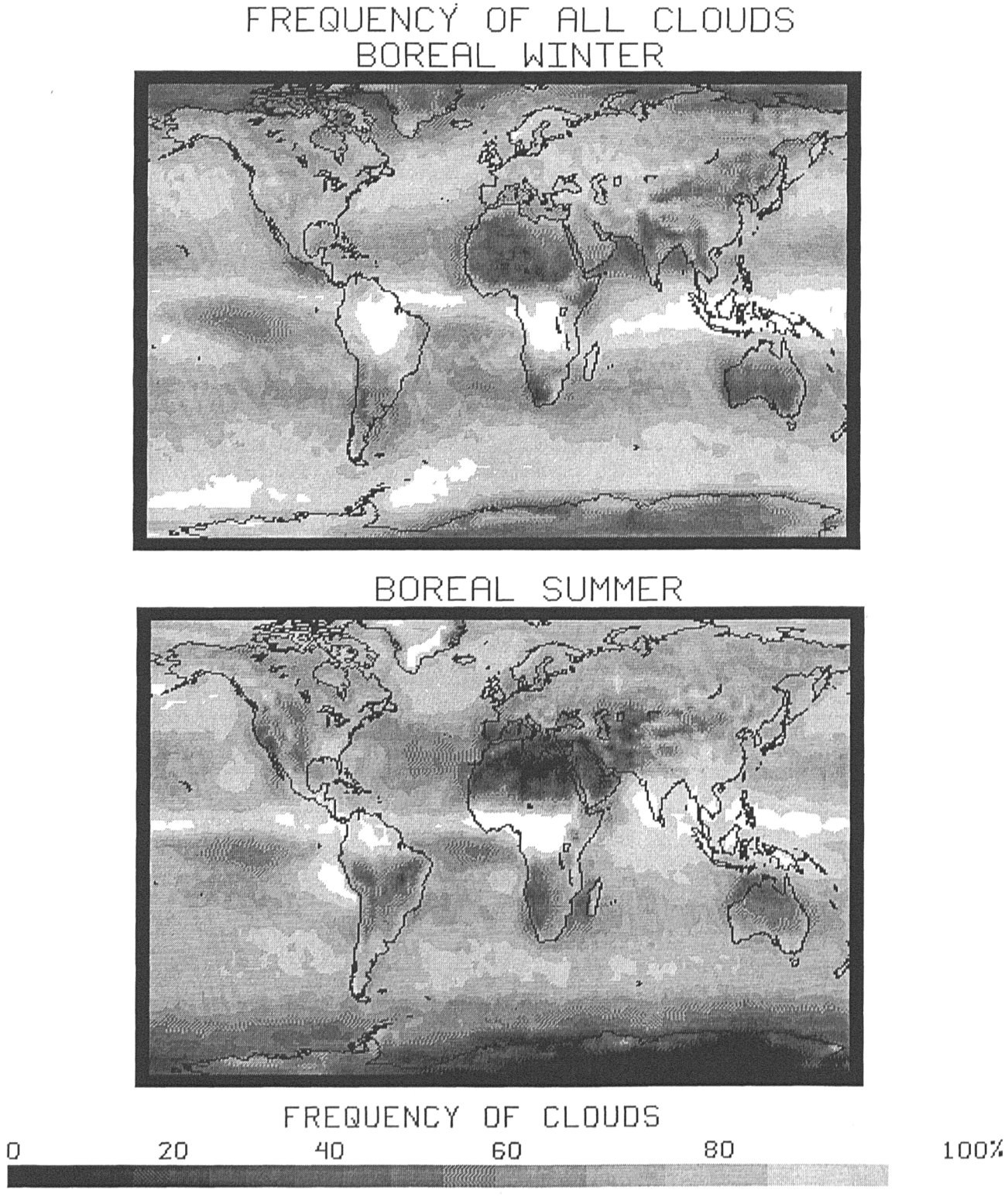

Figure 6.11: (upper panel) The geographic frequency of transmissive clouds for the boreal winters (December, January, and February) during the observation period June 1989 through May 1997. (lower panel) The geographic frequency of cloud detection for the boreal summers (June, July, August) during the observation period June 1989 through May 1997. (b)

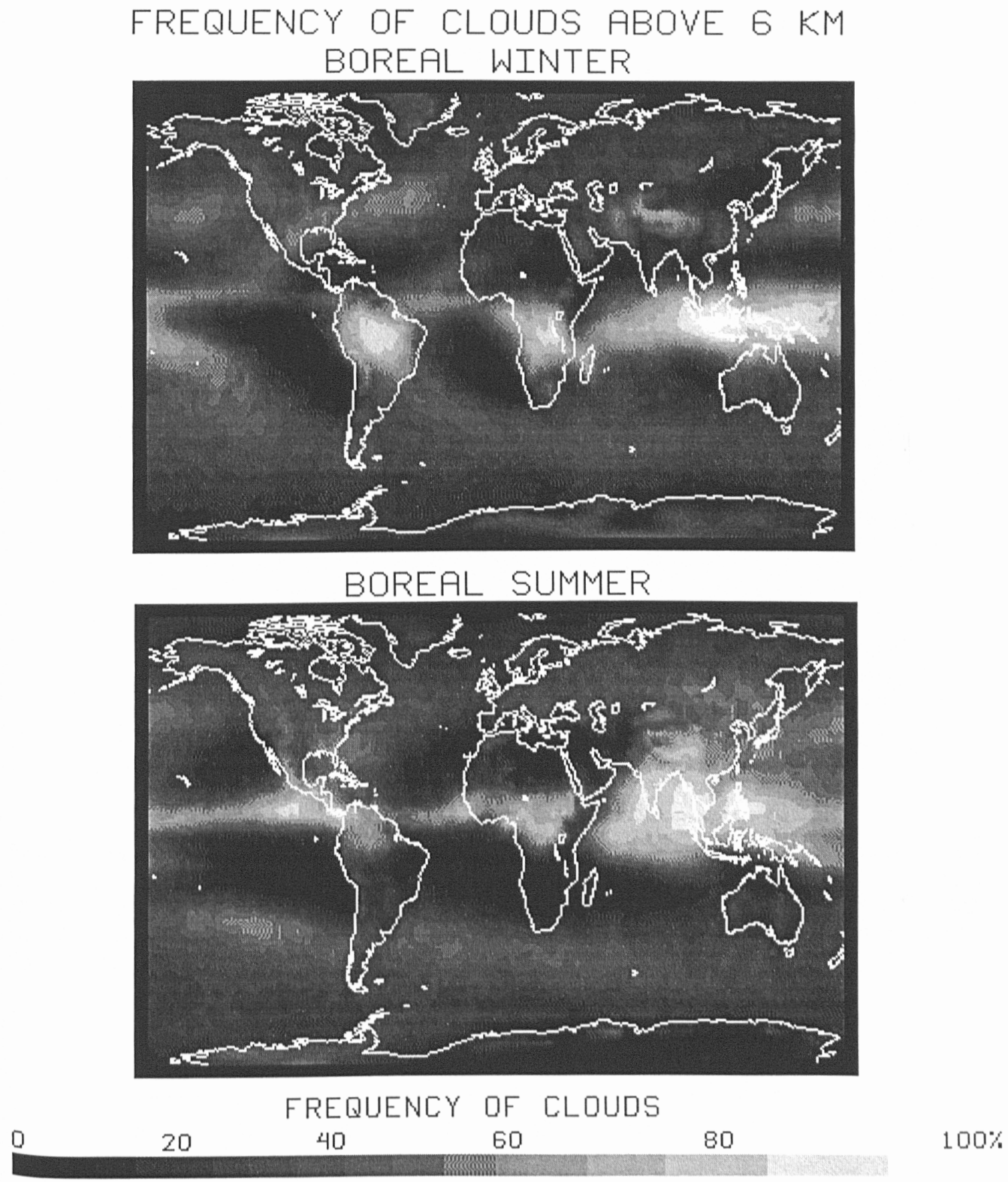

Figure 6.12: The frequency of high (above 6 km) cloud detection in a HIRS FOV from 1989 to 1997.

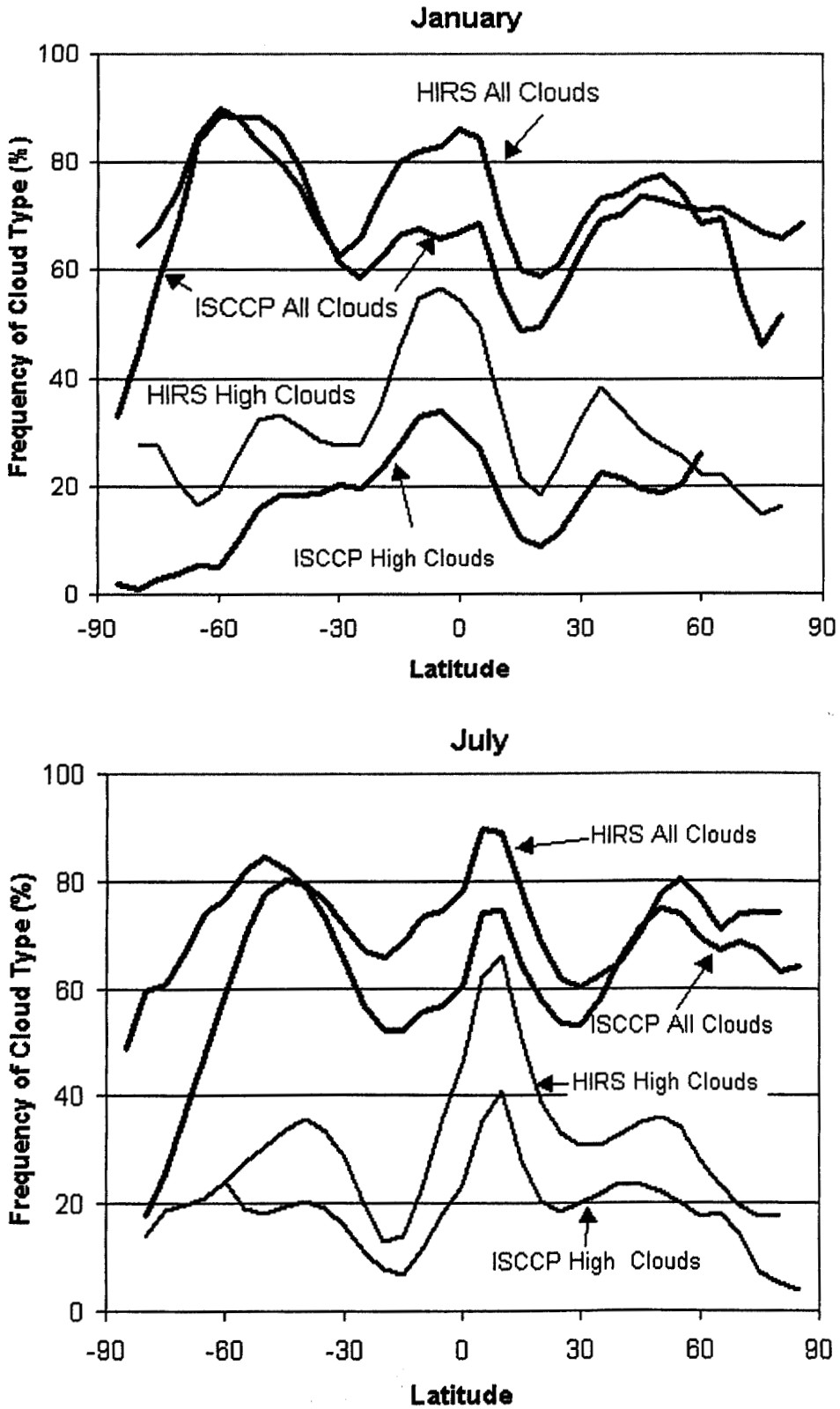

Figure 6.13: The frequency of detection of all clouds (total cloud) and high cloud (above 440 hPa) for the UW HIRS and the ISCCP analyses. ISCCP high clouds are the sum of cirrus, cirrostratus, and deep convective cloud frequencies. (top) Results from four Januarys in 1990-93 were averaged. (bottom) Results from five Julys in 1989 – 1993.

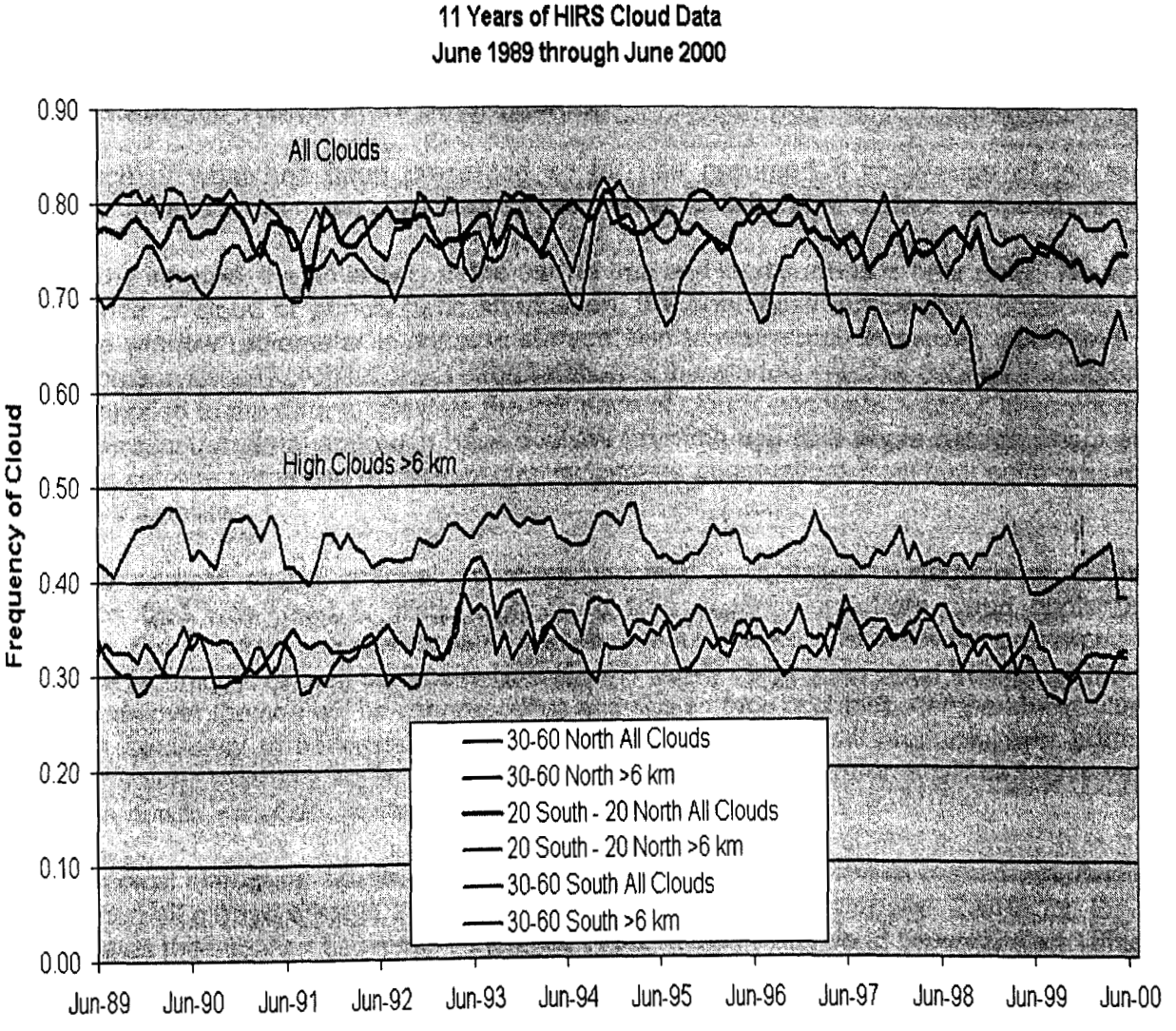

Figure 6.14. High cloud and all cloud observations found in HIRS measurements from June 1989 through June 2000. Polar orbiters NOAA 10 through 15 are part of this data set. NOAA 12 replaced NOAA 10 in September 1991, and NOAA 14 replaced NOAA 11 in April 1995. NOAA 15 replaced NOAA 12 in October 1998. Cloud observations over land from NOAA 11 are discarded because of the influence of the orbit drift.

CHAPTER 7

SURFACE TEMPERATURE

7.1 Sea Surface Temperature Determination

Much of what has been presented so far has assumed a knowledge of the surface temperature. In this section, we shall discuss techniques to determine surface temperature.

In the infrared, the emissivity of the earth's sea and land surface is near unity. As a result, in the absence of cloud or atmospheric attenuation, the brightness temperature observed with a space-borne window radiometer is equal to surface skin temperature. However, cloud and water vapour absorption usually prohibit direct interpretation of the window channel data so that algorithms need to be applied to the data to alleviate the influence of clouds and water vapour absorption. The algorithms and instrumental approach have evolved from the use of a single window channel on a polar orbiting satellite to the use of multispectral radiometer observations from both polar orbiting and geostationary satellites.

The earliest single channel approach involved a statistical histogram of brightness temperatures that was used to distinguish cloud free observations from cloud contaminated observations and to obtain sea surface temperature measurements. The following assumptions are implicit in the technique: (a) sea surface temperature is slowly varying, so cloud free infrared window measurements over the sea will be very repetitive and sea surface brightness temperature values will have a high frequency of occurrence, and (b) cloud contamination will produce lower brightness temperature values than sea surface and the cloud brightness temperatures will be highly variable over an area due to variations in cloud amount, opacity, and altitude.

A typical histogram situation is shown in Figure 7.1. Part A shows the normal distribution obtained when all measurements are cloud free and no SST gradient exists. Part B, on the other hand, illustrates the situation when more than half of the samples are cloud contaminated. Since the cloud-contaminated radiance temperatures are lower than the cloud free temperatures, they populate the left hand side of the histogram, but also distribute themselves normally. Only the warm side of the normal density curve formed by cloud free observations can be distinguished from the combined data in the histogram. Since the mean of the normal (Gaussian) density function (probability function) formed from clear observations is the most likely value of the SST, several schemes have been developed to infer the mean of a Gaussian probability function from knowledge of the standard deviation S of the density function and knowledge of the geometry of one side of the distribution.

7.1.1 Slope Method

The slope method assumes that the brightness temperature frequency distribution is a normal function of the form

$$f(T) = f_s \exp [-(T - T_s)^2/2\sigma^2]$$

where f is the frequency of occurrence, $f_s = f(T_s)$ is unknown, the standard deviation S is assumed to be known from the characteristics of the measuring instrument, and the mean temperature T_s is the quantity to be determined. Since the standard deviation of a normal probability density function occurs at the inflection points on the curve, then

$$T_s = T_{max} - \sigma$$

where T_{max} is the solution of

$$d^2f/dT^2 = 0 ,$$

and S is determined from the equation

$$\sigma = (\sigma_N^2 + \sigma_E^2)^{½} ,$$

where σ_N and σ_E are the standard deviations, respectively, of the instrument noise and the expected variance of the SST's.

7.1.2 Three Point Method

The three point method also assumes a normal probability function, and solves for T_s by selecting three points (T_i, f_i), (T_j, f_j), and (T_k, f_k) on the warm side of the histogram as follows

$$f_i = f_s \exp [-(T_i - T_s)^2/2\sigma^2]$$

$$f_j = f_s \exp [-(T_j - T_s)^2/2\sigma^2]$$

$$f_k = f_s \exp [-(T_k - T_s)^2/2\sigma^2] .$$

These three equations contain three unknowns f_s, σ, and T_s and can be solved by simple Gaussian elimination. Therefore

$$\ln(f_i/f_j) = [(T_i^2 - T_j^2)-2T_s (T_i - T_j)]/2\sigma^2 ,$$

$$\ln(f_i/f_k) = [(T_i^2 - T_k^2)-2T_s (T_i - T_k)]/2\sigma^2 ,$$

or, finally,

$$T_s = \frac{T_i^2 \ln (f_j/f_k) - T_j^2 \ln (f_i/f_k) + T_k^2 \ln (f_i/f_j)}{2 [T_i \ln (f_j/f_k) - T_j \ln (f_i/f_k) + T_k \ln (f_i/f_j)]}$$

Since a single calculation of T_s can be influenced by noise and by the combination of the three points being slightly non-Gaussian, repeated calculations of T_s are made from all possible unique combinations of three points on the warm side of the histogram. Thus, if there are n useful points on the warm side, then all possible combinations ($i = 1, ..., n - 2$; $j = i + 1, ..., n - 1$; and $k = j + 1, ..., n$) are used to construct a second histogram, called the mean estimate histogram from which the most frequently occurring estimate is taken as the correct one.

7.1.3. Least Squares Method

Another solution is through a least squares fit of the normal distribution probability function to three or more points on the warm end of the observed frequency distribution. It follows from before that

$$\ln (f(T)) = \ln (f_s) - T_s^2/2\sigma^2 + T_sT/\sigma^2 - T^2/2\sigma^2$$

which has the form

$$\ln (f(T)) = A_o + A_1T + A_2T^2 ,$$

where

$$T_s = - A_1/(2A_2) ,$$

and

$$\sigma^2 = - 1/(2A_2) .$$

Thus, given three or more points (f_i, T_i) on the cloud free portion of the histogram, one can solve for T_s and σ using the least squares solution.

7.2 Water Vapour Correction for SST Determinations

Several multispectral methods have evolved to correct for the presence of clouds in the area of interest. The detection of clouds was addressed more fully in the previous chapter. Correction for the effects of water vapour in the atmosphere is addressed here. The brightness temperature observed with a satellite radiometer can be equated to surface skin temperature after the effect of atmospheric water vapour absorption has been taken into account.

The surface temperature can be expressed in terms of the observed clear sky window channel brightness temperature, T_b, and a water vapour correction, ΔT;

$$T_S = T_b + \Delta T .$$

The water vapour correction ranges from a few tenths of a degree Kelvin in very cold and dry atmospheres to nearly 10 K in very warm and moist atmospheres for 11 micron window observations. The corresponding corrections for the 3.7 micron window are about half as large. The water vapour correction is highly dependent on wavelength. To see why this is so, consider that at 3.7 micron, the Planck radiance varies with temperature to approximately the thirteenth power whereas at 11 micron the Planck radiance varies with temperature to approximately the fourth power. Inserting

$$B_\lambda(T) = T^{n\lambda}$$

$$T_{b\lambda} \sim \tau_\lambda(p_s)\, T_s^{n\lambda} + (1 - \tau_\lambda(p_s))\, T_a^{n\lambda}$$

where $\tau_\lambda(p_s)$ is the atmospheric transmittance, T_s is the surface temperature, and T_a is the mean atmospheric temperature. Assuming representative values of 0.8, 300 K, and 270 K for τ_s, T_s, and T_a, respectively, one finds that at 3.7 micron where $n_\lambda = 13$, the brightness temperature observed is 296.5 K as opposed to a value of 294.5 K observed at 11 micron where $n_\lambda = 4$. Clearly for a non-isothermal condition and the same atmospheric transparency, the water vapour correction does depend on wavelength. Figure 7.2a illustrates the water vapour corrections derived for the Nimbus-2 3.7 micron region due to the Planck radiance dependence discussed above. Note also the dependence of the water vapour correction on viewing angle.

The water vapour correction is best evaluated by observing the area of interest in multiple infrared window channels. In the atmospheric window regions, the absorption is weak, so that

$$\tau_w = e^{-k_w u} \sim 1 - k_w u$$

where w denotes the window channel wavelength, and

$$d\tau_w = - k_w du$$

What little absorption exists is due to water vapour, therefore, u is a measure of precipitable water vapour. The RTE can be written in the window region

$$I_w = B_{sw}(1-k_w u_s) + k_w \int_o^{u_s} \bar{B}_w du$$

u_s represents the total atmospheric column absorption path length due to water vapour, where s denotes surface. Defining an atmospheric mean Planck radiance

$$\bar{B}_w = \int_o^{u_s} B_w du \Big/ \int_o^{u_s} du$$

then

$$I_w = B_{sw}(1-k_w u_s) + k_w u_s \bar{B}_w .$$

Since B_{sw} is close to both I_w and B_w, first order Taylor expansion about the surface temperature T_s allows us to linearize the RTE with respect to temperature, so

$$T_{bw} = T_s(1-k_w u_s) + k_w u_s \bar{T}_w ,$$

where $\bar{T}_w$ is the mean atmospheric temperature corresponding to B_w. For two window channel wavelengths (11 and 12 micron) the following ratio can be determined.

$$\frac{T_s - T_{bw1}}{T_s - T_{bw2}} = \frac{k_{w1} u_s (T_s - \bar{T}_{w1})}{k_{w1} u_s (T_s - \bar{T}_{w2})}$$

Assuming that the mean atmospheric temperature measured in the one window region is comparable to that measured in the other, $T_{w1} \sim T_{w2}$, we can simplify to

$$\frac{T_s - T_{bw1}}{T_s - T_{bw2}} = \frac{k_{w1}}{k_{w2}}$$

from which it follows that

$$T_s = T_{bw1} + \frac{k_{w1}}{k_{w2} - k_{w1}} [T_{bw1} - T_{bw2}]$$

This is the split window channel expression for the water vapour correction to the SST. The term split window is used to denote two neighbouring channels in a relatively transparent or window region of the spectrum; one channel for which the atmosphere is highly transparent and the other for which atmospheric water vapour partially absorbed the surface radiance to space. For three window channels (at 3.7, 11, and 12 mm) the analogous expression is

$$T_s = T_{bw1} + \frac{k_{w1}}{2(k_{w2} - k_{w1})} [T_{bw1} - T_{bw2}] + \frac{k_{w1}}{2(k_{w3} - k_{w1})} [T_{bw1} - T_{bw3}]$$

Figure 7.2b provides a graphical representation of the multispectral window channel water vapour correction algorithm. This linear extrapolation technique was first proposed by Anding and Kauth (1970) and initially tested by Prabhakara *et al,* (1974). Accuracies of 1.0-1.5 C absolute and 0.5-1.0 C relative have been routinely achieved in the last few years.

Recently, a more sophisticated algorithm for atmospheric correction has been adopted. It includes a nonlinear term to account for absorption of water vapor in very wet atmospheres. Thus, a quadratic term is added to the regression, as suggested by McMillin and Crosby (1984). The regression equation to correct for atmospheric absorption and re-emission has the form:

$$SST = A0 + A1*T11 + A2*T12 + A3*dT^2$$

where dT = T11 – T12. Table 7.1 summarizes the coefficients applicable to recent multispectral sensors.

The operational satellites currently in use for the SST determinations are the TIROS-N and GOES. The TIROS-N Advanced Very High Resolution Radiometer as well as the High resolution Infrared Sounder (HIRS) are well-suited to measure surface temperatures since they detect radiation in the split window (water vapour absorption and window channels). However, observations from the TIROS-N series of satellites are not always timely (overpasses occur only four times per day over any given region). On the other hand, the GOES Imager offers half hourly images at 4 km resolution (an order of magnitude more measurements of a given ocean surface). Thus, timely observations are available and the influence of clouds can often be alleviated by simply waiting for them to move out of the area of interest. Also, a given geographical region is always observed from the same viewing angle with the GOES Imager so that relative variations of observed surface temperature variations rather than to variations in scan geometry. With multispectral window radiometer data routinely available from the geostationary GOES, it is now possible to perform both precise water vapour correction and cloud filtering through quasi-continuous sampling with just one instrument.

The GOES cloud screening includes temporal continuity along with threshold tests with moisture corrected atmospheric infrared windows and visible reflectances. The following tests are used in the GOES SST algorithm for cloud detection.

$T_{11} > 270$ K	ocean rarely frozen
$T_{11} > T_{12} + 4$ K	clouds affect moisture correction
vis < 4%	clouds reflect more than ocean sfc
$T_{11} - T_{3.9} > 1.5$ K	subpixel clouds
$\Delta T_{11} < 0.3$ K	ΔSST over 1 hr small
-2 K < SST- guess < 5 K	ΔSST over days bounded

GOES SSTs have been routinely generated every three hours in the vicinity of the continental USA since May 1997. The diurnal changes in the GOES SST are noticeable. As an example, Fig. 7.3a shows a three-day composite of the GOES SST around 1200 UTC (early morning), 20-22 May 1998, and Fig. 7.3b shows the difference eight hours later. The magnitude of the difference and the spatial distribution of the SST diurnal variation are remarkable. Variations as large as 3°K are found near the coast, where land contamination is a possible factor, and in regions where the surface wind is weak. Adequate validation and monitoring of such diurnal variations in surface skin temperatures is necessary; the implications if verified are many.

Climate analysis of SST may be vulnerable to the variable sampling times of polar orbiting satellites. A sun-synchronous polar orbiting satellite passes a given geographical location at similar local times each day, nominally shortly after noon and midnight, to measure SST. In the presence of SST diurnal variation, if clouds at a location tend to appear at one of these times (say afternoon),

the climatology will be biased towards the other time (nighttime SST). If clouds tend to appear at both times, the SST climatology must be estimated from other data. If the cloud diurnal variation varies seasonally, say clouds tend to appear in the afternoon in summer but not in winter, the SST will be biased towards the nighttime SST in summer but not in winter.

7.3 Accounting for Surface Emissivity in the Determination of SST

When the sea surface emissivity is less than one, there are two effects that must be considered: (a) the atmospheric radiation reflects from the surface; and (b) the surface emission is reduced from that of a blackbody. The radiative transfer can be written

$$I_\lambda = \varepsilon_\lambda B_\lambda(T_s)\,\tau_\lambda(p_s) + \int_o^{p_s} B_\lambda(T(p))\,d\tau_\lambda(p)$$

$$+ (1-\varepsilon_\lambda)\,\tau_\lambda(p_s) \int_o^{p_s} B_\lambda(T(p))\,d\tau`_\lambda(p)$$

where $\tau`_\lambda(p)$ represents the transmittance down from the atmosphere to the surface. As before in the derivation of the microwave RTE, this can be derived in terms of the transmittance up through the atmosphere to the top, $\tau`_\lambda(p)$. Then as before

$$I_\lambda = \varepsilon_\lambda B_\lambda(p_s)\tau_\lambda(p_s) + \int_{p_s}^{o} B_\lambda(T(p))\,F_\lambda(p)\,d\tau_\lambda(p)$$

where

$$F_\lambda(p) = \{\, 1 + (1 - \varepsilon_\lambda)\,[\frac{\tau_\lambda(p_s)}{\tau_\lambda(p)}]^2 \,\}\,.$$

Assuming that the atmosphere is a single layer whose temperature T_A is the same for both upwelling radiance at the top of the atmosphere and the downwelling at the sea surface, then

$$I_\lambda = \varepsilon_\lambda B_\lambda(p_s)\tau_\lambda(p_s) + B_\lambda(T_A)\,[1-\tau_\lambda(p_s) - (1-\varepsilon_\lambda)\tau_\lambda(p_s)^2 + (1-\varepsilon_\lambda)\tau_\lambda(p_s)]$$

or

$$I_\lambda = \varepsilon_\lambda B_\lambda(p_s)\tau_\lambda(p_s) + B_\lambda(T_A)\,[1 - \varepsilon_\lambda \tau_\lambda(p_s) - \tau_\lambda(p_s)^2 + \varepsilon_\lambda \tau_\lambda(p)^2]\,.$$

Note that as the atmospheric transmittance approaches unity, the atmospheric contribution expressed by the second term becomes zero.

Figure 7.4 shows a plot of the window radiance data observed from an interferometer at ship level and at 20 km altitude in the atmosphere, as well as the GOES satellite radiometer. Figure 7.5 plots these radiances as a function of the correction term. The intercept of a regression line through these data is the Planck radiance corresponding to the sea surface temperature. In order to alleviate any scatter produced by the Planck radiance dependence on wavelength (or wavenumber), the observed radiances I_λ are converted to brightness temperature and then back to radiances for a reference wavelength λo. The emissivity values are taken from the literature (Masuda *et al*, 1988) and the transmittance values are computed from a line by line model in conjunction with an in situ radiosonde profile measurement. The retrieved value in this example yields 295.3 K within .2 K of in situ surface skin hat measurements (Smith *et al*, 1995). The atmospheric reflection correction is comparable to the correction from the reduced surface emittance.

7.4 Estimating Fire Size and Temperature

The most practical and economically feasible manner of monitoring the extent of burning associated with tropical deforestation and grassland management is through remote sensing. To date, many remote sensing methods have utilized multispectral data from the Multispectral Scanner (MSS) on Landsat-1, -2,. ., -5, the Thematic Mapper (TM) on Landsat-4 and -5, and the Advanced Very High Resolution Radiometer (AVHRR) on the NOAA polar orbiters (Tucker *et al*, 1984; Matson and Holben, 1987; Nelson *et al*, 1987; Malingreau and Tucker, 1988). A number of these techniques calculate vegetative indices in order to estimate deforestation areas (Justice *et al*, 1985; Malingreau *et al*, 1985; Townshend *et al*, 1987). However, the extent of deforestation is usually underestimated, mostly due to the inability to distinguish between primary and secondary growth (Malingreau and Tucker, 1988).

Another estimation of the rate of deforestation can be made by monitoring biomass burning. Matson and Dozier (1981) developed a technique utilizing the AVHRR 3.7 micron and 10.8 micron channels to detect subpixel resolution forest fires. The technique provides reasonable estimates of temperature and area of fires in those 1 km pixels that are not saturated (Matson and Holben, 1987). Unfortunately, many of the pixels are saturated and it is difficult to monitor plume activity associated with these subpixel fires, since the NOAA polar orbiting satellite has only one day time pass over a given area. The Geostationary Operational Environmental Satellite offer continuous viewing and less pixel saturation (because the pixel resolution is 4 km on GOES-8 or 16 km on GOES-7). Furthermore, the fire plumes can be tracked in time to determine their motion and extent. Thus, the GOES satellite offers a unique ability to monitor diurnal variations in fire activity and transport of related aerosols.

The different brightness temperature responses in the two infrared window channels can be used to estimate the temperature of the target fire as well as the subpixel area it covers. Typically, the difference in brightness temperatures between the two infrared windows at 3.9 and 11.2 microns is due to reflected solar radiation, surface emissivity differences, and water vapour attenuation. This normally results in brightness temperature differences of 2-4 K. Larger differences occur when one part of a pixel is substantially warmer than the rest of the pixel. The hotter portion will contribute more radiance in shorter wavelengths than in the longer wavelengths. This can be seen in Figure 7.6 which depicts a portion of a line of VAS data over South America at 1831 UTC on 24 August 1988. Pixels a, b, and c represent areas where subpixel fires are burning. The largest temperature difference occurs at location b where the 11 micron brightness temperature value is 306.2 K and the 4 micron brightness temperature is 321.4 K. Warm areas surrounding these pixels are previously burned regions.

The fire extent and temperature within a field of view can be determined by considering the upwelling thermal radiance values obtained by both channels (Matson and Dozier, 1981; Dozier, 1981). For a given channel, λ, the radiative transfer equation indicates

$$R_\lambda(T) = \varepsilon_\lambda B_\lambda(Ts)\, \tau_\lambda(s) + \int_0^1 B_\lambda(T)\, d\tau_\lambda$$

When the GOES radiometer senses radiance from a pixel containing a target of blackbody temperature T_t occupying a portion p (between zero and one) of the pixel and a background of blackbody temperature T_b occupying the remainder of the pixel (1-p), the following equations represent the radiance sensed by the instrument at 4 and 11 micron.

$$R_4(T_4) = p\, R_4(T_t) + \varepsilon_4\, (1\text{-}p)\, R_4\,(T_b) + (1\text{-}\varepsilon_4)\, \tau_4(s)\, R_4(solar)$$

$$R_{11}(T_{11}) = p\, R_{11}(T_t) + \varepsilon_{11}\, (1\text{-}p)\, R_{11}(T_b)$$

The observed short wave window radiance also contains contributions due to solar reflection that must be distinguished from the ground emitted radiances; solar reflection is estimated from differences in background temperatures in the 4 and 11 micron channels. Once T_b is estimated from nearby pixels, these two nonlinear equations can be solved for T_t and p. In this study, the solution to the set of equations is found by applying a globally convergent bisection technique followed by Newton's method.

Atmospheric correction implicit in these equations are important. Burning or smouldering fires are usually covered by clouds and smoke containing organic particles of varying sizes and shapes, necessitating a correction to the transmittance. Most of the smoke is composed of water vapour, but there are other constituents as well (Andreae *et al*, 1988; Browell *et al*, 1988). The 11 micron channel is more affected by atmospheric water vapour than the 4 micron channel. With Nimbus-2 data, it was found that the water vapour correction for a moist atmosphere is approximately 4 K at 300 K for the 11 micron window and 2 K at 300 K for the 4 micron window (Smith *et al*, 1970). By calculating a linear regression relationship between the GOES visible brightness counts and GOES infrared window brightness temperature in a variety of haze conditions (approximately 50) and extrapolating to clear sky conditions, the Nimbus corrections were found to be appropriate for the GOES data studied (Prins and Menzel, 1994).

Emissivity investigations for vegetation similar to that found in the selva and cerrado suggest an emissivity for tropical rainforest of .96 in the 4 micron region and .97 in the 11 micron region, while the emissivity of dry grassland is .82 and .88 respectively (American Society of Photogrammetry, 1983).

The algorithm proceeds as follows. A fire is identified and a nearby fire free area is located. All observed brightness temperatures over the fire are adjusted for smoke attenuation; 2 K is added to the 4 micron brightness temperatures and 4 K is added to the 11 micron brightness temperatures. T_4 and T_{11} represent the smoke corrected brightness temperatures over the fire for the two spectral bands. The background temperature, T_{b11}, is determined from the 11 micron brightness temperature in a nearby fire-free pixel (p=0) that is adjusted for surface emissivity. Subsequently, the short-wave window reflected radiance for this same fire-free pixel, R_{4solar}, is solved. The input parameters T_{b11}, T_4, T_{11}, and R_{4solar} are now all in place; thus the equations can be solved for p and T_t (Prins and Menzel, 1994).

The process of fire identification is strongly dependent on image interpretation. A fire was suspected if the haze corrected 3.9 micron observed brightness temperature showed a 4 K increase over the 3.9 micron background temperature and the haze corrected 11.2 micron observed temperature displayed a 1 K increase above the 11.2 micron background temperature. Hot spots were not considered fires unless they were accompanied by some indication of a fire in the visible channel, such as a smoke plume. The temporal resolution of the GOES data is extremely useful in two ways. First, a hot spot is often evident in the infrared channels at a certain time period, but the corresponding visible channel showed little or no indication of a fire, possibly due to obscuration by a plume produced by a fire located upwind. A visible image a half hour earlier usually clarified whether a fire is located there. Second, it is difficult to distinguish regular clouds from plumes in a single image. By looping a series of half hourly visible images it is quite easy to identify the point sources of fires, since they remain at a constant location over time.

In South America GOES-8 is being used to continue monitoring trends in biomass burning and to catalogue the extent and transport of associated aerosols. The Automated Biomass Burning Algorithm (ABBA) developed by Prins and Menzel (1994) was used to monitor the 1995 biomass burning season in South America with GOES-8. Multi-spectral diurnal imagery (3-hourly) were collected from June through September to provide a clear picture of biomass burning activities throughout the burning season including estimates of sub-pixel size and mean temperature and information on smoke/aerosol transport. Preliminary GOES-8 ABBA results obtained during the

Smoke, Clouds, and Radiation (SCAR-B) experiment in Brazil (15 August - 15 September 1995) suggest that the peak burning time is in the middle of the afternoon (1745 UTC). Figure 7.7 shows that the number of fires detected at 1745 UTC is 2 to 4 times greater than that observed 3 hours earlier or later and 20 times greater than that observed at 1145 UTC. The majority of the fire activity is concentrated along the perimeter of the Amazon in the Brazilian states of Para, Mato Grosso, Amazonas, and Rondonia. There is also considerable activity in Bolivia, Paraguay, and Northern Argentina. Compared to GOES-VAS, the improved spatial resolution available with GOES-8 provides much greater detail concerning fire activity and other surface features. During SCAR-B smoke was evident over a large portion of the continent east of the Andes Mountains in the GOES visible images. A large smoke pall covering over 4 million km^2 was observed from 21 August through 11 September. Figure 7.8 indicates that at the height of this burning period the smoke pall extended over nearly 7 million km^2. Transport over the Atlantic Ocean was observed on 13 days during the SCAR-B field programme. On at least two days a thin plume of smoke was tracked to the Prime Meridian.

Table 7.1:

Surface Skin Temperature regression relationships expressed as a Linear Combination of Infrared Window Brightness Temperatures, $Ts = A0 + \Sigma\, Ai*Tbi + + \Sigma\, Bi*(\Delta Tbi)^2$. The root mean square (RMS) of the fit with respect to buoy reports is also indicated.

GOES Imager on GOES-8

A0	A(11.0)	A(12.0)	$B(11.0\text{-}12.0)^2$	RMS
-6.411	2.2160	-1.1900	0.2017	0.7 K

GOES Imager on GOES-9

A0	A(11.0)	A(12.0)	$B(11.0\text{-}12.0)^2$	RMS
-6.9510	2.8200	-1.7927	0.0756	0.7 K

AVHRR on NOAA-12

A0	A(11.0)	A(12.0)	RMS
10.11	3.5428	-2.5792	0.6 K

AVHRR on NOAA-14

A0	A(11.0)	A(12.0)	RMS
-5.31	3.1569	-2.1396	0.6 K

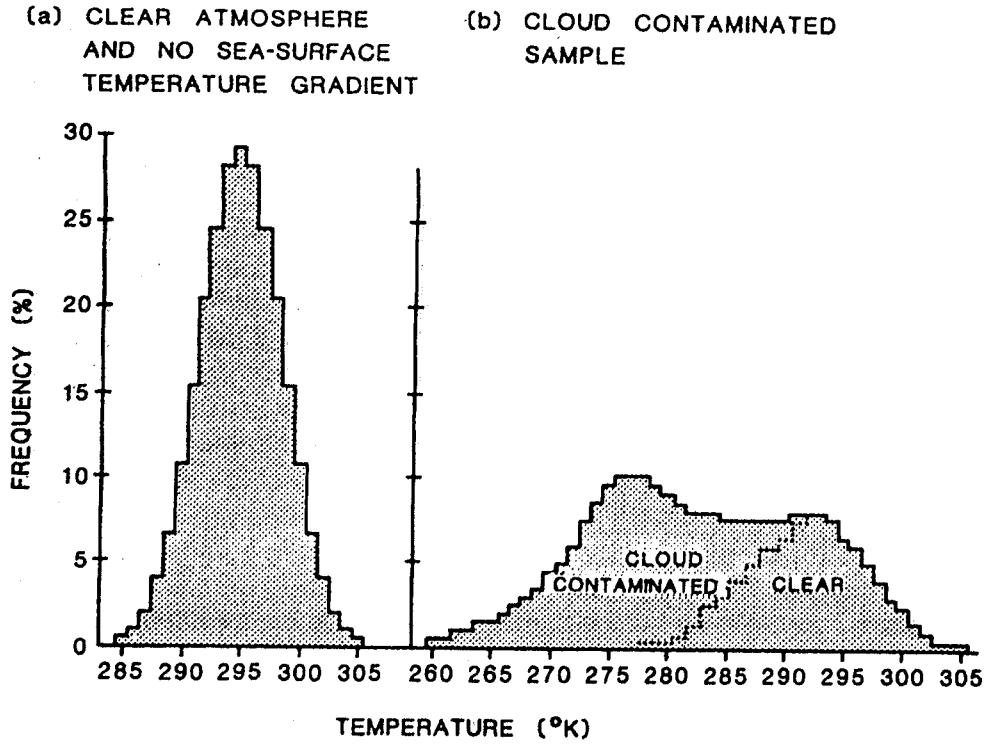

Figure 7.1: Histograms of infrared window brightness temperature in cloud free and cloud contaminated conditions.

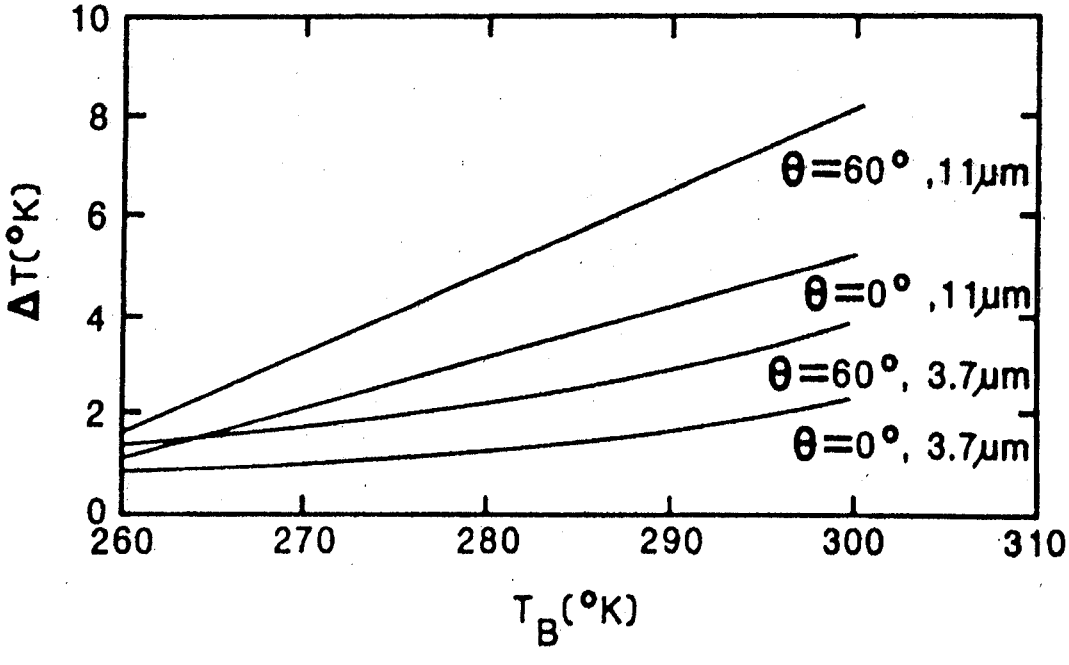

Figure 7.2a: Statistical relations of the water-vapour correction as a function of observed brightness temperature for two spectral channels and two viewing angles.

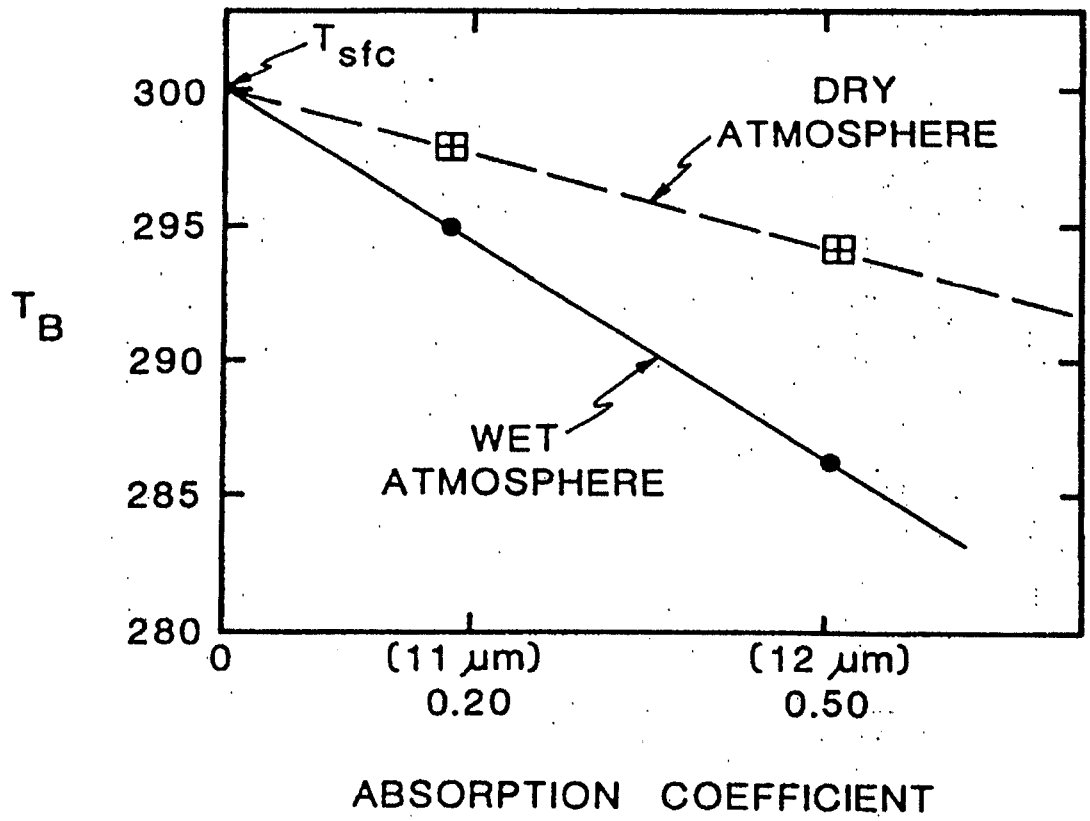

Figure 7.2b: Graphic representation of the linear relation between water vapour attenuation and brightness temperature for two different atmospheric conditions.

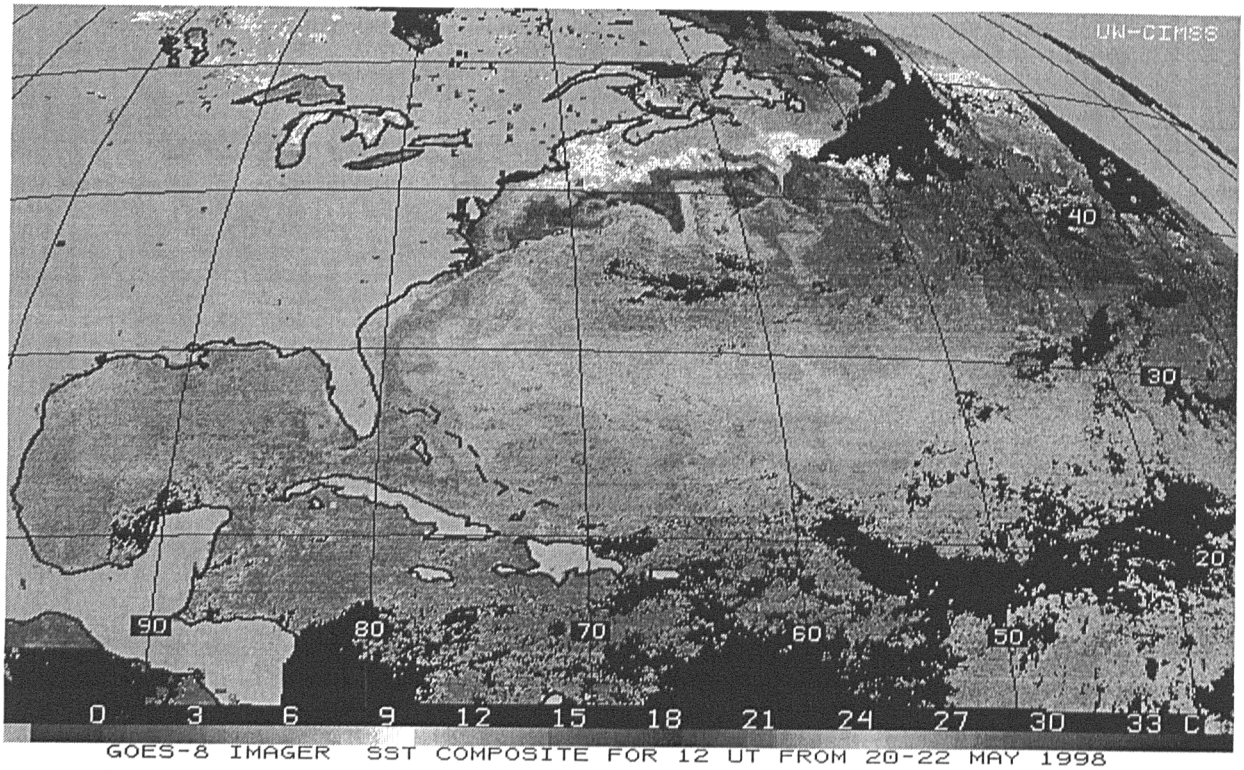

Figure 7.3a: Three-day composite of 1200 UTC GOES SST (early morning), May 20-22, 1998.

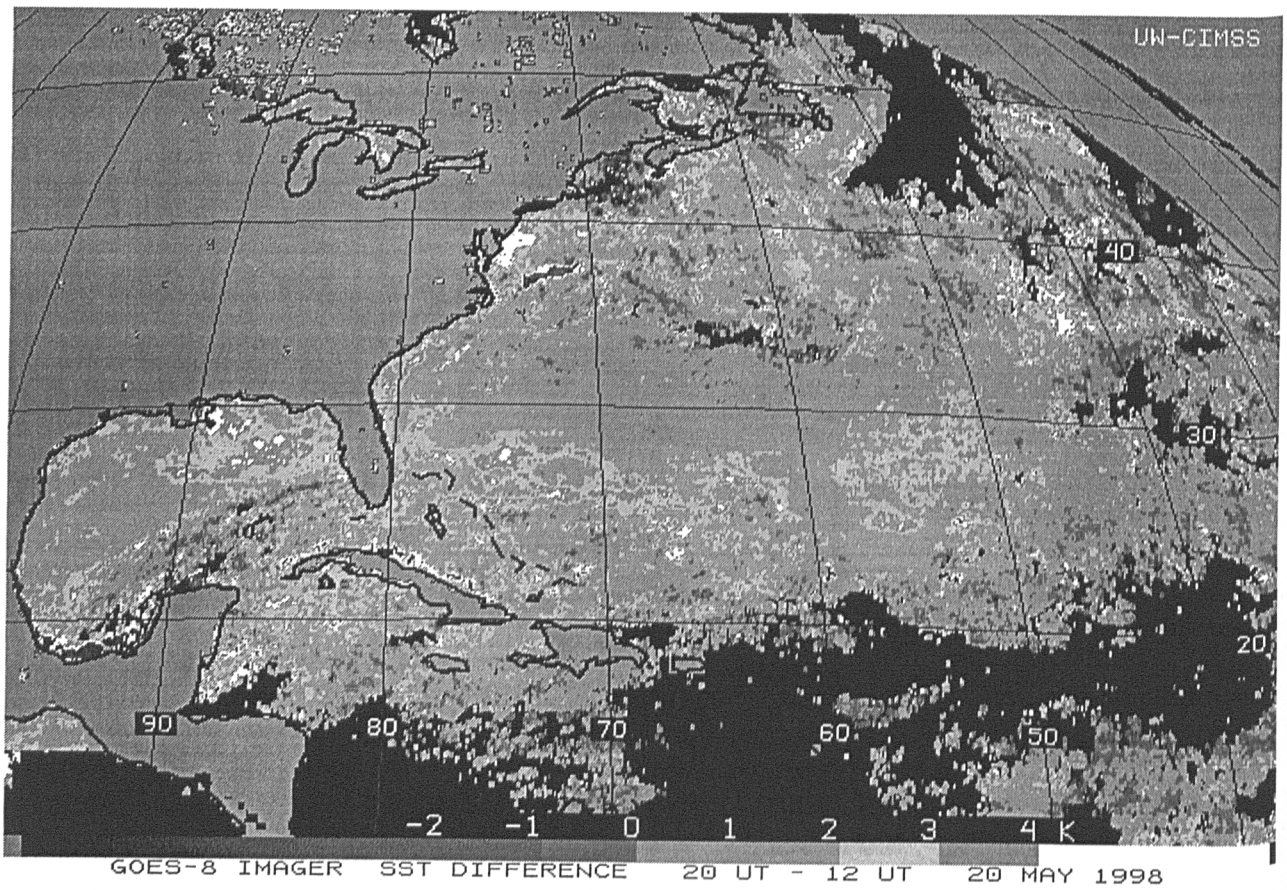

Figure 7.3b: Three-day composite of the difference in the GOES SST at 2000 UTC (afternoon) and 1200 UTC (early morning) for May 20-22, 1998. Differences greater than 3 K occur in clear skies in the tropics where the surface winds are less than 5 m/s (hence the ocean is relatively smooth).

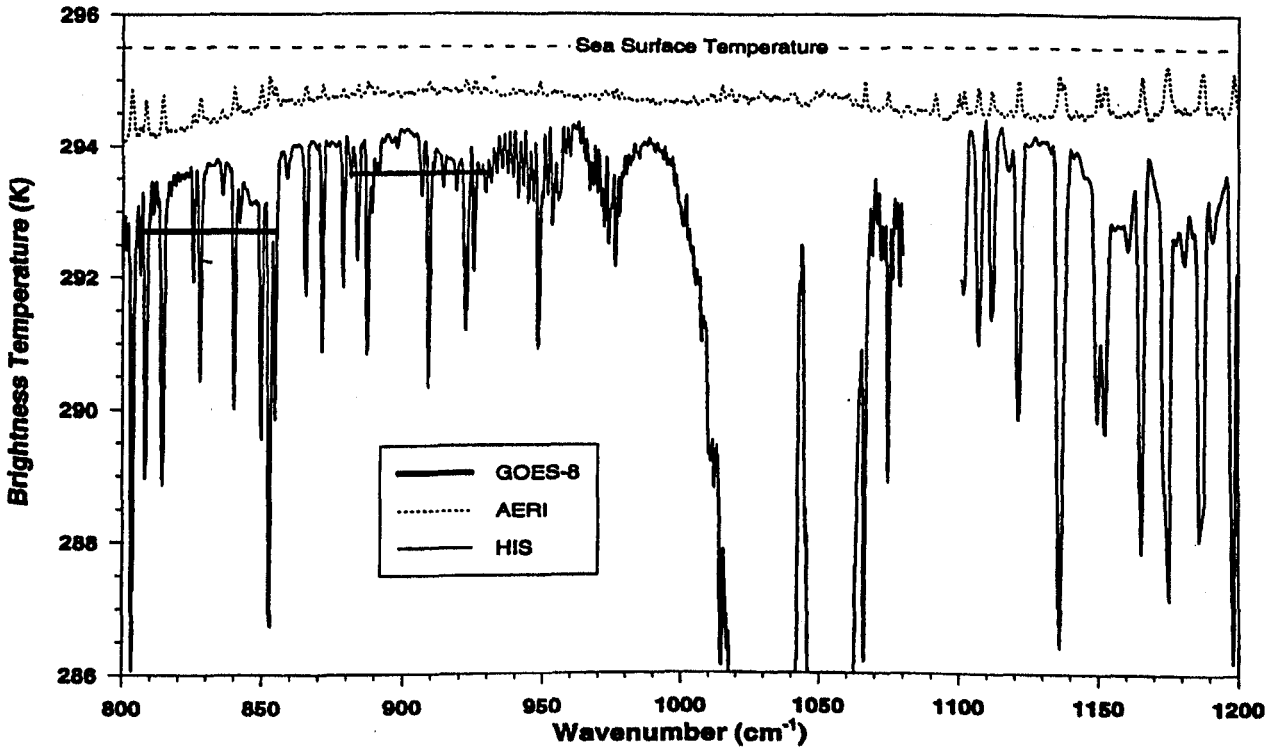

Figure 7.4: Comparison of ocean brightness temperatures measured by a ship borne interferometer (AERI), by an interferometer (HIS) on an aircraft at 20 km altitude, and the geostationary sounder (GOES-8). Corrections for atmospheric absorption of moisture, non-unit emissivity of the sea surface, and reflection of the atmospheric radiance from the sea surface have not been made.

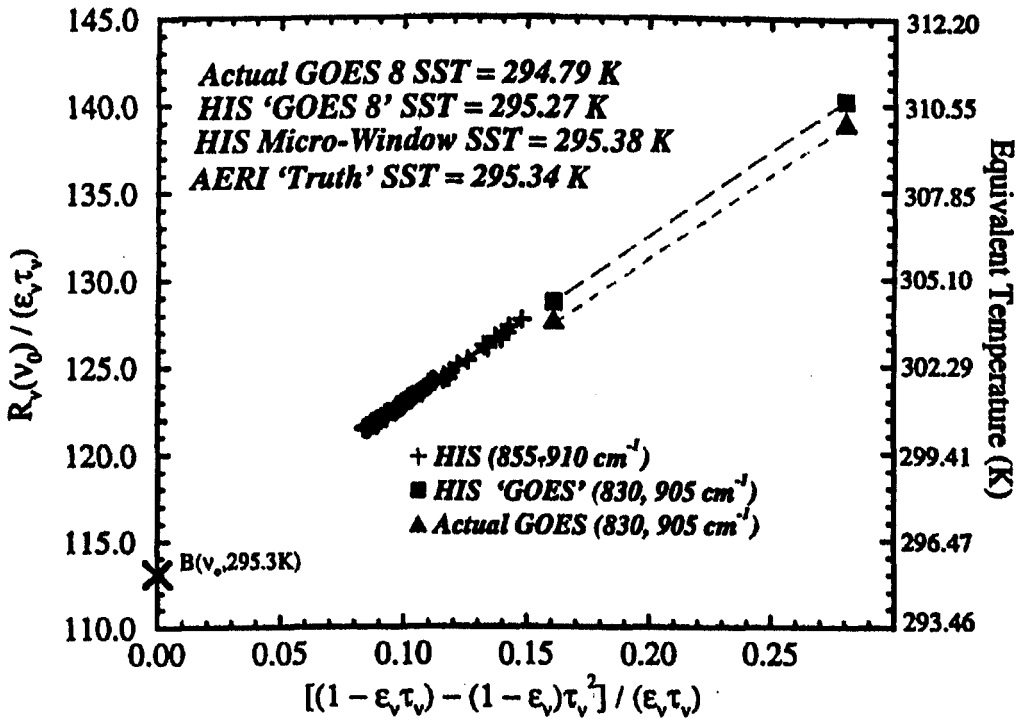

Figure 7.5: HIS and GOES radiance observations plotted in accordance with the radiative transfer equation including corrections for atmospheric moisture, non-unit emissivity of the sea surface, and reflection of the atmospheric radiance from the sea surface. Radiances are referenced to 880 cm-1. The intercept of the linear relationship for each data set represents a retrieved surface skin blackbody radiance from which the SST can be retrieved.

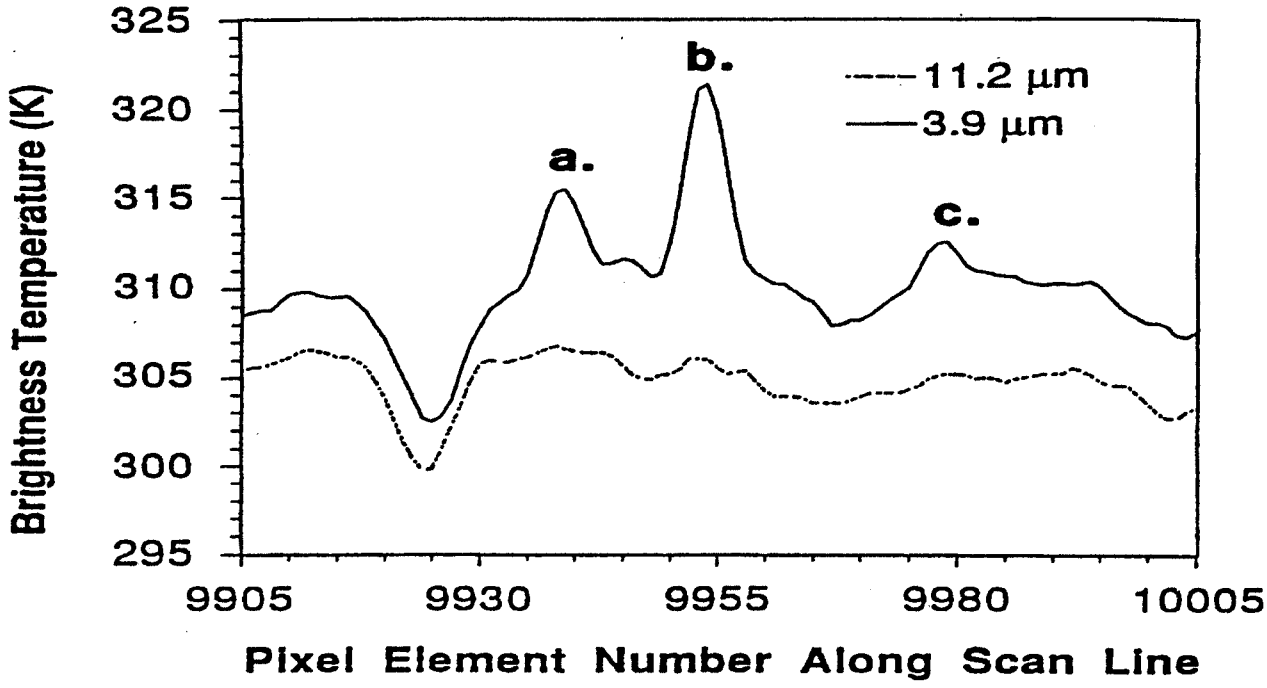

Figure 7.6: GOES VAS brightness temperatures at 3.9 and 11.2 microns plotted for one scan line over grassland burning in South America.

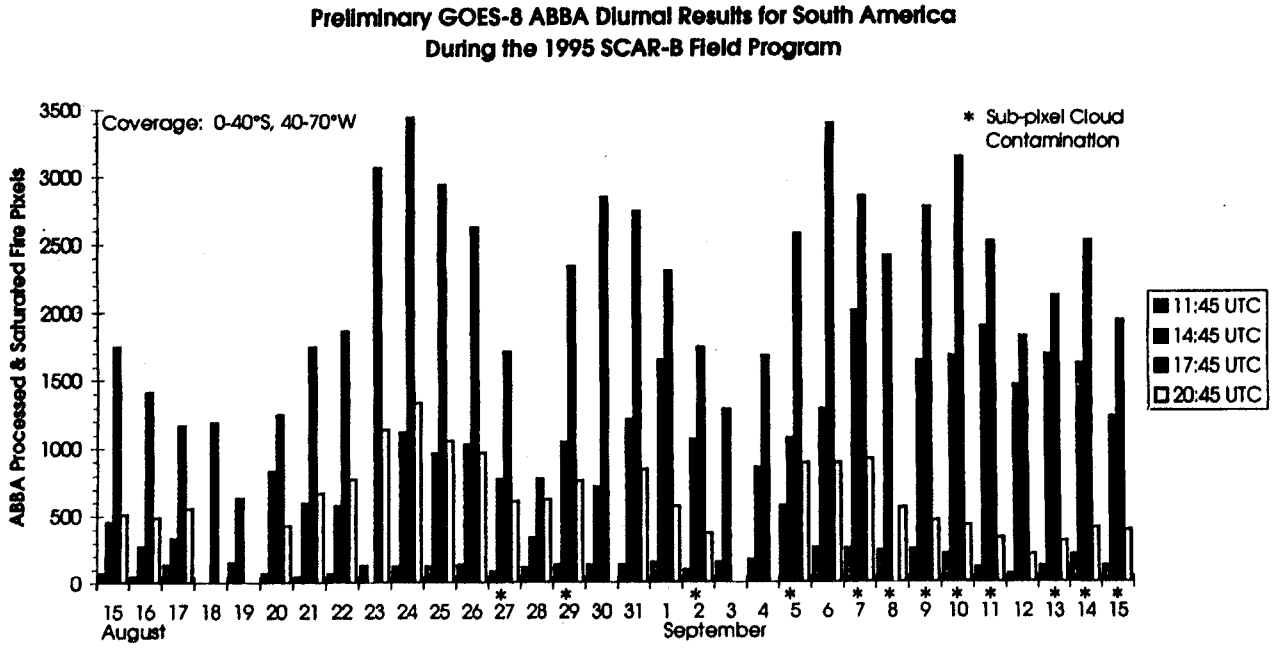

Figure 7.7: Diurnal Variation in the detection of biomass burning in South America with GOES-8 in August-September 1995. Prominent daily peak at 1745 UTC is evident.

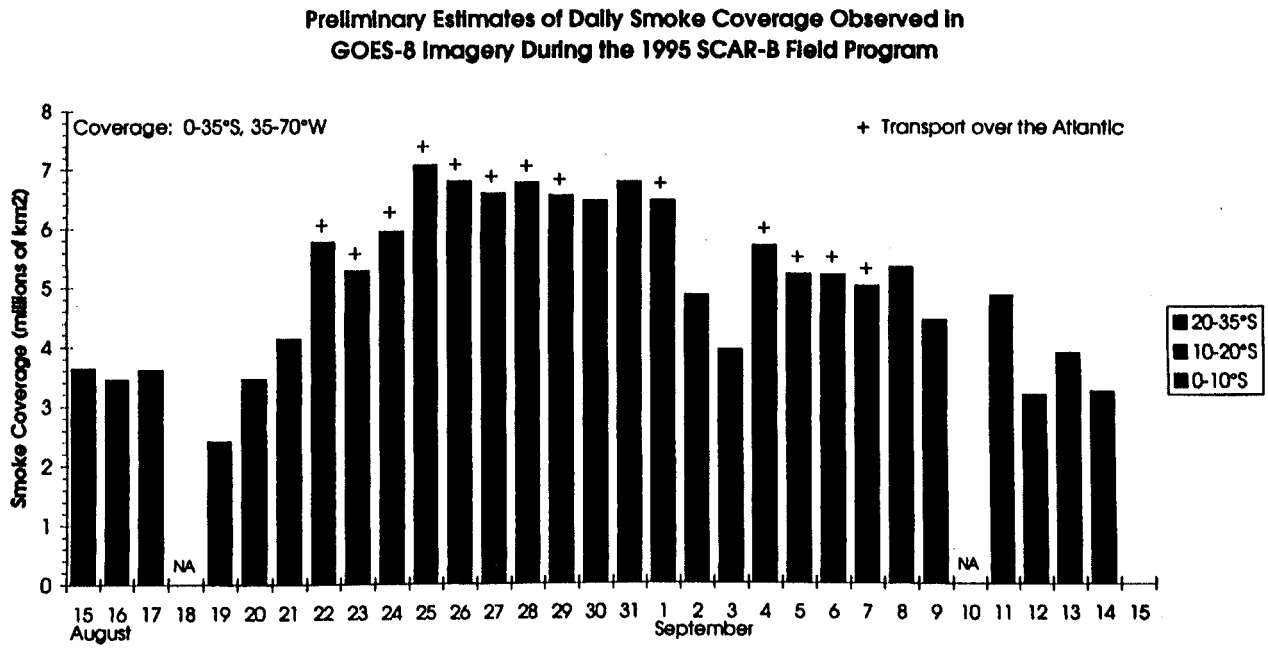

Figure 7.8: Estimates of daily smoke coverage over South America observed in GOES-8 visible imagery during August-September 1995.

CHAPTER 8

TECHNIQUES FOR DETERMINING ATMOSPHERIC PARAMETERS

8.1 Total Water Vapour Estimation

8.1.1 Split Window Method

The split window method can be used to specify total water vapour concentration from clear sky 11 and 12 micron brightness temperature measurements. In the previous derivation in section 7.2, it was shown that for a window channel

$$u_s = \frac{T_{bw} - T_s}{k_w (\bar{T}_w - T_s)}$$

Obviously, the accuracy of the determination of the total water vapour concentration depends upon the contrast between the surface temperature, T_s, and the effective temperature of the atmosphere, $\bar{T}_w$. In an isothermal situation, the total precipitable water vapour concentration is indeterminate. The split window approximation allows us to write

$$T_s = \frac{k_{w2}T_{bw1} - k_{w1}T_{bw2}}{k_{w2} - k_{w1}}$$

and if we express $\bar{T}_w$ as proportional to T_s

$$\bar{T}_w = a_w T_s ,$$

then a solution for u_s follows:

$$u_s = \frac{T_{bw2} - T_{bw1}}{(\alpha_{w1}-1)(k_{w2}T_{bw1} - k_{w1}T_{bw2})}$$

$$= \frac{T_{bw2} - T_{bw1}}{\beta_1 T_{bw1} - \beta_2 T_{bw2}}$$

The coefficients β_1 and β_2 can be evaluated in a linear regression analysis from prescribed temperature and water vapour profile conditions coincident with in situ observations of u_s. The weakness of the method is due to the time and spatial variability of α_w and the insensitivity of a stable lower atmospheric state when $T_{bw1} \sim T_{bw2}$ to the total precipitable water vapour concentration.

8.1.2 Split Window Variance Ratio

Following the procedure outlined for the split window moisture correction for SST of Chapter 6, we now develop the technique known as the Split Window Variance Ratio for estimating the total precipitable water vapour in an atmospheric column over one fov. Recall that for atmospheric windows with minimal moisture absorption, we write

$$I_w = B_{sw}\,(1-k_w u_s) + k_w u_s \bar{B}_w\,.$$

Consider neighbouring fovs and assume that the air temperature is invariant, then the gradients can be written

$$\Delta I_w = \Delta B_{sw}\,(1-k_w u_s)$$

where Δ indicates the differences due to different surface temperatures in the two fovs. Convert to brightness temperatures with a Taylor expansion with respect to one of the surface temperatures, so that

$$[I_w(fov1)-I_w(fov2)] = [B_{sw}(fov1)-B_{sw}(fov2)](1-k_w u_s)$$

$$[T_w(fov1)-T_w(fov2)] = [T_s(fov1)-T_s(fov2)](1-k_w u_s)\,.$$

Using the split windows we can arrive at an estimate for u_s in the following way. Write the ratio

$$\frac{1-k_{w1}u_s}{1-k_{w2}u_s} = \frac{dI_{w1}\,dB_{sw2}}{dI_{w2}\,dB_{sw1}}$$

$$\frac{1-k_{w1}u_s}{1-k_{w2}u_s} = \frac{[I_{w1}(fov1)-I_{w1}(fov2)]\,[B_{sw2}(fov1)-B_{sw2}(fov2)]}{[I_{w2}(fov1)-I_{w2}(fov2)]\,[B_{sw1}(fov1)-B_{sw1}(fov2)]}$$

$$\frac{1-k_{w1}u_s}{1-k_{w2}u_s} = \frac{[T_{w1}(fov1)-T_{w1}(fov2)]\,[T_s(fov1)-T_s(fov2)]}{[T_{w2}(fov1)-T_{w2}(fov2)]\,[T_s(fov1)-T_s(fov2)]}$$

$$\frac{1-k_{w1}u_s}{1-k_{w2}u_s} = \frac{[T_{w1}(fov1)-T_{w1}(fov2)]}{[T_{w2}(fov1)-T_{w2}(fov2)]}$$

since the surface temperature cancels out. Therefore

$$\frac{1-k_{w1}u_s}{1-k_{w2}u_s} = \frac{\Delta T_{w1}}{\Delta T_{w2}}$$

or

$$u_s = (1 - \Delta_{12})/(k_{w1} - k_{w2}\Delta_{12}),$$

where Δ_{12} represents the ratio of the deviations of the split window brightness temperatures. The deviation is often determined from the square root of the variance.

The assumption in this technique is that the difference in the brightness temperatures from one fov to the next is due only to the different surface temperatures. It is best applied to an instrument with relatively good spatial resolution, so that sufficient samples can be found in an area with small atmospheric variations and measurable surface variations in order to determine the variance of the brightness temperatures accurately. The technique was suggested by the work of Chesters *et al*

(1983) and Kleespies and McMillin (1986); Jedlovec (1990) successfully applied it to aircraft data with 50 meter resolution to depict mesoscale moisture variations preceding thunderstorm development.

8.1.3 Perturbation of Split Window RTE

The total precipitable water vapour and the surface temperature can be determined from split window observations of a scene. Assuming that the temperature profile is well known for a given fov (so that δT is zero), then the perturbation form of the radiative transfer equation (see section 5.8.2 of Chapter 5) can be written

$$\delta T_b = \delta T_s \left[\frac{\partial B_s}{\partial T_s} / \frac{\partial B}{\partial T_b} \right] \tau_s + \delta u_s \int_o^{p_s} \frac{\partial \tau}{\partial u} \left[\frac{\partial B}{\partial p} / \frac{\partial B}{\partial T_b} \right] dp$$

which reduces to the form

$$\delta T_b = a\, \delta T_s + b\, \delta u_s .$$

where a and b are calculable from the initial guess. The split window offers two equations and the two unknowns T_s and u_s are readily solved.

This technique is very dependent on the accurate absolute calibration of the instrument.

8.1.4 Microwave Split Window Estimation of Atmospheric Water Vapour and Liquid Water

One can derive atmospheric water information from channels with frequencies below 40 GHz in the microwave spectrum. The 22.2 GHz channel has modest water vapor sensitivity and the 31.4 GHz channel has window characteristics; the two together are considered the microwave split window (analogous to the 11 and 12 micron infrared split window). Recalling the microwave form of the radiative transfer equation,

$$T_{b\lambda} = \varepsilon_{\lambda s} T_s(p_s)\, \tau_\lambda(p_s) + \int_{p_s}^{o} T(p)\, F_\lambda(p) \frac{\partial \tau_\lambda(p)}{\partial \ln p}\, d \ln p$$

where

$$F_\lambda(p) = \{ 1 + (1 - \varepsilon_\lambda) \left[\frac{\tau_\lambda(p_s)}{\tau_\lambda(p)} \right]^2 \} ,$$

one can write for the microwave windows

$$T_{b\lambda} = \varepsilon_{\lambda s} T_s \tau_{\lambda s} + T_A [1 - \tau_{\lambda s} - (1 - \varepsilon_{\lambda s})\, \tau_{\lambda s}^2 + (1 - \varepsilon_{\lambda s})\, \tau_{\lambda s}]$$

where T_A represents an atmospheric mean temperature. Using $\tau_{\lambda s} \sim 1 - a_\lambda$ and $\tau_{\lambda s}^2 \sim 1 - 2a_\lambda$ in he window regions (where water absorption a_λ is small), this reduces to

$$T_{b\lambda} = \varepsilon_{\lambda s} T_s\, \tau_{\lambda s} + T_A [1 - \varepsilon_{\lambda s} \tau_{\lambda s} - \tau_{\lambda s}^2 + \varepsilon_{\lambda s} \tau_{\lambda s}^2] ,$$

$$T_{b\lambda} = \varepsilon_{\lambda s} T_s\, (1 - a_\lambda) + T_A [1 - \varepsilon_{\lambda s} (1 - a_\lambda) - (1 - 2a_\lambda) + \varepsilon_{\lambda s} (1 - 2a_\lambda)] ,$$

$$T_{b\lambda} = \varepsilon_{\lambda s} T_s\, (1 - a_\lambda) + a_\lambda T_A [2 - \varepsilon_{\lambda s}] .$$

But for low layers of moisture detected in the split window $T_s \sim T_A$, so

$$T_{b\lambda} = \varepsilon_{\lambda s} T_s + 2\, a_\lambda T_s [1 - \varepsilon_{\lambda s}] .$$

Writing $\tau_{\lambda s}$ = $\tau_{\lambda s}$ (liquid) $\tau_{\lambda s}$ (vapor) ~ [1-Q/Qo] [1- U/Uo], where Q is the total liquid concentration with respect to reference Qo and U is the total vapor concentration with respect to reference Uo, we get

$$T_{b\lambda} = \varepsilon_{\lambda s} T_s + 2\, T_s [1 - \varepsilon_{\lambda s}]\, [Q/Qo + U/Uo].$$

If $\varepsilon_{\lambda s}$ and T_s are known, then measurements in the microwave split window offer solutions for Q and U (2 equations and 2 unknowns). Over oceans where the surface temperature and emissivity are reasonably well known and uniform, Q and U can be determined within 10%; over land reliable solutions remain elusive.

8.2 Total Ozone Determination

Ozone is an important atmospheric constituent found in the atmosphere between 10 and 50 km above the earth's surface. Because it absorbs ultraviolet rays from the sun, ozone protects man from the harmful effects of ultraviolet radiation. Also, ozone is a prime source of thermal energy in the low stratosphere and has been shown to be a useful tracer for stratospheric circulation. Prabhakara *et al,* (1970) have exploited remote sensing of the total ozone using satellite infrared emission measurements and their studies reveal a strong correlation between the meridional gradient of total ozone and the wind velocity at tropopause levels. Shapiro *et al,* (1982) have indicated a possibility to predict the position and intensity of jet streams using total ozone measured by satellite.

Recently, there has been increased interest in atmospheric ozone, due primarily to its role in complex middle atmospheric photochemistry and the critical ecological effect associated with ozone depletion induced by anthropogenic impacts and natural processes. By means of satellite observations, the evolution of the "ozone hole" and its interannual variability can be detected and even predicted. The main satellite instruments used for monitoring ozone are the Total Ozone Monitoring Sensor (TOMS) (Bowman and Krueger 1985; McPeters *et al*, 1996; 1998) and the Solar Backscatter Ultraviolet (SBUV) spectrometer (Heath *et al*, 1975; 1978). In order to predict the evolution of ozone on time scales of a few days to a week, reliable global measurements of the three-dimensional distribution of ozone are needed. However, neither the TOMS nor the SBUV can provide measurements at night; infrared (IR) radiance measurements as well as microwave limb sounders can. This section discusses infrared detection of ozone.

8.2.1 Total Ozone from Numerical Iteration

Ma *et al (1983) suggested a method for obtaining total ozone with high spatial resolution from* the TIROS-N/NOAA series of satellites. The ozone concentration is mapped with the 9.6 μm ozone radiance observations by the High-resolution Infrared Radiation Sounder (HIRS). The meteorological inferences have a resolution of 75 km. The influence of clouds must be screened out to produce reliable ozone determinations.

Ozone concentration is related to radiance to space through the transmittance $\tau_\lambda(p)$. As shown in the water vapour profile solution, using a first order Taylor expansion of Planck function in terms of temperature and integrating the RTE by parts, yields the expression

$$T_{b\lambda} - T_{b\lambda}^{(n)} = \int_o^{p_s} [\tau_\lambda(p) - \tau_\lambda^{(n)}(p)]\; X_\lambda(p)\, \frac{dp}{p}$$

where $T_{b\lambda}$ is the measured brightness temperature, $T_{b\lambda}^{(n)}$ is the brightness temperature calculated for a n^{th} estimate of the ozone profile, $\tau_\lambda^{(n)}(p)$ is the corresponding transmittance profile, and

$$X_\lambda(p) = \left[\frac{\partial B_\lambda(T)}{\partial T}\Big|_{T=T_{av}} \Big/ \frac{\partial B_\lambda(T)}{\partial T}\Big|_{T=T_{b\lambda}} \right] \frac{\partial T(p)}{\partial \ln p}$$

Using the mathematical derivation used for water vapour retrieval, one can relate the brightness temperature measured by HIRS in the ozone 9.6 μm band to the ozone concentration, v(p):

$$T_{b\lambda} - T_{b\lambda}^{(n)} = \int_o^{p_s} \ln \frac{v(p)}{v^{(n)}(p)} Z_\lambda^{(n)}(p) \frac{dp}{p}$$

where

$$Z_\lambda^{(n)}(p) = \tau_\lambda^{(n)}(p) \ln \tau_\lambda^{(n)}(p) X_\lambda \ .$$

As suggested by Smith's generalized iteration solution, we assume that the correction to the ozone concentration $v(p) - v^{(n)}(p)$ is independent of p, so that

$$\frac{v(p)}{v^{(n)}(p)} = \exp\left[\frac{T_{b\lambda} - T_{b\lambda}^{(n)}}{\int_o^{p_s} Z_\lambda^{(n)}(p) \frac{dp}{p}} \right] = \gamma_\lambda^n$$

Consequently, for every pressure level, one can use this iterative procedure to estimate the true ozone concentration profile

$$v^{(n+1)}(p_j) = v^{(n)}(p_j) \gamma_\lambda^n$$

Convergence is achieved as soon as the difference between the measured ozone brightness temperature and that calculated is less than the measurement noise level (approximately 0.2 C). The first guess ozone profile is constructed using regression relations between the ozone concentration and the infrared brightness temperature observations of stratospheric carbon dioxide emission and the microwave brightness temperatures observations of stratospheric and tropospheric oxygen emission to space. Since ozone is a prime source of thermal energy in the low stratosphere and the upper troposphere, there is excellent correlation between the ozone concentration and the brightness temperatures observed in the HIRS carbon dioxide and MSU oxygen channels. Due to the fact that ozone and temperature sounding data yield good statistics only up to 10 mb (about 30 km), above 10 mb the ozone and temperature profiles are extrapolated using the lapse rate of USA standard ozone and temperature profiles between 10 mb and 0.1 mb (up to about 50 km). Above 50 km, the ozone contribution to the outgoing radiance is negligible.

The profile shape and the vertical position of the peak ozone mixing ratio corresponding to the ozone guess profile is crucial to obtaining a satisfactory retrieval since only one ozone channel radiance in the 9.6 μm band is used. This is because the true ozone profile is assumed to have the same shape as the first guess. Therefore, to make the ozone guess profile sufficiently accurate in both shape and position of the ozone peak mixing ratio, adjustments to the vertical position and amplitude of the guess peak mixing ratio are made based on the difference between the observed brightness temperature and the calculated brightness temperature using the ozone guess profile.

8.2.2 Physical Retrieval of Total Ozone

Another approach to retrieving the total column ozone concentration is found in the perturbation form on the RTE. Assuming that the temperature and moisture profiles as well as the surface temperature are well known for a given FOV, then the perturbation form of the radiative transfer equation reduces to

$$\delta T_{oz} = \int_o^{p_s} \delta\tau \frac{\partial T}{\partial p} \left[\frac{\partial B}{\partial T} \Big/ \frac{\partial B}{\partial T_{oz}} \right] dp$$

where T_{oz} is the 9.6 μm brightness temperature. Finally, assume that the transmittance perturbation is dependent only on the uncertainty in the column of ozone density weighted path length *v* according to the relation

$$\delta\tau = \frac{\partial T}{\partial v}\,\delta v$$

Thus

$$\delta T_{oz} = \int_0^{p_s} \delta v \frac{\partial T}{\partial p} \frac{\partial \tau}{\partial v} \left[\frac{\partial B}{\partial T} \Big/ \frac{\partial B}{\partial T_{oz}}\right] dp = f[\delta v]$$

where f represents some function.

As in the profile retrieval, the perturbations are with respect to some a priori condition which may be estimated from climatology, regression, or more commonly from an analysis or forecast provided by a numerical model. In order to solve for δv from the 9.6 μm radiance observations δT_{oz}, the perturbation profile is represented in terms of the 9.6 μm weighting function (used as the basis function φ(p)); so

$$\delta v = \alpha \varphi$$

where α is computed from the initial guess.

Adjustments to the vertical position and amplitude of the guess peak mixing ratio are made based on the difference between the observed brightness temperature and the calculated brightness temperature using the ozone guess profile. Specifically the vertical position is adjusted by

$$\Delta p = a + b\,(T^{cal}_{oz} - T^{obs}_{oz})$$

where a and b are dependent on latitude and are obtained from linear regression in an independent set of conventional sounding data.

Li *et al* (2000) have applied the physical algorithm to GOES Sounder data. They start with a first guess from a statistical regression of GOES sounder radiances against ozone mixing ratio profiles. The statistical algorithm consists of the following expression:

$$\ln(O_3(p)) = A_0 + \sum_{j=1}^{15} A_j Tb_j + \sum_{j=1}^{15} A_j' Tb_j^2 + C_1 p_s + C_2 \sec\theta + C_3 \cos(\frac{M-6}{12}\pi) + C_4 \cos(LAT),$$

where A, A' and C are the regression coefficients, θ is the local zenith angle of GOES FOV, M is the month from 1 to 12, and LAT is the latitude of the GOES FOV, j is the GOES band index. Since the logarithm of the water vapor mixing ratio or ozone mixing ratio is more linear to the radiance than the mixing ratio in the radiative transfer equation, $\ln(O_3(p))$ is used as a predictand in the regression. Study shows that the accuracy of ozone estimates using 15 spectral bands is better than using less spectral bands. Month and latitude are used as additional predictors since mid-stratospheric ozone is a complex function of latitude, season and temperature. In addition, atmospheric ozone variation is highly associated with stratospheric dynamics. The physical retrieval makes a modest improvement upon the regression first guess.

Figure 8.1a shows the monthly % RMSD; it is less than 8% for all months in 1998 and 1999, with a minimum in the summer. From July to September, the % RMSD is less than 5%, indicating good agreement between GOES-8 ozone estimates and TOMS ozone measurements. Figure 8.1b shows a scatter plot of co-located GOES-8 ozone estimates and TOMS ozone measurements for June 1998 and January 1999. GOES-8 ozone estimates both in summer and in winter have good correlation with TOMS measurements. Although the ozone variation in winter is larger than in summer, the GOES-8 ozone estimates capture those variations well. To ascertain the longer-term quality and tendencies of the GOES-8 ozone estimates, single-site comparisons with ground-based Dobson-Brewer measurements were performed. Figure 8.1c shows the GOES-8 total ozone estimates for Bismarck, ND (46.77°N, 100.75°W) in 1998 along with the co-located TOMS and ground-based ozone measurements. Ground-based ozone values are seen to vary from approximately 260 DU to 390 DU. Both TOMS and GOES ozone values match the range of ground-based ozone values well. However, GOES ozone estimates have larger bias and RMSD (-15.5 DU of bias and 25.4 DU of RMSD) than TOMS (-2 DU of bias and 17 DU of RMSD).

8.2.3 HIRS Operational Algorithm

An alternate approach for estimating total atmospheric column ozone follows the NOAA operational HIRS algorithm. Total ozone is separated into upper and lower stratospheric contributions. Warm ozone in the upper stratosphere would be estimated directly from the model first guess; cold ozone in the lower stratosphere is estimated directly from its effect on the 9.6 μm channel radiance. Determination of lower stratospheric ozone requires an estimate of foreground temperature T_f and background temperature T_b. T_f is estimated from the model first guess 50 mb temperature. T_b is estimated from the infrared window brightness temperature in the absence of any ozone. The effects of upper stratospheric ozone are removed from the 9.6 μm radiance value by the following extrapolation

$$R`_{oz} = [R_{oz} - A_u R(30mb)] / [1-A_u]$$

where from the model first guess we calculate

$$A_u = 0.18 \sqrt{ESU(lat)}$$

$$ESU = EQ(lat) + SW$$

$$EQ = 0.9 + 1.1 \cos(lat)$$

$$SW = DT [1 + DT (2+DT)] * [270 + lat] / 9000,$$

$$DT = LR * WA / 40$$

$$LR = T(60mb) - T(100mb) -1,$$

which is the tropopause lapse rate, and

$$WA = 2 * T(60mb) - T(30mb) - 205,$$

which is the lower stratospheric temperature anomaly. Then

$$R'_{oz} = \tau_{ls} R_b - (1 - \tau_{ls}) R_f$$

where τ_{ls} is the transmittance through the lower stratosphere, R_b is the radiance from the background, and R_f is the radiance from the foreground. Solving for τ_{ls} yields the amount of total ozone by inverting Beer's law.

8.3 Determination of Cloud Height and Effective Emissivity

The determination of cloud heights is important for many meteorological applications, especially the estimation of the pressure-altitude of winds obtained by tracing clouds from time sequenced satellite images. Several methods for determining cloud heights using satellite data have been developed over the years. One method (Fritz and Winston, 1962) compares the infrared window channel brightness temperature with a vertical temperature profile in the area of interest to obtain the height of the cloud. This infrared window cloud height determination assumes the cloud is opaque and fills the satellite instruments field-of-view, and thus it works fine for dense stratoforms of cloud. However, it is inaccurate for semi-transparent cirrus clouds and small element cumulus clouds. A second method (Mosher, 1976; Reynolds and Vonder Haar, 1977) improves the infrared window channel estimate of cloud top height by allowing for fractional cloud cover and by estimating the cloud emissivity from visible reflectance data. Using a multiple scattering model, the visible brightness of the cloud is used to calculate the optical thickness, from which the infrared emissivity of the cloud can be computed. Although this bi-spectral method is an improvement over the first method, it is still inaccurate for semi-transparent cirrus clouds. A third method utilizes stereographic observations of clouds from two simultaneously scanning geosynchronous satellites (Hasler, 1981). These stereo height measurements depend only on straightforward geometrical relationships and offer more reliable values than the previously discussed infrared-based methods. However, the stereo method is limited to the overlap region of the two satellites and to times when simultaneous measurements can be orchestrated.

The CO_2 absorption method enables one to assign a quantitative cloud top pressure to a given cloud element using radiances from the CO_2 spectral bands. Recalling that the radiance from a partly cloudy air column region by

$$I_\lambda = \eta\, I_\lambda^{cd} + (1-\eta)\, I_\lambda^{cl}$$

where η is the fractional cloud cover, I_λ^{cd} is the radiance from the cloud obscured field of view, and I_λ^{cl} is the radiance from a clear field of view for a given spectral band λ. The cloud radiance is given by

$$I_\lambda^{cd} = \varepsilon_\lambda\, I_\lambda^{bcd} + (1-\varepsilon_\lambda)\, I_\lambda^{cl}$$

where ε_λ is the emissivity of the cloud, and I_λ^{bcd} is the radiance from a completely opaque cloud (black cloud). Using the RTE, we can write

$$I_\lambda^{cl} = B_\lambda(T(p_s))\, \tau_\lambda(p_s) + \int_{p_s}^{o} B_\lambda(T(p))\, d\tau_\lambda\,,$$

$$I_\lambda^{bcd} = B_\lambda(T(p_c))\, \tau_\lambda(p_c) + \int_{p_c}^{o} B_\lambda(T(p))\, d\tau_\lambda\,.$$

where p_c is the cloud top pressure. Integrating by parts and subtracting the two terms we get

$$I_\lambda^{cl} - I_\lambda^{bcd} = \int_{p_c}^{p_s} \tau_\lambda(p)\, dB_\lambda$$

therefore

$$I_\lambda^{cl} - I_\lambda = \eta\varepsilon_\lambda \int_{p_s}^{p_c} \tau_\lambda(p)\, dB_\lambda\,,$$

where $\eta\varepsilon_\lambda$ is often called the effective cloud amount. The ratio of the deviations in cloud produced radiances and corresponding clear air radiances for two spectral channels, λ_1 and λ_2, viewing the same field of view can thus be written

$$\frac{I^{cl}_{\lambda 1} - I_{\lambda 1}}{I^{cl}_{\lambda 2} - I_{\lambda 2}} = \frac{\varepsilon_{\lambda 1} \int_{p_s}^{p_c} \tau_{\lambda 1}(p)\, dB_{\lambda 1}}{\varepsilon_{\lambda 2} \int_{p_s}^{p_c} \tau_{\lambda 2}(p)\, dB_{\lambda 2}}$$

If the wavelengths are chosen close enough together, then $\varepsilon_1 = \varepsilon_2$, and one has an expression by which the pressure of the cloud within the field of view (FOV) can be specified.

The left side can be determined from radiances observed by the sounder (HIRS and the GOES Sounder) and clear air radiances calculated from a known temperature and moisture profile. Alternatively, the clear air radiances could be provided from spatial analyses of HIRS or GOES Sounder clear sky radiance observations. The right side is calculated from known temperature profile and the profiles of atmospheric transmittance for the spectral channels as a function of P_c, the cloud top pressure. The optimum cloud top pressure is determined when the absolute difference [right $(\lambda_1,\lambda_2,)$ - left $(\lambda_1,\lambda_2,P_c)$] is a minimum.

These are two basic assumptions inherent in this method: (a) the cloud has infinitesimal thickness; and (b) the cloud emissivity is the same for the two spectral channels. The maximum possible error caused by assumption (a) is one-half the cloud thickness. Errors approaching one-half the cloud thickness occur for optically thin clouds (integrated emissivity roughly less than .6); for optically thick clouds (integrated emissivity roughly greater than .6) the error is small, typically one-fourth the cloud thickness or less. Errors due to assumption (b) can be minimized by utilizing spectrally close channels.

Once a cloud height has been determined, an effective cloud amount can be evaluated from the infrared window channel data using the relation

$$\eta\varepsilon_w = \frac{I_w - I_w^{cl}}{B_w(T(p_c)) - I_w^{cl}}$$

where w represents the window channel wavelength, and $B_w(T(p_c))$ is the window channel opaque cloud radiance.

Using the ratios of radiances of the three to four CO_2 spectral channels on the polar or geostationary sounder, two to three separate cloud top pressures can be determined (for example 14.2/14.0 and 14.2/13.3). If $(I_\lambda - I_\lambda^{cl})$ is within the noise response of the instrument (roughly 1 mw/m^2/ster/cm^{-1}) the resulting p_c is rejected. Using the infrared window and the two cloud top pressures, two effective cloud amount determinations are made. To select the most representative cloud height P_{ck}, the algorithm checks the differences between the observed values of $(I_\lambda - I_\lambda^{cl})$ and those calculated from the radiative transfer equations for the two possible cloud top pressures and effective cloud amounts,

$$[(I - I^{cl})_\lambda - \eta\varepsilon_k \int_{p_s}^{p_{ck}} \tau_\lambda\, dB_\lambda] = M_{\lambda k}\,.$$

P_{ck} is chosen when

$$\sum_{\lambda=1} M_k^2$$

is a minimum, where the sum is over the CO_2 channels needed to derive the cloud top pressure values.

If neither ratio of radiances (14.2/14.0 or 14.0/13.3) can be reliably calculated because the cloud induced radiance difference ($I - I^{ch}$) is within the instrument noise level, then a cloud top pressure is calculated directly for the sounder observed 11.2 μm infrared window channel brightness temperature and the temperature profile. In this way, all clouds can be assigned a cloud top pressure either by CO_2 absorption or by infrared window calculations.

Menzel *et al,* (1983) utilized the CO_2 absorption method to make several comparisons of cloud heights determined by different techniques; the comparisons were randomly made over several different cloud types including thin cirrus clouds. The CO_2 heights were found to be reliable within about a 50 mb root mean square deviation of other available height determinations. The CO_2 heights produced consistently good results over thin cirrus where the bi-spectral heights were inconsistent. This is demonstrated in Fig. 8.2, where bi-spectral and CO_2 heights are plotted along a cirrus anvil blowing off the top of a thunderstorm at 1348 GMT 14 July 1982 over western Missouri and eastern Kansas. As one moves away from the dense cumulus clouds towards the thin cirrus, the CO_2 absorption method maintains high altitudes while the bi-spectral method frequently underestimates the altitude by varying amounts depending on the thinness of the cirrus clouds.

The considerable advantage of the CO_2 absorption method is that it is not dependent on the fractional cloud cover or the cloud emissivity (in fact, the effective cloud amount is a by-product of the calculations).

8.4 Geopotential Height Determination

The geopotential Φ at any point in the atmosphere is defined as the work that must be done against the earth's gravitational field in order to raise a mass of 1 kg from sea level to that point. In other words, Φ is the gravitational potential for unit mass. The units of geopotential are 1 kg^{-1} or $m^2 s^2$. The force (in newtons) acting on 1 kg at height z above sea level is numerically equal to g. The work (in joules) in raising 1 kg from z to z+dz is g dz; therefore,

$$d\Phi = g\,dz = -\alpha\,dp$$

where a is the reciprocal of the density of air. The geopotential $\Phi(z)$ at height z is thus given by

$$\Phi(z) = \int_0^z g\,dz$$

where the geopotential $\Phi(0)$ at sea level (z = 0) has, by convention, been taken as zero. It should be emphasized that the geopotential at a particular point in the atmosphere depends only on the height of that point and not on the path through which the unit mass is taken in reaching that point. The work done in taking a mass of 1 kg from point A with geopotential Φ_A to point B with geopotential Φ_B is $\Phi_B - \Phi_A$.

We can also define a quantity called the geopotential height Z as

$$Z = \frac{\Phi(z)}{g_o} = \frac{1}{g_o}\int_0^z g\,dz$$

where g_o is the globally averaged acceleration due to gravity at the earth's surface (taken as 9.8 ms^{-2}). Geopotential height is used as the vertical coordinate in most atmospheric applications in which

energy plays an important role. It can be seen from Table 8.1 that the values of z and Z are almost the same in the lower atmosphere where $g_o \sim g$.

From the ideal gas law and the hydrostatic equation, we are able to write

$$\frac{dp}{dz} = -\frac{pg}{RT}$$

so that

$$\Phi_2 - \Phi_1 = -R \int_{p_1}^{p_2} T \frac{dp}{p}$$

or

$$Z_2 - Z_1 = \frac{R}{g_o} \int_{p_2}^{p_1} T \frac{dp}{p}.$$

Therefore, having derived a temperature profile from sounding radiance measurements, it is possible to determine geopotential heights (or thicknesses). It is readily apparent that the thickness of the layer between any two pressure levels p_2 and p_1 is proportional to the mean temperature of the layer; as T increases the air between the two pressure levels expands so that the layer becomes thicker.

Geopotential heights and thicknesses are being processed routinely from GOES soundings. Comparison with conventional radiosonde and dropwindsonde determinations for 1982-83 are shown in Table 8.2 for 1982-83. Most comparisons were made with the raobs at 1200 GMT wherever GOES soundings were sufficiently close in space and time (within approximately two hours and 100 km). Thickness derived from GOES temperature soundings showed a mean difference of only 10-30 metres when compared with raobs and 5-10 metres when compared with dropsondes.

Geopotential thickness are also routinely evaluated from the TIROS polar orbiters, but here the 850-500 and 850-200 mb layers are estimated from a linear combination of the four MSU brightness temperature observations. Regression coefficients are determined from an analysis of radiosonde data. The 850-500 and 850-200 mb thicknesses are useful for weather forecasting, since contour analyses of these quantities describe the direction and speed of the circulation at mid-tropospheric and jet stream levels, respectively. The accuracies of the MSU derived thicknesses are comparable to the accuracies experienced with the GOES derived heights and thicknesses. Figure 8.3 shows an example comparison of the NOAA-6 MSU estimates of the 850-500 and 850-200 mb thickness patterns with those obtained from radiosonde observations. The patterns are very similar.

8.5 Microwave Estimation of Tropical Cyclone Intensity

It has been observed that the upper tropospheric temperature structure of tropical cyclones is characterized by a well-defined warm temperature anomaly at upper levels in well-developed storms. An intense tropical cyclone with an eye produced by subsidence within the upper tropospheric anticyclone develops a warm core due to adiabatic warming. One theory is the warm air produced by subsidence within the eye is entrained into the eye wall where strong upward motions transport this warmer air to high levels where it then diverges outward away from the eye region.

It has been shown to be possible to monitor the intensity of tropical cyclones as categorized by its surface central pressure and maximum sustained wind speed at the eye wall with satellite microwave observations. The relationship between surface pressure and the intensity of the warm core comes from the ideal gas law and the hydrostatic equation

$$\frac{dp}{p} = -\frac{g}{RT} dz$$

or

$$\ln\left(\frac{p_s}{p_t}\right) = \frac{g}{R}\int_o^{z_t}\frac{dz}{T}$$

where p_s is the surface pressure and p_t and z_t are the pressure and height of some level which is undisturbed by the tropical cyclone below. Thus, the surface pressure is inversely related to the temperature of the column of air above. Observations show that the transition between the lower level cyclone and upper level anti-cyclone occurs in the vicinity of 10 km. Applying the above equation at the eye and its environment we find

$$\ln\left(\frac{p_s^{eye}}{p_t}\right) = \frac{g}{R}\frac{z_t}{T_{av}^{eye}}$$

and

$$\ln\left(\frac{p_s^{env}}{p_t}\right) = \frac{g}{R}\frac{z_t}{T_{av}^{env}}$$

where T_{av} is the mean temperature of the column between the surface and the undisturbed pressure level. Combining these expressions we can write

$$p_s^{eye} = p_s^{env}\ \exp\left[-\frac{gz_t}{R}\left(\frac{T_{av}^{eye} - T_{av}^{env}}{T_{av}^{eye}\,T_{av}^{env}}\right)\right]$$

Using z_t = 10 km and setting $T_{av}^{eye}\,T_{av}^{eye} \sim (250\ K)^2$ then

$$p_s^{eye} \sim p_s^{env} \exp\left[-.0055\,\Delta T_{av}\right]$$

$$\sim p_s^{env}\left[1 - .0055\,\Delta T_{av}\right].$$

Assuming $p_s^{env} \sim 1000$ mb, then

$$p_s^{eye} - 1000 = -5.5\,\Delta T_{av}$$

so that a 55 mb surface pressure depression is approximately associated with a 10 C contrast between the mean temperatures of the cyclone eye and its environment.

It has been found that the tropical cyclone warm core is usually strongest at about 250 mb. In addition, the amplitude of the upper tropospheric temperature anomaly is well-correlated with the amplitude of the mean temperature of the tropospheric column below 10 km. Therefore, the deviation of the temperature field at 250 mb provides a measure of the strength of the warm core, which then is correlated to storm surface intensity. Furthermore, a correlation should also exist for maximum surface winds as they are directly related to the pressure field (although not pure gradient winds because of frictional effects).

In the work of Velden *et al*, (1984), ΔT_{250} is compared to observed surface central pressure and maximum winds, where ΔT_{250} is the gradient of the 250 mb temperature field defined as the core temperature minus the average environmental temperature at a six degree radius from the storm core. Linear regression is used to find a best fit for the data. After studying over 50 cases, they found that the standard error of estimates for the central pressure and maximum wind are 6 mb and 10 knots,

respectively. Figure 8.4 shows these results. Figure 8.5 shows a comparison of National Hurricane Centre (now called Tropical Prediction Center) versus satellite estimates of the central surface pressure and maximum sustained wind speed for the duration of Hurricane Barry. TOVS microwave intensity estimates continue to augment existing methods.

8.6 Satellite Measure of Atmospheric Stability

One measure of the thermodynamic stability of the atmosphere is the total-totals index

$$TT = T_{850} + TD_{850} - 2T_{500}$$

where T_{850} and T_{500} are the temperatures at the 850- and 500-mb levels, respectively, and TD_{850} is the 850-mb level dew point. TT is traditionally estimated from radiosonde point values. For a warm moist atmosphere underlying cold mid-tropospheric air, TT is high (e.g., 50-60 K) and intense convection can be expected. There are two limitations of radiosonde derived TT: (a) the spacing of the data is too large to isolate local regions of probable convection; and (b) the data are not timely since they are available only twice per day.

If we define the dew point depression at 850 mb, $D_{850} = T_{850} - TD_{850}$, then

$$TT = 2(T_{850} - T_{500}) - D_{850} .$$

Although point values of temperature and dew point cannot be observed by satellite, the layer quantities observed can be used to estimate the temperature lapse rate of the lower troposphere ($T_{850} - T_{500}$) and the low level relative moisture concentration D_{850}. Assuming a constant lapse rate of temperature between the 850- and 200-mb pressure levels and also assuming that the dew point depression is proportional to the logarithm of relative humidity, it can be shown from the hydrostatic equation that

$$TT = 0.1489\ \Delta Z_{850\text{-}500} - 0.0546\ \Delta Z_{850\text{-}200} + 16.03\ \ln RH,$$

where ΔZ is the geopotential thickness in metres and RH is the lower tropospheric relative humidity, both estimated from either TIROS or GOES radiance measurements as explained earlier.

Smith and Zhou (1982) reported several case studies using this approach. Figure 8.6 shows the total-totals stability index as observed by radiosondes and infrared from TOVS data on 31 March 1981. One can see the coarse spacing of the radiosonde observations (Fig. 8.6(a)). The analysis of satellite data possesses much more spatial detail since the spacing of the data is only 75 km (Fig. 8.6(b)). There is general agreement in the high total-totals over Illinois and Missouri, but also some areas of disagreement (e.g., Nebraska). In this case, the radiosonde data are not as coherent an indicator of the region of intense convection as are the satellite data.

Also shown on the satellite TT analysis are the streamlines of the wind observed at the surface. On this occasion, it appears that the unstable air observed along the Illinois-Iowa border at 1438 GMT was advected into central Wisconsin and supported the development of a tornadic storm at 2315 GMT.

Table 8.1

Values of the Geometric Height (z), Geopotential height (Z), and Acceleration Due to Gravity (g) at 40 Latitude

z(km)	Z(km)	g(ms^{-2})
0	0	9.802
1	1.000	9.798
10	9.9869	9,771
20	19.941	9.741
30	29.864	9.710
60	59.449	9.620
90	88.758	9.531
120	117.795	9.443
160	156.096	9.327
200	193.928	9.214
300	286.520	8.940
400	376.370	8.677
500	463.597	8.427
600	548.314	8.186

Table 8.2

Summary of Comparisons Between GOES(VAS) and Radiosonde Data For Bermuda, San Juan and West Palm Beach (1 August-30 November 1983)

Parameter	Mean (VAS-RAOB)	Standard Deviation	Range	Number of Cases
Z850 (m)	7	10	-23 to 31	68
Z700	13	13	-21 to 36	67
Z500	18	19	-26 to 38	67
Z400	22	20	-37 to 66	65
Z300	30	27	-52 to 71	63
Z200	32	37	-63 to 110	62
Z500-850 (m)	12	15	-31 to 63	69
Z400-850	16	18	-42 to 50	67
Z300-850	23	26	-63 to 71	65
Z500-700	6	12	-28 to 52	68
Z400-700	10	16	-39 to 35	66
Z200-400	9	28	-78 to 60	63

Summary of Comparisons between VAS and ODW for 14-15 and 15-16 September 1982

Parameter	Mean (VAS-RAOB)	Standard Deviation	Range	Number of Cases
Z850 (m)	-6	23	-68 to 26	42
Z700	0	22	-58 to 41	42
Z500	1	24	-56 to 44	35
Z400	2	27	-54 to 47	24
Z400-850 (m)	11	17	-16 to 45	24
Z500-850	6	14	-18 to 43	35
Z400-700	4	14	-16 to 34	24

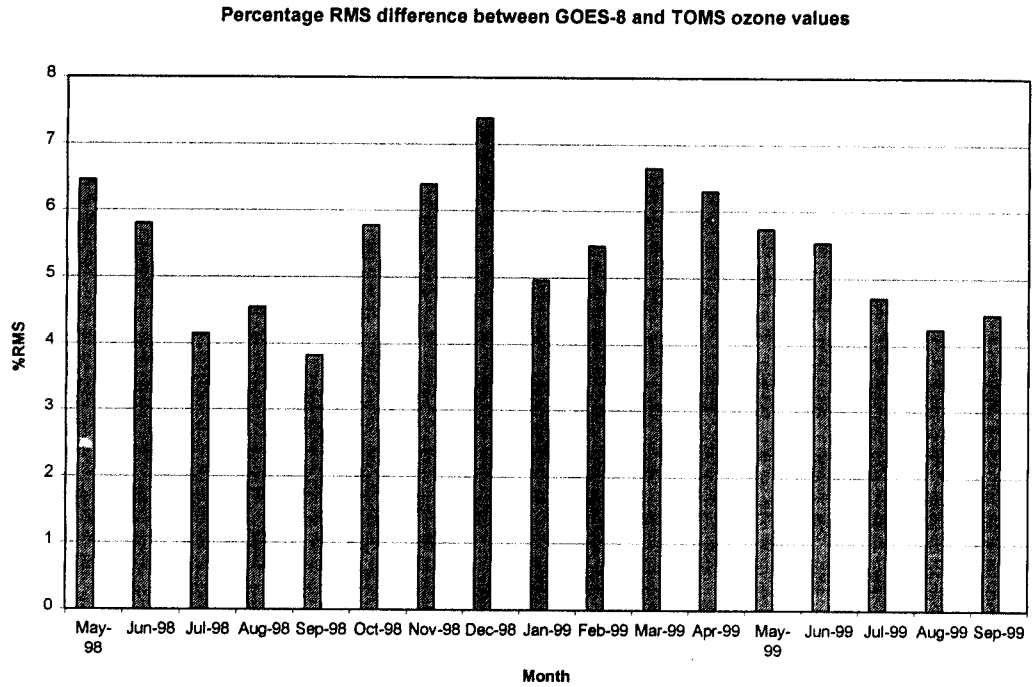

Figure 8.1a: The monthly % RMSD between the GOES-8 ozone estimates and the TOMS ozone measurements between May 1998 and September 1999.

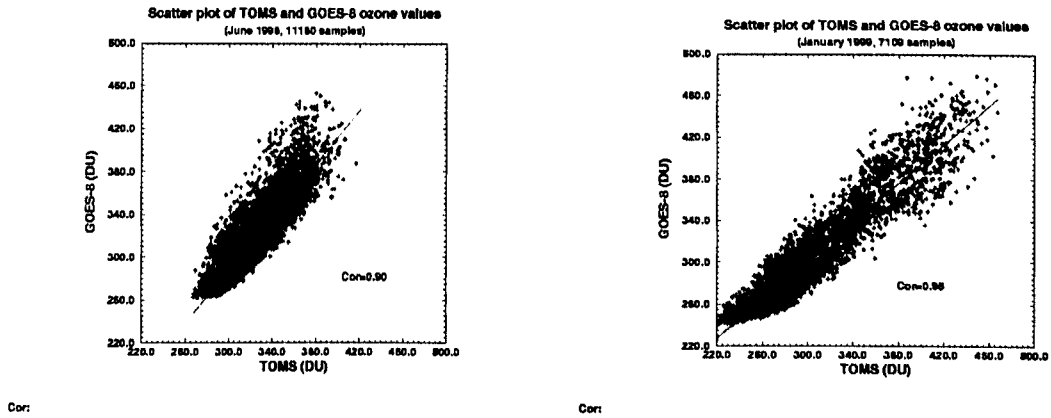

Figure 8.1b: Scatter plot of co-located GOES-8 ozone estimates and the TOMS ozone measurements for June 1998 (left) and January 1999 (right).

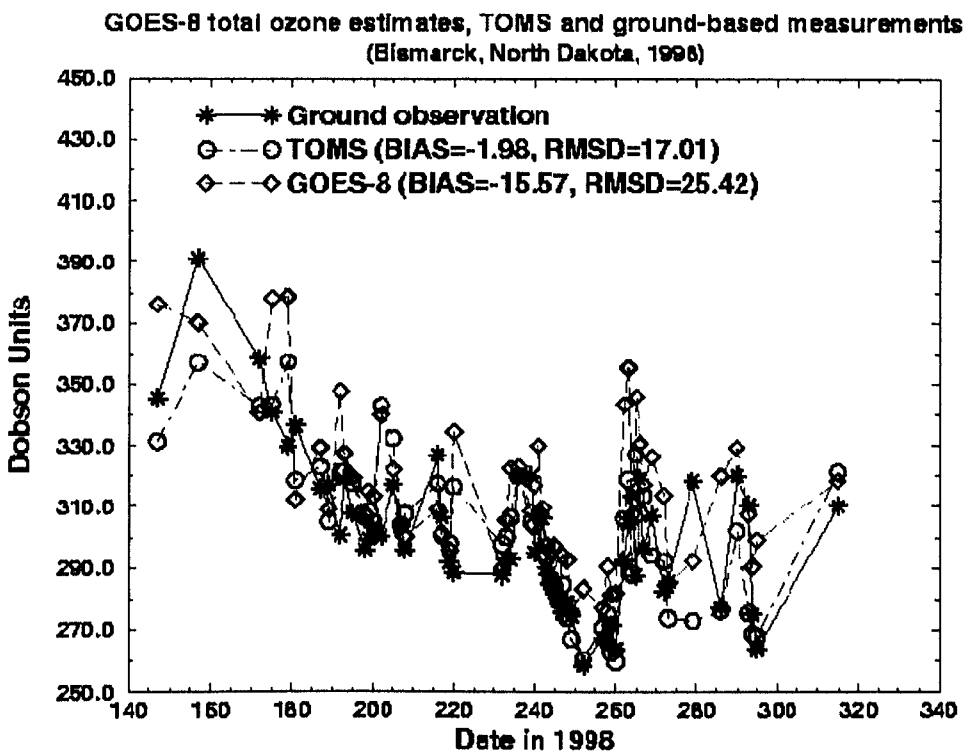

Figure 8.1c: GOES-8 total ozone estimates for Bismarck, North Dakota (46.77°N, 100.75°W) in 1998 along with the TOMS and ground-based ozone measurements.

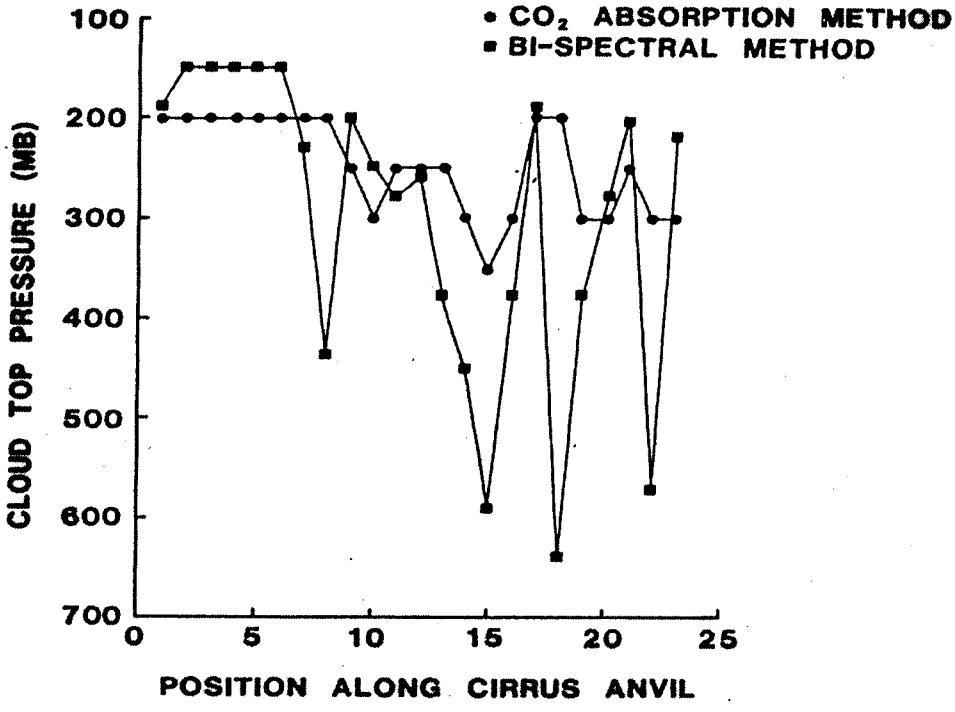

Figure 8.2: Bi-spectral and CO_2 absorption cloud-top pressures (mb) plotted versus the position along a cirrus anvil emanating from the thunderstorm over Missouri and Kansas of 1348 GMT 14 July 1982.

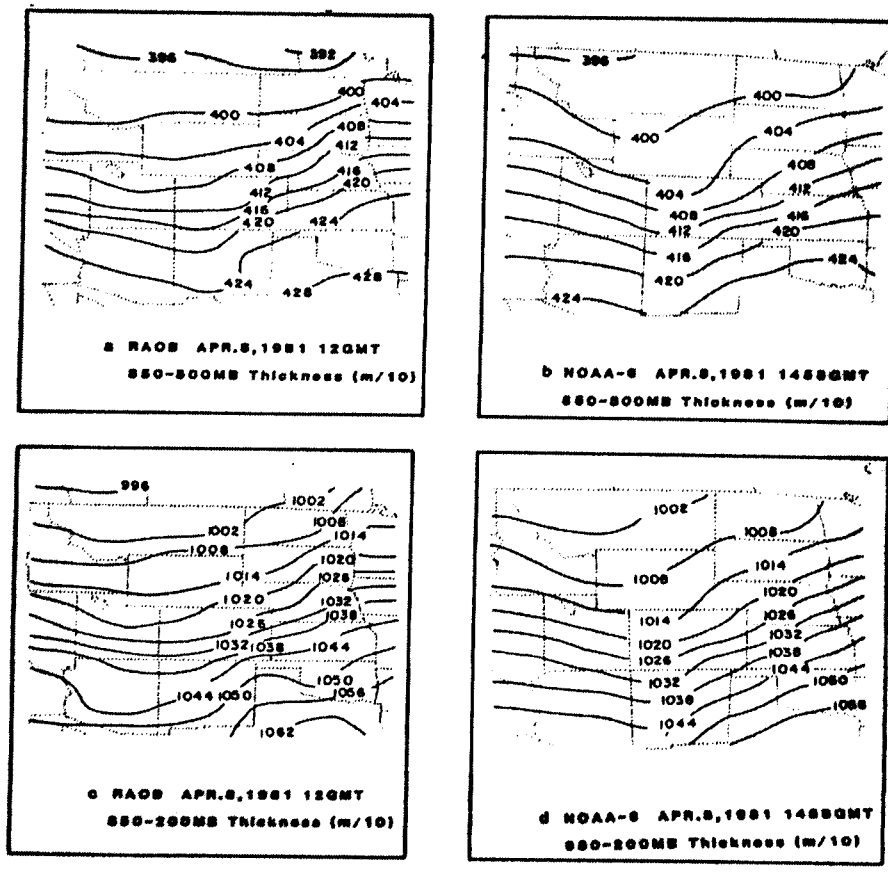

Figure 8.3: Comparison of NOAA-6 MSU estimates of 850-500 and 850-200 mb thickness patterns with those obtained from radiosonde observations.

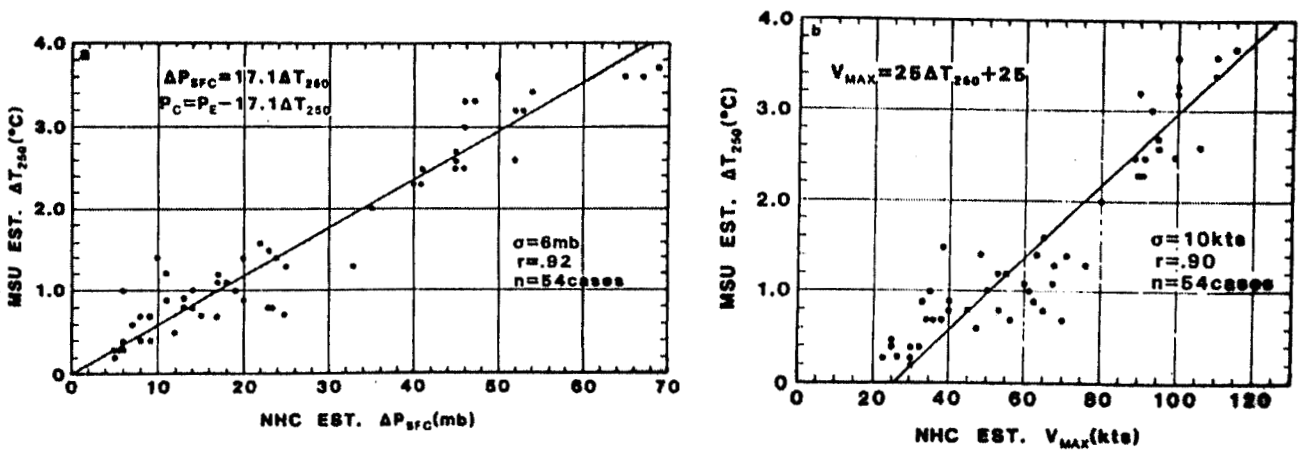

Figure 8.4: Comparison of ΔT_{250} versus the National Hurricane Centre estimated (left) central surface pressure P_C, and (right) maximum winds V_{max}. P_E is the average environmental surface pressure surrounding the storm at a 6 degree radius, n is the number of cases, r is the correlation coefficient, and σ is the standard deviation. (from Velden *et al*, 1984).

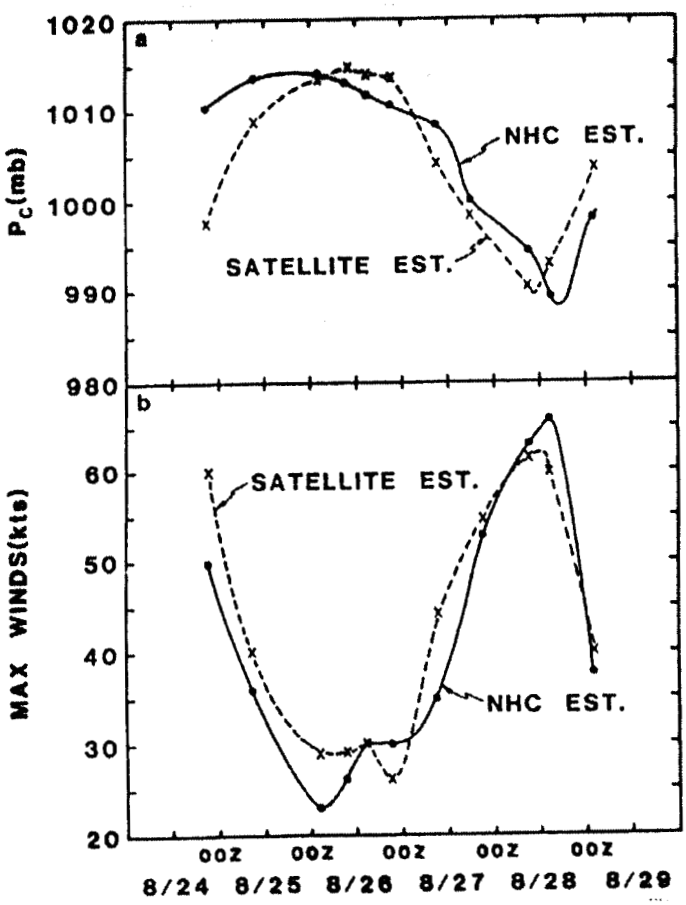

Figure 8.5: Comparison of National Hurricane Center versus satellite estimates of central surface pressure for the duration of Hurricane Barry. (from Velden *et al*, 1984).

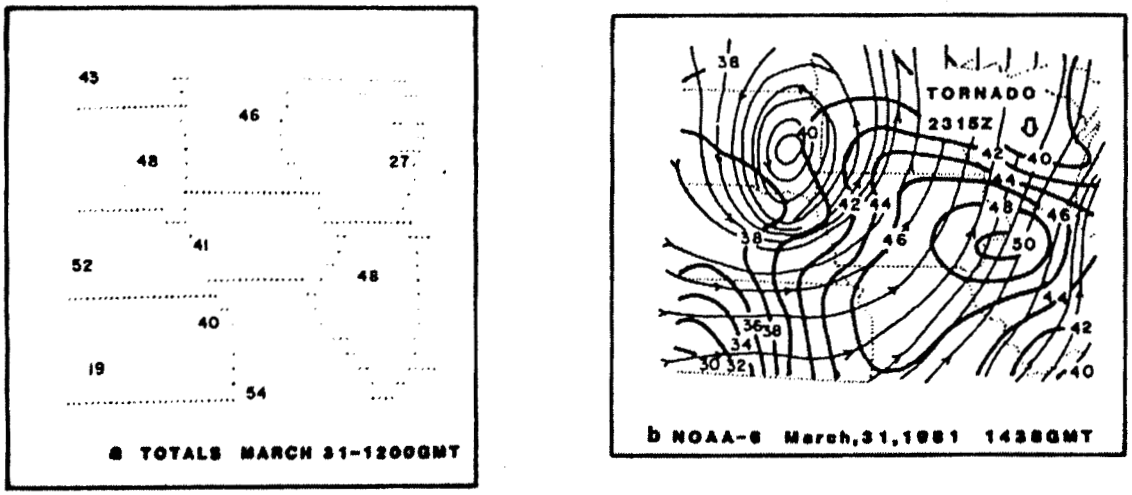

Figure 8.6: Radiosonde observations of total-totals (left) and a contour analysis (heavy lines) of NOAA-6 derived stability values with streamlines (thin lines) of the surface wind superimposed (right).

CHAPTER 9

TECHNIQUES FOR DETERMINING ATMOSPHERIC MOTIONS

9.1 Atmospheric Motion

There are a variety of forces influencing the motion of an air parcel in the atmosphere. Considering that the earth is a rotating frame of reference with a angular velocity ω, the acceleration in can be written as the vector sum

$$\frac{d\vec{V}}{dt} = \vec{g}$$ (the gravitational acceleration, roughly 9.8 m/s^2)

$-2\,\vec{\omega} \times \vec{V}$ (the Coriolis acceleration, about .002 m/s^2 at mid-latitudes for a parcel travelling at the speed of 20 m/s)

$-\vec{\omega} \times \vec{\omega} \times \vec{r}$ (the Centrifugal acceleration, .034 m/s^2 at the equator)

$-1/\rho\,\vec{\nabla}p$ (the acceleration due to pressure gradient forces, .002 m/s^2 at mid- latitude for $\Delta p/\Delta n$ = 3 mb/100 km and ρ = 1.2 kg/m^3)

$-k\vec{V}$ (the frictional deceleration)

The balance of different combinations of these forces are discussed next.

9.2 Geostrophic Winds

Geostrophic flow results from the balance of the Coriolis and pressure gradient forces. The equations for the latitudinal, u, and meridional, v, components of the velocity are given by

$$fv = \frac{1}{\rho}\frac{\partial p}{\partial x} \quad \text{and} \quad fu = -\frac{1}{\rho}\frac{\partial p}{\partial y},$$

where the Coriolis parameter f = 2 ω sin (latitude) which is roughly 10^{-4} sec^{-1} at mid-latitudes.

Geostrophic winds are parallel to isobars with the pressure decreasing to the left of the flow in the northern hemisphere. At low latitudes, where f is small, it is difficult to establish this kind of balance. The geostrophic approximation should not be applied in equatorial regions.

9.3 Gradient Winds

Gradient winds represent motion parallel to isobars subject to balanced Coriolis, centrifugal, and pressure gradient forces. The three way balance is shown in Figure 9.1 for cyclonic and anti-cyclonic trajectories. In both cases, the centrifugal force is directed outward from the centre of curvature of the air trajectories (denoted by the dashed lines) and has a magnitude given by V^2/R_T, where R_T is the local radius of curvature. In effect, a balance of forces can be achieved with a wind

velocity smaller than would be required if the Coriolis force were acting alone. Thus, in this case, it is possible to maintain a sub-geostrophic flow parallel to the isobars. For the anti-cyclonically curved trajectory, the situation is just the opposite: the centrifugal force opposes the Coriolis force and, in effect, necessitates a super-geostrophic wind velocity in order to bring about a three-way balance of forces.

If P_n denotes the normal component of the pressure gradient force per unit mass and f the Coriolis parameter, we can write

$$p_n = fV \pm \frac{V^2}{R_T}$$

The geopotential height fields derived from the TIROS or VAS data can be used to evaluate the gradient wind. This is accomplished by realizing

$$P_n = -\frac{1}{\rho}\frac{\partial p}{\partial n} = -g_o \frac{\partial Z}{\partial n}$$

and then solving for V by using the quadratic formula.

Figure 9.2 shows streamlines and isotachs of 300 mb gradient winds derived from VAS temperature profile data, where the curvature term is approximated from the geopotential height field contours. As can be seen, the depiction of the flow is quite detailed with a moderately intense subtropical jet streak propagating east-south-eastward in time. Such wind fields in time sequence are especially useful in nowcasting applications.

Gradient winds have also been compared on a routine basis with conventional radiosonde and dropwindsonde determinations by NHC as part of the NOVA programme. During 1982, the VAS gradient winds averaged about 30% shower than the conventionally observed winds. Several factors may be contributing to this discrepancy: ageostrophic motions, deficient height fields in data void areas, and inaccurate determination of the normal derivation of the geopotential height due to the resolution of the analysis field. Most likely, the last factor is very significant. Whatever the cause, for 1982 NHC concluded that gradient winds were less useful than cloud motion winds in their analyses.

9.4 Thermal Winds

Thermal winds give a measure of the vertical wind shear. This can be seen qualitatively by considering two surfaces of constant pressure in a vertical cross section, as in Figure 9.3. Since the geostrophic wind is proportional to the slopes of the isobaric surfaces, the geostrophic wind increases with elevation because the upper pressure surface is more inclined than the lower. The increased slope for the higher surface is revealed in the finite-difference form of the hydrostatic equation:

$$\Delta z \approx -\frac{\Delta p}{\rho g}$$

The pressure difference between the two surfaces is the same for columns A and B, so the difference in separation between them is due to a decrease in density in going from A to B. The average pressure is the same in the two columns, so column B has a higher average temperature than column A. In this way we see that the geostrophic wind with elevation must be associated with a quasi-horizontal temperature gradient.

As this previous discussion indicates, the temperature gradient is measured along an isobaric surface, not along a horizontal surface. Thus, the vertical wind shear can be related to the horizontal gradient of temperature plus a correction term involving the slope of the isobaric surface and the temperature variation in the vertical. However, since the slopes of isobaric surfaces are generally quite small (of the order of 1/5000), the correction term is usually quite small also.

Quantitatively, the thermal wind relation is derived from the geostrophic wind equations,

$$fv = \frac{1}{\rho}\frac{\partial p}{\partial x} \quad \text{and} \quad fu = -\frac{1}{\rho}\frac{\partial p}{\partial y},$$

together with the hydrostatic equation and the equation of state,

$$g = -\frac{1}{\rho}\frac{\partial p}{\partial z} \quad \text{and} \quad \rho = \frac{p}{RT}.$$

Note that there are five dependent variables, u, v, ρ, p, T and only four equations. A complete solution is not possible, but a useful interrelationship is readily available if ρ is eliminated in the geostrophic and hydrostatic expressions by means of the equation of state. This yields:

$$\frac{fv}{T} = R\frac{\partial \ln p}{\partial x}; \quad \frac{fu}{T} = -R\frac{\partial \ln p}{\partial y}; \quad \frac{g}{T} = -\frac{\partial \ln p}{\partial z}$$

After cross differentiating, the results are:

$$\frac{\partial}{\partial z}\left(\frac{fv}{T}\right) = -\frac{\partial}{\partial x}\left(\frac{g}{T}\right); \quad \left(\frac{\partial}{\partial z}\right)\left(\frac{fu}{T}\right) = \frac{\partial}{\partial y}\left(\frac{g}{T}\right).$$

Rearranging, we get the thermal wind equations in differential form

$$\frac{\partial v}{\partial z} = \frac{g}{fT}\frac{\partial T}{\partial x} + \frac{v}{T}\frac{\partial T}{\partial z}$$

$$\frac{\partial u}{\partial z} = -\frac{g}{fT}\frac{\partial T}{\partial y} + \frac{u}{T}\frac{\partial T}{\partial z}$$

They have the characteristics which were physically anticipated since the first terms on the right are the contribution of the horizontal temperature gradient, and the second terms on the right are correction terms involving the slopes of the isobaric surface (u, v) and the vertical temperature gradients. The correction terms on the right are indeed relatively small. For the fractional rate of change of u with height, the correction term is $(1/T)(\partial T/\partial z)$. Even if the lapse rate is as high as the dry adiabatic, this is about four percent per kilometre. The normal shear of west wind with height in the troposphere in middle latitudes is approximately 25 percent per kilometre. Thus, it is apparent that the additional term in question does not usually make a major contribution to the vertical wind shear, although there are situations were it must be taken into account.

Thus in the simpler form we write

$$\frac{\partial v}{\partial z} \approx \frac{g}{fT}\frac{\partial T}{\partial x}; \qquad \frac{\partial u}{\partial z} \approx -\frac{g}{fT}\frac{\partial T}{\partial y}$$

These equations require that for v to increase with height temperature must increase to the east, and for u to increase with height temperature must increase to the south, in the Northern Hemisphere. The fact that actual westerly winds in middle latitudes normally increase in strength going upward through the troposphere is to be explained, therefore, as a result of the normal decrease of temperature towards the poles in the troposphere.

By taking the difference at two levels (denoted here by a lower level 1 and upper level 2), one finds

$$v_2 - v_1 = (z_2 - z_1) \frac{g_o}{fT}\frac{\partial T}{\partial x}$$

Or one can substitute for the geopotential height to write

$$v_2 - v_1 = \ln\left(\frac{p_1}{p_2}\right)\frac{R}{f}\frac{\partial T}{\partial x}$$

A similar expression for the u component of the wind is readily derived.

Through the use of the thermal wind equation, it is possible to define a wind field from geopotential height observations at two reference levels and temperature profiles over the area of interest. Thus, a set of sea level pressure observations together with a grid of TIROS or VAS infrared temperature soundings constitutes a sufficient observing system for determining the three dimensional distribution of the thermal wind velocities.

9.5 Inferring Winds From Cloud Tracking

Geostationary satellite imagery has been used as a source of wind observations since the launch of the first spin scan camera aboard the Application Technology Satellite (ATS 1) in December 1966. It was recognized immediately that features tracked in a time sequence of images could provide estimates of atmospheric motion. Historically, wind vectors have been produced from images of visible (for low level vectors) and infrared long-wave window radiation (for upper and low level vectors and some mid level vectors). More recently, in order to improve the coverage at mid levels and over cloud free areas, wind tracking has been applied to water vapour imagery at 6.7 and 7.2 microns (see Figure 9.4 for an example from Meteosat).

The basic elements of wind vector production have not changed since their inception. These are: (a) selecting a feature to track or a candidate target; (b) tracking the target in a time sequence of images to obtain a relative motion; (c) assigning a pressure height (altitude) to the vector; and (d) assessing the quality of the vector. Initially, these elements were done manually (even to the point of registering the images into a movie loop), but the goal has always been to automate procedures and reduce the time consuming human interaction.

To use a satellite image, the feature of interest must be located accurately on the earth. Since the earth moves around within the image plane of the satellite because of orbit effects, satellite orbit and attitude (where the satellite is and how it is oriented in space) must be determined and accounted for. This process of navigation is crucial for reliable wind vector determination. With the assistance of landmarks (stars) to determine the attitude (orbit) of the spacecraft over time, earth location accuracies within one visible pixel (one km) have been realized.

The basic concept behind the cloud drift winds is that some clouds are passive tracers of the atmosphere's motion in the vicinity of the cloud. However, clouds grow and decay with lifetimes which are related to their size. To qualify for tracking, the tracer cloud must have a lifetime that is long with respect to the time interval of the tracking sequence. The cloud must also be large compared with the resolution of the images. This implies a match between the spatial and temporal resolution of the image sequence. In order for a cloud to be an identifiable feature on an image, it generally must occupy an area at least ten to 20 pixels across (where pixel denotes a field of view). Hence for full resolution 1.0 km GOES visible data, the smallest clouds which can be used for tracking are 10 to 20 km across. Experience has shown that a time interval of approximately 3 to 10 min between images is necessary to track clouds of this size, with the shorter time interval being required for disturbed situations. For 4 km infrared images, the cloud tracers are about 100 km across, are tracked at half hour intervals, and represent an average synoptic scale flow. Water vapour images are found to hold features longer and are best tracked at hourly intervals (a longer time interval offers better accuracy of the tracer if the feature is not changing).

Cloud drift winds compare within 5 to 8 m/s with radiosonde wind observations. However, it must be recognized that cloud winds represent a limited and meteorologically biased data set. The cloud winds generally yield measurements from only one level (the uppermost layer of the cloud) and from regions where the air is going up (and producing clouds). Even with the water vapour motions enhancing the cloud drift winds, the meteorological bias persists. Satellite derived winds are best used over data sparse regions to fill in some of the data gaps between radiosonde stations and between radiosonde launch times.

9.5.1 Current Operational Procedures

Operational winds from GOES are derived from a sequence of three navigated and earth located images taken 30 minutes apart. Cloud Motion Vectors (CMVs) are calculated by a three-step objective procedure. The initial step selects targets, the second step assigns pressure altitude, and the third step derives motion. Altitude is assigned based on a temperature/pressure derived from radiative transfer calculations in the environment of the target. Motion is derived by a pattern recognition algorithm that matches a feature within the "target area" in one image within a "search area" in the second image. For each target two winds are produced representing the motion from the first to the second, and from the second to the third image. An objective editing scheme is then employed to perform quality control: the first guess motion, the consistency of the two winds, the precision of the cloud height assignment, and the vector fit to an analysis are all used to assign a quality flag to the "vector" (which is actually the average of the two vectors).

Water Vapor Motion Vectors (WVMVs) are inferred from the imager band at 6.7 microns which sees the upper troposphere and sounder bands at 7.0 and 7.5 microns which see deeper into the troposphere. WVMVs are derived by the same methods used with CMVs. Heights are assigned from the water vapour brightness temperature in clear sky conditions and from radiative transfer techniques in cloudy regions.

In 1998, the National Environmental Satellite, Data, and Information Service (NESDIS) operational GOES-8/9/10 CMV and WVMV production increased to every three hours with high spatial density tracers derived from visible, infrared window, and water vapour images. The number of motion vectors has increased dramatically to over 10 000 vectors for each winds data set. The quality of the wind product is being reported monthly in accordance with the Coordination Group for Meteorological Satellites (CGMS) reporting procedures (Schmetz *et al*, 1997 and 1999); this involves direct comparisons of collocated computed cloud motions and radiosonde observations. It reveals GOES cloud motion wind RMS differences to be within 6.5 to 7 m/s with respect to raobs, with a slow bias of about .5 m/s; water vapour motions RMS differences are within 7 to 7.5 m/s (Nieman *et al*, 1997). The NESDIS operational winds inferred from infrared window and water vapour images continue to perform well. Figure 9.5 presents the summary from a recent twelve month period. The next few paragraphs describe the current operational procedures.

(a) Tracer Selection

In the 1990s, tracer selection for GOES winds was improved. In the old tracer selection algorithm, the highest pixel brightness values within each target domain were found, local gradients were computed around those locations, and adequately large gradients were assigned as target locations. In the new tracer selection algorithm, maximum gradients are subjected to a spatial-coherence analysis. Too much coherence indicates such features as coastlines and thus is undesirable. The presence of more than two coherent scenes often indicates mixed level clouds; such cases are screened. The resulting vectors from the new scheme (Figure 9.6) show a much higher density of tracers in desirable locations.

(b) Height Assignment Techniques

Semi-transparent or sub-pixel clouds are often the best tracers, because they show good radiance gradients that can readily be tracked and they are likely to be passive tracers of the flow at a single level. Unfortunately their height assignments are especially difficult. Since the emissivity of the cloud is less than unity by an unknown and variable amount, its brightness temperature in the infrared window is an overestimate of its actual temperature. Thus, heights for thin clouds inferred directly from the observed brightness temperature and an available temperature profile are consistently low.

Presently heights are assigned by any of three techniques when the appropriate spectral radiance measurements are available (Nieman *et al*, 1993). In opaque clouds, infrared window (IRW) brightness temperatures are compared to forecast temperature profiles to infer the level of best agreement which is taken to be the level of the cloud. In semi-transparent clouds or sub-pixel clouds, since the observed radiance contains contributions from below the cloud, this IRW technique assigns the cloud to too low a level. Corrections for the semi-transparency of the cloud are possible with the carbon dioxide (CO2) slicing technique (Menzel *et al*, 1983) where radiances from different layers of the atmosphere are ratioed to infer the correct height. A similar concept is used in the water vapour (H2O) intercept technique (Szejwach, 1982), where the fact that radiances influenced by upper tropospheric moisture (H2O) and IRW radiances exhibit a linear relationship as a function of cloud amount is used to extrapolate the correct height.

An IRW estimate of the cloud height is made by averaging the infrared window brightness temperatures of the coldest 25 percent of pixels and interpolating to a pressure from a forecast guess sounding (Merrill *et al,* 1991).

In the CO2 slicing technique, a cloud height is assigned with the ratio of the deviations in observed radiances (which include clouds) from the corresponding clear air radiances for the infrared window and the CO2 (13.3 micron) channel. The clear and cloudy radiance differences are determined from observations with GOES and radiative transfer calculations. Assuming the emissivities of the two channels are roughly the same, the ratio of the clear and cloudy radiance differences yields an expression by which the cloud top pressure of the cloud within the FOV can be specified. The observed differences are compared to a series of radiative transfer calculations with possible cloud pressures, and the tracer is assigned the pressure that best satisfies the observations. The operational implementation is described in Merrill *et al*, (1991).

The H2O intercept height assignment is predicated on the fact that the radiances for two spectral bands vary linearly with cloud amount. Thus a plot of H2O (6.5 micron) radiances versus IRW (11.0 micron) radiances in a field of varying cloud amount will be nearly linear. These data are used in conjunction with forward calculations of radiance for both spectral channels for opaque clouds at different levels in a given atmosphere specified by a numerical weather prediction of temperature and humidity. The intersection of measured and calculated radiances will occur at clear sky radiances

and cloud radiances. The cloud top temperature is extracted from the cloud radiance intersection (Schmetz *et al*, 1993).

Satellite stereo height estimation has been used to validate H2O intercept height assignments. The technique is based upon finding the same cloud patch in several images. For cloud motion, the cloud needs to change slowly relative to the image frequency. For stereo heights, the cloud needs to be distinct and appear nearly the same from the two viewpoints (after re-mapping to the same projection). Campbell (1998) built upon earlier work of Fujita and others (Fujita, 1982) to develop a method which adjusts for the motion of the cloud so that simultaneity is not required for the stereo height estimate. A test analysis was performed with Meteosat – 5 / 7 data; stereo heights and H2O intercept heights agreed within 50 hPa. As more geostationary and polar orbiting satellites remain in operation, the prospects for geometric stereo height validations of the operational IRW, H2O intercept, and CO2 slicing heights become very promising.

(c) Objective Editing

Automated procedures for deriving cloud-motion vectors from a series of geostationary infrared-window images first became operational in the National Oceanic and Atmospheric Administration (NOAA) in 1993 (Merrill *et al*, 1991). NESDIS has been producing GOES-8 / 9 / 10 cloud motion vectors without manual intervention. Suitable tracers are automatically selected within the first of a sequence of images (see section 2a) and heights are assigned using the H2O intercept method. Tracking features through the subsequent imagery is automated using a covariance minimization technique (Merrill *et al.* 1991) and an automated quality-control algorithm (Hayden and Nieman, 1996) is applied. Editing the CMVs through analyses with respect to a first guess wind and temperature profile field involves speed adjustment, height adjustment, and quality assessment (Figure 9.7). This procedure, with some modifications, is also used to infer water vapour motion vectors; tracer selection is based on gradients within the target area and vector heights are inferred from the water vapour brightness temperatures.

To mitigate the slow bias found in upper-level GOES CMV in extra-tropical regions, each vector above 300 hPa is incremented by 8 percent of the vector speed. There are indications that the slow bias can be attributed to: (a) tracking winds from sequences of images separated by too much time, (b) estimating atmospheric motion vectors from inappropriate tracers, and (c) height assignment difficulties. Some also suggest that cloud motions will not indicate full atmospheric motions in most situations.

A height adjustment is accomplished through a first-pass analysis of the satellite-derived CMV at their initially assigned pressure height and data from a coincident National Centers for Environmental Prediction (NCEP) short-term aviation model forecast. The analysis is a 3-dimensional objective analysis (Hayden and Purser, 1995) of the wind field using background information from the numerical forecast. The pressure altitudes of the CMVs are adjusted by minimizing a penalty function given by

$$B_{m,k} = \left(\frac{V_m - V_{i,j,k}}{F_v}\right)^2 + \left(\frac{T_m - T_{i,j,k}}{F_t}\right)^2 + \left(\frac{P_m - P_{i,j,k}}{F_p}\right)^2 + \left(\frac{dd_m - dd_{i,j,k}}{F_{dd}}\right)^2 + \left(\frac{s_m - s_{i,j,k}}{F_s}\right)^2$$

$V = velocity,\ T = temperature,\ P = pressure,\ dd = direction,\ s = speed$

Subscript *m* refers to a measurement; *i* and *j* are horizontal dimensions in the analysis, and k is the vertical level. The *F* are weighting factors given to velocity, temperature, pressure, direction, and speed; default values are 2 ms^{-1}, 10 ^{o}C, 100 hPa, 1000 degrees, and 1000 ms^{-1} respectively. Increasing a value of F downweights that component. As currently selected, neither speed or direction factor into the computation of the penalty. Note that these default selections give equal "worth" to a

2 ms^{-1} discrepancy, a 10 degree temperature discrepancy, or a 100 hPa discrepancy. Further details can be found in Velden *et al*, (1998).

The pressure levels for height adjustment in hPa are 925, 850, 775, 700, 600, 500, 400, 350, 300, 250, 200, 150, and 100. The pressure or height reassignment is constrained to 100 hPa. A tropopause test looks for lapse rates of less than 0.5 K per 25 hPa above 300 hPa and prohibits re-assignment to stratospheric heights.

(d) Quality Flags

A quality assessment for each vector is accomplished by a second analysis using the CMVs at the reassigned pressure altitudes and by inspecting the local quality of the analysis and the fit of the observation to that analysis. Thresholds are given for rejecting the data. Accepted data and the associated quality estimate, denoted by RFF for Recursive Filter Flag, are passed to the user (Hayden and Purser, 1995).

Several options are available for regulating the analysis, the penalty function, and the final quality estimates. These have been optimized, over several years of application, for the operational GOES CMVs. However the optimization may be situation dependent; what works best with GOES CMVs may not be optimal for WVMVs or winds generated at higher density, or winds generated with an improved background forecast, etc. Research on optimal tuning of this system in its various applications continues (Velden *et al*, 1998).

The EUropean organization for the exploitation for METeorological SATellites (EUMETSAT) has developed a quality indicator (QI) for use with Meteosat data that checks for direction, speed, and vector consistency in the vector pairs (derived from the three images in the wind determining sequence). In addition, consistency with nearest neighbours' vectors and with respect to a forecast model are factored in. A weighted average of these five consistency checks becomes the QI.

Depending on the synoptic situation between 10 and 33% of the processed tracers are rejected in the cloud vector inspection and quality flag assignment. A combination of the EUMETSAT QI and the NESDIS RFF wind quality indicators has been shown to enhance utilization of the high-density CMVs in numerical weather prediction models and is in the process of being implemented (Holmlund *et al*, 1999).

(e) Recent Upgrades

The major operational changes in the past years are summarized as follows: (1) Winds inferred from visible image loops as well as sounder mid-level moisture sensitive bands were added to operations by summer 1998; (2) This enabled ensemble auto-editing, where the combined wind sets from visible, infrared window, three water vapour sensitive bands are compared for consistency. The dependency on a numerical weather prediction (NWP) model first guess was diminished; (3) A dual pass auto-editor was put in place by summer 1998 that relaxes rejection criteria for winds around a feature of interest and use normal procedures elsewhere. This enables better retention of the tighter circulation features associated with tropical cyclones and other severe weather; (4) Water vapour winds were designated as being determined in clear skies or over clouds; the clear sky WVMVs are representative of layer mean motion while cloudy sky WVMVs are cloud top motion; (5) A quality flag that combines QI and RFF has been attached to each wind vector indicating the level of confidence resulting from the post-processing.

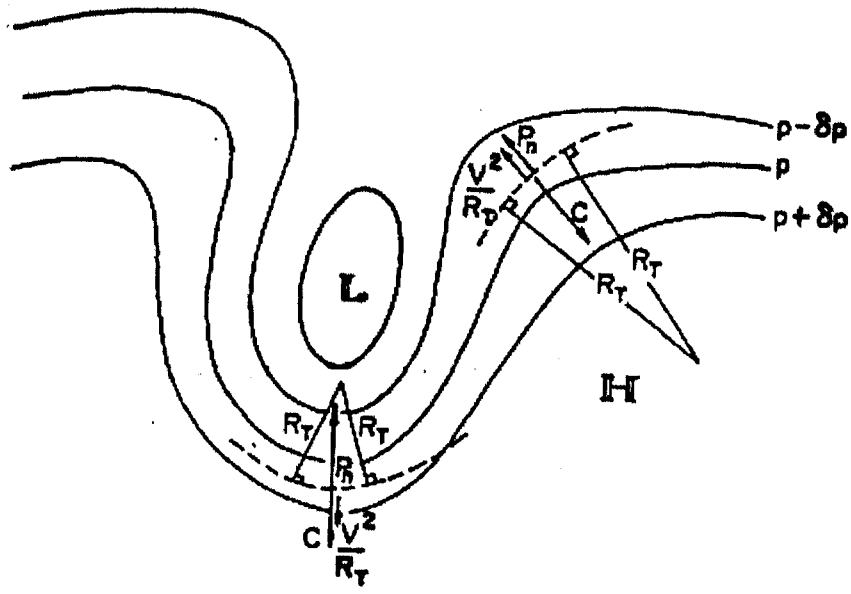

Figure 9.1: The three-way balance between the horizontal pressure gradient force, the Coriolis force and the centrifugal force, in flow along curved trajectories (----) in the Northern Hemisphere.

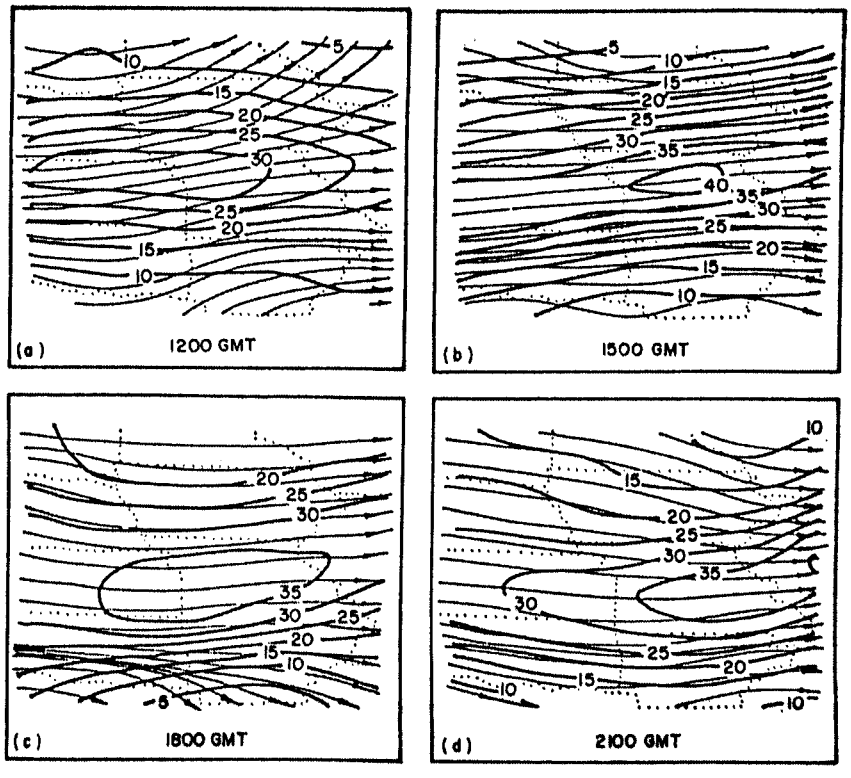

Figure 9.2: Streamlines and isotachs (ms^{-1}) of 300 mb gradient wind calculated from VAS temperature soundings: (a) 12 GMT; (b) 15 GMT; (c) 18 GMT; and (d) 21 GMT on 20 July 1981.

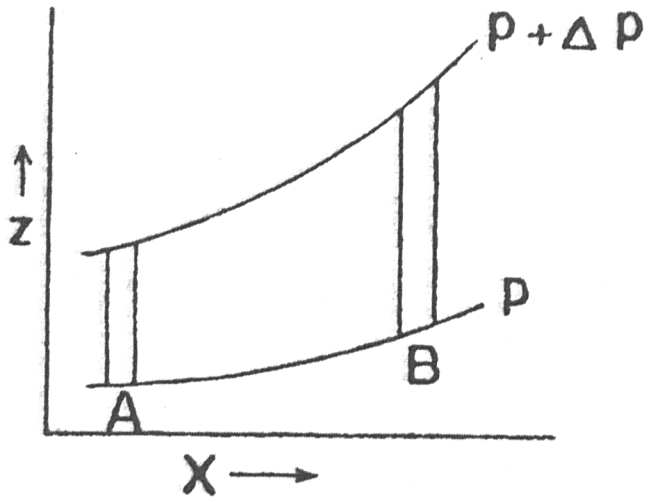

Figure 9.3: A depiction of isobaric surfaces indicating that the geostrophic wind increases with elevation because the upper pressure surface is more inclined than the lower.

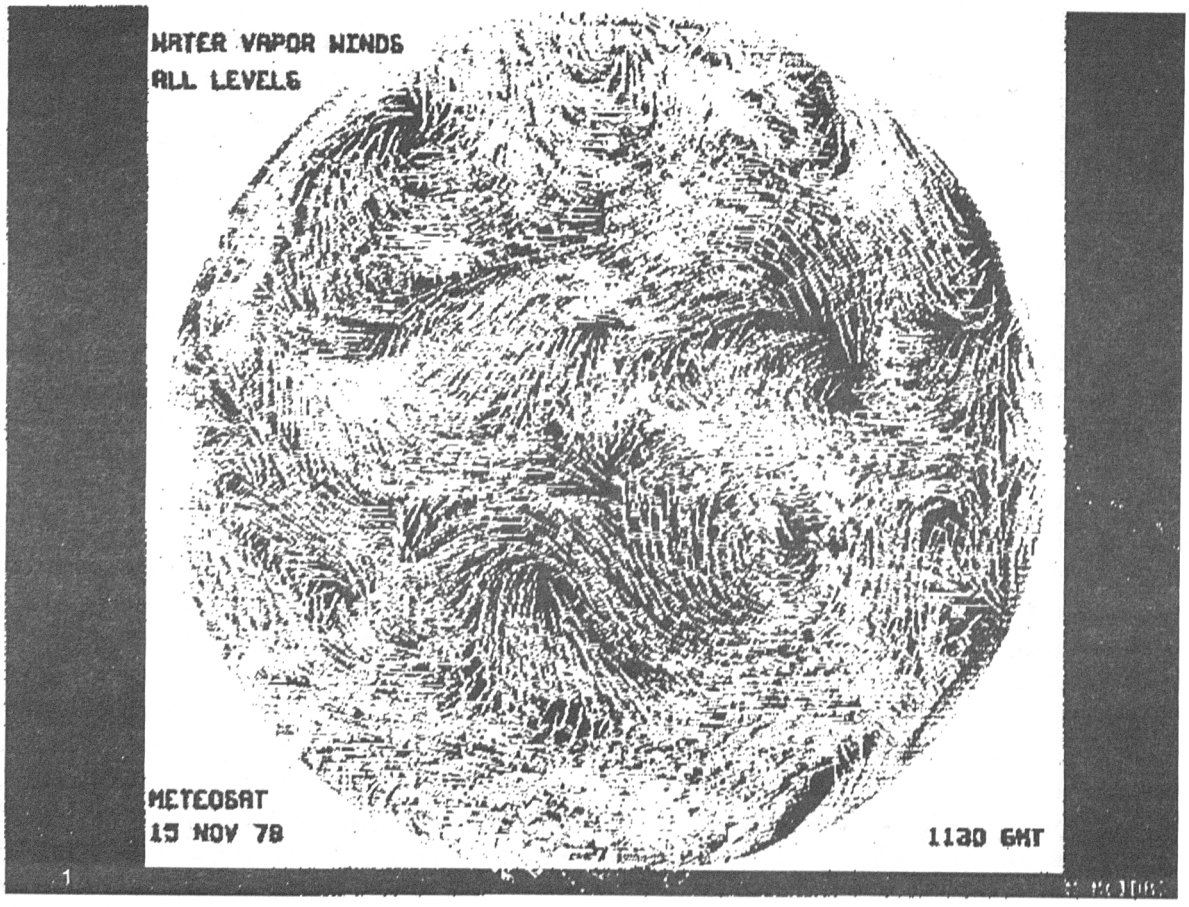

Figure 9.4: Water vapour winds derived from a sequence of half hourly Meteosat 6.7 micron images; from a data set developed by Verner Suomi.

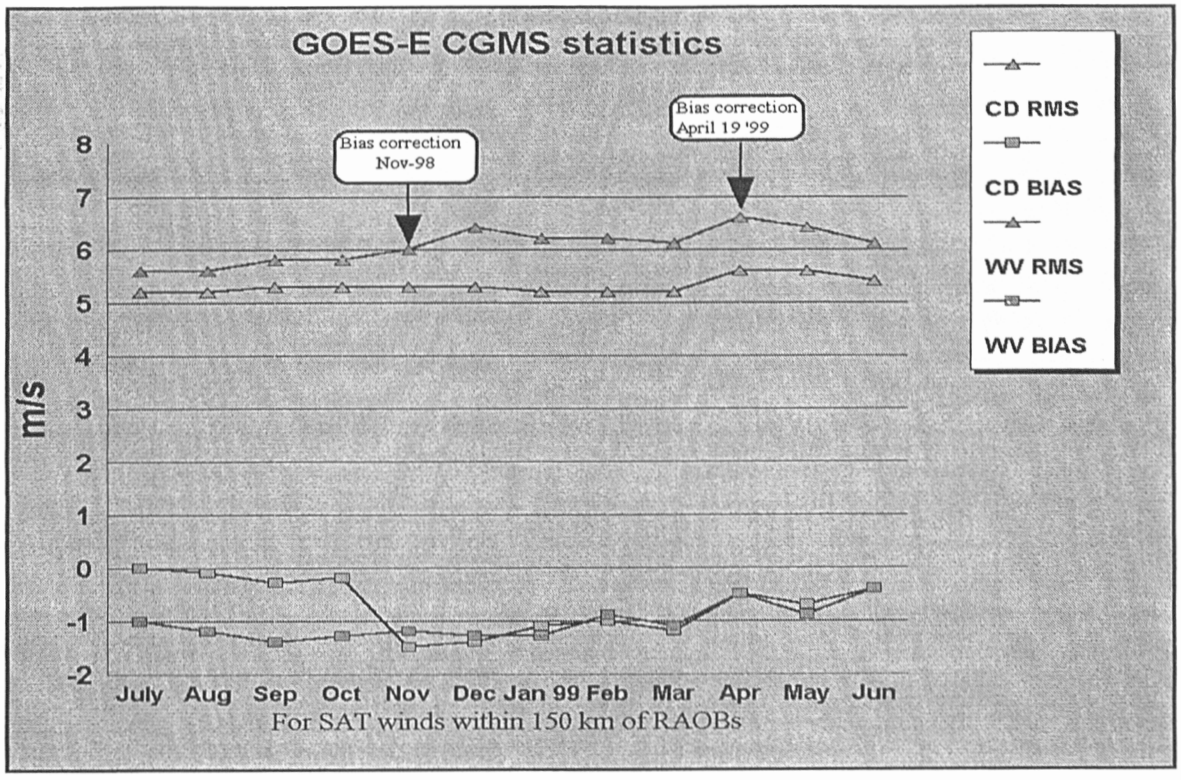

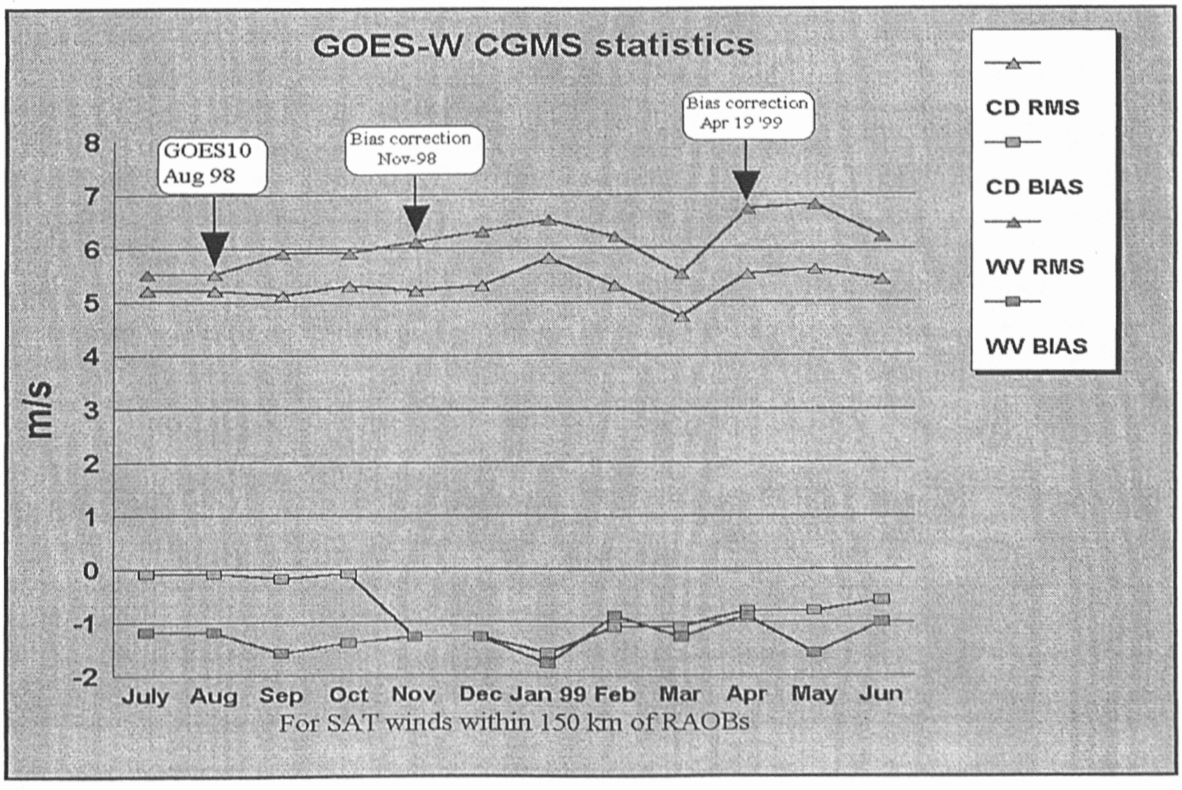

Figure 9.5. CGMS statistics (bias and root mean square) for GOES-8 (GOES-E) and GOES-10 (GOES-W) cloud drift (CD) and water vapour motion (WV) winds for July 1998 through June 1999.

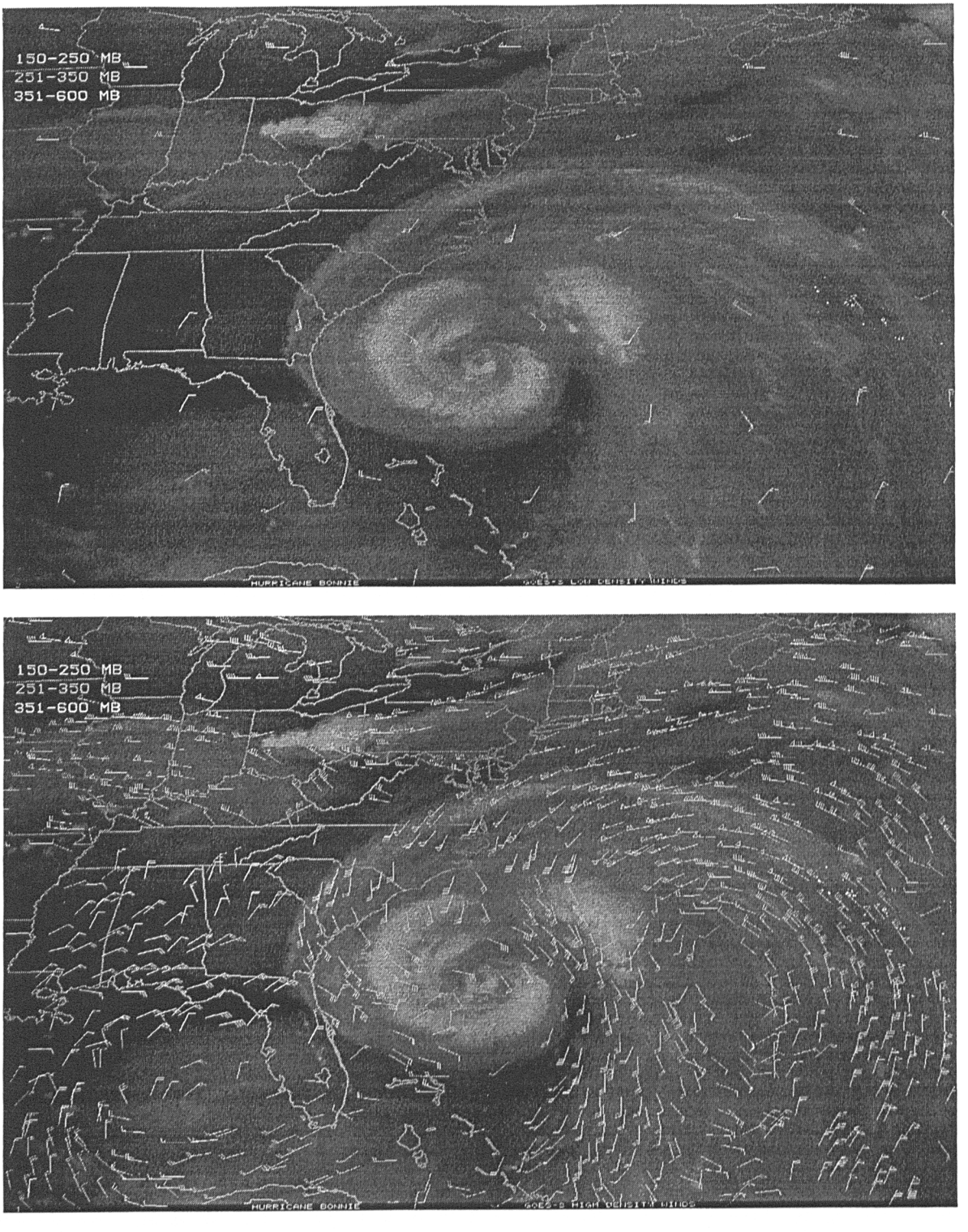

Figure 9.6. Vector distribution resulting from the pre-GOES-8 (top) and post-GOES-8 (bottom) tracer selection capabilities. Wind vectors shown represent the improvements in the vector density realized in this decade. The images are from 25 August 1998 during Hurricane Bonnie. Heights of the wind vectors (see section 2b) are indicated by colour; yellow between 150 and 250 hPa, orange between 251 and 350 hPa, and white between 351 and 600 hPa.

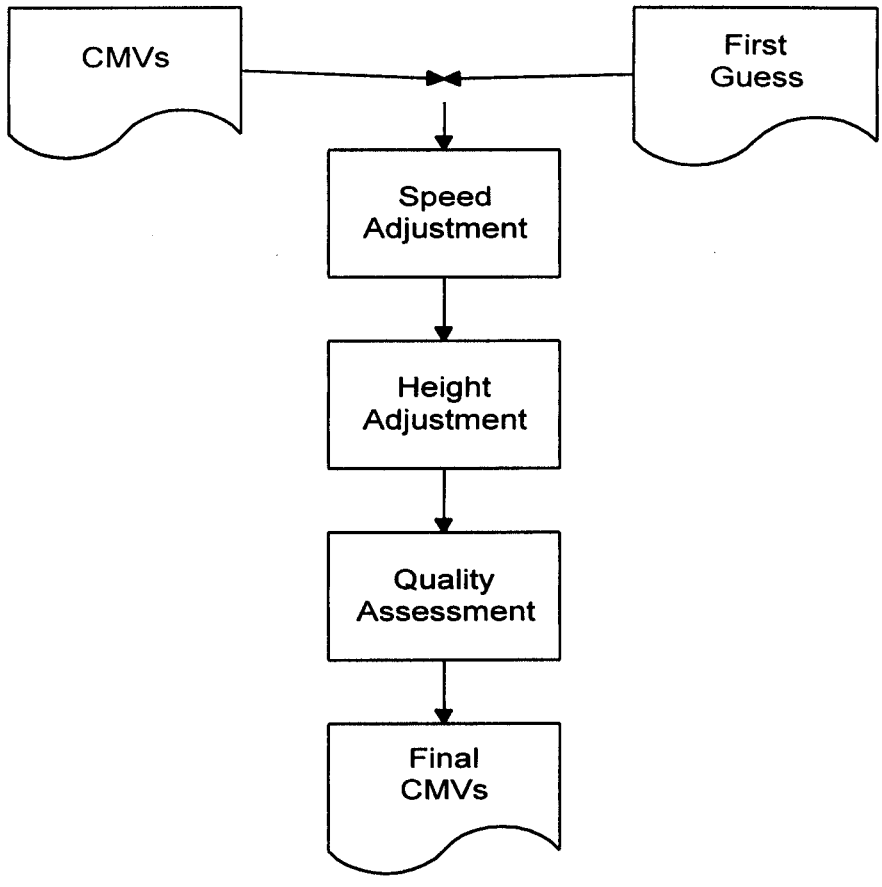

Figure 9.7. Simple schematic of the procedure for editing cloud motion vectors.

CHAPTER 10

APPLICATIONS OF GEOSTATIONARY SATELLITE SOUNDING DATA

10.1 Detection of Temporal and Spatial Gradients

The algorithms for deriving meteorological parameters from sounding radiance data have been implemented by NOAA/NESDIS so that real time GOES data ingest is translated into near real time (within one hour) parameter production. Some spatial averaging is done to reduce instrument noise. Soundings are performed every 50 to 100 km in clear skies. To ensure reliable detection of cloud contamination, objective cloud checking and editing of the data is performed in the automated processing prior to the spatial averaging and calculation of meteorological parameters. After completion of the automated processing, derived product images or contour analyses of the results are displayed for nowcasting or forecasting applications.

It is important to note that the major strength of satellite measurements is the detection of temporal or spatial gradients for a given parameter. Comparison of absolute values a given parameter with another technique for measuring or inferring the same parameter is often misleading. The comparison of GOES retrievals to radiosonde measurements is not ideal due to differing measurement characteristics (point versus volumetric), co-location errors (matches are restricted to 0.25 degrees), time differences (within one hour), and radiosonde errors (Pratt 1985; Schmidlin 1988). However, it has become the standard approach for GOES sounding validation. A study of the GOES retrievals for eleven months (April 1996 to February 1997) indicates that they are more accurate than the NCEP short-term, regional forecasts, for both temperature and moisture, even in the vicinity of the radiosonde where they must necessarily be verified (Schmit 1996).

The following sections present applications of GOES sounding data where gradients in space and time revealed atmospheric conditions not readily found in other measurements.

10.2 VAS Detection of Rapid Atmospheric Destabilization

VAS data obtained on 20 July 1981 demonstrate the VAS nowcasting capabilities. Although hourly results were achieved, they are too numerous to present here; instead, three-hourly results are presented. The overall synoptic situation is shown in Figure 10.1 in the full disc (MSI) 11 micron window and 6.7 micron H_2O images that were obtained on 20 July at mid-day (1730 GMT). The 11 micron image shows that the United States is largely free of clouds, except near the United States-Canadian border where a cold front persists. However, in the 6.7 micron upper tropospheric moisture image, a narrow band of moist air (delineated by the low radiance grey and white areas of the image) stretches from the Great Lakes into the south-western United States.

Figure 10.2 shows contours of derived upper tropospheric relative humidity superimposed over the VAS 6.7 micron brightness temperature images. In this case, the narrow band of moist upper tropospheric air stretching across northern Missouri is the southern boundary of an upper tropospheric jet core (this was shown in Figure 9.2). The south-eastward projection of this moist band and associated jet core is evident. The bright cloud seen along the Illinois-Missouri border in the 21 GMT water vapour image corresponds to a very intense convective storm which developed between 18 and 21 GMT and was responsible for severe hail, thunderstorms, and several tornadoes in the St. Louis, Missouri region.

An objective of the VAS real-time parameter extraction software is to provide an early delineation of atmospheric stability conditions antecedent to intense convective storm development. For this purpose, a total-totals stability index is estimated (as described in Chapter 8). On this day, the atmosphere was moderately unstable over the entire mid-western United States, yet intense localized convection was not observed during the morning hours. In order to delineate regions of

expected intense afternoon convection, three-hourly variations of stability (total-totals) were computed and displayed over the current infrared window cloud imagery on an hourly basis. Figure 10.3a shows the result for 18 GMT. A notable feature is the narrow zone of decreasing stability (positive three-hour tendency of total-totals) stretching from Oklahoma across Missouri and southern Illinois into western Indiana (the +2 contour is drawn boldly in Figure 10.3a). Also shown in Figure 10.3a are the surface reports of thunderstorms which occurred between 21 and 23 GMT. Good correspondence is seen between the past three-hour tendency toward instability and the thunderstorm activity three to five hours ahead.

Figure 10.3b shows the one-hour change in the total-totals index between 17 GMT and 18 GMT. The greatest one-hour decrease of atmospheric stability is along the border between northern Missouri and central Illinois where the tornado-producing storm developed during the subsequent three-hour period (see Figure 10.2d). The stability variation shown was the largest one-hour variation over the entire period studied, 12-21 GMT.

A few detailed sounding results will now be presented for the Missouri region. The soundings were retrieved from VAS DS data with high spatial resolution (roughly 100 km) using the interactive processing algorithms described by Smith and Woolf (1981). Figure 10.4 presents radiosonde observations of 700 mb temperature and retrievals of 700 mb temperature from GOES-5 VAS DS radiance data for a region surrounding the state of Missouri on 20 July 1981. Figure 10.5 shows a similar comparison for the 300 mb dewpoint temperature. Even though the VAS values are actually vertical mean values for layers centred about the indicated pressure levels, it can be seen from the 12 GMT observations that the VAS is broadly consistent with the available radiosondes while at the same time delineating important small scale features which cannot be resolved by the widely spaced radiosondes. This is very obvious in the case of moisture (Figure 10.5) where the horizontal gradients of dewpoint temperature are as great as 10 C over a distance of less than 100 km.

The temporal variations of the atmospheric temperature and moisture over the Missouri region are observed in detail by the three-hour interval VAS observations presented in Figures 10.4 and 10.5. For example, in the case of the 700 mb temperature, the VAS observes a warming of the lower troposphere with a tongue of warm air protruding in time from Oklahoma across southern Missouri and northern Arkansas; the maximum temperatures is observed around 18 GMT in this region. Although it is believed to be a real diurnal effect, undetected by the 12-hour interval radiosonde data, it is possible that it has been exaggerated by the influence of high skin surface temperature. This problem needs to be investigated further. The temporal variation of upper tropospheric moisture may be seen in Figure 10.5; a narrow intense moist tongue (high dewpoint temperature) across north-western Missouri steadily propagates south-eastward with time. The dewpoint temperature profile results achieved with the interactive profile retrieval algorithm are consistent with the layer relative humidity produced automatically in real time (shown in Figure 10.2). It is noteworthy that over central Missouri, where the intense convective storm developed, the VAS observed a very sharp horizontal gradient of upper tropospheric moisture just prior to and during the storm genesis between 18 and 21 GMT. Here again, the inadequacy of the radiosonde network for delineating important spatial and temporal features is obvious. The discrepancy between the 21 MT VAS and 24 GMT radiosonde observation over southern Illinois (Figure 10.5) is due to the existence of deep convective clouds. A radiosonde observed a saturated dewpoint value of -34 degrees Centigrade in the cloud while VAS was incapable of sounding through the heavily clouded area. Nevertheless, it appears that the VAS DS data provide, for the first time, the kind of atmospheric temperature and moisture observations needed for the timely initialization of a mesoscale numerical model for predicting localized weather.

Figure 9.2 shows streamlines and isotachs of 300 mb gradient winds derived from the VAS temperature profile data, where the curvature term was approximated from the geopotential contours. There is agreement (not shown) between the VAS 12 GMT gradient winds and the few radiosonde observations in this region. As can be seen, there is a moderately intense subtropical jet stream

which propagates east-south eastward with time. Note that at 18 GMT, the exit region of the jet is over the area where the severe convective storm developed. As shown by Uccellini and Kocin (1981), the mass adjustments and isallobaric forcing of a low level jet produced under the exit region of an upper tropospheric jet streak can lead to rapid development of a convectively unstable air mass within a three to six-hour time period.

Figure 10.6 shows the three-hour change of total precipitable water prior to the severe convective storm development. The instantaneous fields from which Figure 10.6 was derived showed a number of short-term variations. Nevertheless, it is probably significant that a local maximum exists over the location of the St. Louis storm prior to its development. It is suspected that the convergence of lower tropospheric water vapour is a major mechanism for the thermodynamic destabilization of the atmosphere leading to severe convection between 18 and 21 GMT along the Missouri-Illinois border.

The VAS geostationary satellite sounder demonstrated the exciting new opportunities for real-time monitoring of atmospheric processes and for providing, on a timely basis, the vertical sounding data at the spatial resolution required for initializing mesoscale weather prediction models. Results from this case study and others not reported here suggested that VAS detected, several hours in advance, the temperature, moisture, and jet streak conditions forcing severe convective development. This work was reported by Smith *et al* in 1982. The operational geostationary sounding capability demonstrated by the experimental VAS was realized with the operational GOES Sounder (Menzel and Purdom, 1994)

10.3 Operational GOES Sounding Applications

An effective display of the sounding information is the derived product image (DPI) wherein a product such as total column precipitable water vapour (PW) is colour coded and clouds are shown in shades of gray (Hayden *et al*, 1996). Routinely, three DPIs are generated by NESDIS every hour depicting atmospheric stability, atmospheric water vapour, and cloud heights. Each FOV thus contains information from the GOES sounder with the accuracy discussed in the previous sections, but the time sequences of the GOES DPI make the information regarding changes in space and time much more evident.

One example of an atmospheric stability DPI is shown in Figure 10.7. The GOES-8 lifted index (LI) image (bottom panel) indicates very unstable air over central Wisconsin at 2046 UTC on 18 July 1996. Generally unstable air (LI of -3 to -7 C) is evident along the synoptic scale cold front which ran just south of the Minnesota and Iowa border. However, the most unstable air is indicated as small local pockets in central Wisconsin (LI of -8 to -10 C). These localized regions stand in sharp contrast to the stable air (positive LIs) seen entering Wisconsin from Minnesota. Three hours later a tornado devastated Oakfield, WI. The GOES visible image clearly shows the associated cloud features (top panel). A timely tornado warning by the NWS helped to prevent any loss of life, in spite of heavy property damage. This stability information from the GOES sounder was available and supported the warning decision.

Another example of the lifted index of atmospheric stability DPI from 25 June 1998 is shown in Figure 10.8. On this afternoon a cold front moved south across the western Great Lakes; extreme instability, high moisture, surface convergence associated with the front, and an upper level vorticity pattern across Minnesota / Wisconsin all favoured strong convective development. More than ten instances of severe weather (including four tornadoes) were reported that evening along the Wisconsin / Illinois border. The DPI sequence (Figure 10.8, top) shows the progression of the unstable region; at 00 UTC, radiosonde reports of lifted indices are overlaid as are the wind reports (Figure 10.8, bottom). The GOES and the radiosonde are in close agreement, but the radiosonde network is unable to detail the area under severe weather threat.

Figure 10.9 show the LI DPI from 1200 to 1800 UTC on 3 May 1999 in the south- mid-western United States. A line of unstable air is moving across Oklahoma and Texas. A tornado devastated Oklahoma City at 0000 UTC. NWS forecasters are using the GOES DPI to fill in gaps in the conventional data network. Hourly sequences of GOES DPI help to confirm atmospheric trends. The sounder is able to provide useful information to the forecaster in the nowcasting arena.

Sounder data also has been used to improve forecasts of the minimum and maximum diurnal temperatures. Using the sounder estimates of cloud heights and amounts, the 24 hour forecast of hourly changes in surface temperature can be adjusted significantly. Figure 10.10 shows an example from 20 April 1997 at Madison, WI. The forecast without sounder data indicated a maximum temperature of 64 F should be expected at 2100 UTC (9 hours after 1200 UTC). With sounder data this was changed to 59 F expected two hours earlier at 1900 UTC (7 hours after 1200 UTC). The surface observations in Madison, WI reported a maximum temperature of 58 F at 2000 UTC. This information is being produced daily for agricultural applications in various locations throughout Wisconsin; early feedback has been very positive (Diak *et al*, 1998).

During July and August 1999 forecasters in the United States were asked to comment on their operational use of sounder data. 37 forecast offices and 4 national centres participated in the evaluation, providing 635 responses via a web based questionnaire. Forecasters used the Sounder products as tools to evaluate the potential of a wide variety of weather events, including tornadoes, severe thunderstorms, monsoon precipitation, and flash flood events. Their responses showed that in over 79% of all non-benign weather situations, the use of GOES sounder products led to improved forecasts and the issuance of improved forecast products. Overall, forecasters found the sounder products to be valuable operational tools, providing information on the vertical structure of the atmosphere, especially the moisture distribution, with a temporal and spatial resolution not available from any other source.

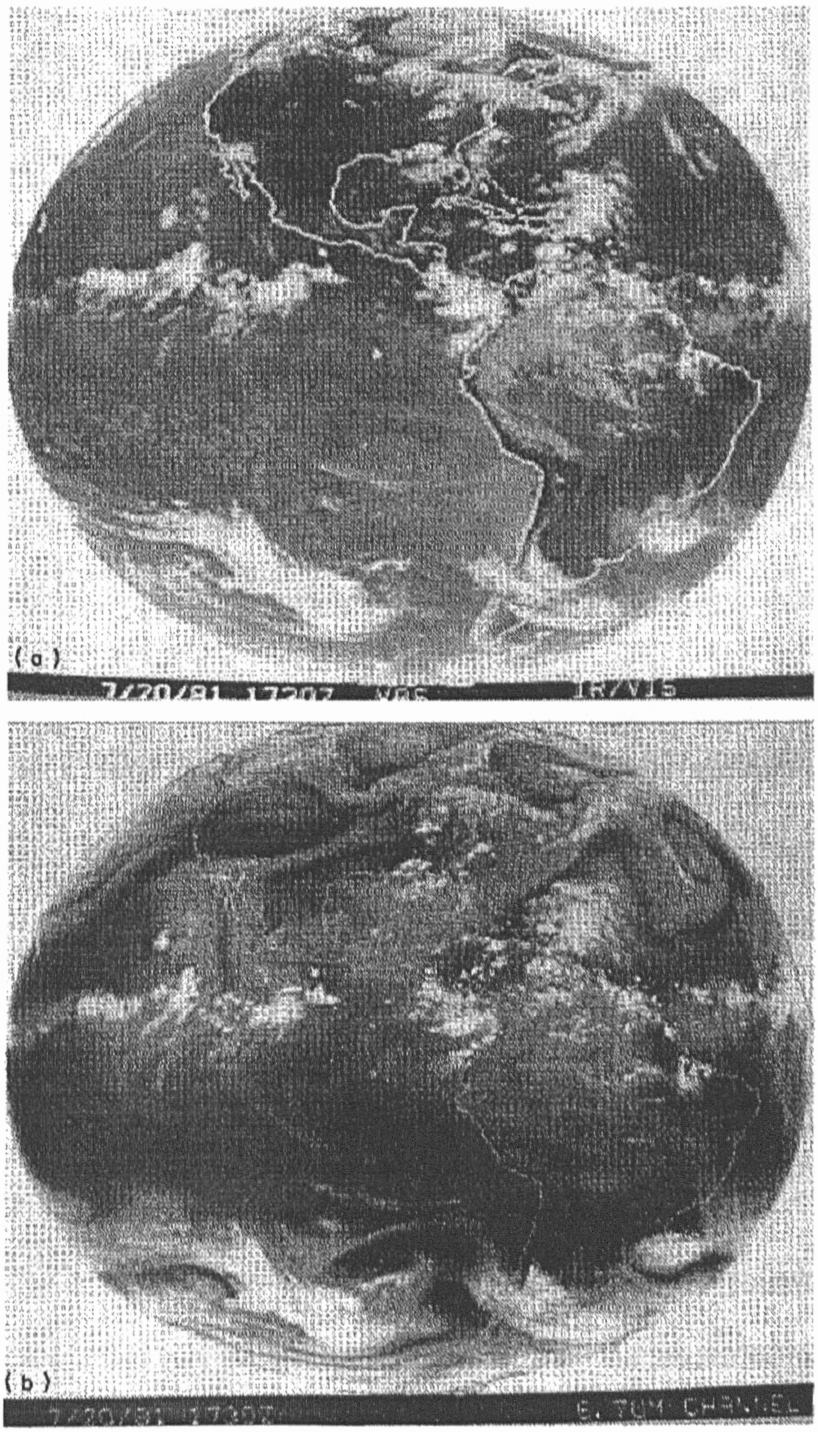

Figure 10.1: Full disk images obtained on 20 July 1981 between 1730 and 1800 GMT; (a) long-wave infrared window at 11.2 microns, and (b) water vapour band at 6.7 microns.

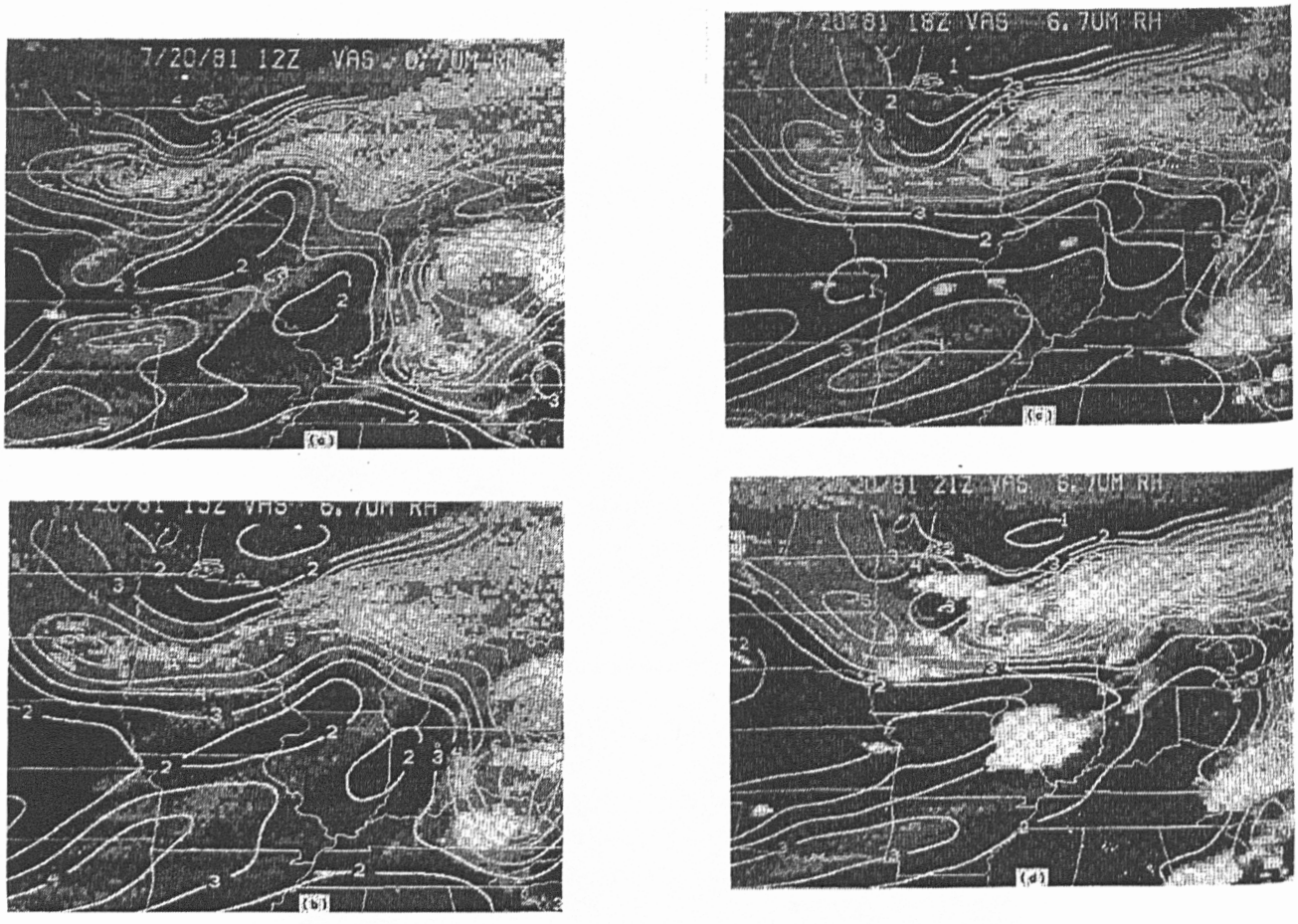

Figure 10.2: Upper tropospheric relative humidity (%/10) superimposed over the VAS image of 6.7 micron atmospheric water vapour radiance emission for (a) 12 GMT, (b) 15 GMT, © 18 GMT, and (d) 21 GMT on 20 July 1981.

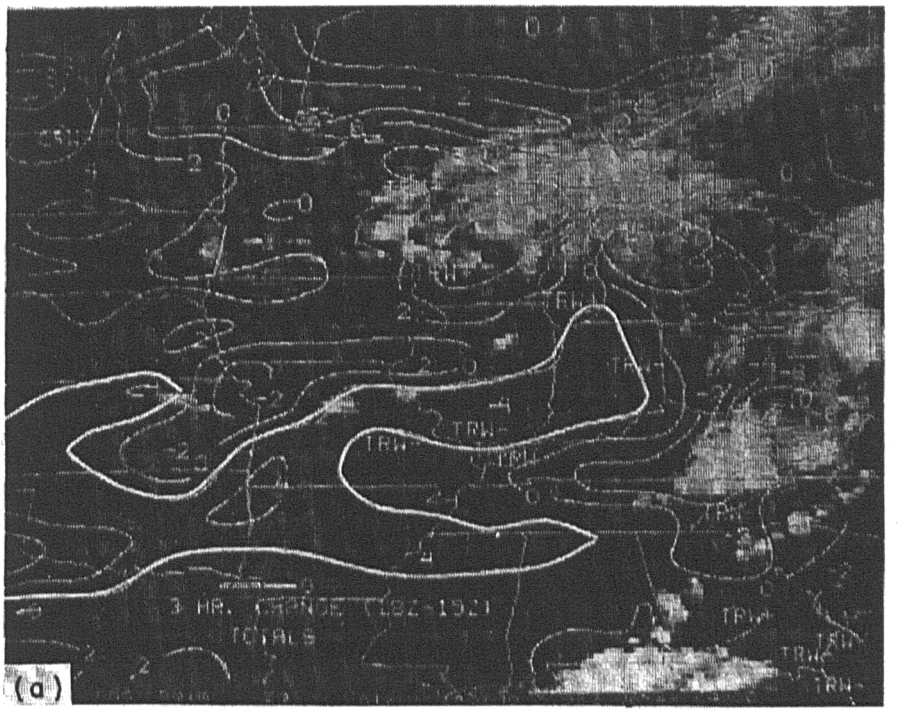

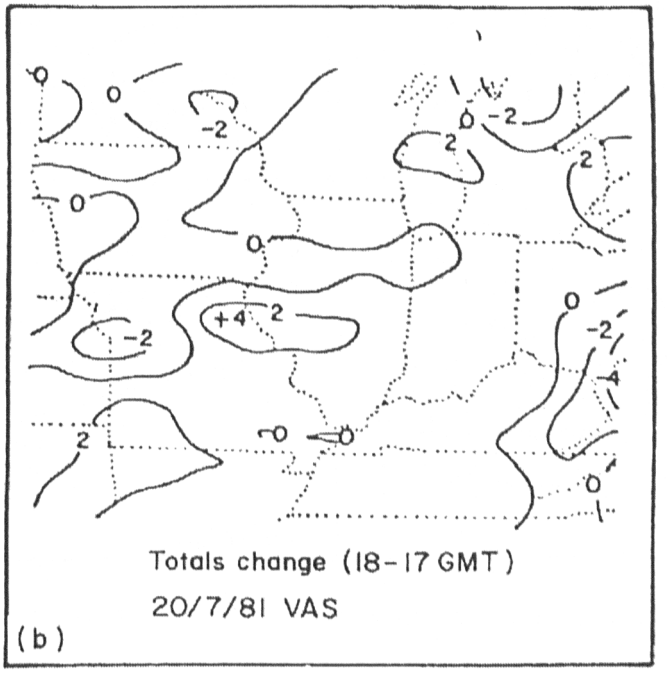

Figure 10.3: (a) Three hour variation of VAS derived Total-Totals Index (degree Centigrade) between 15 and 18 GMT on 20 July 1981 superimposed over the 18 GMT VAS infrared window image of cloudiness. The symbols of thunderstorms (TRW) which were observed between 20 and 23 GMT are also shown. (b) One hour variation of VAS derived Total-Totals Index (degree Centigrade) between 17 and 18 GMT on 20 July 1981 showing that the maximum one hour change (4 degrees C) occurred at the location of and just prior to the development of a severe convective storm.

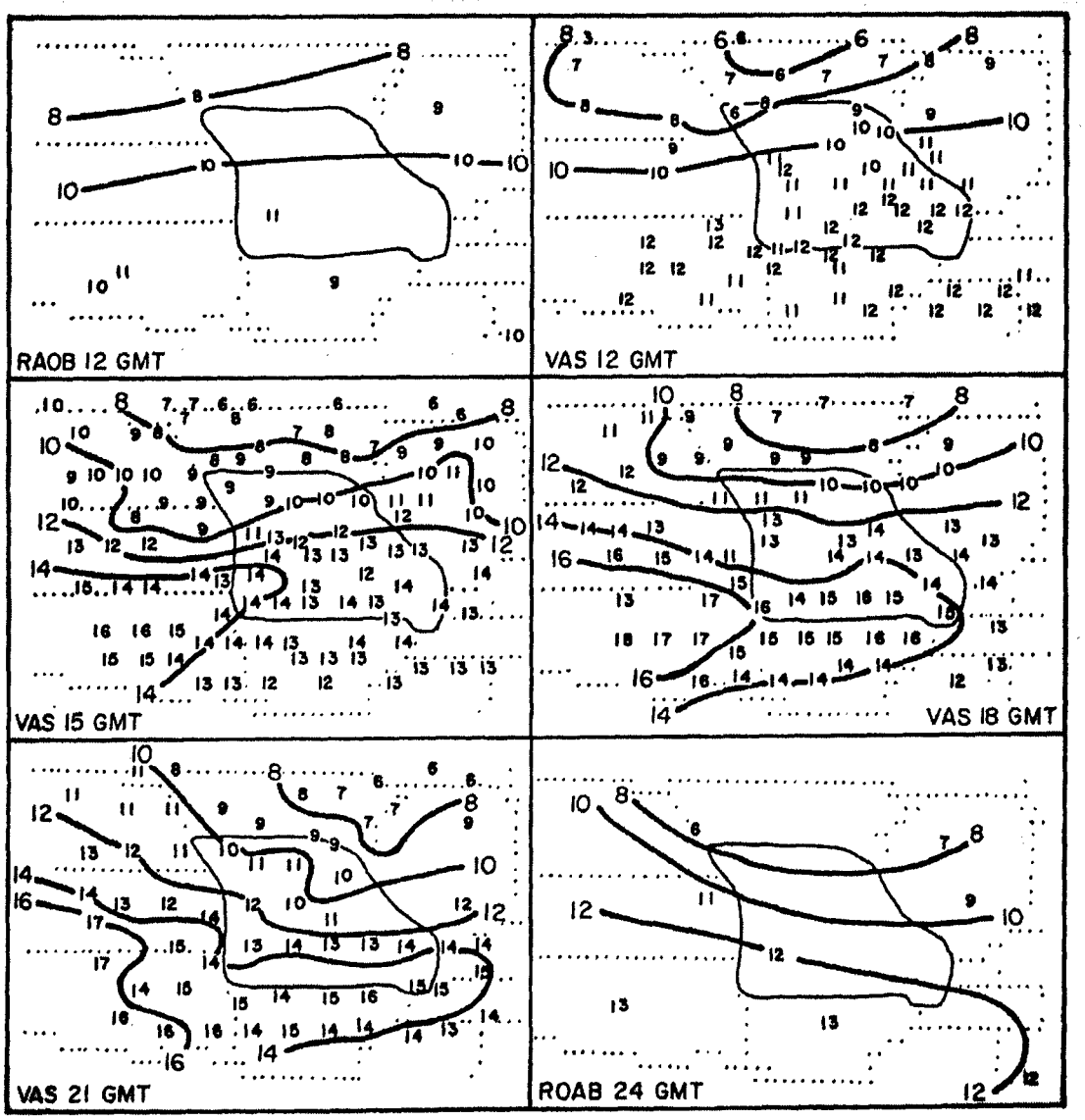

Figure 10.4: Radiosonde and VAS observations of 700 mb temperature (degree Centigrade) on 20 July 1981.

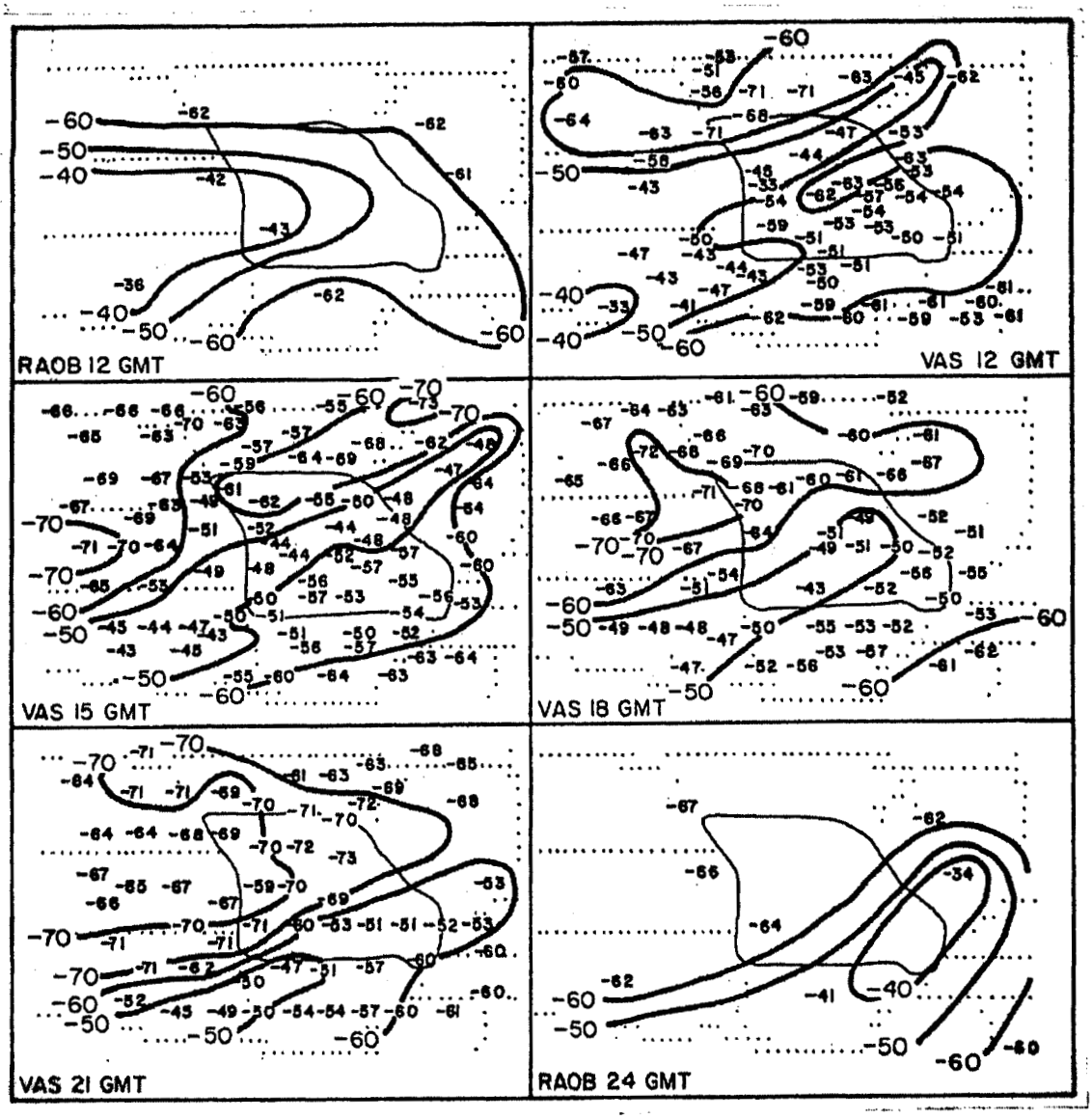

Figure 10.5: Radiosonde and VAS observations of 300 mb dewpoint temperature (degrees Centigrade) on 20 July 1981.

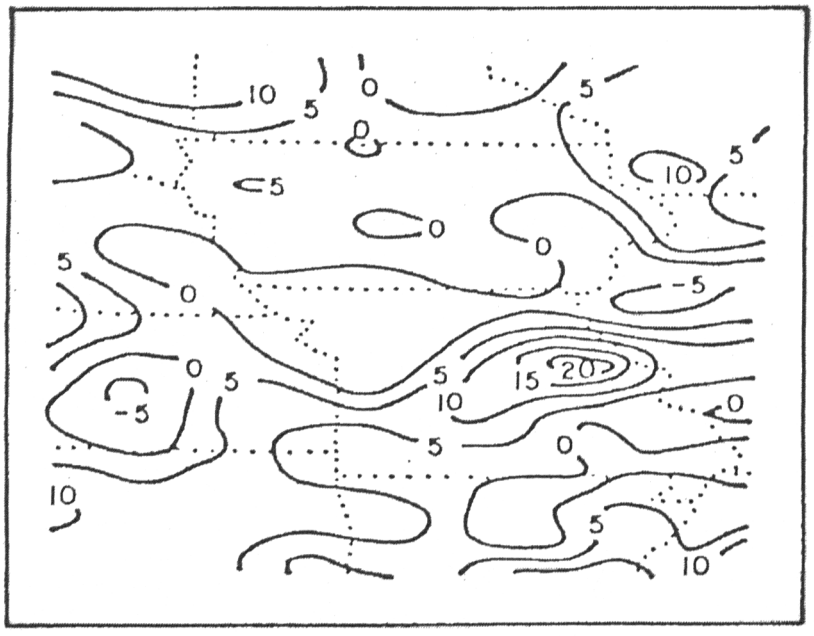

Figure 10.6: Three hour change of precipitable water vapour (millimetres) between 15 and 18 GMT on 29 July 1981.

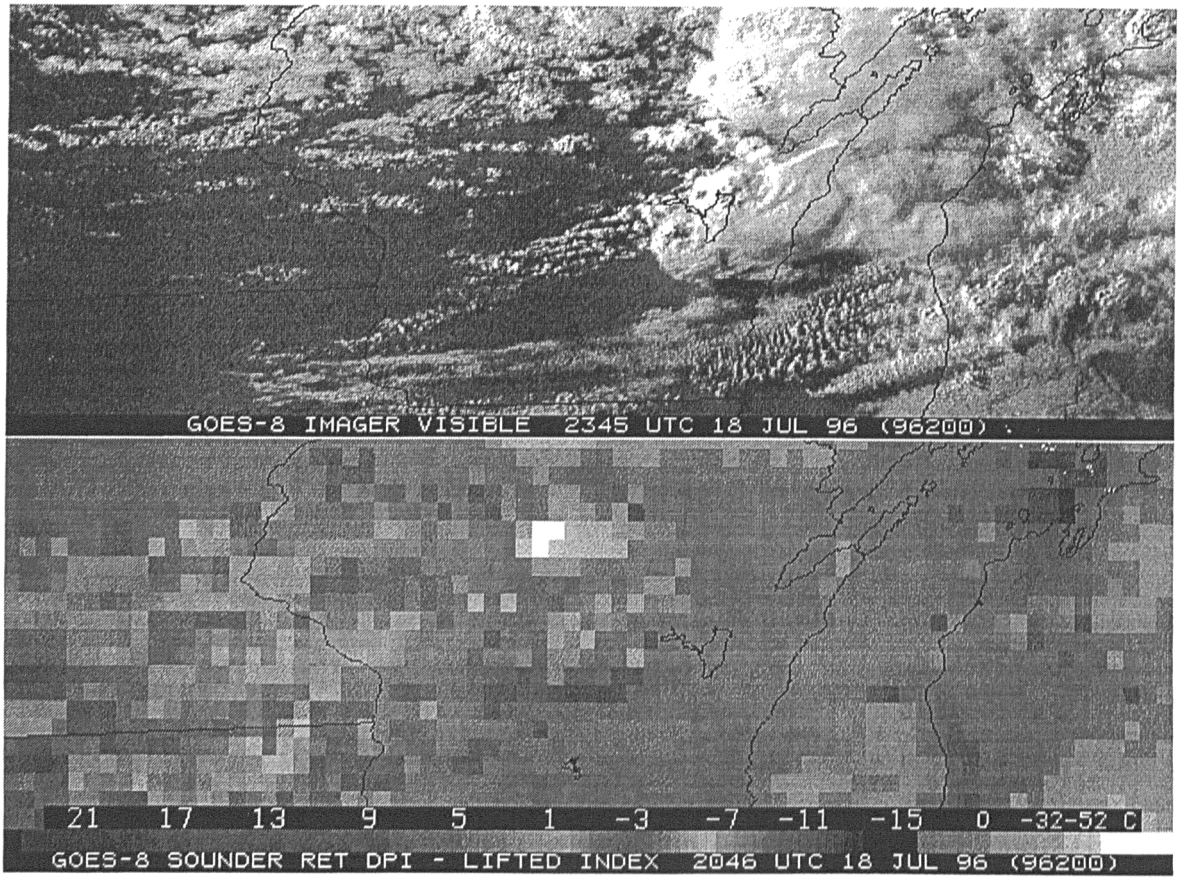

Figure 10.7: An example of the atmospheric stability DPI from 18 July 1996. The GOES-8 lifted index image (bottom panel) indicates very unstable air over central Wisconsin at 2046 UTC. Three hours later a tornado devastated Oakfield, Wisconsin. The GOES visible image from 2345 UTC clearly shows the associated cloud features (top panel).

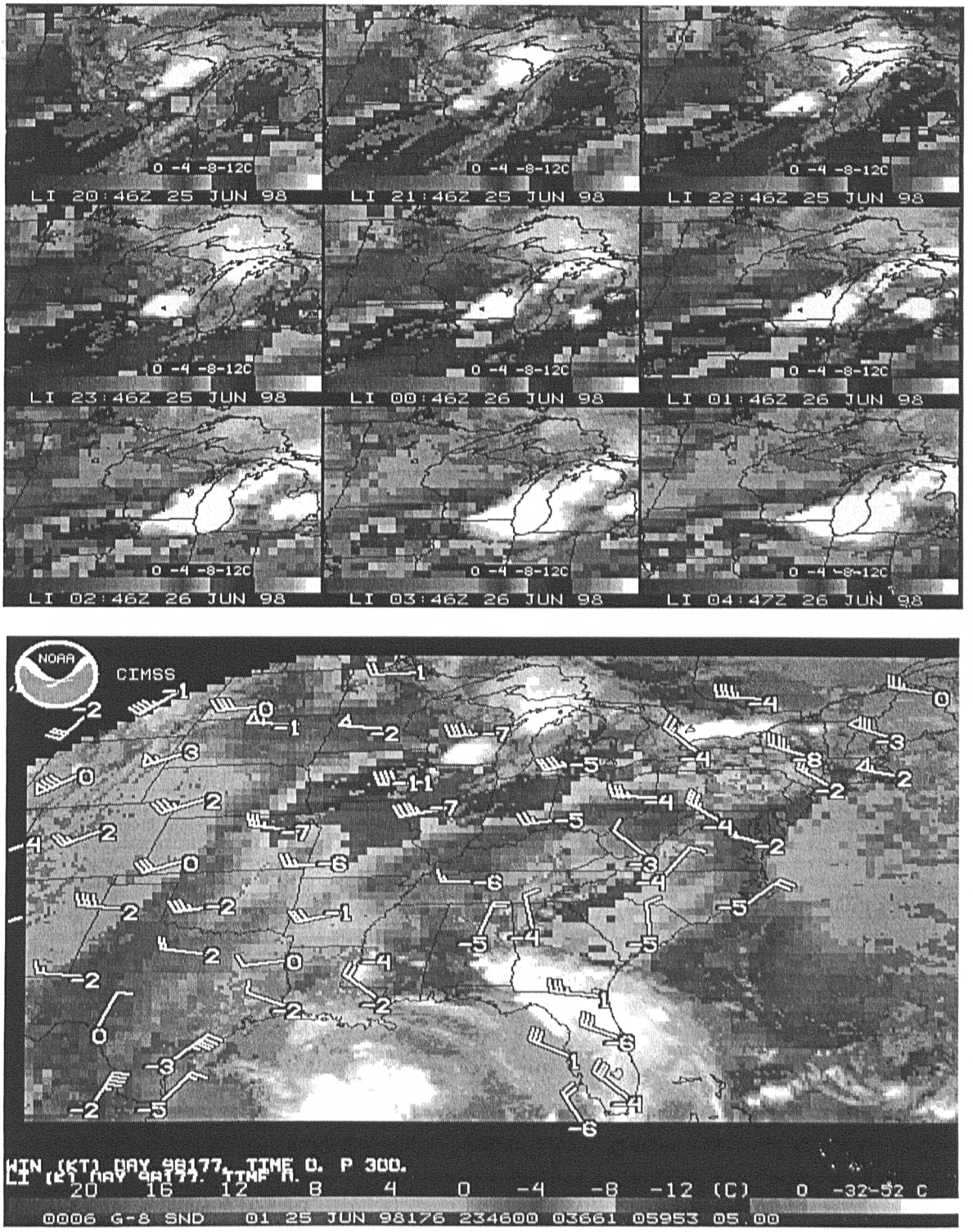

Figure 10.8: (top) GOES DPI of Lifted Index from 2046 to 0446 UTCat 2346 UTC on 25 June 1998 show extreme instability associated with a frontal passage across Minnesota and Wisconsin. (bottom) Radiosonde reports of lifted indices are overlaid on 2346 UTC DPI as are the wind reports.

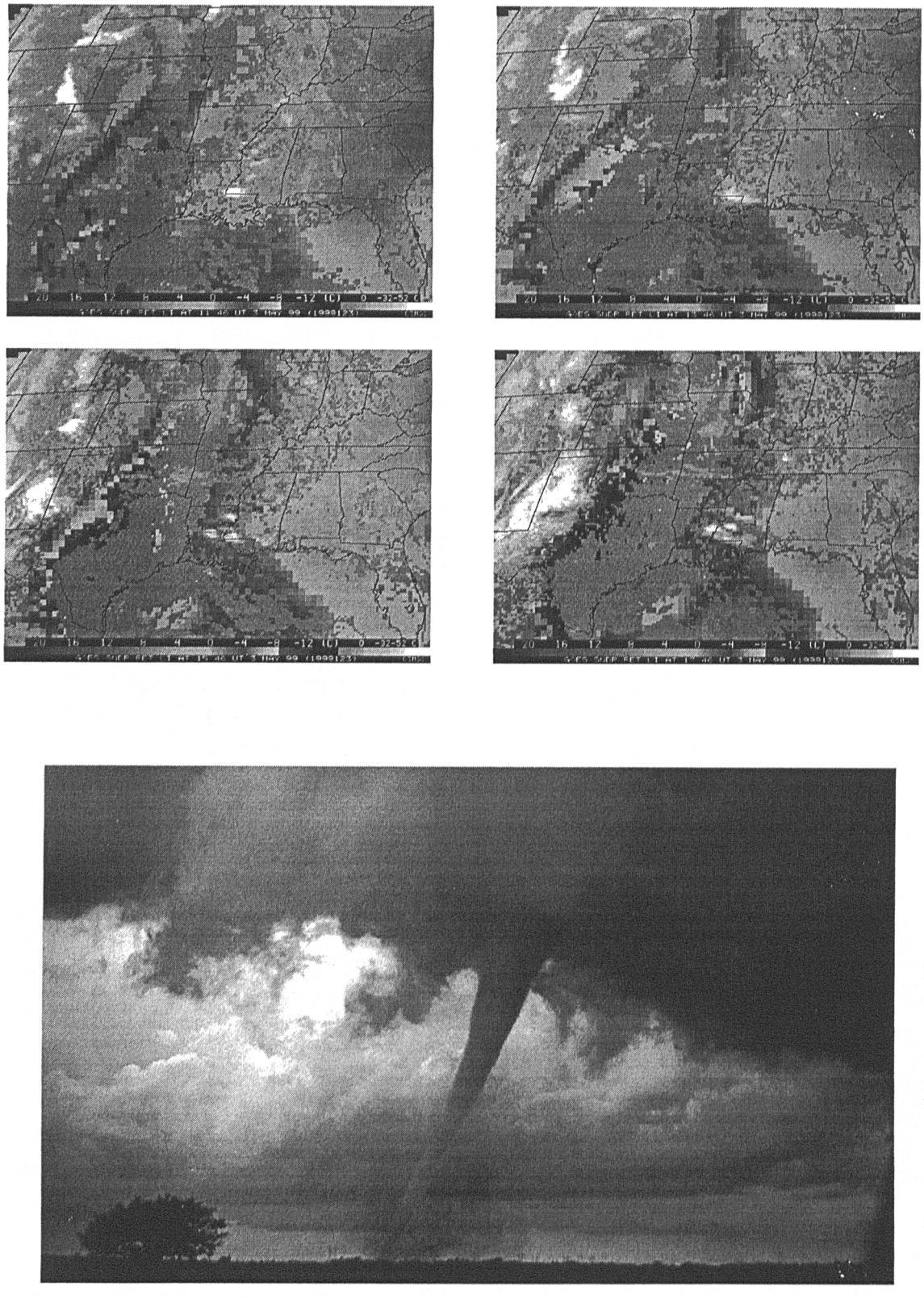

Figure 10.9: (top) GOES DPI of Lifted Index from 1146 to 1746 UTC on 3 May 1999 show extreme instability associated with a frontal passage across Oklahoma and Texas. (bottom) Tornado in vicinity of Oklahoma City viewed at 0000 UTC.

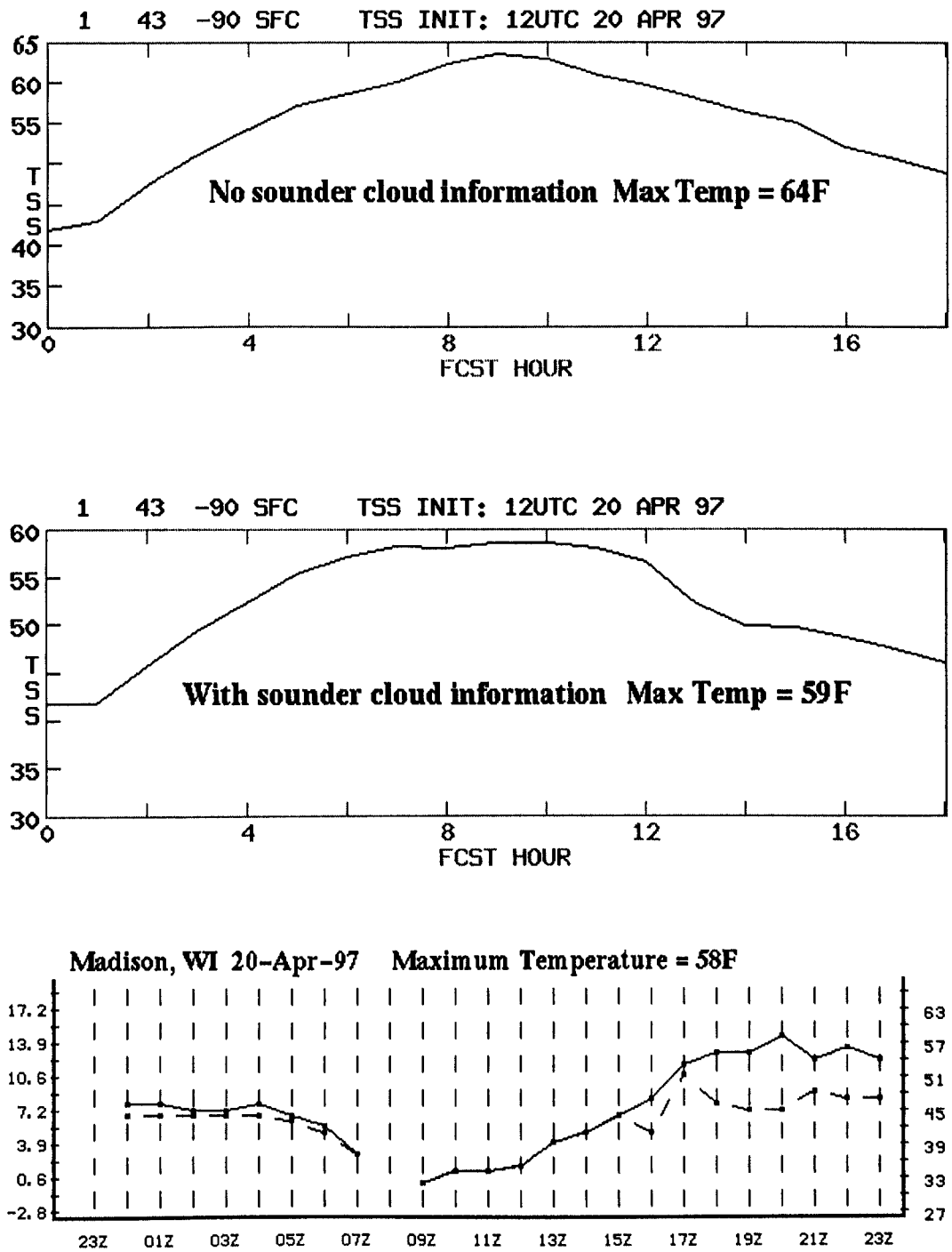

Figure 10.10: Maximum temperatures forecast with and without GOES sounder data for 20 April 1997 in Madison, WI. Without sounder data a maximum temperature of 64 degrees F at 2100 UTC was forecast (9 hours after 1200 UTC, top panel) and with sounder data he forecast was adjusted to 59 degrees F at 1900 UTC (7 hours after 1200 UTC, middle panel); the surface observations report a maximum temperature of 58 degrees F at 2000 UTC (bottom panel).

CHAPTER 11

SATELLITE ORBITS

11.1 Orbital Mechanics

Newton's laws of motion provide the basis for the orbital mechanics. Newton's three laws are briefly: (a) the law of inertia which states that a body at rest remains at rest and a body in motion remains in motion unless acted upon by a force; (b) force equals the rate of change of momentum for a body; and (c) the law of equal but opposite forces. For a two body system comprising of the earth and a much smaller object such as a satellite, the motion of the body in the central gravitational field can be written

$$\vec{dv} / dt = -GM \vec{r} / r^3$$

where $\vec{v}$ is the velocity of the body in its orbit, G is the universal gravitational constant (6.67 x 10**11 N m**2/kg**2), M is the mass of the earth, and r is position vector from the centre of mass of the system (assumed to be at the centre of the earth). The radial part of this equation has the more explicit form

$$m\, d^2r/dt^2 - mr\omega^2 = -GMm/r^2$$

where ω is the angular velocity and m is the satellite mass. The second term on the left side of the equation is often referred to as the centrifugal force

The total energy of the body in its orbit is a constant and is given by the sum of the kinetic and potential energies

$$E = 1/2\, m\, [(dr/dt)^2 + r^2\omega^2] - mMG/r\,.$$

The angular momentum is also conserved so that

$$L = m\omega r^2\,,$$

which allows us to rewrite the energy

$$E = 1/2\, m\, (dr/dt)^2 + L^2/(2mr^2) - mMG/r\,.$$

The magnitude of the total energy reveals the type of orbit;

$E > 0$	implies an unbounded hyperbola,
$E = 0$	unbounded parabola,
$E < 0$	bounded ellipse,
$E = -G^2M^2m^3/(2L^2)$	bounded circle.

The last two terms of the total energy can be considered as an effective potential energy, which has a minimum for the radius of the circular orbit.

The circular orbit requires that the radius remain constant (so dr/dt equals zero) through the balance of the gravitational and centrifugal forces

$$GMm/r^2 = m\omega^2 r$$

or

$$r = L^2/(m^2MG) .$$

This leads to the expression for the total energy of the satellite in a bounded circle.

It is also worth noting that the conservation of angular momentum is directly related to Kepler's law of equal areas swept out in equal time, since

$$dA/dt = r^2\omega/2 = L/(2m) = \text{constant} .$$

The derivative with respect to time can be rewritten as a derivative with respect to angle through the conversion

$$d/dt = (L/mr^2)d/d\theta$$

so that

$$m\, d^2r/dt^2 = (L/r^2)d/d\theta[(L/mr^2)dr/d\theta]$$

and using u = 1/r this becomes

$$[d^2u/d\theta^2 + u] = GMm^2/L^2 .$$

The solution has the form of the equation for a conic section

$$1/r = [GMm^2/L^2]\,[1 + \varepsilon \cos\theta]$$

where the eccentricity ε is given by

$$\varepsilon^2 = [1 + 2EL^2/(G^2M^2m^3)]$$

The point of closest approach, the perigee, occurs for $\theta = \pi$; the apogee occurs for $\theta = 0$.

11.2 The Geostationary Orbit

Let us continue our discussion of the circular orbit. Using the definition of angular velocity $\omega = 2\pi/\tau$ where τ is the period of the orbit, then

$$GMm/r^2 = m\omega^2 r$$

becomes

$$GM/r^3 = 4\pi^2/\tau^2 .$$

For the geostationary orbit, the period of the satellite matches the rotational period of the earth so that the satellite appears to stay in the same spot in the sky. This implies that τ = 24 hours = 8.64x10**4 seconds, and the associated radius of the orbit r = 4.24x10**7 metres or a height of about 36,000 km. The geostationary orbit is possible at only one orbit radius.

For a polar circular orbit with τ = 100 minutes = 6x10**4 seconds, we get r = 7.17x10**6 metres or a height of about 800 km. Polar orbits are not confined to a unique radius, however the type of global coverage usually suggests a range of orbit radii.

It is useful to note that

$$g = 9.8 \text{ m/s}^2 = GM/R^2$$

where R is the radius of the earth (about 6400 km).

11.3 Orbital Elements

A detailed knowledge of orbits allows the determination of what areas will be viewed by the satellite, how often, and when. Proper adjustment of the orbit can enhance repeated coverage of one area at the same time each day or repeated coverage of the same area every few minutes throughout the day. The coverage depends on six orbital elements.

To a first approximation a satellite close to the earth has an elliptical orbit. The orientation of the satellite orbit plane is described by (a) the inclination of the satellite orbit plane with respect to the earth equatorial plane denoted by I, and (b) the right ascension of the ascending node, Ω, measured eastwards relative to Aries (representing a fixed point in the heavens). The shape and size of the satellite orbit is given by (c) the semi-major axis of the ellipse denoted by a, and (d) the eccentricity of the ellipse, denoted by ε. The orientation of the orbit in the orbit plane is given by (e) the argument of the perigee or the angle between the ascending node and the perigee denoted by w. And finally (f) θ denotes the angular position of the satellite in its orbit. These are the six orbital elements that are necessary to calculate the trajectory of the satellite in its orbit; they are shown in Figures 11.1 and 11.2.

The geostationary orbit provides good temporal (half hourly) and spatial coverage over the equatorial regions (but its viewing angle to the polar regions is poor). On the other hand the polar orbit provides good coverage of the polar regions every 100 minutes (but its viewing over the equatorial regions is incomplete and less frequent). Thus, studies over the tropics and the ITCZ (Inter Tropical Convergence Zone) rely mostly on geostationary satellite data, while the Arctic and Antarctic polar studies depend primarily on polar orbiting satellite data.

The elliptical orbit is an approximation; there are several small perturbing forces which are mentioned briefly here. (a) The earth is not spherical; it exhibits equatorial bulge which perturbs the orbital elements. This is an important correction; (b) Atmospheric drag significantly slows satellites below a height of 150 km, but is very small for orbit heights greater than 1500 km; (c) Solar wind and radiation slightly influence the orbit of satellites with low density; (d) The gravitational influence of the other bodies in the solar system, particularly the sun and the moon, are small but nonzero; (e) Relativistic effects are very small.

The primary influence of the non spherical earth gravitational field is to rotate the orbital plane, to rotate the major axis within the orbital plane, and to change the period of the satellite.

11.4 Gravitational Attraction of Non-spherical Earth

The earth's gravitational field is not that of a point mass, rather it is the integrated sum over the bulging earth. The potential energy for a satellite of mass m a distance r from the centre of mass of the earth is written

$$PE = - Gm \int_{\text{earth}} dM/s$$

where the integration is over the mass increment dM of the earth which is a distance s from the satellite. This integration yields a function in the form

$$PE = -GMm/r \left[1 - \sum_{n=2,\ldots} J_n (R/r)^n P_n(\cos\theta)\right]$$

where the J_n are coefficients of the n^{th} zonal harmonics of the earth's gravitational potential energy and the $P_n(\cos\theta)$ are Legendre polynomials defined by

$$P_n(x) = \frac{1}{n2^n} \frac{d^n}{dx^n} [(x^2-1)^n] .$$

The most significant departure from the spherically symmetric field comes from the n=2 term, which corrects for most of the effects of the equatorial bulge. Therefore

$$PE = -GMm/r \left[1 - J_2 (R/r)^2 (3\cos^2\theta - 1)/2 + \ldots\right]$$

where J_2 = 1082.64x10**-6. At the poles P_2 = 2 and at the equator P_2 = -1. The coefficients for the higher zonal harmonics are three orders of magnitude reduced from the coefficient of the second zonal harmonic.

Equatorial bulge primarily makes the angle of the ascending node vary with time.

11.5 Sun synchronous Polar Orbit

The equatorial bulge primarily makes the angle of the ascending node vary with time. The variation is given by

$$d\Omega/dt = -3/2\ J_2 (GM)^{1/2} R^2 a^{-7/2} (1-\varepsilon^2)^{-2} \cos i$$

Through suitable selection of the orbital inclination i, the rotation of the orbital plane can be made to match the rotation of the earth around the sun, yielding an orbit that is sun synchronous. The negative sign indicates a retrograde orbit, one with the satellite moving opposite to the direction of the earth's rotation. The rotation rate for sun synchronous orbit is given by

$$\Omega = 2\pi/365.24 \text{ radians/year} = 2 \times 10^{-7} \text{ rad/sec} .$$

which is approximately one degree per day. Such a rate is obtained by placing the satellite into an orbit with a suitable inclination; for a satellite at a height of 800 km (assuming the orbit is roughly circular so that a = r), we find i = 98.5 degrees which is a retrograde orbit inclined at 81.5 degrees. The inclination for sun synchronous orbits is only a weak function of satellite height; the high inclination allows the satellite to view almost the entire surface of the earth from pole to pole.

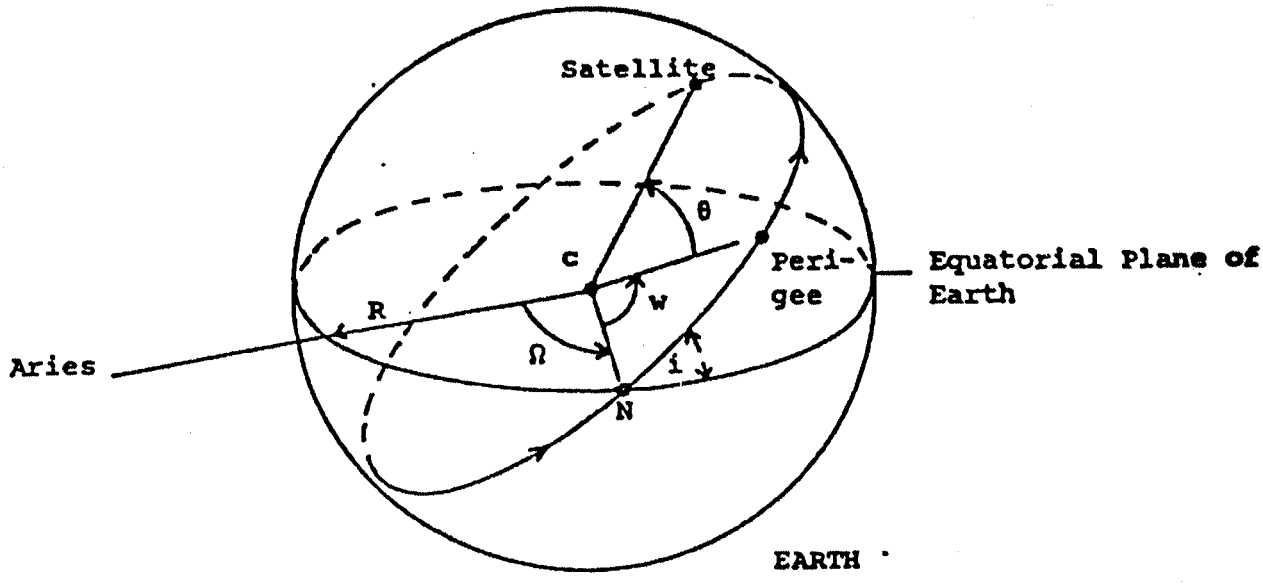

Figure 11.1: Orbital elements for an elliptical orbit showing the projection of the orbit on the surface of a spherical earth. C is the centre of the earth and R is the equatorial radius. i is the inclination of the orbit relative to the equatorial plane, Ω is the right ascension of the ascending node with respect to Aries, a is the semi-major axis of the ellipse, ε is the eccentricity, w is the argument of the perigee, and Θ is the angular position of the satellite in its orbit.

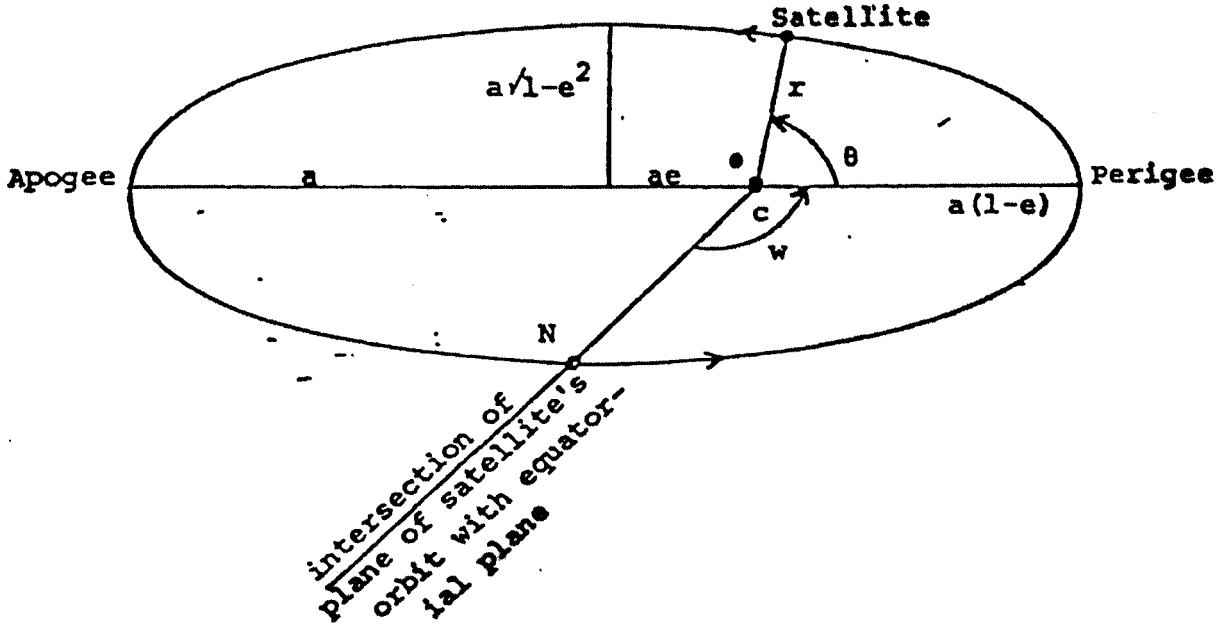

Figure 11.2: Elements of an elliptical orbit in the plane of the satellite orbit..

CHAPTER 12

RADIOMETER DESIGN CONSIDERATIONS

12.1 Components and Performance Characteristics

The optics, detectors, and electronics are the basic elements of a radiometer. The optics collect the radiation, separate or disperse the spectral components, and focus the radiation to a field stop. The detectors, located behind the field stop, respond to the photons with a voltage signal. That voltage signal is amplified by the electronics and converted into digital counts.

Performance of a radiometer is characterized by its responsivity, detectivity, and calibration. The responsivity is a measure of the output per input. The detectivity is expressed as the ratio of the responsivity per noise voltage. Calibration attempts to reference the output to known inputs.

12.2 Spectral Separation

The earth emitted radiation is detected in several spectral regions by radiometers where the spectral separation is accomplished by one of the following approaches. Band pass filters can be used to separate the infrared spectrum into parts of roughly 20 (cm^{-1}). Grating spectrometers and interferometers are capable of spectral resolution ($\lambda / \Delta\lambda$) of about 1 / 1000. All three have been used to remote sense the earth.

12.3 Design Considerations

12.3.1 Diffraction

The mirror diameter defines the ability of the radiometer to resolve two point sources on the earth surface. The Rayleigh criterion indicates that the angle of separation , θ, between two points just resolved (maxima of the diffraction pattern one point lies on the minima of the diffraction pattern of the other point)

$$\sin \theta = \lambda / d$$

where d is the diameter of the mirror and λ is the wavelength. The GOES satellite mirror diameter is 30 cm, so at infrared window wavelengths (10 microns) the resolution is about 1 km. This follows from

$$10^{-5} \text{ m} / 3 \times 10^{-3} \text{ m} = 3.3 \times 10^{-4} = r / 36{,}000 \text{ km}$$

or

$$r = 1 \text{ km} = \text{resolution.}$$

Diffraction is an important consideration when seeking clear FOVs in the vicinity of clouds. Clouds can affect measured radiances even when they are not directly in the FOV of the sensor. When clouds are close enough to the FOV, diffraction causes some of the radiation received by the sensor to emanate from the clouds instead of from the clear area within the FOV. As clouds are typically colder than the clear earth-atmosphere, measured radiances are lower than expected from a clear FOV. Sensors in geostationary orbit are usually diffraction limited because the FOV is small for the mirror diameter in order to achieve maximum spatial resolution. Thus when sounding with the geostationary sounders, the clear FOV must be sufficiently far away from cloud contamination to assure correct profile retrieval or a correction must be applied for cloud diffraction into the FOV.

Figure 12.1a shows the calculated diffraction effects for the new GOES imager for infrared window radiation in a clear scene of brightness temperature 300 K surrounded by clouds of 220, 260,

or 280 K. The size of the clear scene is varied and the change in brightness temperature is plotted. These results use a FOV radius of 2 km, a mirror diameter of 31 cm, and a wavelength of 11 microns. Diffraction effects are noticeable for clear scenes as large as 50 km radius; for a cold cloud at 220 K, the brightness temperature of a 10 radius clear hole is too cold by about 1.5 K. Figure 12.1b shows the same plot for the GOES sounder infrared window with an 4 km radius FOV and the same optics; the diffraction effect is mitigated somewhat by the larger FOV of the sounder. Figure 12.1 indicates that to obtain clear sky brightness temperature within 1 K the clear area must be at least 15 km (10 km) in radius for the imager (sounder).

Diffraction is usually specified by encircled energy, the fraction of the total detected signal emanating from a circle of given size. For the GOES-8 imager infrared window this is given by 60% of the signal must come from a circle of one FOV diameter, 73% from 1.25 FOV diameter, and 79% from 1.5 FOV diameter.

12.3.2. The Impulse or Step Response Function

The detector collects the incident photons over a sampling time and accumulates a voltage response, which is filtered electronically. This is often characterized by the impulse (or step) response function, which details what the response of the sensor is to a delta (or step) function input signal. The response function is determined from the characteristics of the prealiasing filter which collects the voltage signal from the detector at the sampling times.

A perfect response of the detector continuously sampling a scene with a 100% contrast bar extending one FOV is indicated in Figure 12.2. As the detector crosses the contrast bar, the response ramps up linearly from 0 to 1 in the time it takes to move a distance of one FOV and then ramps down from 1 to 0 in a symmetric fashion. The actual response of the GOES-8 filter is also indicated in Figure 12.2. The shape a delay of the signal are noticeable. The filter delay causes an offset which can be corrected electronically. Sampling occurs every 183 microseconds or 1.75 times per FOV; the sampling interval is 4/7 of the time it takes to move one FOV.

Correcting for the time offset, the percentage of the total signal appearing in the samples preceding and following the correlated sample peak can be estimated. For GOES-8 infrared window samples one finds that sample N-2 has 4.3% of the total signal, N-1 has 26.5%, N peaks with 44.8%, N+1 has 23.4%, and N+2 has 1.0%. This causes a smearing of cloud edges and other radiance gradients.

Figure 12.3 shows the step response function for GOES-8. The filter output takes about 400 (or about 2 samples) microseconds to respond full scale to the step function input at time t=0.

12.3.3 Detector Signal to Noise

The noise equivalent radiance for an infrared detector can be expressed as

$$NEDR(\nu) = \gamma \, [Ad \, \Delta f]^{1/2} / [Ao \, \tau(\Delta\nu) \, \Omega \, D^* \, \Delta\nu]$$

where

γ is the preamplifier degradation factor which includes the effects of both preamplifier noise and signal loading

Ad is the detector area in cm2

Δf is the effective electronic bandwidth of the radiometer

Ao is the mirror aperture area in cm2

$\tau(\Delta\nu)$ is the transmission factor of the radiometer optics in the spectral interval $\Delta\nu$

Ω is the solid angle of the FOV in steradians

D* is the specific spectral detectivity of the detector in the spectral band in cm $Hz^{1/2}$ / watt, and

$\Delta\nu$ is the spectral bandwidth of the radiometer at wavenumber ν in cm-1.

Figure 12.4 indicates the spectral regions where the InSb and HgCdTe detectors show skill in detecting infrared radiation. The values of NEDR for the GOES-8 imager are indicated below.

Band	Wavelength (micron)	Detector	NEDR (mW/m2/ster/cm-1)	NEDT (K)
1	.52 - .75	Silicon	(3 of 1023 counts is noise)	
2	3.83-4.03	InSb	0.0088	0.23 @ 300 K
3	6.5 - 7.0	HgCdTe	0.032	0.22 @ 230 K
4	10.2-11.2	HgCdTe	0.24	0.14 @ 300 K
5	11.5-12.5	HgCdTe	0.45	0.26 @ 300 K

12.3.4 Infrared Calibration

The radiometer detectors are assumed to have linear response to infrared radiation, where the target output voltage is given by

$$Vt = \alpha\, Rt + Vo$$

and Rt is the target input radiance, α is the radiometer responsivity, and Vo is the system offset voltage. The calibration consists of determining α and Vo. This is accomplished by exposing the radiometer to two different external radiation targets of known radiance. A blackbody of known temperature and space (assumed to emit no measurable radiance) are often used as the two references. If z refers to space, bb the blackbody, the calibration can be written as

$$Vz = \alpha\, Rz + Vo$$

$$Vbb = \alpha\, Rbb + Vo$$

where

$$\alpha = [Vbb - Vz]/[Rbb - Rz]$$

and

$$Vo = [Rbb\, Vz - Rz\, Vbb]/[Rbb - Rz]$$

Using Rz=0 this yields

$$Rt = Rbb\,[Vt - Vz] / [Vbb - Vz].$$

For HgCdTe detectors there sometimes is a non-linearity in the response to high photon bombardment occurring in the infrared window. In this case the IR calibration equation is given by,

$$R = q C^2 + m C + b$$

where R = calibrated scene radiance (dropping the t for target),
C = digital counts (derived from the detector voltage with a linear analogue to digital converter),
q = second order gain (non-linear term),
m = first order gain (slope), and
b = count offset.

The second order gain is estimated before launch in vacuum tests as a function of radiometer temperature. The first order gain is obtained from the blackbody and space looks in flight (this occurs within every 20 minutes with GOES-8),

$$m = [Rbb - q (Cbb^2 - Cz^2)] / [Cbb - Cz]$$

and the count offset is updated after every space look (about every 2 minutes for GOES-8) using,

$$b = -m Cz - q Cz^2$$

where Rbb is calculated from blackbody thermistor data telemetered down from the spacecraft, and

Cbb = digital counts during blackbody view, and

Cz = digital counts during space view (before blackbody view).

The scan mirror of the radiometer telescope is usually not a perfect reflector, so there is some emission from the mirror that must be accounted for in the calibration algorithm. If the scan mirror emissivity is isotropic (independent of viewing angle), then its contributions to the target, blackbody, and space looks is constant and does not affect the calibration algorithm. However if the scan mirror emissivity changes with viewing angle, then the radiance detected must be written

$$R` = [1 - \varepsilon(\theta)] Rt + \varepsilon(\theta) Rm$$

where Rm denotes the mirror emitted radiance, Rt is the target radiance, and $\varepsilon(\theta)$ is the scan mirror emissivity at angle θ. Then including the correction for the scan mirror emissivity variation, the first order gain is calculated after each blackbody view using,

$$m` = [Rbb` - q (Cbb^2 - Cz^2)] / [Cbb - Cz]$$

where

$$Rbb` = [1 - \varepsilon(\theta bb)] Rbb + [\varepsilon(\theta bb) - \varepsilon(\theta z)] Rm$$

and

θbb = scan mirror angle while viewing the blackbody (incidence angle of bb radiation is about 45 degrees),
θz = scan mirror angle while viewing space (at about 40 and 50 degrees),

The offset is also adjusted through m`

$$B` = -m` Cz - q Cz^2$$

The scan mirror emissivity corrected radiances are then calculated using,

$$R` = \{ q C^2 + m` C + b` - [\varepsilon(\theta bb) - \varepsilon(\theta z)] Rm \} / \{1 - \varepsilon(\theta)\}$$

Figure 12.5 shows the emissivity changes with angle and wavelength for the GOES-8 scan mirror. The radiance corrections, $\Delta R = R` - R$, for GOES-8 infrared window radiances are about 2 mW/m2/ster/cm-1 which convert to 1.2 C for a scene of 300 K.

The GOES-VAS satellites, which spin at 100 rpm, experience small diurnal temperature excursions. However, the GOES-8/9 satellites are three-axes stabilized so temperatures within the sensors vary by tens of degrees K over a 24 hour period. Therefore, the coefficients in the calibration equation must be updated frequently. To accomplish this, both the imager and the sounder view space routinely. The sounder views its blackbody every twenty minutes, while the imager normally views its blackbody every ten minutes unless doing so interrupts an image in process. At the most, the imager operates 30 minutes between blackbody views, e.g., when it makes a full-disk image. Drift in detector response (often referred to as 1/f noise (Bak *et al*,1987)) dictates that the space and blackbody calibration looks occur frequently enough to keep changes in calibration within the specified noise levels. The ground system processing interpolates between calibration events, so that different calibration coefficients are determined for each data sample to account for the linear portion of the detector drift.

12.3.5 Bit Depth

The range of radiances expected for earth and atmosphere in a given spectral band must be converted to digital counts of fixed bit depth. This introduces truncation error. For n bit data, the radiance range, must be covered in 2^n even increments. Consider the GOES-8 imager truncation errors indicated in the following table.

Band	λ	Bit Depth	Rmax	ΔR	Tmax	ΔT(230)	ΔT(300)
	(micron)		(mW/m2/ster/cm-1)			(degrees Kelvin)	
1	.65	10			(better detail in images)		
2	3.9	10	3.31	0.003	335	2.14	0.09
3	6.7	10	48.3	0.047	320	0.33	0.06
4	10.7	10	147.7	0.144	320	0.20	0.09
5	12.0	10	166.5	0.163	320	0.19	0.09

For earth scenes of 300 K, the truncation errors are small, less than a tenth of a degree Kelvin. However for cloud scenes of 230 K, the errors become greater than 2 K in the 3.9 micron band; this causes clouds to appear very noisy in this spectral band.

It is important that the truncation error is less than the error introduced by detector noise; this is true for GOES-8 since the NEDT at 300 K is about .2 C.

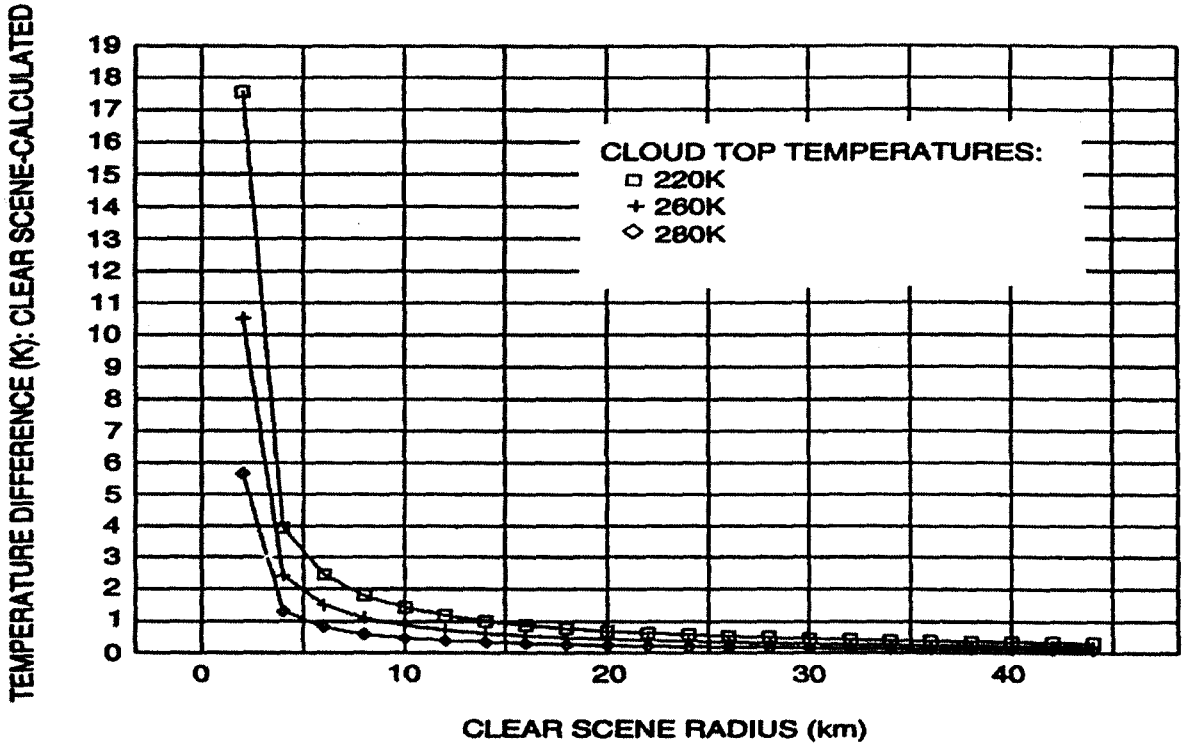

Figure 12.1a: Calculated diffraction effects for GOES imager infrared window radiation with a 2 km radius FOV in a clear scene of brightness temperature 300 K surrounded by clouds of 220, 260, or 280 K.

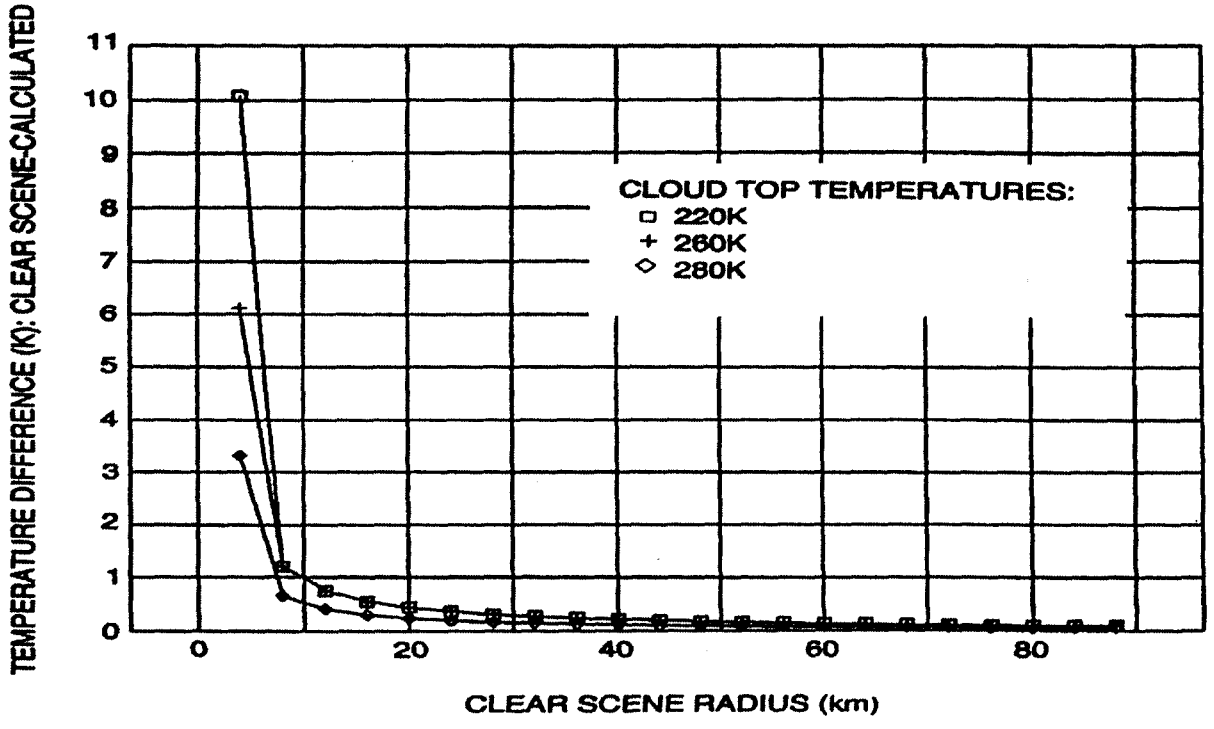

Figure 12.1b: Same plot for GOES sounder infrared window with a 4 km radius FOV and the same optics.

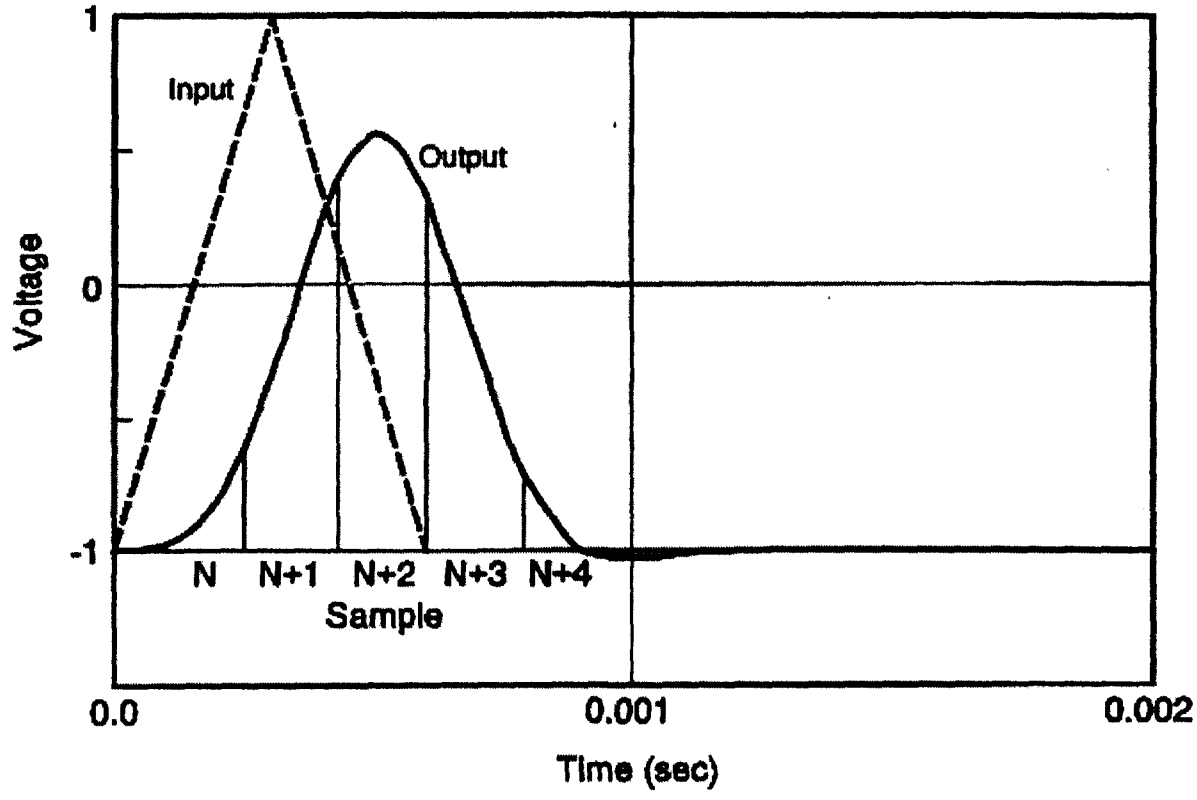

Figure 12.2: Perfect and actual response of the GOES-8 detector continuously sampling a scene with a 100% contrast bar extending one FOV.

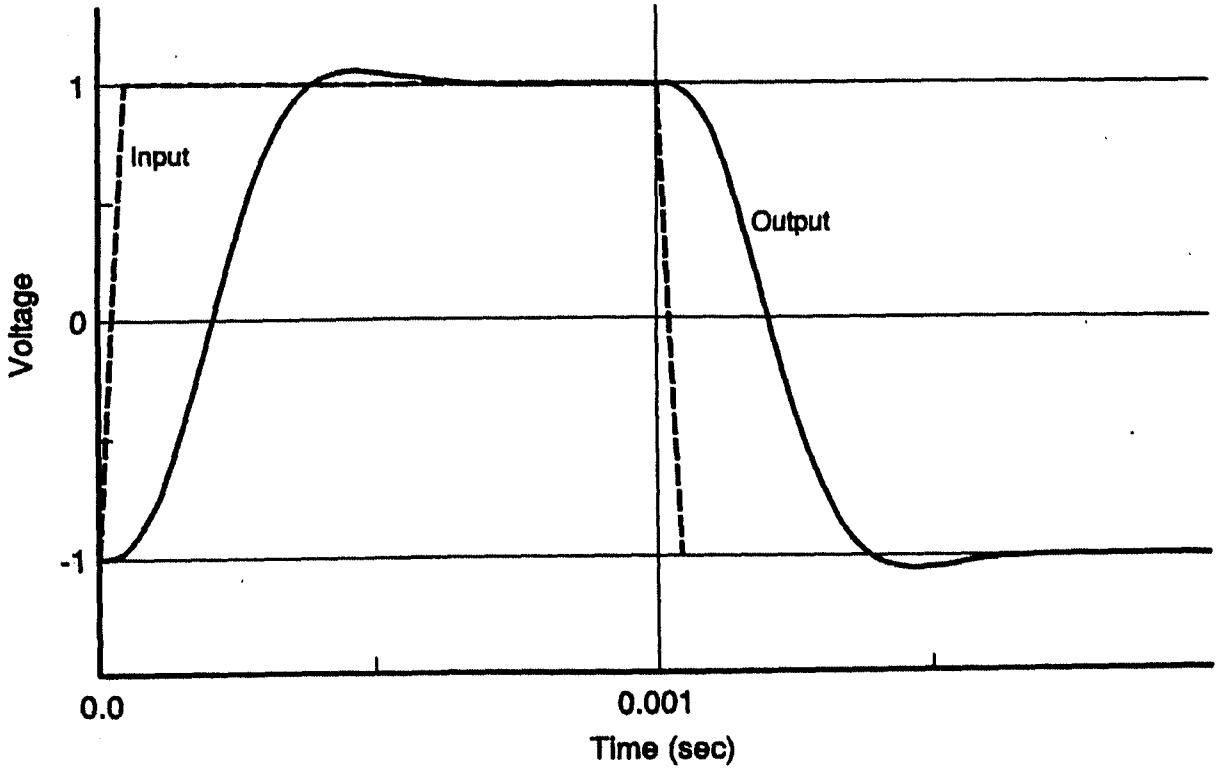

Figure 12.3: The step response function for GOES-8.

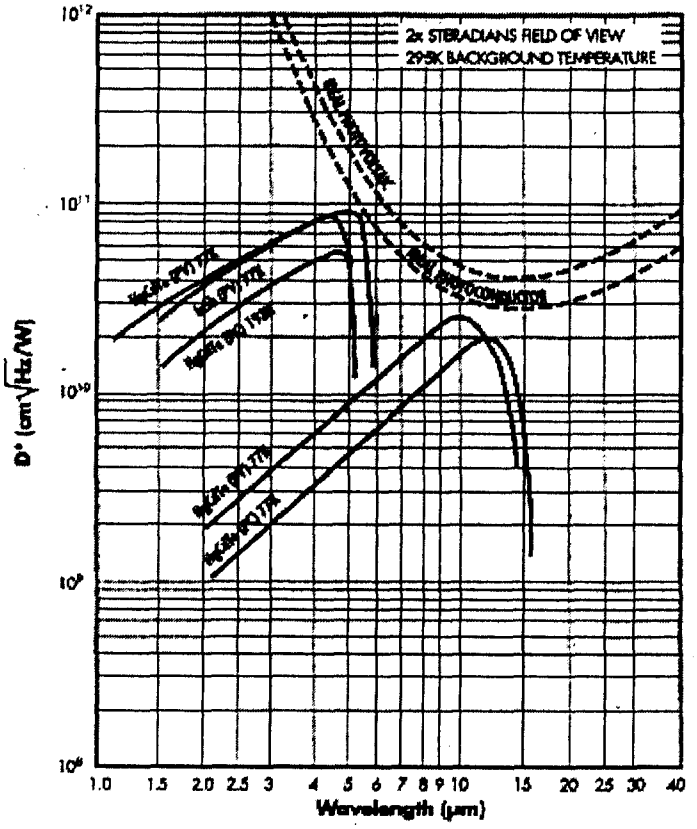

Figure 12.4: Detectivity of InSb and HgCdTe detectors as a function of spectral region.

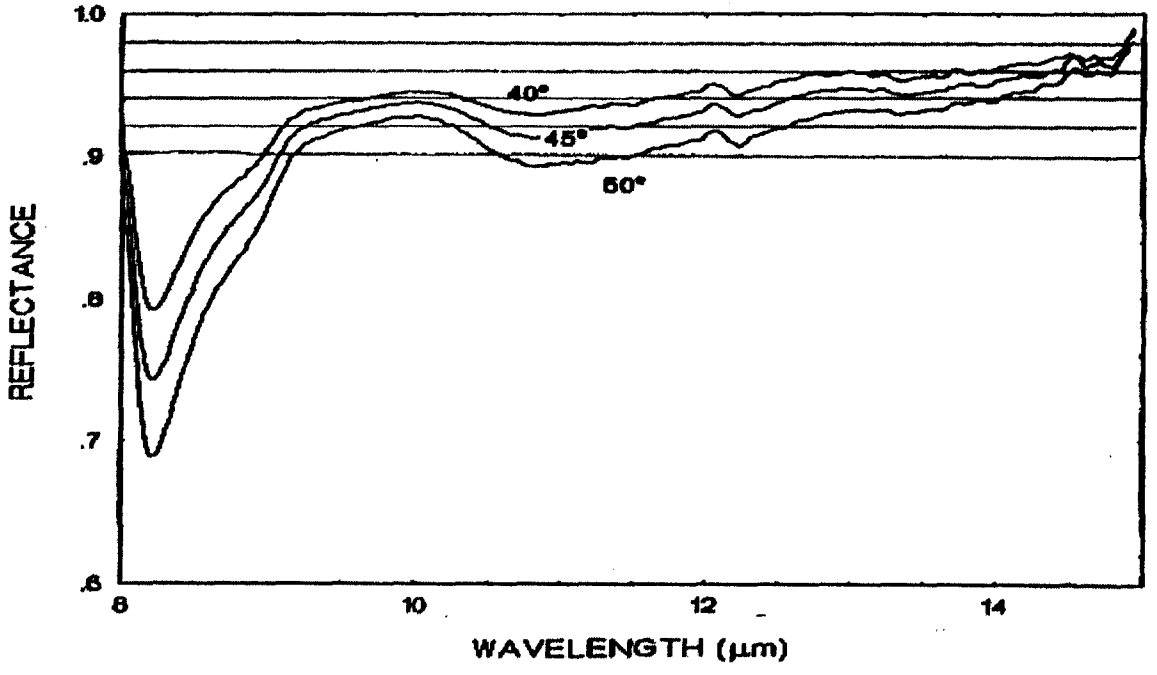

Figure 12.5: Emissivity changes with angle and wavelength for GOES-8 scan mirror.

APPENDIX A

EIGENVALUE PROBLEMS

A.1 Summary of Matrices

A column vector is indicated by

$$f = \begin{bmatrix} f_1 \\ f_2 \\ . \\ . \\ . \\ f_N \end{bmatrix}$$

A matrix consisting of M rows and N columns is defined by

$$A = \begin{bmatrix} A_{11} & A_{12} & \cdots & A_{1N} \\ A_{21} & A_{22} & \cdots & A_{2N} \\ A_{31} & A_{32} & \cdots & A_{3N} \\ . & & & \\ . & & & \\ . & & & \\ A_{M1} & A_{M2} & \cdots & A_{MN} \end{bmatrix}$$

A is said to be an M x N matrix which is denoted by A_{ij}. The vector f is considered as a M x 1 matrix.

The product of a M x N matrix with a N x K matrix gives a M x K matrix. It is obvious that matrix multiplication is not commutative, that is AB is not equal to BA. When C = AB we have

$$C_{ik} = \Sigma A_{ij} B_{jk} .$$

Matrix products are associative so that A(BC) = (AB)C.

On the basis of the rule of matrix multiplication, the product of a row vector (1 x N) and a column vector (N x 1) gives a (1 x 1) matrix, or the scalar product

$$f^t f = f_1 f_1 + f_2 f_2 + \ldots + f_N f_N.$$

But the product of a column vector (N x 1) and a row vector (1 x N) gives a (N x N) matrix, or a vector product

$$f f^t = \begin{bmatrix} f_1 f_1 & f_1 f_2 & \cdots & f_1 f_N \\ f_2 f_1 & f_2 f_2 & \cdots & f_2 f_N \\ & & & \\ . & & & \\ . & & & \\ f_N f_1 & f_N f_2 & \cdots & f_N f_N \end{bmatrix}$$

To summarize these few properties of matrix multiplication: (a) matrix multiplication is not commutative, (b) the ji element of AB is the sum of products of elements from the jth row of A and ith column of B, and (c) the number of columns in A must equal the number of rows in B if the product AB is to make sense.

There are several matrices that are related to A. They are:

(a) A^t which is the transpose of A so that $[A^t]_{ij} = [A]_{ji}$,

(b) A^* which is the complex conjugate of A so that

$$[A^*]_{ij} = [A]^*_{ij},$$

(c) A^+ which is the adjoint of A so that $[A^+]_{ij} = [A]^*_{ji}$, and

(d) A^{-1} which is the inverse of A so that $A^{-1}A = AA^{-1} = I$, where I denotes the identity matrix.

A few definitions follow:

(a) A is real if $A^* = A$,

(b) A is symmetric if $A^t = A$,

(c) A is antisymmetric if $A^t = -A$,

(d) A is Hermitian if $A^+ = A$,

(e) A is orthogonal if $A^{-1} = A^t$, and

(f) A is unitary if $A^{-1} = A^+$.

A.2 Eigenvalue Problems

To understand some of the techniques for solving the radiative transfer equation it is necessary to review solutions to eigenvalue problems. When a operator A acts on a vector x, the resulting vector Ax is in general distinct from x. However there may exist certain non-zero vectors for which Ax is just a multiple of x. That is

$$A\,x = \lambda\,x$$

or written out explicitly

$$\Sigma\, A_{ij}\, x_j = \lambda\, x_i \quad I=1,\ldots,n \ .$$

Such a vector is called an eigenvector of the operator A, and the constant λ is called an eigenvalue. The eigenvector is said to belong to the eigenvalue. Consider an example where the operator A is given by

$$\begin{bmatrix} 1 & 2 & 3 \\ 4 & 5 & 6 \\ 7 & 8 & 9 \end{bmatrix} = A \; ; \begin{bmatrix} x_1 \\ x_2 \\ x_3 \end{bmatrix} = x \, .$$

So we are trying to solve

$$x_1 + 2x_2 + 3x_3 = \lambda x_1$$

$$4x1 + 5x_2 + 6x_3 = \lambda x_2$$

$$7x_1 + 8x_2 + 9x_3 = \lambda x_3$$

For a nontrivial solution the determinant of coefficients must vanish

$$\begin{bmatrix} 1-\lambda & 2 & 3 \\ 4 & 5-\lambda & 6 \\ 7 & 8 & 9-\lambda \end{bmatrix} = 0$$

This produces a third order polynomial in λ whose three roots are the eigenvalues λ_i.

There are several characteristics of the operator A that determine the character of the eigenvalue. Briefly summarized they are (a) if A is hermitian, then the eigenvalues are real and the eigenvectors are orthogonal (eigenvectors of identical or degenerate eigenvalues can be made orthogonal through the Gram Schmidt process) and (b) if A is a linear operator, then the eigenvalues and eigenvectors are independent of the coordinate system. A proof of (b) is quickly apparent.

$$A\,x = \lambda\,x$$

Let Q represent an arbitrary coordinate transformation, then

$$\gamma^{-1} A\,x = \lambda\,\gamma^{-1} x$$

$$\gamma^{-1} A\,\gamma\,\gamma^{-1} x = \lambda\,\gamma^{-1} x$$

$$A'\,x' = \lambda\,x' \, .$$

Thus if x is an eigenvector of the linear operator A, its transform

$$x' = \gamma^{-1} x$$

is an eigenvector of the transformed matrix

$$A' = \gamma^{-1} A \gamma,$$

and the eigenvalues are the same.

It is often desirable to make a transformation to a coordinate system in which A' is a diagonal matrix and the diagonal elements are the eigenvalues. The desired transformation matrix consists of the eigenvectors of the original matrix A.

$$\gamma = \begin{bmatrix} e_1 & e_2 & e_n \\ \downarrow & \downarrow & \downarrow \end{bmatrix}$$

where the j^{th} col consists of components of eigenvector e_j. For the transformation to be unitary, the eigenvectors must be orthonormal (orthogonal and normalized).

A.3 CO_2 Vibration Example

Consider the problem of molecular vibrations in CO_2, which is shown schematically as a simple linear triatomic molecule system consisting of three masses connected by springs of spring constant k. Let x_i represent deviations from the equilibrium position.

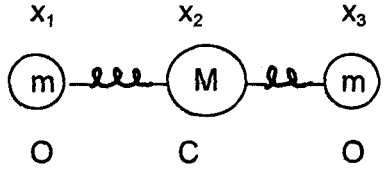

The kinetic energy of this system can be written

$$T = \frac{1}{2} \sum_i m_i v_i^2 = \frac{1}{2} v^t M v$$

where v represents dx/dt. The potential energy is given by

$$P = \frac{1}{2} \sum_{ij} P_{ij} x_i x_j = \frac{1}{2} x^t P x$$

where

$$P = P_o + \sum_i \left(\frac{\partial P}{\partial x_i}\right)_o x_i + \frac{1}{2} \sum_{ij} \left(\frac{\partial^2 P}{\partial x_i \partial x_j}\right)_o x_i x_j$$

and without loss of generality let $P_o = 0$ and use the fact that $\partial P/\partial x = 0$ at equilibrium. Then Lagrange's equation:

$$\frac{d}{dt}\frac{\partial T}{\partial v} + \frac{\partial P}{\partial x}$$

with

$$T = \frac{1}{2} mv^2 \text{ and } P = \frac{1}{2} kx^2,$$

becomes

$$mv = - kx .$$

This suggests a solution of the form $x_i = a_i \sin(\omega_i t + \delta_i)$, so that

$$\sum_j P_{ij} a_j - \omega^2 T_{ij} a_j = 0 .$$

Now the potential energy is written

$$P = \frac{1}{2} k (x_2 - x_1)^2 + \frac{1}{2} k (x_3 - x_2)^2$$

$$= \frac{1}{2} k (x_1^2 + 2x_2^2 + x_3^2 - 2x_1x_2 - 2x_2x_3) ,$$

so the matrix operator is,

$$P = \begin{bmatrix} k & -k & 0 \\ -k & 2k & -k \\ 0 & -k & k \end{bmatrix}$$

which is real and symmetric. And the kinetic energy is written

$$T = \frac{1}{2} m (x_1^2 + x_3^2) + \frac{1}{2} Mx_2^2 ,$$

so the matrix operator is

$$T = \begin{bmatrix} m & o & o \\ o & M & o \\ o & o & m \end{bmatrix}$$

which is diagonal. So, we find $| P - \omega^2 T | = 0$ implies

$$\det A = \begin{bmatrix} k-\omega^2 m & -k & o \\ -k & 2k-\omega^2 M & -k \\ o & -k & k-\omega^2 m \end{bmatrix} = 0$$

and direct evaluation of the determinant leads to the cubic equation

$$\omega^2(k-\omega^2 m)(kM + 2km - \omega^2 Mm) = 0 \ .$$

This yields the three roots

$$\omega_1 = 0 \ , \ \omega_2 = [k/m]^{1/2} \ , \ \omega_3 = [(k/m)(1+2m/M)]^{1/2}.$$

Now solve for the eigenvectors. For $\omega_1 = 0$

$$\begin{bmatrix} k & -k & 0 \\ -k & 2k & -k \\ 0 & -k & k \end{bmatrix} \begin{bmatrix} a_{11} \\ a_{12} \\ a_{13} \end{bmatrix} = 0 \Rightarrow a_{11} = a_{12} = a_{13}$$

which represents a translation since the centre of mass doesn't move $mx_1 + Mx_2 + mx_3 = 0$.

For $\omega_2 = [k/m]^{1/2}$

$$\begin{bmatrix} 0 & -k & 0 \\ -k & 2k-kM/m & -k \\ 0 & -k & 0 \end{bmatrix} \begin{bmatrix} a_{21} \\ a_{22} \\ a_{23} \end{bmatrix} = 0 \Rightarrow a_{22} = 0, \ a_{21} = -a_{23}$$

which represents a vibration in the breathing mode with the carbon molecule stationary and the oxygen molecules moving in opposite directions.

For $\omega_3 = [(k/m)(1+2m/M)]^{1/2}$

$$\begin{bmatrix} -2mk/M & -k & 0 \\ -k & -kM/m & -k \\ 0 & -k & -2mk/M \end{bmatrix} \begin{bmatrix} a_{31} \\ a_{32} \\ a_{33} \end{bmatrix} = 0 \Rightarrow a_{31} = a_{33} \ , \ a_{32} = -(2m/M)a_{31}$$

which represents the carbon molecule motion offset by the combined motion of the oxygen molecules.

Recalling that the mass of the proton is given by $m_p = 1.67 \times 10^{-27}$ Kg, that the spring constant for the CO_2 is roughly $k \sim 1.4 \times 10^3$ J/m2 (from the second derivative of the potential curves), and that $m = 16m_p$ while $M = 12m_p$, then

$$\omega_3 = \left[\frac{1.4 \times 10^3}{16 \times 1.67 \times 10^{-27}} \left(1 + \frac{32}{12}\right)\right]^{1/2} = [.192 \times 10^{30}]^2 = .438 \times 10^{15},$$

and

$$\lambda = \frac{2\pi c}{\omega} = \frac{2\pi\ 3 \times 10^8}{.438 \times 10^{15}} \sim 4.3 \times 10^{-6}\ \text{m} = 4.3\ \mu\text{m}$$

This simple one dimensional model of the CO_2 molecular motions yields the absorption wavelength of 4.3 micron observed in the spectra. Considering two dimensional vibrations yields the solution at 15 micron.

APPENDIX B

REFERENCES

The following references are a few of the available articles that either summarize an important aspect of Satellite Meteorology or indicate a recent development. They are attached so that the interested reader can delve further.

Ackerman, S.A., W.L. Smith and H.E. Revercomb, 1990: The 27-28 October 1986 FIRE IFO cirrus case study: spectral properties of cirrus clouds in the 8-12 micron window. *Mon. Wea. Rev.*, **118**, 2377-2388.

Ackerman, S.A., K.I. Strabala, H.E. Gerber, L.E. Gumley, W.P. Menzel, and S-C. Tsay, 1998: Retrieval of effective microphysical properties of clouds: A wave cloud case study. *J. Geophys. Res.*, **25**, 1121-1124.

Ackerman, S.A., K.I. Strabala, W.P. Menzel, R.A. Frey, C.C. Moeller, and L.I. Gumley, 1998: Discriminating clear-sky from clouds with MODIS. *J. Geophys. Res.*, **103**, D24 , 32141-32158.

Adler, R.F. and D.D. Fenn, 1979: Thunderstorm intensity as determined from satellite data. *J. Appl. Meteor.*, **18**, 502-517.

Adler, R.F. and A.J. Negri, 1981: A satellite technique to estimate tropical convective and stratiform rainfall. *J. Appl. Meteor.*, **27**, 30-51.

Alishouse, J.C., S. Snyder, J. Vongsathorn, and R.R. Ferraro, 1990: Determination of oceanic total precipitable water from the SSM/I. *IEEE Trans. Geo. Rem. Sens.*, **28**, 811-816.

Allison, L.J., R. Wexler, C. Laughlin and W. Bandeen, 1977: Remote sensing of the atmosphere from environmental satellites. X-901-77-132 Preprint, Goddard Space Flight Center, Greenbelt, Md., 111pp.

Allison, L.J. (ed), A. Schnapf, B.C. Diesen, III, P.S. Martin, A. Schwalb, and W.R. Bandeen, 1980: Meteorological *Satellites. NASA TM 80704*, Goddard Space Flight Center, Md., 71pp.

American Society of Photogrammetry, 1983: Manual of Remote Sensing, 2nd ed., Falls Church, VA: 94-98.

Anderson, R.K. 1974: Application of meteorological satellite data in weather analysis and forecasting. Technical *Note 124, WMO No. 333*, World Meteorological Organization, Geneva, Switzerland, 275pp.

Anding, D. and R. Kauth, 1970: Estimation of sea surface temperature from space. *Remote Sensing of the* Environment, **1**, 217-220.

Andreae, M.O., E.V. Browell, M. Garstang, G.L. Gregory, R.C. Harriss, G. F. Hill, D. J. Jacob, M.C. Pereira, G.W. Sachse, A.W. Setzer, P.L. Silva Dias, R.W. Talbot, A.L. Torres, and S.C. Wofsy, 1988: Biomass-burning emissions and associated haze layers over Amazonia. *J. Geophys. Res.*, **93**, 1509-1527.

Atlas, R., M. Ghil, and M. Halem, 1982: The effect of model resolution and satellite sounding data on GLAS model forecasts. *Mon. Wea. Rev.*, **110**, 662-682.

Aune R.M., 1996: Initializing cloud predications using the GOES-8 sounder. *Proceedings of the Eighth* Conference *on Satellite Meteorology and Oceanography*, January 28 - February 2, 1996, Atlanta, GA, Amer. Meteor. Soc., 408-412.

Bak, P., C. Tang, and K. Wiesenfeld, 1987: Self-organized criticality: An explanation of 1/f noise. *Phy. Rev. Lett.*, **59**, 381-384.

Bandeen. W.R., M. Halem, and I. Strange, 1965: A radiation climatology in the visible and infrared from the TIROS meteorological satellite. *NASA Technical Note*, TN-D-2534.

Barrett, E.C., G. D'Souza, and C. H. Power, 1986: Bristol techniques for the use of satellite data in rain cloud and rainfall monitoring. *J. Brit. Interplan. Soc.*, **39**, 517-526.

Barton, I.J., 1983: Dual channel satellite measurements of sea surface temperature. *Quart. J. Roy. Meteor.* Soc., **60**, 197-205.

Bates, J.J. and W.L. Smith, 1985: Sea surface temperature: observation from geostationary satellites. *J. Geophys. Res.*, **90**, 11609-11618.

Baum, B.B., P.F. Soulen, K.I. Strabala, M.D. King, S.A. Ackerman, W.P. Menzel, and P. Yang, 2000: Remote sensing of cloud propertiesusing MODIS airborne simulator imagery during SUCCESS. *Jour. Geophys. Res.*, **105**, D9, 11781-11792.

Bengtsson, L., 1981: The impact of FGGE on global medium range forecasts. Characteristics of atmospheric planetary circulations and associated model forecast skill during FGGE case studies selected by WGNE. Proceedings of the International Conference on Early Results of FGGE and Large-Scale Aspects of its Monsoon Experiments, Tallahassee, Florida, 12-17 January 1981.

Bowman, K.P., and A.J. Krueger, 1985: A global climatology of total ozone from the Nimbus 7 total ozone mapping spectrometer. *J. Geophys. Res.*, **90**, 7967-7976.

Bristor, C.L., and W. Pichel, 1974: Three-D cloud viewing using overlapping pictures from two geostationary satellites. *Bull. Amer. Meteor. Soc.*, **55**, 1353-1355.

Browell, E.V., G.L. Gregory, and R.C. Harriss, 1988: Tropospheric ozone and aerosol distributions across the Amazon Basin. *J. Geophys. Res.*, **93**, 1431-1451.

Brower, R.L., H.S. Gohrband, W.G. Pichel, T.L. Signore, and C.C. Walton, 1976: Satellite derived sea surface temperatures from NOAA spacecraft. U.S. Department of Commerce, National Oceanic and Atmospheric Administration, National Environmental Satellite Service, Washington, D.C., NOAA Technical Memorandum NESS 78, 76pp.

Browning, K. A., 1982: Nowcasting. Academic Press, New York, 256 pp.

Campbell, G.G., 1998: Applications of synchronous stereo height and motion analysis. Proceedings of the fourth International Winds Workshop, EUMETSAT publication **24**, 271-278.

Chahine, M.T., 1970: A general relaxation method for inverse solution of the full radiative transfer equation. *J. Atmos. Sci.*, **27**, 960.

Chahine, M.T., 1974: Remote sounding of cloudy atmospheres I: the single cloud layer. *J. Atmos. Sci.*, **31**, 233-243.

Chedin, A. (ed.), 1989: Technical Proceedings of the Fifth International TOVS Study Conference, Toulouse, France, 24-28 July 1989.

Chesters, D., L.W. Uccellini, and W. D. Robinson, 1983: Low-level water vapor fields from the VISSR Atmospheric Sounder (VAS) "split window" channels. *J. Clim. Appl. Meteor.*, **22**, 725-743.

Chesters, D., W.D. Robinson, and L. W. Uccellini, 1987: Optimized retrievals of precipitable water from the VAS split window. *Jour. Clim. Appl. Meteor.*, **26**, 1059-1066.

Chung, S., S.A. Ackerman, P.F. van Delst, and W.P. Menzel, 2000: Calculations and Interferometer Measurements of Ice Cloud Characteristics. *Jour Appl. Meteor.*, **39**, 634-644.

CIRA, 1994: Introduction to GOES-8, Wide World Web Address; http:// www. cira.colostate.edu.RAMM.overview

CIMSS, 1995: Introducing the GOES-8 sounder. Wide World Web Address: http://cloud.ssec.wisc.edu/sounder/g8.html

Coakley, J.A. and F.P. Bretherton, 1982: Cloud cover from high-resolution scanner data: Detecting and allowing for partially filled fields of view. *J. Geophys. Res.*, **87**, 4917-4932.

COMET, 1992: Boundary Layer Detection and Convective Initiation module. University Corporation for Atmospheric Research, Boulder, CO.

COMET, 1995: Introduction to GOES-8/9: Computer Based Learning Module. University Corporation for Atmospheric Research, Boulder, CO.

Crowson, D.L., 1949: Cloud observations from rockets. *Bull. Amer. Meteor. Soc.*, **30**, 17-22.

Deschamps, P.Y. and T. Phulpin, 1980: Atmospheric correction of infrared measurements of sea surface temperature using channels at 3.7, 11, and 12 um. *Boundary-Layer Meteorology*, **18**, 131-145.

Diak, G.R., M.C. Anderson, W.L. Bland, J.M. Norman, J.M. Mecilkalski, and R.A. Aune, 1998: Agricultural management decision aids driven by real time satellite data. *Bull. Amer. Meteor. Soc.*

Dvorak, V.F., 1972: A technique for the analysis and forecasting of tropical cyclone intensities from satellite pictures. *NOAA TM, NESS 36*, NOAA, NESS, U.S. Dept. of Commerce, Washington, D.C.

Dvorak, V.F., 1984: Tropical cyclone intensity analysis using satellite data. *NOAA Tech. Rep., NESDIS 11,* Washington, D.C.

Dvorak and Wright, 1977: Tropical cyclone intensity analysis using enhanced infrared satellite data. Proc. 11th Tech. Conf. on Hurricanes and Tropical Met., Dec. 13-15, Miami, Amer. Meteor. Soc., Boston, 268-273.

Ebert, E., 1989: Analysis of polar clouds from satellite imagery using pattern recognition and a statistical cloud analysis scheme. *J. Appl. Meteor.*, **28**, 382-399.

Eigenwillig, N. and H. Fischer, 1982: Determination of mid-tropospheric wind vectors by tracking pure water vapor structures in METEOSAT water vapor image sequences. *Bull. Amer. Meteor. Soc.*, **63**, 44-58.

Ellis. J. and T.H. Vonder Haar, 1976: Zonal averaged radiation budget measurements from satellites for climate studies. Atmospheric Science Paper #240, Colorado State University, Fort Collins, Colorado.

Ellrod, G., 1992: Potential applications of GOES-I 3.9 um infrared imagery. 6th Conf. on Sat. Meteor. and Oceonog., Atlanta, January 5-10, Amer. Meteor. Soc., Boston, 184-187.

Eyre, J.R., 1984: Detection of fog at night using Advanced Very High Resolution Radiometer Imagery (AVHRR). Meteorological *magazine*, **113**, 266-271.

Eyre, J.R. and W.P. Menzel, 1989: Retrieval of Cloud Parameters from Satellite Sounder Data: A Simulation Study. *Jour. Appl. Met.*, Vol. **28**, 267-275.

Fleming, H.E. and W.L. Smith, 1971: Inversion techniques for remote sensing of atmospheric temperature profiles. Reprint from Fifth Symposium on Temperature, Instrument Society of America, 400 Stanwix Street, Pittsburgh, Pennsylvania, 2239-2250.

Follansbee, W.A., 1973: Estimation of average daily rainfall from satellite cloud photographs. *NOAA Tech.* Memo *NESS 44*, Dept. of Commerce, Washington, D.C., 39 pp.

Frey, R.A., B.A. Baum, W.P. Menzel, S.A. Ackerman, C.C. Moeller, and J.D. Spinhirne, 1999: A comparison of cloud top heights computed from airborne lidar and MAS radiance data using CO2 slicing. *J. Geophys. Res.*, **104**, D20, 24547-24555.

Friday, E.W., Jr., 1989: The National Weather Service forecast and warning program outlook. GOES I-M Operational Satellite Conference, April 3-9, Arlington, VA, Dept. of Commerce, NOAA, Washington, D.C., 110-125.

Fritz, S. and J.S. Winston, 1962: Synoptic use of radiation measurements from satellite TIROS-II. *Mon.* Wea. *Rev.*, **110**, 198-216.

Fritz, S., D.Q. Wark, H.E. Fleming, W.L. Smith, H. Jacobowitz, D.T. Hilleary, and J.C. Alishouse, 1972: Temperature sounding from satellites. U.S. Department of Commerce, National Oceanic and Atmospheric Administration, National Environmental Satellite Service, Washington, D.C., *NOAA Technical Report NESS 59*, 49 pp.

Frolich, C., 1977: Contemporary measures of the solar constant. Solar Output and Its Variation, O.R. White (ed.), Colorado Associated University Press, Boulder, Colorado, 93-109.

Fujita, T.T., 1978: Manual of downburst identification for project Nimrod. *SMRP 156*, Univ. of Chicago, Chicago, IL, 104pp.

Fujita, T.T., 1982: Infrared, stereo, cloud motion, and radar-echo analysis of SESAME-day thunderstorms. 12th Conf. on Severe Local Storms, Jan 11-15, San Antonio, TX, Amer. Meteor. Soc., Boston, MA, 213-216.

Fujita, T., K. Watanabe, and T. Izawa, 1969: Formation and structure of equatorial anticyclones caused by large-scale cross-equatorial flows determined by ATS-1 photographs. *J. Appl. Meteor.*, **8**, 649-667.

Fujita, T., E. Pearl and W. Shenk, 1975: Satellite-tracked cumulus velocities. *J. Appl. Mereor.* **14**, 407-413.

Gao, B.-C., and A.F. H. Goetz, 1991: Cloud area determination from AVIRIS data using water vapor channels near 1 micron. *J. Geophys. Res.*, **96**, 2857-2864.

Gao, B.-C., A.F. H. Goetz, and W. J. Wiscombe, 1993: Cirrus cloud detection from airborne imaging spectrometer data using the 1.38 micron water vapor band. *Geophys. Res. Letter*, **20**, no. 4, 301-304.

Gentry, R., T. Fujita, and R. Sheets, 1970: Aircraft, spacecraft, satellite, and radar observations of hurricane Gladys. *J. Appl. Meteor.*, **9**, 837-860.

Goerss, J. S., C.S. Velden and J. D. Hawkins, 1998: The impact of multispectral GOES-8 wind information on Atlantic tropical cyclone track forecasts in 1995: Part II: NOGAPS forecasts. *Mon. Wea. Rev.*, **126**, 1202-1218.

Gomberg, L. and S.M. McElroy, 1985: Remote sensing of the earth with the Defense Meteorological satellite. Monitoring Earth's Ocean, Land, and Atmosphere from Space - Sensor, Systems, and Applications. A. Schnapf, (ed), American Institute of Aeronautics and Astronautics, New York, NY, 96-128.

Greenfield, S.W., and W. . Kellogg, 1951: Inquiry into the feasibility of weather reconnaissance from a satellite vehicle. *USAF Project RAND Report R-218*; unclassified ed. 1960, Report N-365, 43pp.

Griffith, C.G., W.L. Woodley, P.G. Grube, D.W. Martin, J. Stout and D.N. Sikdar, 1978: Rain estimates from geosynchronous satellite imagery: visible and infrared studies. *Mon. Wea. Rev.*, **106**, 1153-1171.

Grody, N. G., A. Gruber, and W. Shen, 1980: Atmospheric water content over the tropical Pacific derived from the Nimbus-6 scanning microwave spectrometer. *J. Appl. Meteor.*, **19**, 986-996.

Gruber, A., 1977: Determination of the Earth-atmosphere radiation budget from NOAA satellite data. *NOAA Tech. Rep., NESS 76*, Department of Commerce, Washington, Dc, 28pp.

Gurka, J.J., 1978: The role of inward mixing in the dissipation of fog and stratus. *Mon. Wea. Rev.*, **106**, 1633-1635.

Hallgren, R.E., 1985: Welcome from AMS. Second International Satellite Direct Broadcast Services Users' Conference, April 15-19, Baltimore, MD, U.S. Dept of Commerce, Washington, DC, 14-15.

Hanel, R.A., B. Schlachman, F.D. Clark, C.H. Prokesh, J.B. Taylor, W.M. Wilson, and L. Chaney, 1970: The NIMBUS-3 Michelson Interferometer. *Appl. Optics*, **9**, 1767-1773.

Hasler, A.F. 1981: Stereographic observations from geosynchronous satellites: An important new tool for the atmospheric sciences. *Bull. Amer. Meteor. Soc.*, **62**, 194-212.

Hasler, A.F., K. Palaniappan, C. Kambhammetu, P. Black, E. Uhlhorn and D. Chesters, 1998: High-resolution wind fields within the inner core and eye of a mature tropical cyclone from GOES 1-min images. *Bull. Amer. Meteor. Soc.*, **79**, 2483-2496.

Hass, I.S. And R. Shapiro, 1982: The NIMBUS satellite system - Remote sensing R&D platform of the 70s. NASA *Conference Publication 2227*, 17-30.

Hayden, C.M. and R.J. Purser, 1995: Recursive filter objective analysis of meteorological fields - applications to NESDIS operational processing. *J. Appl. Meteor.*, **34**, 3-15.

Hayden, C.M. and S J. Nieman, 1996: A primer for tuning the automated quality control system and for verifying satellite-measured drift winds. NOAA Technical Memorandum NESDIS 43. 27 pp. U. S. Department of Commerce.

Hayden, C.M., W.L. Smith, H.M. Woolf, 1981: Determination of moisture from NOAA polar orbiting satellite sounding radiances. *J. Appl. Meteor.*, **20**, 450-466.

Hayden, C.M., 1988: GOES-VAS simultaneous temperature-moisture retrieval algorithm. *J. Appl. Meteor.*, 27, 705-733.

Hayden, C.M. and T.J. Schmit, 1994: GOES-I temperature and moisture retrievals and associated gradient wind estimates. *Proceedings of the Seventh Conference on Satellite Meteorology and Oceanography*, June 6-10, 1994, Monterey, CA, Amer. Meteor. Soc., 477-480.

Hayden, C.M., G.S. Wade, and T.J. Schmit, 1996: Derived Product Imagery from GOES-8. *J. Appl. Meteor.*, **35**, 153-162

Hayden, C.M., T.J. Schmit, and A.J. Schreiner, 1998: The cloud clearing for GOES product processing. *NOAA/NESDIS Technical Report.*

Heath, D.F., A J. Krueger, H.A. Roeder, and B.D. Henderson, 1975: The solar backscatter ultraviolet and total ozone mapping spectrometer (SBUV/TOMS) for NIMBUS G. *Optical Engineering*, **14**, 323-331.

Heath, D.F., A.J. Krueger, and H. Park, 1978: The Solar Backscatter Ultraviolet (SBUV) and Total Ozone Mapping Spectrometer (TOMS) experiment. *The Nimbus-7 User's Guide.* C. R. Madrid, Ed., NASA Goddard Space Flight Center, Greenbelt, MD, 175-211.

Heymsfield, G.M., G. Szejwach, S. Scholtz, and H. Blackmer, 1983. Upper tropospheric structure of Oklahoma tornadic storms on May 2, 1979, II: Proposed explanation of "V" pattern and internal warm region in infrared observations. *J. Atmos. Sci.*, **40**, 1739-1755.

Holmlund, K., 1993: Operational water vapor wind vectors from Meteosat imagery data. Second International Wind Workshop, Tokyo, EUMETSAT, Darmstadt-Eberstadt, Germany, 77-84, ISSN 1023-0416.

Holmlund, K., C.S. Velden and M. Rohn, 1999: Enhanced automated quality control applied to high-density GOES winds derived during the North Pacific Experiment (NORPEX). *Mon. Wea. Rev.*

Hubert, L.F. and L.F. Whitney, Jr., 1971: Wind estimation from geostationary-satellite pictures. *Mon. Wea. Rev.*, **99**, 665-672.

Hubert, L.F. and P.E.. Lehr, 1967: Weather Satellites. Blaisdell Publishing Company, 120pp.

Huh, O.K., C.C. Moeller, W.P. Menzel, L.J. Rouse, and H.H. Roberts, 1996: Remote sensing of turbid coastal and estuarine waters: a method of multispectral water-type analysis. *Journal of Coastal Research*, **12**, 984-995.

Isaacs, R.G., R.N. Hoffman, and L.D. Kaplan, 1986: Satellite remote sensing of meteorological parameters for global numerical weather prediction. *Rev. Geophys.*, **24**, 701-743.

Inoue, T., 1987: A cloud type classification with NOAA 7 split window measurements. *J. Geophys. Res.*, **92**, 3991-4000.

Jedlovec, G.J., 1985: An evaluation and comparison of vertical profile data from the VISSR Atmospheric Sounder (VAS). *J. Atmos. Oceanic Tech.*, **2**, 559-581.

Jedlovec, G.J., 1990: Precipitable water estimation from high resolution split window radiance measurements. *Jour. Appl. Meteor.*, **29**, 863-877.

Johnson, D.S., 1982: Development of the operational program for satellite meteorology. *NASA Conference Publication 2257*, 34-40.

Johnson, D.S., 1994: Evolution of the U. S. Meteorological Satellite Program; 1994 Verner E. Suomi Lecture. *Bull. Amer. Meteor. Soc.*, **75**, 1705-1708.

Justice, C.O., J.R.G. Townshend, B.N. Holben, and C.J. Tucker, 1985: Analysis of the phenology of global vegetation using meteorological satellite data. *Int. J. of Remote Sensing*, **6**, 1271-1318.

Kaplan, L.D., 1959: Inferences of atmospheric structures from satellite remote radiation measurements. *J. Opt. Soc. Am.*, **49**, 1004-1014.

Kaplan, L.D., M. T. Chahine, J. Susskind, J. E. Searl, 1977: Spectral band passes for high precision satellite sounder. *Appl. Optics*, **16**, 322-325.

Kaufman, Y.J., and C. Sendra, 1988: Algorithm for atmospheric corrections of visible and near IR satellite imagery. *Int. J. Remote Sens.*, **9**, 1357-1381.

Kaufman, Y.J., A. Setzer, D. Ward, D. Tanre, B.N. Holben, V.W.J.H. Kirchhoff, W.P. Menzel, M.C. Pereira, and R. Rasmussen, 1992: Biomass Burning Airborne and Spaceborne Experiment in the Amazonas (BASE-A). *Jour. Geophys. Res.*, Vol **97**, No. D13, 14581-14599.

Kaufman, Y.J., C.O. Justice, L.P. Flynn, J.D. Kendall, E.M. Prins, L. Giglio, D.E. Ward, W.P. Menzel, and A.W. Setzer, 1998: Potential global fire monitoring from EOS-MODIS. *J. Geophys. Res.*, **103**, D24, 32215-32238.

Kellogg, W.W., 1966: Satellite meteorology and the academic community. Satellite data in meteorological research. NCAR-TN-11, van de Boogaard, H.M.E. (ed), National Center For Atmospheric Research, Boulder, Co, 5-14.

Kidder, S.Q., W.M. Gray and T.H. Vonder Haar, 1978: Estimating tropical cyclone central pressure and outer winds from satellite microwave data. *Mon. Wea. Rev.*, **106**, 1458-1464.

Kidder, S. Q. and T.H. Vonder Haar, 1995: Satellite Meteorology - An Introduction. Academic Press, New York.

King, J.I.F., 1956: The radiative heat transfer of planet earth. Scientific Use of Earth Satellites, University of Michigan Press, Ann Arbor, Michigan, pp.133-136.

King, M.D., Y.J. Kaufman, W.P. Menzel, and D. Tanre, 1992: Remote sensing of cloud, aerosol, and water vapor properties from the Moderate Resolution Imaging Spectrometer (MODIS). *IEEE Trans. Geosci. Remote Sensing*, **30**, 2-27.

King, M.D., W.P. Menzel, P.S. Grant, J.S. Myers, G.T. Arnold, S. Platnick, L.E. Gumley, S. Tsay, C.C. Moeller, M. Fitzgerald, K.S. Brown, and F. Osterwisch, 1996: Airborne scanning spectrometer for remote sensing of cloud, aerosol, water vapor, and surface properties. *Jour. Atmos. and Oceanic Tech.*, **13**, 777-794.

Kleespeis, T.J. and L.M. McMillin, 1984: Physical retrieval of precipitable water using the split window technique. Preprints Conf. on Satellite Meteorology/Remote Sensing and Applications, AMS, Boston, 55-57.

Langland, R., *et al*, 1999: The North Pacific Experiment (NORPEX-98): Targeted observations for improved North American weather forecasts. *Bull. Amer. Meteor. Soc.*

LeMarshall, J.F., 1988: An intercomparison of temperature and moisture fields derived from TOVS data by different techniques. Part I: Basic statistics. *J. Appl. Meteor.*, **27**, 1011-1030.

Li, J., and W.W. Wolf, W.P. Menzel, W. Zhang, H.-L. Huang, and T.H. Achtor, 2000: Global soundings of the atmosphere from ATOVS measurements: The algorithm and validation. *Jour. Appl. Meteor.*, **39**, 1248-1268.

Lord, R. J., W.P. Menzel, and L.P. Pecht, 1984: ACARS Wind Measurements: An Intercomparison with Radiosonde, Cloud Motion and VAS Thermally Derived Winds. *J. Atmos. and Oceanic Tech.*, Vol. **1**, No. 2, 131-137.

Ma, X.L., W.L. Smith, and H.M. Woolf, 1984: Total ozone from NOAA satellites--a physical model for obtaining observations with high spatial resolution. *J. Clim. Appl. Meteor.*, **23**, 1309-1314.

Ma, X., T.J. Schmit, and W.L. Smith 1998: A non-linear physical retrieval algorithm - Its Application to the GOES-8/9 sounder. Accepted by *J. Appl. Meteor.*

Maddox, R., 1980: Mesoscale convective complexes. *Bull. Amer. Meteor. Soc.*, **61**, 1374-1387.

Malingreau, J.P., G. Stephens, and L. Fellows, 1985: Remote sensing of forest fires: Kalimantan and North Borneo in 1982-83. *Ambio*, **14**, 314-321.

Malingreau, J.P., and C.J. Tucker, 1988: Large-scale deforestation in the south-eastern Amazon Basin of Brazil. *Ambio*, **17**, 49-55.

Masuda, K., T. Takashima, and Y. Takayama, 1988: Emissivity of Pure Sea Waters for the Model Sea Surface in the Infrared Window Regions. *Remote Sensing of the Environment*, **24**, 313-329.

Matson, M., E P. McClain, D.F. McGinnis, Jr., and J.A. Pritchard, 1978: Satellite detection of urban heat islands. *Mon. Wea. Rev.*, **106**, 1725-1734.

Matson, M. and J. Dozier, 1981: Identification of subresolution high temperature sources using a thermal IR sensor. *Photogramm. Eng. Remote Sensing*, **47**, 1311-1318.

Matson, M., and B. Holben, 1987: Satellite detection of tropical burning in Brazil. *Int. J. of Remote Sensing*, **8**, 509-546.

Matson, M., S.R. Schneider, B. Aldridge, and B. Satchwell, 1984: Fire detection using the NOAA-series satellites. NOAA Technical Report NESDIS 7, Washington, DC: Department of Commerce, 34 pp.

McClain, E. P., W. Pichel, C. Walton, A. Ahmad, and J. Sutton, 1982: Multi-channel improvements to satellite-derived global sea surface temperatures. *Adv. Space Res.*, **2**, 43-47.

McClain, E.P., W.G. Pichel, and C. C. Walton, 1985: Comparative performance of AVHRR based multichannel sea surface temperatures. *J. Geophys. Res.*, **89**(C6), 11587-11601.

McMillin, L.M. and H.E. Fleming, 1976: Atmospheric transmittance of an absorbing gas: A computationally fast and accurate transmittance model for absorbing gases with constant mixing ratios in homogeneous atmospheres. *Appl. Optics,* **15**, pg. 358.

McMillin, L.M. and C. Dean, 1982: Evaluation of a new operational technique for producing clear radiances. *J. Appl. Meteor.*, **12**, 1005-1014.

McMillin, L.M., D.Q. Wark, J.M. Siomkajlo, P.G. Abel, A. Werbowetzki, L.A. Lauritson, J. A. Pritchard, D.S. Crosby, H.M. Woolf, R.C. Luebbe, M.P. Weinreb, H.E. Fleming, F.E. Bittner, and C.M. Hayden, 1983: Satellite infrared soundings from NOAA Spacecraft. U.S. Department of Commerce, National Oceanic and Atmospheric Administration, National Environmental Satellite Service, Washington, D.C., NOAA Technical Report NESS 65, 112 pp.

McPeters, R.D., P.K. Bhartia, A.J. Krueger, J.R. Herman, B.M. Schlesinger, C.G. Wellemeyer, C.J. Seftor, G. Jaross, S.L. Taylor, T. Swissler, O. Torres, G. Labow, W. Byerly, and R.P. Cebula, 1996: Nimbus-7 Total Ozone Mapping Spectrometer (TOMS) Data Products User's Guide. *NASA Reference Publication* 1384, National Aeronautics and Space Administration, Washington, DC.

McPeters, R D., P K. Bhartia, A.J. Krueger, J.R. Herman, C.G. Wellemeyer, C.J. Seftor, G. Jaross, O. Torres, L. Moy, G. Labow, W. Byerly, S.L. Taylor, T. Swissler and R.P. Cebula, 1998: Earth Probe Total Ozone Mapping Spectrometer (TOMS) Data Products User's Guide. NASA *Reference Publication* 206895, National Aeronautics and Space Administration, Washington, DC.

Meeks, M.L. and A.E. Lilley, 1963: The microwave spectrum of oxygen in the earth's atmosphere. *J.* Geophys. *Res.*, **68**, 1683-1703.

Menzel, W.P., W.L. Smith, and L.D. Herman, 1981: Visible Infrared Spin-Scan Radiometer Atmospheric Sounder Radiometric Calibration: An Inflight Evaluation from Intercomparisons with HIRS and Radiosonde Measurements. *Appl. Optics*, Vol. **20**, No. 20, 3641-3644.

Menzel, W.P., W.L. Smith, and T. Stewart, 1983: Improved cloud motion wind vector and altitude assignment using VAS. *J. Clim. Appl. Meteor.,* **22**, 377-384.

Menzel, W.P. and A. Chedin, 1990: Summary of the fifth international TOVS study conference. *Bull. Amer.* Meteor. *Soc.*, **71**, 691-693.

Menzel, W.P. and A. Chedin, 1991: Summary of the Sixth International TOVS Study Conference. *Bull. Amer. Meteor. Soc.*, **72**, 1543-1545.

Menzel, W.P., E.C. Cutrim, and E.M. Prins, 1991: Geostationary Satellite Estimation of Biomass Buring in Amazonia during BASE-A. Global Biomass Burning, Levine, J. S., editor, MIT Press, p. 41-46.

Menzel, W.P., D.P. Wylie, and K.I. Strabala, 1992: Seasonal and Diurnal Changes in Cirrus Clouds as seen in Four Years of Observations with the VAS. *J. Appl. Meteor.*, **31**, 370-385.

Menzel, W. P. and J. F. W. Purdom, 1994: Introducing GOES-I: The first of a new generation of geostationary operational environmental satellites. *Bull. Amer. Meteor. Soc.*, **75**, 757-781.

Menzel, W.P., F.C. Holt, T.J. Schmit, R.M. Aune, A.J. Schreiner, G.S. Wade, G.P. Ellrod, and D.G. Gray, 1998. Application of the GOES-8/9 soundings to weather forecasting and nowcasting. Bull. *Amer. Meteor. Soc.*, **79**, 2059-2077.

Merrill, R.T., W.P. Menzel, W. Baker, J. Lynch, E. Legg, 1991: A report on the recent demonstration of NOAA's upgraded capability to derive satellite cloud motion winds. *Bull. Amer. Meteor. Soc.*, **72**, 372-376.

Meyers, W.D., 1985: The Defense Meteorological Satellite Program: A Review of Its Impact. Monitoring Earth's Ocean, Land, and Atmosphere from Space - Sensor, Systems, and Applications. A. Schnapf, (ed),American Institute of Aeronautics and Astronautics, New York, NY, 129-149.

Mosher, F.R., 1976: Cloud height determination. COSPAR Proceedings on the Symposium for Meteorological Observations from Space: Their Contribution to the First GARP Global Experiment, NCAR, Boulder, CO, 201-204.

Nagel, R. and C.M. Hayden, 1971: The use of satellite-observed cloud patterns in northern hemisphere 500-mb numerical analysis. *NOAA Technical Report NESS 55*, Dept. of Commerce, Washington, D.C., 55 pp.

Nelson, R., N. Horning, and T.A. Stone, 1987: Determining the rate of forest conversion in Mato Grosso, Brazil, using Landsat MSS and AVHRR data. *Int. J. of Remote Sensing*, **8**, 1767-1784.

Nieman, S.A., J. Schmetz, and W.P. Menzel, 1993: A comparison of several techniques to assign heights to cloud tracers. *J. Appl. Meteor.*, **32**, 1559-1568.

Nieman, S.J., W.P. Menzel, C.M. Hayden, D. Gray, S.T. Wanzong, C.S. Velden, and J. Daniels, 1997: Fully automated cloud drift winds in NESDIS operations. *Bull. Amer. Meteor. Soc.*, **78**, 1121-1133.

NOAA, 1984: The March 28, 1984 Carolina Tornado Outbreak. Disaster Survey Report to the Administrator. NOAA, U.S. Dept of Commerce, Washington, D.C.

Obasi, G.O.P., 1985: Keynote Address. Second International Satellite Direct Broadcast Services Users' Conference, April 15-19, Baltimore, MD, U.S. Dept of Commerce, Washington, DC, 16-21.

Oliver, V.J., R.K.Anderson, and E.W. Ferguson, 1964: Some examples of detection of jet streams from TIROS photographs. *Mon. Wea. Rev.*, **96**, 470-471.

Oliver, V. J., and E.W. Ferguson, 1966: The use of satellite data in weather analysis. Satellite data in meteorological research, van de Boogaard, H.M.E. (ed), 1966 NCAR-TN-11, National Center For Atmospheric Research, Boulder, Co, 349pp.

Phillips, N.A., L.M. McMillin, D. Wark, and A. Gruber, 1979: An evaluation of early operational temperature soundings from TIROS-N. *Bull. Amer. Meteor. Soc.*, **60**, 1118-1197.

Pielke, R.A., 1987: The challenge of using mesoscale data in mesoscale models. Symp. Mesoscale Analysis and Forecasting, Vancouver, Canada, August, 1987, ESA SP-282, 651-652.

Plokhenko, Y. and W.P. Menzel, 2000: The effects of surface reflection on estimating the vertical temperature-humidity distribution from spectral infrared measurements. *Jour Appl. Meteor.*, **39**, 3-14.

Prabhakara, C., B.J. Conrath, and R.A. Hanel, 1970: Remote sensing of atmospheric ozone using the 9.6 micron band. *J. Atmos. Sci.*, **26**, 689-697.

Prabhakara, C., G. Dalu, and V. G. Kunde, 1974: Estimation of sea surface temperature from remote sensing in the 11 to 13 um window region. *J. Geo. Res.*, **79**, 5039-5044.

Pratt, R. W., 1985: Review of radiosonde humidity and temperature errors. *J. Atmos. Oceanic Tech.*, **2**, 404-407.

Prins, E.P. and W.P. Menzel, 1994: Trends in South American Biomass Burning Detected with the GOES-VAS from 1983-1991. *Jour. Geo. Rev.*, **99**, 16719-16735.

Prins, E.M., J.M. Feltz, W.P. Menzel, and D.E. Ward, 1998: An overview of GOES-8 diurnal fire and smoke results for SCAR-B and the 1995 fire season in South America. J. Geophys. Res., 103, D24, 31821-31836.

Purdom, J.F. W., 1976: Some uses of high resolution GOES imagery in the mesoscale forecasting of convection and its behavior. *Mon. Wea. Rev.*, **104**, 1474-1483.

Purdom, J.F. W., 1982: Integration of research aircraft data and 3 minute interval GOES data to study the genesis and development of deep convective storms. Preprints, 12th Conference on Severe Local Storms, 11-15 January, San Antonio, TX, Amer. Meteor. Soc., 269-271.

Purdom, J.F. W., 1985: The application of satellite sounding and image data to the Carolina tornado outbreak of 28 March 1984. 14th Conf. on Severe local Storms, Indianapolis, Oct 29-Nov 1, Amer. Meteor. Soc., Boston, 276-279.

Purdom, J.F. W., 1993: Satellite observations of tornadic thunderstorms. The Tornado: Its Structure, Dynamics, Prediction, and Hazards. *Geophysical Monograph*, **79**, American Geophysical Union, 265-274.

Purdom, J.F. W., 1995: Observations of thunderstorms and hurricanes using one-minute interval GOES-8 imagery. Abstracts, Week B, International Union of Geodesy and Geophysics, XXI General Assembly, Boulder, Co, July 2-14, 1995,

Purdom, J.F. W. and J.G. Gurka, 1974: The effect of early morning cloud cover on afternoon understorm development. 5th Conf. on Wea. Fcst. and Analysis., St. Louis, Mo, Amer. Meteor. Soc., Boston, 58-60.

Purdom, J.F.W., and P.N. Dills, 1993: Cloud motion and height measurements from multiple satellites including cloud heights and motions in polar regions. Second International Wind Workshop, Tokyo, EUMETSAT, Darmstadt-Eberstadt, Germany, 245-248, ISSN 102-0416.

Purdom, J.F.W. and W.P. Menzel, 1996: Evolution of satellite observations in the United States and their use in meteorology. Chapter 5 of Historical Essays on Meteorology 1919-1995 (ed. J.R. Fleming), 99-155.

Rasmussen, E.A., and J.F W. Purdom, 1992: Investigation of a polar low using geostationary satellite data. 6th Conf. on Sat. Meteor. and Oceanog., Jan 5-10, Atlanta, GA, Amer. Meteor. Soc., Boston, 120-122.

Rao, C.R.N., L.L. Stowe, E.P. McClain, and J. Saper, 1988: Development and application of aerosol remote sensing with AVHRR data from the NOAA satellites. Aerosols in Climate, Deepak Publishing, Hampton, VA, 69-80.

Rao, P.K., S.J. Holmes, R.K. Anderson, J.S. Winston and P.E. Lehr, 1990: Weather Satellites: Systems, Data, and Environmental Applications. Amer. Meteor. Soc., Boston, 503pp.

Raymond W.H., R.M. Aune, 1998: Improved precipitation forecasts using parameterized precipitation drag in a hydrostatic forecast model. *Monthly Wea Rev*, **126**, 693-710.

Revercomb, H.E., H. Buijis, H.B. Howell, D.D. LaPorte, W.L. Smith, and L.A. Sromovsky, 1988: Radiometric calibration of IR Fourier transform spectrometers: Solution to a problem with the High spectral resolution Interferometer Sounder. *Appl. Opt.*, **27**, 3210-3218.

Reynolds, D. and T. Vonder Haar, 1977: A bi-spectral method for cloud parameter determination. *Mon Wea. Rev.*, **105**, 446-457.

Rodgers, C.D., 1971: Some theoretical aspects of remote sounding in the earth's atmosphere. *J. Quan. Spec. Rad. Trans.*, **11**, 767.

Rodgers, C.D., 1976: Retrieval of atmospheric temperature and composition from remote measurements of thermal radiation. *Rev. of Geophysics and Space Physics*, **14**, 609-624.

Rosenkranz, P.W., M.J. Komichak, and D.H. Staelin, 1982: A method for estimation of atmospheric water vapor profiles by microwave radiometry. *J. Appl. Meteor.*, **21**, 1364-1370.

Rossow, W.B., and A.A. Lacis, 1990: Global and seasonal cloud variations from satellite radiance measurements. Part II: Cloud properties and radiative effects. *J. Clim.*, **3**, 1204-1253.

Rossow, W.B. and L.C. Garder, 1993: Cloud detection using satellite measurements of infrared and visible radiances for ISCCP. *J. Clim.*, **6**, 2341-2369.

Sadler, J.C., 1968: Average cloudiness in the tropics from satellite observations. East-West Center Press, Honolulu, HI, 22pp.

Salisbury, J.W. and D.M. D'Aria, 1992: Emissivity of terrestrial materials in the 8-14 micron atmospheric window. *Remote. Sens. Environ.*, **42**, 83-106.

Schnapf, A., 1982: The development of the TIROS global environmental satellite system. NASA Conference Publication 2227: Meteorological Satellites: Past, Present and Future (available from NASA Scientific and Technical Information Branch, Washington, D.C. 20546).

Schnapf, A. (ed), 1985: Monitoring Earth's Ocean, Land, and Atmosphere from Space - Sensor, Systems, and Applications. American Institute of Aeronautics and Astronautics, New York, NY. 830 pp.

Schereschewsky, P., 1945: Clouds and states of the sky. Handbook of Meteorology, Berry, Bollay, Beers (eds.), McGraw Hill, New York, NY, 1068 pp.

Schmetz, J., K. Holmlund, J. Hoffman, B. Strauss, B. Mason, V. Gaertner, A. Koch, and L. van de Berg, 1993: Operational cloud motion winds from METEOSAT infrared images. *J. Appl. Meteor.*, **32**, 1206-1225.

Schmetz, J., W.P. Menzel, C. Velden, X. Wu, L. Van de Berg, S. Nieman, C. Hayden, K. Holmlund, and C. Geijo, 1995: Monthly Mean Large Scale Analyses of Upper Tropospheric Humidity and Wind Field Divergence Derived from Three Geostationary Satellites. *Bull. Amer. Meteor. Soc.*, Vol. **76**, No. 9, 1578-1584.

Schmetz, J., H.P. Roesli, and W. P. Menzel, 1997: Summary of the Third International Winds Workshop. *Bull. Amer. Meteor. Soc.*, **78**, 893-896.

Schmetz, J., D. Hinsman, and W. P. Menzel, 1999: Summary of the Fourth International Winds Workshop. *Bull. Amer. Meteor. Soc.*, **80**, 893-899.

Schmidlin, F.J., 1988: WMO international radiosonde comparison, phase II final report, 1985. Instruments *and observing methods report*, No. 29 WMO/TD No. 312, WMO, Geneva, Switzerland.

Schmit, T.J., 1996: Sounder bias correction of the east-west gradient. *Technical Proceedings of the Society of* Photo-*Optical Instrumentation Engineers International Symposium on GOES-8 and Beyond*, August 4-9, 1996, Denver CO, Int. Soc. for Optical Eng., **2812**, 630-637.

Schreiner, A.J., D. Unger, W.P. Menzel, G. Ellrod, K. Strabala, and J. Pellet, 1993: A comparison of ground and satellite observations of cloud cover. *Bull. Amer. Meteor. Soc.*, **74**, 1851-1861.

Scofield, R. and V. J. Oliver, 1977: A scheme for estimating convective rainfall from satellite imagery. *NOAA Tech Memo NESS 86*, Dept. of Commerce, Washington, D.C., 47 pp.

Scorer, R.S., 1990: Satellite as microscope. Ellis Horwood, New York, 268 pp.

Segal, M., J.F.W. Purdom, J.L. Song, R.A. Pielke and Y. Mahrer, 1986: Evaluation of cloud shading effects on the generation and modification of mesoscale circulations. *Mon. Wea. Rev.*, **114**:7, 1201-1212

Shapiro, M.A., A.J. Krueger, and P.J. Kennedy, 1982: Nowcasting the position and intensity of jet streams using a satellite borne total ozone mapping spectrometer. Published in Nowcasting, K A. Browning (ed.), Academic Press, Inc., (London) Ltd., pp. 137-145.

Sheets, R.C., 1990: The National Hurricane Center - Past, Present, and Future. *Weather and* Forecasting, **2**, 185-232.

Shenk, W.E., 1985: Cloud motion derived winds: their accuracy, coverage, and suggestions for future improvements. NASA Symposium on Global Wind Measurements, July 29-Aug 1, Columbia, MD, NASA, 123-128.

Shenk, W.E. and E.R. Kreins, 1975: The NASA severe storm research program. 9th Conf. on severe local storms, Norman, OK, Amer. Meteor. Soc., Boston, 468-473.

Shenk, W.E., and F.Mosher, 1987: Suggested severe local storm operational scenarios for GOES-I/M. NASA *TM 100688*, NASA, Washington, D.C.

Shenk, W. E., T.H. Vonder Haar and W. L. Smith, 1987: An evaluation of observations from satellites for the study and prediction of mesoscale events and cyclone events. *Bull. Amer. Meteor. Soc.*, **68**, 21-35.

Smith, W.L., 1970: Iterative solution of the radiative transfer equation for temperature and absorbing gas profiles of an atmosphere. *Appl. Optics,* **9**, 1993-1999.

Smith, W.L., H.M. Woolf, and W.J. Jacob, 1970: A regression method for obtaining real time temperature and geopotential height profiles from satellite spectrometer measurements and its application to NIMBUS-3 SIRS observations. *Mon. Wea. Rev.*, **98**, 582-603.

Smith, W.L., P.K. Rao, R. Koffler, and W.R. Curtis, 1970: The determination of sea surface temperature from satellite high-resolution infrared window radiation measurements. *Mon. Wea. Rev.*, **98**, 604-611.

Smith, W.L. and H.B. Howell, 1971: Vertical distribution of atmospheric water vapor from satellite infrared spectrometer measurements. *J. Appl. Meteor.*, **10**, 1026.

Smith, W.L., H.M. Woolf, and H.E. Fleming, 1972: Retrieval of atmospheric temperature profiles from satellite measurements for dynamical forecasting. *J. Appl. Meteor.*, **11**, 113.

Smith, W.L., D.T. Hilleary, J.C. Fischer, H.B. Howell, and H.M. Woolf, 1974a: NIMBUS ITPR Experiment. *Appl. Optics*, **13**, 499-506.

Smith, W.L., D. H. Staelin, and J.T. Houghton, 1974b: Vertical temperature profiles from satellites - results from second generation instruments aboard NIMBUS-5. Proceedings of the COSPAR Symposium on Approaches to Earth Survey Problems Through the Use of Space Techniques, Akademie-Verlag, Berlin, 123-143.

Smith, W.L. and H.M. Woolf, 1976: The use of eigenvectors of statistical covariance matrices for interpreting satellite sounding radiometer observations. *J. Atmos. Sci.*, **35**, 1127-1140.

Smith, W.L., Woolf, H.M., Hayden, C.M., Wark, D.Q. and McMillin, L.M., 1979: The TIROS-N operational vertical sounder. *Bull. Amer. Met. Soc.*, **60**, 1177-1187.

Smith, W.L., F.W. Nagle, C.M. Hayden, and H.M. Woolf, 1981a: Vertical Mass and Moisture Structure from TIROS-N. *Bull. Amer. Met. Soc.*, **62**, 388-393.

Smith, W.L., V.E. Suomi, W.P. Menzel, H.M. Woolf, L.A. Sromovsky, H. E. Revercomb, C.M. Hayden, D.N. Erickson, and F.R. Mosher, 1981b: First Sounding Results from VAS-D. *Bull. Amer. Met. Soc.*, **62**, 232-236.

Smith, W.L., V.E. Suomi, F.X. Zhou, and W.P. Menzel, 1982: Nowcasting applications of geostationary satellite atmospheric sounding data. Published in Nowcasting, K. A. Browning (ed.), Academic Press, Inc., (London) Ltd., pp. 123-135.

Smith, W.L. and F.X. Zhou, 1982: Rapid extraction of layer relative humidity, geopotential thickness, and atmospheric stability from satellite sounding radiometer data. *Appl. Optics*, **21**, 924-928.

Smith, W.L., 1983: The retrieval of atmospheric profiles from VAS geostationary radiance observations. *Jour. Atmos. Sciences.*, **40**, 2025-2035.

Smith, W.L., 1985: Satellites. Chapter 10 of the Handbook of Applied Meteorology, edited by D.D. Houghton. published by John Wiley and Sons.

Smith, W.L., G.S. Wade, and H.M. Woolf, 1985: Combined atmospheric sounder/cloud imagery-a new forecasting tool. *Bull. Amer. Met. Soc.*, **66**, 138-141.

Smith, W.L., H.M. Woolf, and A.J. Schreiner, 1985: Simultaneous retrieval of surface and atmospheric parameters: a physical and analytically direct approach. Advances in Remote Sensing, A. Deepak, H.E. Fleming, and M.T. Chahine (Eds.), ISBN 0-937194-07-7, 221-232.

Smith, W.L., W.P. Bishop, V.F. Dvorak, C.M. Hayden, J.H. McElroy, F.R. Mosher, V.J. Oliver, J.F. Purdom, and D.Q. Wark, 1986: The Meteorological Satellite: Overview of 25 years of operation. *Science*, **231**, 455-462.

Smith, W.L., 1991: Atmospheric soundings from satellites - false expectation or the key to improved weather prediction. Royal Meteorological Society, Symons Memorial Lecture, London, UK, May 16, 1990. *Jour. Roy. Meteor. Soc.*, **117**, 267-297.

Smith, W. L., R.O. Knuteson, H.E. Revercomb, W. Feltz, H.B. Howell, W.P. Menzel, N. Nalli, O. Brown, J. Brown, P. Minnett, and W. McKeown, 1996: Observations of the infrared radiative properties of the ocean - Implications for the measurement of sea surface temperature via satellite remote sensing. *Bull. Amer. Meteor. Soc.*, **77**, 41-51.

Soden, B.J., C S. Velden and R.E. Tuleya, 1999: The impact of satellite-derived winds on GFDL hurricane model forecasts. *Mon. Wea. Rev.*

SS/LORAL, 1995: Performance in space. CD/ROM, Space Systems LORAL, 3825 Fabian Way, Palo Alto, CA 94303

Staelin, D.H., A.H. Barrett, J.W. Waters, F.T. Barath, E.J. Johnston, P.W. Rosenkranz, N.E. Gaut, and W.B Lenoir, 1973: Microwave Spectrometer on the NIMBUS-5 Satellite: Meteorological and Geophysical Data. *Science*, **182**, 1339-1341.

Staelin, D.H., 1976: Measurements and interpretation of the microwave spectrum of the terrestrial atmosphere near 1 cm wavelength. *J. Geo. Res.*, **71**, 2875.

Staelin, D.H., K.F. Kunzi, R.L. Pettyjohn, R.K.L. Poon, R.W. Wilsox, and J.W. Waters, 1976: Remote sensing of atmospheric water vapor and liquid water with the Nimbus-5 microwave spectrometer. *J. Appl. Meteor.,* **15**, 1204-1214.

Stowe, L.L., E.P. McClain, R. Carey, P. Pellegrino, G. Gutman, P. Davis, C. Long, and S. Hart, 1991: Global distribution of cloud cover derived from NOAA/AVHRR operational satellite data. *Adv. Space Res.*, **11**, 51-54.

Stowe, L.L., R.M. Carey, and P.P. Pellegrino, 1992: Monitoring the Mt. Pinatubo Aerosol Layer with NOAA/11 AVHRR Data. *Geo. Res. Lett.*, **19**, 159-162.

Strabala, K.I., S.A. Ackerman, and W.P. Menzel, 1994: Cloud Properties Inferred from 8-12μm Data. *J. Appl. Meteor.*, **33**, 212-229.

Strand, O.N. and E.R. Westwater, 1968: Statistical estimation of the numerical solution of a Fredholm integral equation of the first kind. *J. Ass. Comp. Mach.*, **15**, 100.

Suomi, V.E., 1958: The radiation balance of the earth from a satellite. Annals of the IGY, Vol. 1, 331-340.

Suomi, V.E., 1969: Recent developments in satellite techniques for observing and sensing the atmosphere. *The Global Circulation of the Atmosphere,* Royal Meteorological Society, London, G. A. Corby, Ed., 222-234.

Suomi, V.E. and R. Parent, 1968: A color view of planet earth. *Bull. Amer. Meteor. Soc.*, **49**, 74-75.

Suomi, V.E., R. Fox, S.S. Limaye, and W.L. Smith, 1983: McIDAS III: A Modern Interactive Data Access and Analysis System. *J. Clim. Appl. Met.*, **22**, 766-778.

Szejwach, G., 1982: Determination of semi-transparent cirrus cloud temperatures from infrared radiances: application to Meteosat. *J. Appl. Meteor.*, **21**, 384.

Tarpley, J.D., S.R. Schneider, and R.L. Money, 1984: Global Vegetation indices from the NOAA-7 meteorological satellite. *J. Climate Appl. Meteor.*, **23**, 491-494.

Tepper, M., 1982: Early program development and implementation. NASA Conference Publication 2257, 5-33.

Tikhonov, A.N., 1963: On the solution of incorrectly stated problems and a method of regularization. Dokl. Acad. Nauk. USSR, **151**, 501.

Townshend, J.R. G., C. . Justice, and V. Kalb, 1987: Characterization and classification of South American land cover types using satellite data. *Int. J. of Remote Sensing*, **8**, 1189-1207.

Tucker, C. ., B. . Holben, and T. . Goff, 1984: Intensive forest clearing in Rondonia, Brazil, as detected by satellite remote sensing. *Remote Sensing of Environment*, **15**, 255-261.

Turchin, V.F. and V.Z. Nozik, 1969: Statistical regularization of the solution of incorrectly posed problems. Izv. Acad. Sci. USSR Atmos. Oceanic Phys., **5**, 14.

Twitchell, P.F., E.A. Rasmussen, and K.L. Davidson (ed), 1989: Polar and Arctic Lows. A. Deepak Publishing, Hampton, VA., 420pp.

Twomey, S., 1963: On the numerical solution of Fredholm integral equations of the first kind by the inversion of the linear system produced by quadrature. *J. Ass. Comput. Mach.*, **10**, 97.

Twomey, S., 1977: An introduction to the mathematics of inversion in remote sensing and indirect measurements. Elsevier, New York.

Uccellini, L.W. and D.R. Johnson, 1979: The coupling of upper and lower tropospheric jet streaks and implications for the development of severe convective storms. *Mon Wea. Rev.*, **107**, 682-703.

van de Boogaard, H.M.E. (ed), 1966. Satellite data in meteorological research. NCAR-TN-11, National Center For Atmospheric Research, Boulder, Co, 349pp.

Vaughn, W.W., 1982: Meteorological satellites - Some early history. *NASA Conference Publication 2227*, 1-2.

Velden, C.S., 1987: Satellite observations of Hurricane Elena using the VAS 6.7 micron water vapor channel. *Bull. Amer. Meteor. Soc.*, **68**, 210-215.

Velden, C.S. and W.L. Smith, 1983: Monitoring tropical cyclone evolution with NOAA satellite microwave observations. *J. Climate Appl. Meteor.*, **22**, 714-724.

Velden, C.S., W.L. Smith and M. Mayfield, 1984: Applications of VAS and TOVS to tropical cyclones. *Bull. Amer. Meteor. Soc.*, **65**, 1059-1067.

Velden, C.S., C.M. Hayden, W.P. Menzel, J.L. Franklin and J.S. Lynch, 1992: The impact of satellite-derived winds on numerical hurricane track forecasting. *Weather and Forecasting*, **7**, 107-118.

Velden, C.S., C.M. Hayden, S.J. Nieman, W P. Menzel, and S. Wanzong, 1997: Upper-tropospheric winds derived from geostationary satellite water vapor observations. *Bull. Amer. Meteor. Soc.*, **78**, 173-195.

Velden, C.S., T.L. Olander and S. Wanzong, 1998: The impact of multispectral GOES-8 wind information on Atlantic tropical cyclone track forecasts in 1995. Part I: Dataset methodology, description, and case analysis. *Mon. Wea. Rev.*, **126**, 1202-1218.

Velden, C.S., D. Stettner and J. Daniels, 2000: Wind vector fields derived from GOES rapid-scan imagery. 10th Conf. on Satellite Meteorology, Long Beach, CA., Amer. Meteor. Soc., Boston, MA.

Vicente, G.A., R.A. Scofield, and W.P. Menzel, 1998: The operational GOES infrared rainfall estimation technique. Bull. Amer. Meteor. Soc., **79**, 1883-1898.

Vonder Haar, T.H., G.G. Campbell, E.A. Smith, A. Arking, K. Coulson, J. Hickey, F. House, A. Ingersoll, H. Jacobowitz, L. Smith, and L. Stowe, 1981: Measurements of the earth radiation budget from satellites during the first GARP global experiment. *Advance Space Research*, **1**, 285-297,

Walton, C., 1980: Deriving sea surface temperatures from TIROS-N data. Remote Sensing of Atmospheres and Oceans, Academic Press, 547-579.

Wark, D.Q., 1961: On indirect temperature soundings of the stratosphere from satellites. *J. Geo. Res.*, **66**, 77.

Wark, D.Q., and H.E. Fleming, 1966: Indirect measurements of atmospheric temperature profiles from satellites. *Mon. Wea. Rev.*, **94**, 351-362.

Wark, D.Q., D.T. Hilleary, S.P. Anderson, and J.C. Fischer, 1970: NIMBUS satellite infrared spectrometer Experiments. *IEEE Trans. Geosci. Electron.*, **GE-8**, 264-270.

Weinreb, M.P. and D.S. Crosby, 1972: Optimization of spectral intervals for remote sensing of atmospheric temperature profiles. *Remote Sensing of the Environment*, **2**, 193-201.

Weinreb, M., 1996: Real-world calibration of GOES-8 and -9 sensors. *Technical Proceedings of the Society of Photo-Optical Instrumentation Engineers International Symposium on GOES-8 and Beyond*, August 4-9, 1996, Denver CO, Int. Soc. for Optical Eng., **2812**, 572-586.

Weinreb, M., M. Jamieson, N. Fulton, Y. Chen, J.X. Johnson, J. Bremer, and J. Baucom, 1997: Operational calibration of the imagers and sounders on the GOES-8 and -9 satellites. *NOAA* Technical *Memorandum NESDIS 44*, pp. 32.

Weinstein, M. and V.E. Suomi, 1961: Analysis of satellite infrared radiation measurements on a synoptic scale. *Mon. Wea. Rev.*, **89**, 419-428.

Weiss, C.E. and J.F.W. Purdom, 1974: The effect of early morning cloud cover on afternoon thunderstorm activity. *Mon. Wea. Rev.*, **102**, 400-401.

Welch, R.M., S.K. Sengupta, A.K. Goroch, P. Rabindra, N. Rangaraj, and M. S. Navar, 1992: Polar cloud and surface classification using AVHRR imagery: An intercomparison of methods. J. Appl. Meteor., 31, 405-420, 1992.

Weldon, R.B. and S.J. Holmes, 1991: Water Vapor Imagery. NOAA Tech. Rep. NESDIS 57, US Department of Commerce, NOAA, NESDIS, Washington, D.C. 213 pp.

Wexler, H., 1954: Observing the weather from a satellite vehicle. British Interplanetary Society, 13, 269-276.

Wu, X., W.P. Menzel, and G.S. Wade, 1999: Estimation of Sea Surface Temperatures using GOES-8/9 radiance measurements. Bull. Amer. Met. Soc., 80, 1127-1138.

Wylie, D.P. and W.P. Menzel, 1989: Two Years of Cloud Cover Statistics Using VAS. Jour. Clim., 2(4), 380-392.

Wylie, D.P., W.P. Menzel, H.M. Woolf, and K.I. Strabala, 1994: Four Years of Global Cirrus Cloud Statistics using HIRS. Jour. Clim., 7, 1972-1986.

Wylie, D.P. and W.P. Menzel, 1999: Eight years of global high cloud statistics using HIRS. Jour. Clim., 12, 170-184.

Yamanouchi, T., K. Suzuki, and S. Kawaguci, 1987: Detection of clouds in Antarctica from infrared multispectral data of AVHRR. J. Meteor. Soc. Japan, 65, 949-962.

Zandlo, J.A., W.L. Smith, W.P. Menzel, and C.M. Hayden, 1982: Surface temperature determination from an amalgamation of GOES and TIROS-N radiance measurements. Appl. Meteor., 21, 44-50.

Zapotocny, T.H., S.J. Nieman, W.P. Menzel, E. Rogers, D.F. Parrish, G.J. DiMego, J.P. Nelson III, M. Baldwin, and T.J. Schmit, 2000: A case study of the sensitivity of the Eta Data Assimilation System. Weather and Forecasting, **15**, 603-621.

APPENDIX C

PROBLEMS

Problem Set for Chapter 2

1. (a) Given that $c = f\lambda$ and $\nu = 1/\lambda$, derive expressions relating the df and $d\nu$ corresponding to a linewidth $d\lambda$. (b) An infrared window centred at 900 wavenumbers has a bandpass width of 100 wavenumbers. What is the bandpass width and central wavelength in microns?

2. What fraction of the radiative flux emitted by the sun is intercepted by the earth?

3. What is the ratio of the blackbody radiances, $B(\lambda)$, at 300 K and 6000 K at (a) .5 μm, (b) 10 μm, and (c) 20 GHz?

4. (a) What is the monochromatic radiance of the sun at .5 microns (assuming a sun temperature of 5800 K)? (b) What is the monochromatic irradiance at .5 microns at the surface of the sun? (c) What is it at the surface of the earth?

5. Find the wavelength (within 0.1 microns) at which the incoming solar monochromatic irradiance at the top of earth atmosphere is equal to the outgoing terrestrial monochromatic irradiance. Assume the sun and earth are emitting at 6000 K and 300 K respectively.

6. Show that for all periods of equal angular displacement in the earth's annual orbit about the sun, the solar energy falling on the earth is the same. Use conservation of angular momentum and the fact that the solar irradiance varies as the inverse square of the earth sun distance.

7. The maximum intensity of a blackbody at 300 K is 153 mW/m2/ster/cm-1. At what wavenumber does this occur? At what wavenumber and temperature is the maximum intensity of a blackbody twice this value? Derive your answer without calculating the Planck function values explicitly.

8. Prove that $B(\nu_{max}, T) = \text{const}*T^3$.

9. Show that the mean energy of quantized oscillators expressed as

$$\varepsilon_{av} = \frac{\sum_{n=0}^{\infty} nhf\, e^{-nhf/kT}}{\sum_{n=0}^{\infty} e^{-nhf/kT}},$$

equals

$$\varepsilon_{av} = \frac{hf}{e^{hf/kT} - 1}.$$

10. Temperature sensitivity, a, is defined by $dB/B = a*dT/T$. This is a measure of the percentage radiance change versus the percentage temperature change. What is the temperature sensitivity at 200 and 300 K for the short-wave (2500 cm-1) and long-wave (1000 cm-1) windows? Which window is most sensitive to changes in the earth surface temperature?

11. A satellite sensor in polar orbit at 800 km views the earth with a sensor field of view of 20 km in diameter. Assume that the surface of the earth is at 300 K and that the filter in front of the sensor transmits all radiation in the spectral region 820 and 970 wavenumbers. Determine the spectral irradiance detected. How does this change if the field of view is 1 km in diameter and the filter only transmits radiation between 880 to 930 wavenumbers?

12. The Meteosat infrared window covers 790 to 940 cm-1. The GOES infrared window covers to 890 to 980 cm-1. What is the difference in the irradiance detected by the two sensors when viewing a scene at 300 K? What is the difference in brightness temperature detected? Assume that the atmosphere is transparent at these wavelengths.

13. The new GMS-5 water vapour band covers the spectral range of 1400 to 1490 cm-1. Adjust the Planck function to account for the spectral width by replacing T with a+bT, where you must determine a and b by least squares fit over the terrestrial temperature range 180 to 300 K.

$$B_{adj}(\nu_c,T) = B(\nu_c, a+bT) = \int B(\nu,T)\, S(\nu)\, d\nu \,/\, \int S(\nu)\, d\nu$$

Assume that the spectral response, $S(\nu)$,is one inside and zero outside this range and that the centre wavenumber, ν_c, is 1445 cm-1. What is the largest error in brightness temperature in the terrestrial range if you assume a=0 and b=1?

14. A geostationary satellite senses visible (.45 to .55 um) and infrared (9.95 to 10.05 μm) radiation. (a) Determine the ratio of the visible to infrared radiance detected; (b) What is the ratio of visible to infrared energy detected? Use the following information as necessary.

visible bandwidth = infrared bandwidth = .1 micron,
vis detector area = IR detector area = .5 x 10-4 m2,
vis FOV = IR FOV = 4 x 4 km2,
r(visible reflectance at earth sfc) = .5,
T(sun) = 6000 K, T(earth sfc) = 300 K,
R(sun) = 7 x 10+8 m,
R(sun-earth) = 1.5 x 10+11 m,
R(earth-sat) 3.6 x 10+7 m .

15. The Planck function constants have been adjusted. c1 is now 1.191044 x 10-5 mW/(m2*sr*cm-4), down from 1.191066. c2 is now 1.43877 cm*K, down from 1.43883. What is the resulting percentage change in the radiance from a 300 K target at 900 cm-1.

Problem Set for Chapter 3

1. (a) The solar irradiance reaching Jupiter is roughly 50 W/m**2. Assuming the albedo, A, of Jupiter is 60%, calculate the effective temperature, T_e, by equating the absorbed solar radiation with the emitted thermal radiation; (b) If there is an incremental change in albedo, dA/A, what is the corresponding change in effective temperature, dT_e/T_e?

2. If the effective temperature of Mars is 220 K and the surface temperature is 240 K, what is the average absorptance of the atmosphere of Mars to long-wave radiation? Assume that the surface behaves like a blackbody and the atmosphere is transparent to solar radiation; use conservation of energy at the top of the atmosphere and at the surface to derive your answer.

3. Venus is 25% closer to the sun than the earth ($R_{vs} = .75R_{es}$) and its effective temperature is 230 K. What is the albedo of Venus with respect to the earth albedo?

4. The distance of a cylindrical spinning geostationary satellite is about six times the earth radius. The satellite has its spin axis aligned with the earth spin axis. The radius of the cylinder is equal to its height. Calculate the equilibrium temperature of the satellite in the earth-satellite system (ignoring the sun), assuming an effective equilibrium temperature for the earth of 255 K and assuming the satellite is a blackbody.

5. The distance between the earth and the sun varies about 3.3% between a maximum in early July and a minimum in early January. What is the corresponding seasonal change in effective temperature? Assume the earth albedo is 30%.

6. Assume that the surface of the earth acts like a blackbody with surface temperature 300 K, that the average albedo of the earth-atmosphere system for solar radiation is 30%, and that the atmosphere is transparent to solar radiation: (a) What is the average absorptance to long-wave radiation? (b) How much does the absorptance to long-wave radiation have to change to cause a 1 K increase in the surface temperature? (c) How much does the albedo have to change to offset the change in atmospheric long-wave absorptance in order to keep the surface temperature constant? Solve (b) by relating the change in absorptance, da, to the change in surface temperature, dT_s, and then solve (c) by relating da to the change in albedo, dA.

7. (a) Derive an expression for the irradiance emitted by the topmost layer of a multi-layered atmosphere, transparent in the visible, in terms of the absorptivity of the layer in the infrared, a, and the total irradiance of planetary radiation emitted to space, E. (b) Show that for an infinitesimally thin topmost layer, the radiative equilibrium temperature of the top of the atmosphere approaches 84% of the effective radiative equilibrium temperature of the whole planet. Hint: let absorptivity, a, for the thin top-most layer approach zero.

8. Consider the earth to have an albedo of 30% and an atmosphere consisting of two layers. Each layer has an absorptance of 0.1 for incoming solar radiation; the upper (lower) layer has an absorptance of 0.4 (0.6) for outgoing long-wave radiation. Assume that the surface of the earth behaves like a blackbody. Calculate the radiative equilibrium temperatures of the surface of the earth and the two atmospheric layers.

9. (a) The GOES infrared window from geostationary orbit at 36,000 km detects the earth radiance from a surface at 300 K in the infrared window between 890 to 980 cm-1. For simplicity assume constant radiance over this spectral interval to be 120 mW/m2/ster/cm-1. How many 10 micron photons hit the detector every 180 microseconds, if the field of view is 4 km in diameter and the detector surface area is .5 x 10-4 m2? (b) If this were polar orbit at 800 km, what would your answer be?

10. Assume that the angular momentum of the earth due to its motion around the sun is quantized according to Bohr's relation $mvr = nh/2\pi$. What is the quantum number n? Can this quantum number be detected?

11. The Lyman emission lines are associated with transitions of excited states to the ground state of the hydrogen atom. What are the wavenumbers of the first three lines of the Lyman series? From these data infer the wavenumber of the first line of the Balmer series (transitions from the second excited state to the first excited state). Can the hydrogen atom emit (or absorb) in the infrared? Explain.

12. (a) The rotational spectrum of CO2 shows a series of evenly spaced lines 1.5 cm-1 apart. What does this imply about the moment of inertia of the CO2 molecule? (b) The vibrational absorption line for CO2 occurs at 2325 cm-1 (4.3 microns). What does this imply about the "spring constant" of CO2 vibrations given that the mass of a proton is 1.67x10-27 kg?

13. (a) Determine the normal modes of vibration for a linear O_3 molecule; (b) Recalling that the mass of the proton is given by $m_p = 1.67 \times 10^{-27}$ Kg, that the spring constant for the O_3 is roughly $k \sim 3.35 \times 10^2$ J/m2 (from the second derivative of the potential curves), and that mass of O is $16m_p$, find the absorption wavelength of O_3 for the three modes. Appendix A presents a similar calculation for the CO2 molecule.

14. A certain gas has an absorption coefficient of 0.02 m2/kg for all wavelengths. What fraction of a beam of incident radiation is absorbed in passing vertically through a layer containing 1.5 kg/m2 of the gas. How much gas would the layer have to contain in order to absorb one-fifth of the incident radiation?

15. (a) Consider an atmospheric constituent which has a mixing ratio of unity for all heights and whose absorption coefficient at wavelength w is given by

$$kw(p) = kw(0)(p/p0)^{1/2}$$

where p0 is sea level pressure. Derive an expression for sunlight radiance which arrives at sea level, Iw(0), after traversing the atmosphere at zenith angle z, given the radiance incident at the top of the atmosphere, Iw(∞); (b) If the absorption by the total atmosphere is 75% for normal incidence, what is the value of the absorption coefficient at sea level, kw(0)? Use p0 as 1.013 x 10**5 J/m3.

16. The average CO2 concentration in the atmosphere varies by about one percent annually (in part due to foliage release in the autumn). How do the radiance and the brightness temperature at 676 cm-1 in the middle of the CO2 absorption band change in responsey? Explain any approximations you make in deriving your answer.

17. A two-channel (19 and 22 Ghz) microwave radiometer on the ground is looking straight up. The brightness temperature measured is given by

$$T_\nu = (1 - \tau_\nu)\, T_{\text{low atm}}$$

where

$$\tau_\nu = \exp(-k_\nu u).$$

The upper atmosphere does not emit significantly at 19 and 22 Ghz. The moisture is confined to the lower atmosphere which is assumed to be isothermal at 280 K. What is the brightness temperature difference $T_{19} - T_{22}$ as a function of water vapor path length? Use $k_{19} = 3.75 \times 10^{-3}$ kg^{-1}m^2 and $k_{22} = 9.12 \times 10^{-3}$ kg^{-1}m^2 and let u increase from 5 to 40 kg m^{-2} in 5 kg m^{-2} increments.

18. Derive an expression for $d\tau(p,ps)/dp$ in terms of $\tau(ps,0)$, $\tau(p,0)$, and $d\tau(p,0)/dp$ where $\tau(pa,pb)$ is the probability of transmission from pressure level pa to pb for a given wavelength. ps denotes the surface pressure and 0 indicates the pressure at the top of the atmosphere.

19. On a clear day, measurements of the direct solar irradiance E at the surface of the earth in the 1.5 to 1.6 micron wavelength interval give the following values:

Zenith angle (degrees)	E (W/m2)
40	$1.40\ 10^{-3}$
50	1.26
60	1.05
70	0.76

Find the solar irradiance at the top of the atmosphere and the transmittance for normal incidence in this wavelength interval.

20. Consider a slab of material that has a transmittance τ and has a reflectance r at each surface. Derive a expression for the transmitted radiance, I(s), in terms of the incident radiance, I(0), and r and τ.

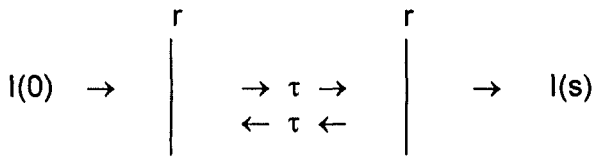

21. The big bang theory predicts that the average radiance from deep space should have a brightness temperature of 2.7 K. This has been observed with microwave remote sensing. In addition the sky near the southern end of the constellation Leo has been noticed to be warmer by about 0.003 K when viewed at 6 cm-1. Assuming this is consistent with a Doppler shift, what is the velocity of south Leo with respect to our part of the universe (e.g. the Milky Way)?

Problem Set for Chapter 4

1. Consider the black and white spheres used by Suomi to measure visible and infrared irradiance in the earth atmosphere. The absorptance of the white ball is .3 and .7 for short and long-wave radiation respectively; for the black ball it is .9 for all wavelengths. The temperature of the white ball is 255 K; for the black ball it is 300 K: (a) What is the outgoing infrared irradiance? (b) If the temperature of the black ball decreases by one degree, is the change in inferred outgoing infrared irradiance greater or smaller than if the temperature of the white ball increases by one degree?

2. Calculate the daily insolation on the top of the atmosphere at (a) the south pole in the winter solstice, and (b) the equator in the vernal equinox. Use the mean earth-sun distance and a solar constant of 1380 W/m2 in your calculations.

3. If one-third of the incident solar energy were absorbed by the atmosphere, what would be the average rate of temperature increase per day of the atmosphere (assuming no loss)? Use for the atmosphere, specific heat at constant pressure Cp = 1005 J kg-1 K-1, density ρ = 1.3 kg m-2, and atmospheric depth (scale height) H = 7 km.

4. Prove that for an atmosphere in infrared radiative equilibrium, the total infrared optical depth is given by the expression

$$\sigma^{*}_{tot} = (T_{sfc}^{4}/T_{top}^{4}) - 2 \ .$$

Start with the equations for irradiance going up and down through the atmosphere.

$$dE\uparrow/d\sigma^* = E\uparrow - \pi B$$

$$-dE\downarrow/d\sigma^* = E\downarrow - \pi B$$

and realize that the net irradiance $E\uparrow - E\downarrow$ is constant at all levels. πB is given by Stefan's Law.

5. Assuming the atmosphere is an absorber with uniform absorption coefficient and uniformly mixed with height, what is the (a) net irradiance (b) the temperature discontinuity at the surface, and (c) the total atmospheric infrared optical depth under radiative equilibrium conditions when the top of the atmosphere is at 201 K and the surface ground temperature is at 280 K?

6. The figure in Chapter 4 depicting annual mean global energy balance for the earth-atmosphere system shows 30 units of radiation (one unit equals 3.43 W/m2) going to sensible and latent heat flux in the atmosphere. If these processes were removed from the picture, how much hotter would the earth surface have to be in order to maintain thermal equilibrium for the earth-atmosphere system?

Problem Set for Chapter 5

1. Consider a three channel radiometer with spectral bands centred at 676.7, 708.7, and 746.7 cm-1 that is sensing radiation from an atmosphere with the following temperature and transmittance profiles.

Pressure	Temperature	Transmittance		
		676.7	708.7	746.7
10mb	233 K	.86	.96	.98
150	222	.05	.65	.87
600	251	.00	.09	.61
1000	280	.00	.00	.21

(a) Use a simple quadrature formula to evaluate the expected upwelling radiance R_ν for each sounding channel from the radiative transfer equation.

$$R_\nu = B_\nu(T_S)\tau_\nu(p_S) + \int_{p_S}^{o} B_\nu(T_p)\, d\tau_\nu$$

$$= B_\nu(T_{1000})\tau_\nu(1000) + 1/2\,(B_\nu(600)+B_\nu(1000))\,(\tau_\nu(600)-\tau_\nu(1000))$$

$$+ 1/2\,(B_\nu(150)+B_\nu(600))\,(\tau_\nu(150)-\tau_\nu(600))$$

$$+ 1/2\,(B_\nu(10)+B_\nu(150))\,(\tau_\nu(10)-\tau_\nu(150))$$

(b) Let p_v denote the pressure level at which the maximum of the weighting function for a given spectral band is located (p_v = 50, 400, 900 mb for 676.7, 708.7, and 746.7 cm^{-1}, respectively). Assume T_s = 280 K is known. Use a guess T(p) of T_{50} = 200, T_{400} = 250, T_{900} = 270 K. Calculate the guessed upwelling radiance I_v for each sounding channel from

$$I_v = B_v(T_S)\,\tau_v(p_S) + B_v(900)\int_{1000}^{600} d\tau_v + B_v(400)\int_{600}^{150} d\tau_v + B_v(50)\int_{150}^{10} d\tau_v$$

$$= B_v(1000)\,\tau_v(1000) + B_v(900)\,(\tau_v(600) - \tau_v(1000)) + B_v(400)\,(\tau_v(150) - \tau_v(600)) + B_v(50)\,(\tau_v(10) - \tau_v(150))$$

(c) Using the relaxation equation developed by Chahine, do two iterations to recover the best estimate of the temperature profile (T_{50}, T_{400}, and T_{900}). This requires iterating as follows:

$$\frac{R_v}{I_v^{old}} = \frac{B_v(T^{new}(p_v))}{B_v(T^{old}(p_v))}$$

(d) What approximations did you make in arriving at your answer? Estimate the errors in your resulting temperature profile.

(e) If you prefer, do two iterations using the Smith Iteration Method for (c) instead of the Chahine Relaxation Method.

2. When the atmosphere is guessed to be isothermal, show that the iteration solution by the Chahine Relaxation Method is independent of the guessed temperature.

3. A microwave radiometer in the window region is viewing a cloud at 400 mb (ε_{cld} = 0.5, T_{cld} = 240 K) obscuring the surface (ε_{sfc} = 1.0, T_{sfc} = 300 K). Assuming the lapse rate a = 10 K per 100 mb and the transmittance τ = 1.0-.0001*p where p is in mb, what is the observed brightness temperature?

4. (a) What brightness temperature will a nadir viewing microwave radiometer operating at 1.35 cm^{-1} (absorption coefficient equal to .0100 m^2/kg) measure over land (assume surface emissivity equal to 1) for the atmospheric moisture and temperature profile given below?

pressure (mb)	Temperature (K)	mixing ratio (g/kg)
0	0	0
200	200	.02
600	240	0.20
800	280	2.00
1000	300	8.00

Start by calculating the transmittance for each layer using the relation

$$\Delta\tau = k\, g^{-1}\, q\, \Delta p$$

and realizing that 100 N/m^2 = 1 mb. (b) What is the new brightness temperature, if the surface emissivity changes to .9?

Problem Set for Chapter 6

1. A hot plume of industrial waste is obstructing the view of an infrared radiometer into the distance. Thus the radiometer senses a hotter temperature. What is the difference of the radiances sensed by the radiometer when viewing a clear FOV and then a plume contaminated FOV? Use the indicated transmittances and blackbody radiances for background, plume, and foreground to calculate your answer.

	Background	plume	foreground
Temperature, T (degrees K)	Tb=300	Tp=340	Tf=300
Planck Rad, B (mW/m2/ster/cm-1)	Bb=115	Bp=195	Bf=115
Transmittance, τ (dimensionless)	τb=.9	τp=.3	τf=.9

2. Consider the simplified model of the short-wave energy balance shown below. The model atmosphere consists of an upper layer with transmittance τ_1, a partial cloud layer with the fractional area f_c covered by clouds with reflectance r_c in either direction, and a lower layer with transmittance τ_2. The earth surface has an average reflectance r_s. Assume that no absorption takes place within the cloud layer and that no scattering takes place within layers 1 and 2. Allow for multiple reflections.

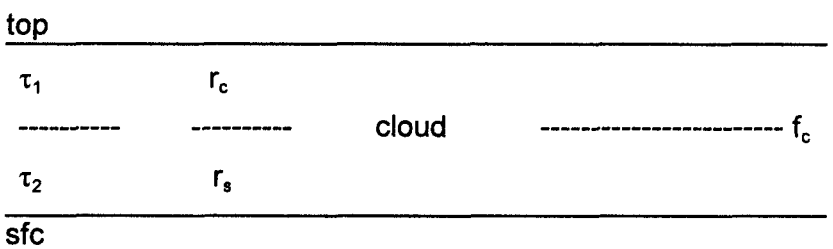

(a) Derive an expression for the planetary albedo; (b). Calculate the albedo for f_c=0.75, r_c=0.5, τ_1=0.95, τ_2=0.90, and r_s=0.15; (c) Use the model to estimate the albedo of a cloud free earth; (d) Use the model to estimate the albedo of a completely cloud covered earth.

3. An infrared radiometer with 4 channels is viewing a clear field of view (fov). The following table presents wavelength and noise equivalent radiance. The surface temperature is 300 K. A little bit of high opaque cloud at 230 K moves in. How much cloud can be present in the fov (what percentage) and still not be detected (be within instrument noise) for each channel? Use B proportional to T^x where x=c2*ν/T.

Channel	Wavenumber (cm-1)	NEDR (mW/m2/ster/cm-1)
1	2500	0.004
2	1450	0.1
3	900	0.1
4	700	0.8

4. Calculate the radiances at 8, 11, 12 μm for a scene of clear sky at 300 K and a cloud at 230 K with varying cloud amount. Let the cloud fraction vary from N = 0.0, 0.2, 0.4, 0.6, 0.8, and 1.0. Convert the radiances to brightness temperatures. Plot brightness temperature differences 8 - 11 versus 11 - 12 for the six different cloud fractions.

Problem Set for Chapter 7

1. A histogram of frequency versus infrared window brightness temperature is tabulated over a portion of the Indian Ocean. A least squares fit of the normal distribution probability function at the warm end of the histogram yields

$$\ln f = -10272.7 + 70.2T - 0.12T^2.$$

What is the SST?

2. Assume that a two channel radiometer is viewing broken clouds. One channel is the long-wave IR window channel and it measures 50 and 60 radiance units from adjacent fields of view (fovs). The other channel is a CO2 sensitive channel and it observes 65 and 80 radiance units respectively from the same two fovs. A nearby cloud free fov yields a window channel measurement of 100 radiance units: (a) What is the cloud free value of the CO2 channel observation? (b) If one fov is completely filled with clouds, what is the percentage cloud cover of the other fov?

3. There is a low layer of mist at 280 K obscuring the ocean at 300 K. A microwave radiometer is measuring sea surface temperature with 18 GHz observations. Assume that the emissivity of sea water is .5 and the optical thickness of the mist is .03. What error does the mist introduce to the brightness temperature determination of SST? Include the effects of surface reflection.

4. A split window channel radiometer measures 96.00 and 102.29 mW/m2/ster/cm-1 for the 11 (909) and 12 (833) micron (cm-1) channels respectively. The estimated atmospheric transmittance is .85 and .75 respectively for the two channels; the estimated sea surface emittance is .97 for both channels. What is the estimated sea surface temperature (SST)? Hint: Use B(833,T) = 9.55+1.03*B(909,T) and set up two equations (from R(833,Tb) and R(909,Tb) measurements) with two unknowns (B(909,Ts) and B(909,Ta)), where Ts is the SST and Ta is the mean atmospheric temperature)

Problem Set for Chapter 8

1. A radiometer observes clear column brightness temperatures of 291 and 282 degrees Kelvin at 11.0 and 12.7 microns respectively: (a) Assuming the water vapour absorption coefficients are .2 and .5 cm**2/g for the two channels, what is the surface temperature? (b) If the mean atmospheric temperature is 257 degrees Kelvin for the 12.7 micron channel, what is the estimated total precipitable water vapour? (c) If the variance in the observed brightness temperatures for 5x5 FOVs for the

12.7 micron channel is one half that for the 11.0 micron channel, what is the estimated total precipitable water vapour from the split window variance ratio?

2. Consider two cloud layers completing filling the satellite sensor field of view. Show that

$$I_{obs} - I_{clr} = \varepsilon 1 \int_{Ps}^{Pc1} \tau \, dB + \varepsilon 2 \int_{Ps}^{Pc2} \tau \, dB - \varepsilon 1 \, \varepsilon 2 \int_{Ps}^{Pc1} \tau \, dB$$

where εi and Pci are the emissivity and cloud pressure of the lower cloud (I=1) and the upper cloud (I=2).

3. The radiances for a cloudy field of view (fov) are measured to be 46.6, 60.3, and 52.5 mW/m2/ster/cm-1 in the 14.0, 13.3, and 11.2 micron channels respectively. The clear radiances inferred from nearby clear fovs are 55.3, 85.0, 84.0 mW/m2/ster/cm-1 respectively: (a) Using the window channel technique, estimate the cloud top pressure in the cloudy fov; (b) Using the CO2 absorption technique, estimate the cloud top pressure in the cloudy fov (see the following table for some of the necessary data). Explain the difference with the infrared window estimation; (c) Estimate the effective cloud amount using the cloud top pressure from (b); (d) If the noise in each measurement is .5 mW/m2/ster/cm-1, what is the range of possible cloud top pressure estimates using the CO2 technique?

P	T	τ14.0	τ13.3	τ11.2	B14.0	B13.3	B11.2
1000	279	.00	.30	.91	111.9	107.3	85.3
850	275	.06	.46	.96	106.0	101.3	79.8
700	266	.12	.61	.99	93.1	88.5	68.0
600	260	.18	.69	.99	85.0	80.4	60.7
500	252	.27	.76	.99	74.8	70.4	51.8
400	244	.38	.82	.99	65.3	61.0	43.8
300	230	.50	.86	.99	50.4	46.5	31.7
200	218	.61	.90	.99	39.3	35.8	23.3
100	214	.79	.94	.99	36.0	32.7	20.8
50	213	.90	.97	.99	35.1	31.9	20.3

4. Consider the effect of rain on 18 GHz microwave radiation. How will the brightness temperature measured by the scanning multichannel microwave radiometer (SMMR) on Nimbus 7 vary as a function of rainfall rate over the ocean? Neglect scattering. Assume that the transmittance of rain in is given by exp[-.022 R z] where R is the rainfall rate in mm/hr and z is the depth in kilometres of the rainfall through which the radiation has been transmitted. Assume that corrections for scan angle are already accounted for. Assume that the sea surface temperature is 300 degrees Kelvin and that the moist adiabatic lapse rate of 6 degrees Kelvin per kilometre occurs in the cloud. Assume that the emissivity of sea water at this temperature is one half. Let the rain shaft be uniform up to the height of the freezing level at 4.5 km and allow no precipitation above that height. Ignore the surface reflection term and let the atmosphere be transparent above the rain shaft. Plot your result as a function of R.

Problem Set for Chapter 9

1. The thermal wind equation says $(\Delta v/\Delta z) = (g / f / T_{av}) (\Delta T/\Delta x)$. At one km height, the wind is 10 m/s and the GOES measures a temperature gradient of 3 K over 100 km. Infer the wind at 2 km height. Use $(g / f / T_{av}) = 400$ m/s/K.

Problem Set for Chapter 12

1. An infrared radiometer with 4 channels is viewing a blackbody with temperature at 300 K. The following table presents wavelengths and noise equivalent temperatures.

Channel	Wavenumber (cm-1)	NEDT (deg K)
1	2500	0.2
2	1450	0.1
3	900	0.1
4	700	0.2

What are the noise equivalent radiances? What are the noise equivalent temperatures when the blackbody has a temperature of 220 K?

2. An infrared window channel radiometer views an earth target of 300 K. The filter has been mistakenly characterized as passing radiation at 900 cm-1, but in reality it passes radiation at 902 cm-1. What is the error in brightness temperature due to this misinformation?

3. Assume that a satellite infrared sensor is viewing a cloud deck above a warm ocean. The infrared radiance of the clouds is B_c and the ocean is B_o. Assume that the radiance to space is represented by a step function as shown below.

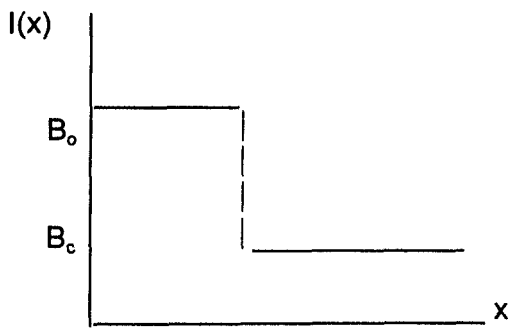

If the spatial resolution of the sensor is gaussian, so that

$$S(x-x_o) = \exp[-(x-x_o)^2/2\sigma^2],$$

where $\sigma = 8$ km

and the sampling is done every 4 km, plot the response of the sensor as it scans across the step function.

4. Assume that a satellite infrared sensor is viewing cold broken clouds above a warm ocean. The infrared radiance of the clouds is B_c and the ocean is B_o. Assume that the clouds are spaced

periodically and that the clouds are roll clouds oriented perpendicular to the scan direction (so that we can consider this to be a one dimensional problem). The spacing between clouds is S and the cloud fraction is N=(1-S/L) as shown below.

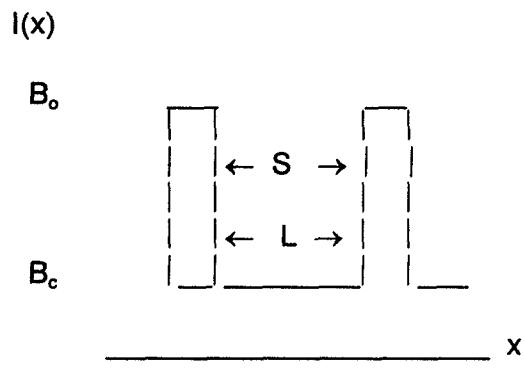

(a) What is the mean radiance over a cycle? What is the standard deviation about this value over a cycle? Plot $\sigma/(B_o-B_c)$ versus N. (b) If the spatial resolution of the sensor is finite and square of width Δ and amplitude $1/\Delta$, so that

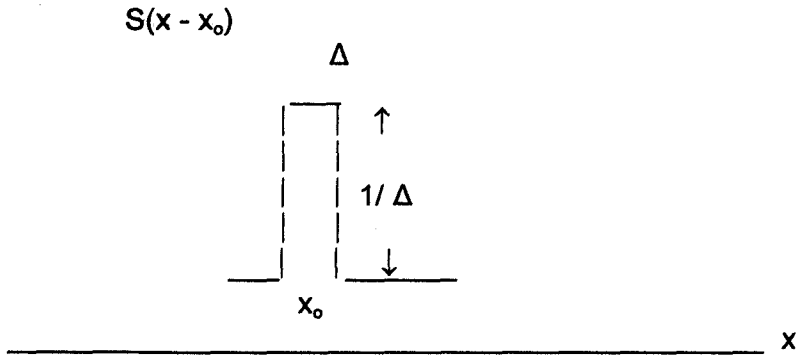

and the satellite sensed radiance is given by

$$R(x_O) = \int_{x_O-\Delta/2}^{x_O+\Delta/2} S(x-x_O)\, I(x)\, dx \ ,$$

what are the mean radiance and standard deviation about this value over a cycle? Assume N is less than 0.5 and that Δ is equal to S/2. Plot $\sigma/(B_o-B_c)$ versus N up to .5.

APPENDIX D

EXAM

D.1 TRUE OR FALSE. Indicate answer by circling T or F. Correct false statements where possible.

T F 1. The speed of electromagnetic radiation increases with increasing frequency.

T F 2. 2000 wavenumbers corresponds to 50 microns.

T F 3. The units of irradiance are energy/time/area.

T F 4. Solar radiance is the same at the sun and earth surface.

T F 5. The maxima of the Planck function per wavelength $B(\lambda max,T)$ and per wavenumber $B(\nu max,T)$ are related by $\lambda max = 1/\nu max$.

T F 6. 99% of the earth emitted irradiance comes from wavelengths greater than 4.0 microns.

T F 7. Wien's law can be derived by differentiating the Planck function with respect to temperature and equating the result with zero.

T F 8. The Stefan-Boltzmann law relates the irradiance to the fourth power of the brightness temperature for a given wavelength.

T F 9. Kirchhoff's law states that for energy to be conserved the absorbed energy must equal the emitted and transmitted energy.

T F 10. When Beer's law is modified to account for emission as well as absorption, it is necessary to invoke Kirchhoff's law to derive Schwarzchild's equation.

T F 11. If a planetary atmosphere is less absorbing in the visible wavelengths than at infrared wavelengths, then the surface temperature of that planet is less than its effective temperature.

T F 12. In the earth atmosphere, down-welling infrared radiation carries less energy than upwelling infrared radiation.

T F 13. Satellite sounding in the microwave (infrared) spectrum is accomplished in the O2 (CO2) absorption bands.

T F 14. Roughly half of the incoming solar radiation makes it to the surface of the earth.

The earth-atmosphere spectrum for a given scene is depicted in the figure below:

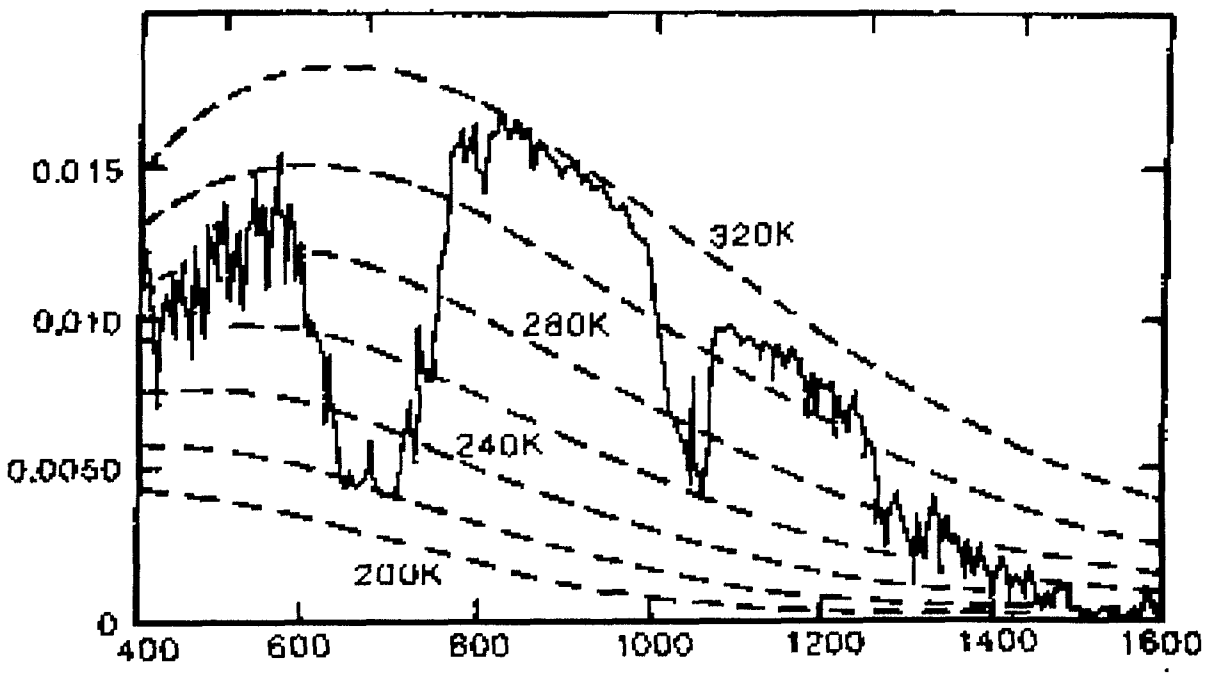

T F 15. The ordinate (y-axis) is radiance in mW/ster/m2/cm-1.

T F 16. The absorption band centres for CO2, O3, and H2O appear near abscissa values of 650, 1050, and 1600 respectively.

T F 17. The plateau between abscissa values 1100 and 1200 is a window region of the atmosphere.

T F 18. The dip at the abscissa value of roughly 800 is the location of the dirty window.

T F 19. In this scene, clouds are affecting the 1100 to 1200 region of the spectrum more than the 900 to 1000 region.

T F 20. The tropopause temperature for this scene is roughly 220 K.

T F 21. The split window temperature difference is about 10 K in this scene.

T F 22. At the band centre of abscissa value 700, the little peak is a result of warming with altitude in the stratosphere.

T F 23. At the band centre of abscissa value 1050, the little peak is the result of O3 absorption in the stratosphere.

T F 24. Instrument noise for the 500 to 600 part of the spectrum is about 5 K.

T F 25. The jagged peaks are the result of rotational absorption bands.

When a cloud at a single level is obscuring the instrument field-of-view, the radiance detected by the satellite infrared radiometer is represented by:

$$I_\lambda^{cd} = (1-\varepsilon_\lambda)B_\lambda(T_s)\tau_\lambda(p_s) + (1-\varepsilon_\lambda)\int_{p_s}^{p_c} B_\lambda(T(p))d\tau_\lambda$$

$$+ \varepsilon_\lambda B_\lambda(T(p_c))\tau_\lambda(p_c) + \int_{p_c}^{o} B_\lambda(T(p))d\tau_\lambda,$$

T F 26. The first two terms are radiative contributions from below the cloud that make it to the top of the atmosphere.

T F 27. The last term represents radiation absorbed by the atmosphere Above the cloud and thus not making it to the top of the atmosphere.

T F 28. The third term is the radiative contribution of the cloud itself that makes it to the top of the atmosphere.

T F 29. The first term is negligible for radiation at 14.0 mm.

T F 30. ε_λ is the earth surface emissivity.

The Earth atmosphere radiation budget measurements from satellite indicate that:

T F 31. The distribution of sunlight with latitude is responsible for our major climatic zones.

T F 32. The net radiation for the earth varies throughout the year in accordance with the earth-sun distance.

T F 33. The solar constant is between 1260 and 1280 W/m2.

T F 34. The albedo and long-wave radiation cycles are roughly in phase.

T F 35. Scattering of terrestrial radiation by the atmospheric constituents is relatively insignificant with regard to the global energy balance.

T F 36. During December, the outgoing long-wave radiation from the earth atmosphere is at a minimum because snow and cloud cover are at a maximum in the northern hemisphere.

T F 37. Outgoing long-wave radiation increases with cloudiness.

T F 38. Earth radiation budget studies have shown that global averages of outgoing terrestrial radiation are in phase with absorbed solar energy on an annual cycle.

T F 39. Reflected sunlight contributions to the radiance measured at 4.0 μm limits the usefulness of such measurements for daylight sea surface temperature determinations.

T F 40. SST determinations rely on alleviating the influence of clouds with split window infrared observations and accounting for the effects of atmospheric water vapour with the long-wave and short-wave infrared window observations.

T F 41. The correction for atmospheric water vapour attenuation in atmospheric windows requires knowledge of the atmospheric water vapour profile.

T F 42. As cloud amount varies (for a single layer of high cloud), the radiance observed in the 11 micron window is linearly related to the radiance observed in the 6.7 micron channel.

T F 43. If the brightness temperature difference 4 micron less 11 micron is greater than 3 K, then the field-of-view is either mostly cloudy or mostly clear.

T F 44. In polar regions, if the brightness temperature at 6.7 microns is warmer than that at 11.0 microns, then the FOV is probably clear.

T F 45. The moisture sensitive channel at 1.38 microns sees cirrus as well as lower stratus clouds.

T F 46. For ice clouds Tb13 ~ Tb11 and Tb11 >> Tb8.6, while for water clouds Tb13 > Tb11 and Tb11 ~ Tb8.6.

T F 47. Broken clouds within a pixel produce Tb11 < Tb4 for the same reason subpixel fires produce Tb4 > Tb11.

T F 48. Threshold brightness temperature tests for clouds using the infrared window are complicated by atmospheric moisture variations and non unit surface emissivity for various bio-regimes.

T F 49. As atmospheric moisture increases, Tb11-Tb12 increases while Tb8.6-Tb11 decreases.

T F 50. Vertical wind shear can be derived from horizontal temperature gradients using the thermal wind equation.

T F 51. Tropical cyclone intensity can be inferred from microwave brightness temperatures gradient between the eye of the storm and the stable surrounding environment. A 10 C gradient implies a pressure drop in the eye of about 5 mb.

T F 52. A column of rain cooler than the earth surface increases the observed brightness temperature in the microwave window over the rain free value.

Regarding geostationary and polar orbiting satellites indicate which characteristic is true for that instrument platform

G P 53. Observes the process itself rather than the effects of the process.

G P 54. Measures spatial gradients of temperature and moisture.

G P 55. Measures radiances in differing solar illuminations.

G P 56. Microwave helps with sounding in clouds.
G P 57. Offers best viewing of the tropics.

G P 58. Used to infer cloud drift winds.

G P 59. Evolved on Nimbus series of satellites.

G P 60. Has orbital period of 24 hours.

G P 61. Used to infer vegetation index.

G P 62. NOAA launched AMSU into this orbit.

D.2. SHORT PROBLEMS (allow 15 minutes per problem)

1. The Planck (P) function is given by

$$B(\lambda,T) = c1 / [\lambda^5 (e^{c2/\lambda T} - 1)]$$

(a) What is the Rayleigh Jeans (RJ) expression, valid in the long wavelength region of the spectrum? (b) Using c2 = 1.4 cm K, estimate (BP - BRJ) / BP for λT = 100 cm K. Keep second order terms for BP and only first order terms for BRJ.

2. If the CO2 concentration in the atmosphere is doubled, the net additional heating of the earth surface and the troposphere has been calculated to be 4 W/m2 (which is the negative net change in outgoing radiative flux density or irradiance at the tropopause). Using the Stefan-Boltzmann law and assuming that the effective temperature of the earth-atmosphere system is 280 K before the CO2 doubling, determine the associated temperature change of the earth-atmosphere system.

3. Venus is 25% closer to the sun than the earth ($R_{vs} = .75R_{es}$). Its effective temperature is 230 K compared to 255 K for the earth. If the earth albedo is 30%, what is the albedo of Venus?

4. Consider an atmosphere where the temperature profile is given by T(p) = 200 + 100 (p/ps) in degrees K. The transmittance for a microwave spectral band is given by $\tau(p) = 1.0 - 0.7$ (p/ps). Assuming reflection is negligible at the earth surface, what is the brightness temperature observed by the microwave sensor in this spectral band? Start with the RTE to develop your answer.

5. A hot plume of industrial waste is obstructing the view of an infrared radiometer into the distance. Thus, the radiometer senses a hotter temperature. What is the difference of the radiances sensed by the radiometer when viewing a clear FOV and then a plume contaminated

FOV? Use the indicated transmittances and radiances for background, plume, and foreground to calculate your answer.

	background	plume	foreground
temperature (degrees Kelvin)	$T_b = 300$	$T_p = 340$	$T_f = 300$
bb radiance (mW/m2/ster/cm-1)	$B_b = 115$	$B_p = 195$	$B_f = 115$
transmittance	$\tau_b = 0.9$	$\tau_p = 0.3$	$\tau_f = 0.9$

6. Two window channels (11 and 12 microns) are viewing the ocean in cloud free conditions. The observed brightness temperatures are 297 K and 293 K. The respective atmospheric transmittances are .97 and .94: (a) What is the ratio of the absorbing powers kw11/kw12? (b) What is the SST?

7. In a cloud free region over the ocean, the infrared window is being used to estimate sea surface temperature. If volcanic ash of .02 optical thickness in the long-wave infrared window and temperature Tc = 220 K obscures the ocean, what error is introduced to the sea surface temperature estimate Ts = 300 K? Express the transmittance of the volcanic ash $\tau = 1-\sigma$, and use the fact that at 900 cm-1 the Planck radiance is proportional to T^4.

8. There is a low layer of mist at 290 K obscuring ocean at 300 K. A radiometer in the microwave window is measuring sea surface temperature (SST). What error does the mist introduce to the SST? Assume that the emissivity of sea water ε_s is .5, the optical thickness of the mist σ_m is .02. Use $\sigma_m = \varepsilon_m = 1-\tau_m$. Include the contributions to the radiometer from the surface, the mist, and the surface reflection.

9. Assume that a two channel radiometer is viewing broken clouds. One channel is the long-wave infrared window channel and it measures energies of 24 and 60 units from adjacent fields of view. The other channel is a CO2 sensitive channel and it observes 36 and 90 units of energy respectively from the same two fields of view. A nearby cloud free measurement in the window channel has 108 units of energy: (a) What is the cloud free value of the CO2 channel observation? (b) If one of the fields of view is completely filled with clouds, what is the percentage cloud cover in the other field of view?

10. A radiometer sensitive in the short wave IR window (ν=2500cm-1) is viewing a 300 K scene when a 600 K fire starts. What fraction of the field of view must be on fire to increase the observed brightness temperature by 1% (3 K)? Use the fact that $B(2500\ \text{cm-1},T) \sim T^{12}$.

11. A histogram of frequency versus infrared window brightness temperature is tabulated over a portion of the Indian Ocean. A least squares fit of the normal distribution probability function at the warm end of the histogram yields

$$\ln f = -10272.7 + 70.2T - 0.12T^2.$$

What is the SST? Show how you arrive at your answer.

12. A window channel microwave radiometer ($\tau = 1$ throughout the atmosphere in the absence of clouds) is viewing a cloud at 400 mb (with $\varepsilon_c = .3$, $T_c = 240$ K) over the earth surface (with $\varepsilon_s = 1.0$, $T_s = 300$ K). Assuming a uniform lapse rate of 10 degrees per 100 mb, what is the observed microwave window brightness temperature?

13. A radiometer is viewing broken clouds. The window channel brightness temperature suggests clouds at 500 mb. The CO2 slicing technique indicates clouds at 400 mb. Estimate the effective emissivity of the clouds in the fov. Use data in the following table to derive your answer.

P	T	B11.2	$-\int_{Ps}^{Pc} \tau(11.2)\, dB(11.2)$
1000	279	85.3	0.00
850	275	79.8	5.23
700	266	68.0	16.71
600	260	60.7	23.88
500	252	51.8	32.68
400	244	43.8	40.64
300	230	31.7	52.60
200	218	23.3	60.95
100	214	20.8	63.37

14. The thermal wind equation says $(\Delta v/\Delta z) = (g / f / Tav)^*(\Delta T/\Delta x)$. At one km height the wind is 10 m/s and the VAS measures a temperature gradient of 3 K over 100 km. Infer the wind at 2 km height. Use (g / f / Tav) = 400 m/s/K.